A new approach to Highly Multiplexed Spectroscopy

CLAIRE LOUISE POPPETT

A new approach to Highly Multiplexed Spectroscopy

Claire L. Poppett

A Thesis presented for the degree of
Doctor of Philosophy

Centre for Advanced Instrumentation
Department of Physics
Durham University
England

August 2011

A new approach to Highly Multiplexed Spectroscopy

Claire L. Poppett

Submitted for the degree of Doctor of Philosophy

August 2011

Abstract

The instrumentation developments within this thesis are primarily aimed at instrumentation for the next generation of telescopes: Extremely large telescopes (ELTs). In the European astronomical community, the highest priority for ground-based optical and near-IR instrumentation has been identified as high-multiplex, multi-object spectroscopy (HMS) [1]. HMS includes both simultaneous observations of multiple faint objects at the limits of detection (Multiple Object Spectroscopy: MOS) and spatially-resolved spectroscopy over contiguous fields of brighter structured objects (Integral Field Spectroscopy: IFS) and a mixture of the two (Diverse Field Spectroscopy: DFS). However, before we can start to build instrumentation for ELTs it is important to: understand fibre characteristics more thoroughly and be able to predict behaviour with the use of a theoretical model (chapter 3); look at new technologies (Photonic Crystal Fibres, chapter 4, Volume Phase Holographic Gratings, chapter 5); use fibres in different ways (MAIFU, chapter 6).

Declaration

The work in this thesis is based on research carried out at the Centre for Advanced Instrumentation, the Department of Physics, University of Durham, England.

No part of this thesis has been submitted elsewhere for any other degree or qualification and it is the sole work of the author unless referenced to the contrary in the text.

Some of the work presented in this thesis has been published in journals - the relevant publications are listed on the following page.

Publications

Refereed Publications

C. L. Poppett and J. R. Allington-Smith Fibre systems for future astronomy: anomalous wavelength-temperature effects *MNRAS*, 379:143–150, 2007.
C. L. Poppett, J. R. Allington-Smith, G. J. Murray Strategies for spectroscopy on extremely large telescopes - III. Remapping switched fibre systems *MNRAS*, 399:443–452, 2009.
C. L. Poppett and J. R. Allington-Smith The dependence of the properties of optical fibres on length *MNRAS*, 404:1349–1354, 2010.

Conference proceedings

C. L. Poppett and J. R. Allington-Smith Coupling efficiency and termination of photonic crystal fibres for astronomy *Proc. SPIE*, 7018:159, 2008.
C. L. Poppett and J. R. Allington-Smith A new method to quantitatively compare focal ratio degradation due to different end termination techniques *Proc. SPIE*, 7735:29, 2010.
G. J, Murray, J. R. Allington-Smith, S. Blake, R. Content U. Lemke, C. Poppett Diverse field spectroscopy: instrument concepts *Proc. SPIE*, 7735:224, 2010.

Acknowledgements

Chapter 3

I would like to thank Tobias Feger for allowing me to analyse the results he obtained when testing non-circular fibres whilst working at the Anglo Australian Observatory.

Chapter 4

I would like to thank Dr Robert Thomson at Herriot Watt University for many useful discussions and also for his help quantifying the transmission losses in the M-PCF. I would also like to thank Prof Tim Birks at Bath University for his advice regarding using M-PCFs in astronomical instrumentation.

Chapter 5

The work presented in chapter 5 was carried out whilst working at the Australian Astronomical Observatory (AAO) and I am extremely grateful to Sam Barden for the opportunity to work on this project. I am also grateful to Luke Gers for sharing his expertise in aligning optics and also his patience in teaching me to surf!

Dedication

First and foremost, my thanks must go to Dr Jeremy Allington-Smith, my thesis advisor, for all of his guidance, patience, and hard work. I truly believe that I would not have achieved or learned as much without him or enjoyed the PhD process as much as I have. I also think it is necessary to record (officially) the best Margaritas recipe in the world: 2 parts tequila, one part triple sec, and one part lime - mix with crushed ice and serve in chilled glasses!

Thanks must also be expressed to my thesis examiners, Dr Richard Myers and Dr Ian Parry, for a strangely enjoyable thesis defence and valuable input.

I have been lucky enough whilst in Durham to have made many good friends without whom I certainly wouldn't have enjoyed my time in Durham as much as I have. Thanks firstly to James Osborn for teaching me to rock climb both inside and outside and being a brilliant house-mate and office-mate along with Graham Murray, Jurgen Schmoll, Paul Clark, Jonny Taylor, Luke Tyas, Tim Morris, Laura Young, Mark Harrison, Rob Harris, Matt Cashmore, Dora Fohring and Scott Silburn. I would never have learnt the importance of proof reading without you all!

Thanks also to friends outside of Physics: Vic Storey, Martin Nixon (for so much more than just coffee and pre-viva breakfasts), Paula Scott (soon to be Lawson!), Keo Phetsaya (for all of your proofreading but also for that magical weekend at Point Perp) and all of my Hawthorn family: Laura, Kat, Sam and Charlotte.

My family have supported me in everything I have ever done both emotionally and financially (even if my mum does tell people I'm an astrologer!). So thank you all for everything, but in particular: thank you mam for proofreading everything from my first year lab report to my PhD thesis; thank you dad for keeping me in supply of pens (you can now stop accosting everybody in the exhibition hall to tell them about me!); thank you Joe for your unending interest in the history of telescopes; and thank you Hayley for turning into somebody that I'm proud to love as my sister.

Last but by no means least, my thanks must go to Jim who first convinced me whilst on a train in Russia that it might be a good idea to be an academic (you were right!). So finally, after 288 hours (each) on trains, 10 holidays, 5200 (roughly) skype hours, and (only) 3 bunches of flowers later.....we made it!

Contents

List of Figures

List of Tables

Astronomy compels the soul to look upwards and leads us from this world to another.

Plato, The Republic

Chapter 1

Introduction

Astronomy has a longer history than any of the other sciences. It is said that man instinctively feels that the heavens above were the source and essence of his life in a deeper sense than the earth beneath, since light and warmth came from heaven. Ancient man believed that the gods who wrote their destiny left messages in the stars, and that the study of the stars was the unfolding of this higher world. It is for this reason that it was believed that Astronomy was the noblest science that human thinking and spiritual effort could be applied to.

Ancient Astronomers were only able to map out celestial orbits since unaided human eyes, which are limited by both sensitivity and resolution, are not very suitable for detailed Astronomical observations. The limit of sensitivity is determined by the sensitivity threshold of the retina. The resolution is limited by the finite physical size of the detectors on the retina and by the small aperture of the eye. Limited resolution makes it impossible for human eyes to separate individual distant sources of light that are closer than about $1'$ apart, or to discern details of their shape or structure on angular scales finer than this.

The invention of the telescope at the beginning of the seventeenth century was an important milestone in the advancement of Astronomy.

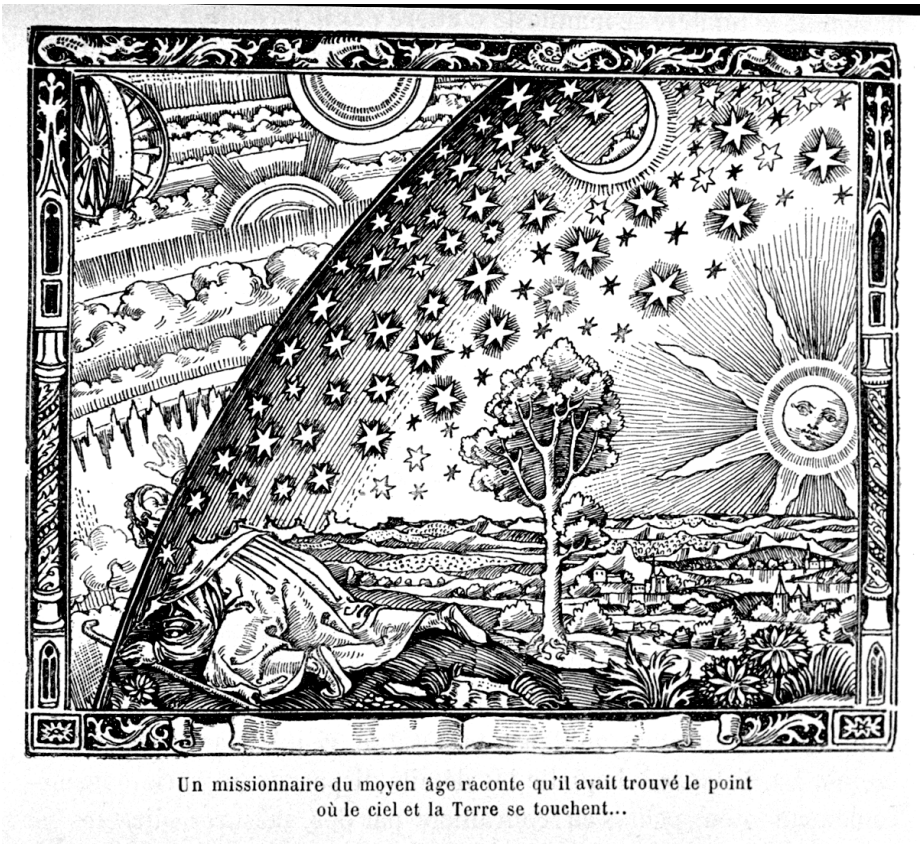

Figure 1.1: A missionary tells that he has found the point at which the earth and the sky meet. This woodcut appears in black and white in Camille Flammarion, L'Atmosphere: Météorologie Populaire (Paris, 1888), p. 163.

1.1 History of Telescopes

The earliest evidence of working telescopes is credited to three spectacle makers from the Netherlands who in 1608 designed the first Refracting Telescope. How-

ever, since the achromatic lens would not be invented until 1733, the telescope suffered from a large amount of chromatic aberration when the lens failed to focus all wavelengths to the same convergence point.

The early telescopes of Galileo, Kepler and Huygens, were all Refracting Telescopes which suffered from these same chromatic aberrations until Huygens derived the best figure for a lens by theory. Huygens derived that if one surface of a lens had a curvature six times smaller than the other surface, the chromatic aberration would be minimised [2]. With his brother, Huygens constructed a telescope with an aperture of 57 mm through which, in 1670, he discovered a satellite orbiting Saturn [3].

One of Newton's great merits is that he was the first person to make a reflecting telescope that could rival the refractors of the time. Although Huygen's refracting design minimised chromatic aberrations, they were not completely eliminated. Newton's design of a reflecting telescope did not suffer the chromatic aberrations suffered by refractors, but did suffer from coma, an off-axis aberration which causes images to flare inward and towards the optical axis. Another problem with early reflecting telescopes was that the speculum metal tarnished quickly. This problem was alleviated by the introduction of silver coated glass mirrors in 1857 and aluminiumised mirrors in 1932.

Modern Astronomical telescopes are mainly large reflecting telescopes and the main factors affecting the observations are sensitivity and angular resolution. Theoretically, the angular resolution should scale inversely with the telescope aperture since $\theta_{\text{res}} \simeq \lambda/D$, however in practice this resolution is never reached because of atmospheric turbulence.

The first improvement in observing capability came when George Hale [4] recognized that the careful selection of an observing site was important. However, it was soon clear that even at the best observing sites, observations were still limited by the seeing.

The first large telescope was built at Mount Palomar in 1949 and had a mirror diameter of 5 m. Thirty years later, the Canada-France-Hawaii Telescope (CFHT), which has a primary mirror of 3.6 m, became operational at Mauna Kea. The scale of this telescope was in keeping with the scale of other telescopes at the time, however, although the physical size of telescopes did not develop, other factors regarding telescope management such as eliminating dome seeing, fast automated guiding, and thermal control, resulted in an increase in sensitivity. Figure 1.2 shows how seeing at the CFHT has improved since first light as a result of improvements in telescope management, corrective optics (HRCAM) and active optics (SIS).

The interest in Cosmology in the 1980s was a major driver in pushing the sensitivity limit by further increasing the mirror diameter or eliminating the atmospheric limitations completely. This led to the current class of 8-10 m telescopes and to the deployment of the first space optical telescope. When telescope size reached 8 m, an improvement in resolving power was also seen due to the necessity of active optics when building telescopes on this scale. Telescopes built since the 1980s use very thin mirrors instead of thicker mirror, which are too thin to keep themselves rigid and in the correct shape. Instead, an array of actuators behind the mirror keeps it in an optimal shape. The telescope may also be segmented into many small mirrors, preventing most of the

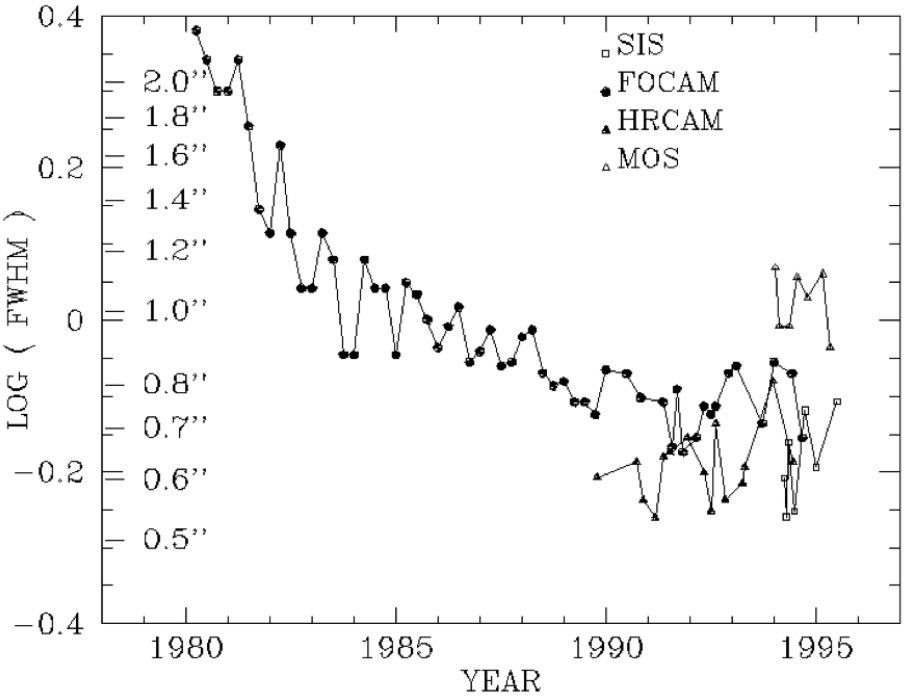

Figure 1.2: Seeing at the Canada-France-Hawaii Telescope (CFHT) on Mauna Kea has improved since 1980 as a result of improvements in telescope management.

gravitational distortion that occurs in large, thick mirrors.

Figure 1.3 shows how telescope aperture has scaled with time and figure 1.4 shows how the average seeing at each site has changed.

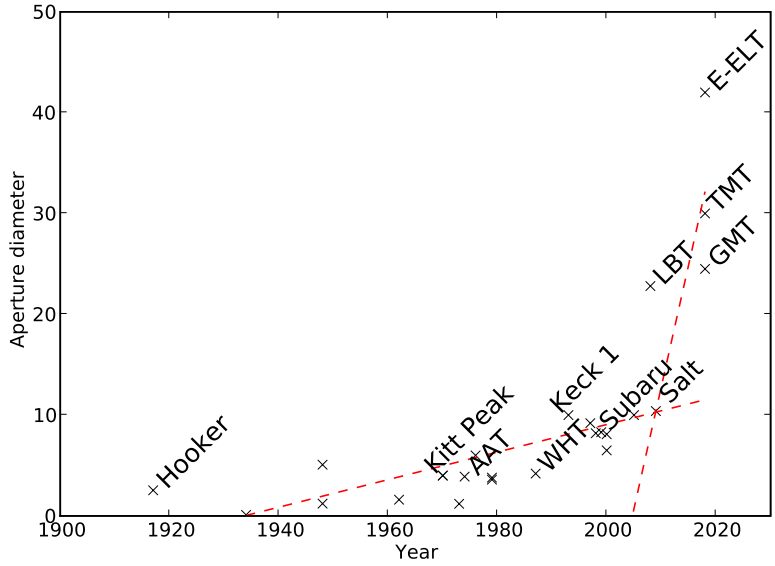

Figure 1.3: The diameter of the aperture of telescopes has increased substantially over the last 100 years. Linear fits show the increased rate at which telescope size is predicted to develop over the next 10 years.

Even with improvements in telescope management producing increased resolution, the theoretical limit is rarely reached as is shown by the solid line in figure 1.4. Under ideal circumstances the resolution of a telescope is limited by the diffraction of light waves and this limit is defined as:

$$\alpha = 1.22\frac{\lambda}{D}, \tag{1.1}$$

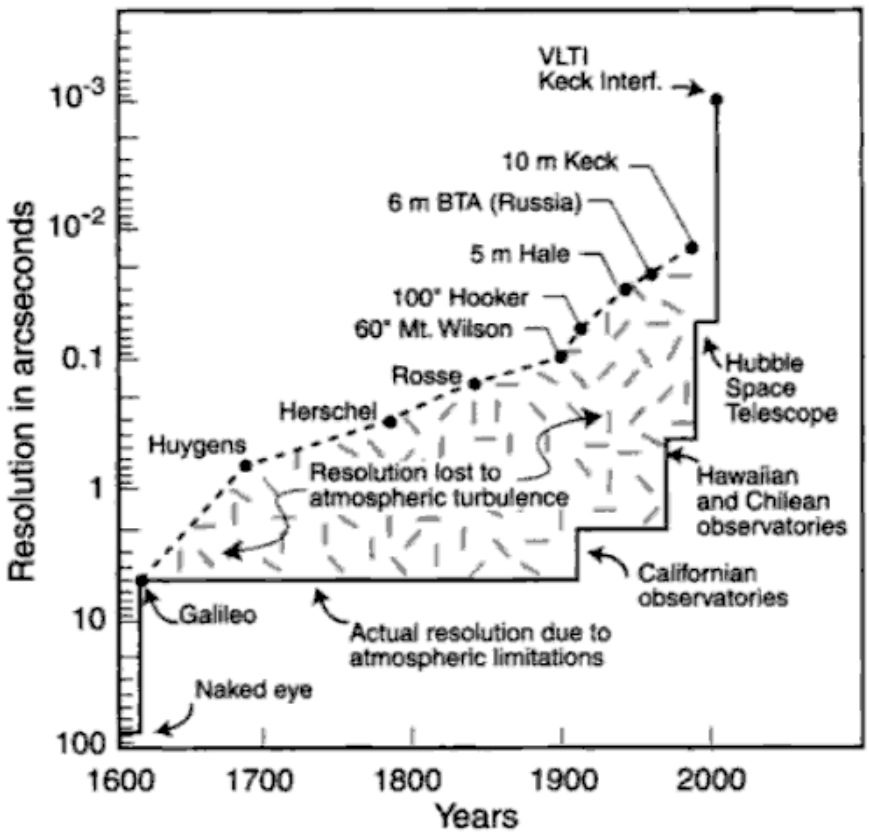

Figure 1.4: The average seeing at telescope sites has improved over the past 200 years due to improvements in site selection and telescope management. Ground based telescopes have never achieved their angular resolution potential due to atmospheric turbulence, however the development of Adaptive Optics (AO) promises to allow seeing to approach theoretical limits over at least part of the sky. Credit: Pierre-Yves Bély, The Design and Construction of Large Optical Telescopes [5].

where λ is the wavelength of the incident light and D is the pupil diameter. However, these limits are rarely achieved in practice due to atmospheric turbulence distorting the image. This problem is beginning to be overcome via Adaptive Optics which uses a real time control system to distort the secondary or subsequent mirrors to compensate for the effects in the atmosphere. The Very Large Telescope (VLT) Laser guide star facility was the first of its kind in the Southern Hemisphere to implement Adaptive Optics, although COME-ON and Adonis were used at La Silla before this. New ventures include Multi-Object Adaptive Optics (MOAO) and Multi-Conjugate Adaptive Optics (MCAO). Figure 1.5 shows the improved resolution which can be achieved when using Adaptive Optics.

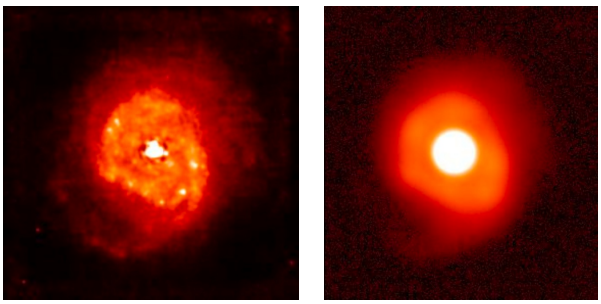

(a) (b)

Figure 1.5: Image of NGC7469 (a starbust galaxy) taken on PUEO at the CFHT with (a) Adaptive Optics module turned on and (b) no Adaptive Optics. The field of view is $10 \times 10''$, with a resolution of $\sim 0.13''$, courtesy of CFHT.

1.2 History of Optical Fibres in Telescopes

It is reported that the use of optical fibres in astronomy was first suggested by Brengt Stromgren in the mid 1950's [6], shortly after fibres were invented. However it was not until the 1970's when the telecommunications industry pushed

the development of a low loss fibre, that their use in astronomical instrumentation was feasible.

John Hill and Roger Angel of the Steward Observatory are credited with building and using the first working multiple-fibre spectrograph [7]. The system, 'Medusa', links the Cassegrain focal plane of the Steward 2.3 m telescope to the spectrograph (mounted immediately behind) with 40 short lengths of optical fibre.

Since this time the unique characteristics of fibres have been taken advantage of in several areas of astronomical instrumentation:

1. To optically multiplex telescopes;
2. As optical feeds to instruments operated remotely from the telescope;
3. As high efficiency image scramblers;
4. As coherence-preserving optical waveguides

Until the past few years, a discussion of fibres would have centred around various types of cylindrical step-index optical fibres and the process by which they transmit light. However, current research is now being focussed in different ways. Whilst it is still important to understand the physical characteristics of fibres and the way in which they propagate light, and indeed this is dealt with in section 3, recent research is beginning to focus on more exotic types of fibre, and the progress which has been made by the telecommunications industry is being exploited. Different types of optical fibres such as deviations away from a cylindrical core and towards square and octagonal cores is being investigated for their mode scrambling ability. Modifications are being made to optical fibres by making them out of different glasses and infusing them with gas to be used as

an absolute wavelength calibration scale. Finally, traditional optical fibres are being abandoned all together in favour of photonic crystal fibres [8] due to the possibility of modifying the design parameters and obtaining properties such as endlessly single mode behaviour or a high non-linearity. Photonic Crystal Fibres are described further, and tested, in chapter 4.

1.3 Spectroscopy

Quantitative astronomical spectroscopy began in 1814 with Joseph von Fraunhofer when he used a slit and a theodolite to produce a beam of sunlight, which he then allowed to fall onto a prism. In 1823 he was able to measure wavelengths and he mapped 324 of the solar lines as shown in figure 1.6. Since this time there have been a great number of advances in astronomical spectroscopy and this culminated in Highly Multiplexed Spectroscopy (HMS) which will be a key observational technique for the next generation of Extremely Large Telescopes (ELTs).

HMS includes both simultaneous observations of multiple faint objects at the limits of detection (Multiple Object Spectroscopy: MOS) and Spatially-Resolved Spectroscopy over contiguous fields of brighter structured objects (Integral Field Spectroscopy: IFS) and a generalisation of the two (Diverse Field Spectroscopy: DFS) which is fully explained in chapter 6. A description of how these individual techniques work and how fibres are utilised is given in chapter 2.

However, before the design of complex spectrographs can be described, some basic principles need to be understood, and an overview of the main theory will be presented in section 1.3.1. Figure 1.7 shows a schematic of a classical

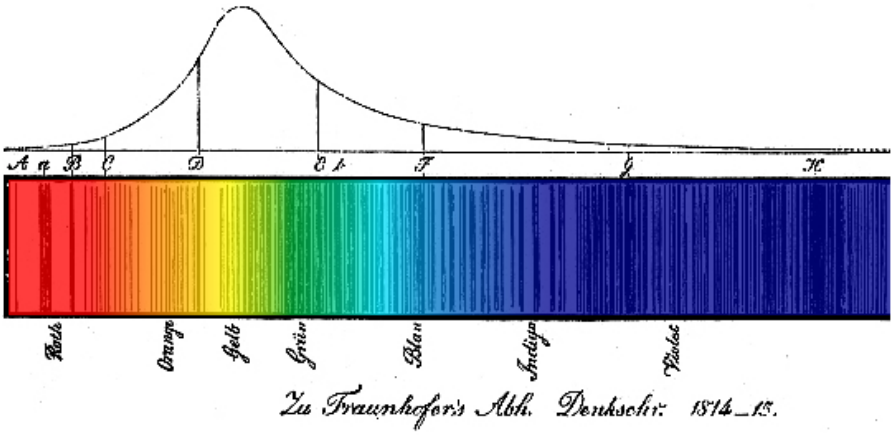

Figure 1.6: The first example of Quantitative Spectroscopy was made in 1814 when Joseph von Fraunhofer mapped 324 of the Solar Lines.

Cassegrain telescope interfacing with a basic spectrograph via an optical feed. The three components labelled A-C show the aspects which are investigated in this thesis. Light is collected at the focal plane by optical fibres (A, chapter 3;4), and then reformatted to form the spectrograph slit (B, chapter 6). The light is then collimated and diffracted off a grating (C, chapter 5). The dispersed light is then refocussed onto a detector and analysed.

1.3.1 Basic principles of spectroscopy

Plane diffraction gratings are the building block of most astronomical spectrographs. A diffraction grating is an optical component with a periodic structure, which splits and diffracts light into several beams travelling in different directions [9]. The directions of these beams depend on the spacing of the grating and wavelength of the light so that the grating acts as the dispersive element. As is shown in figure 1.8, at A the incoming waves are in phase, however, upon diffraction, the waves are only in phase at B if the difference in their path

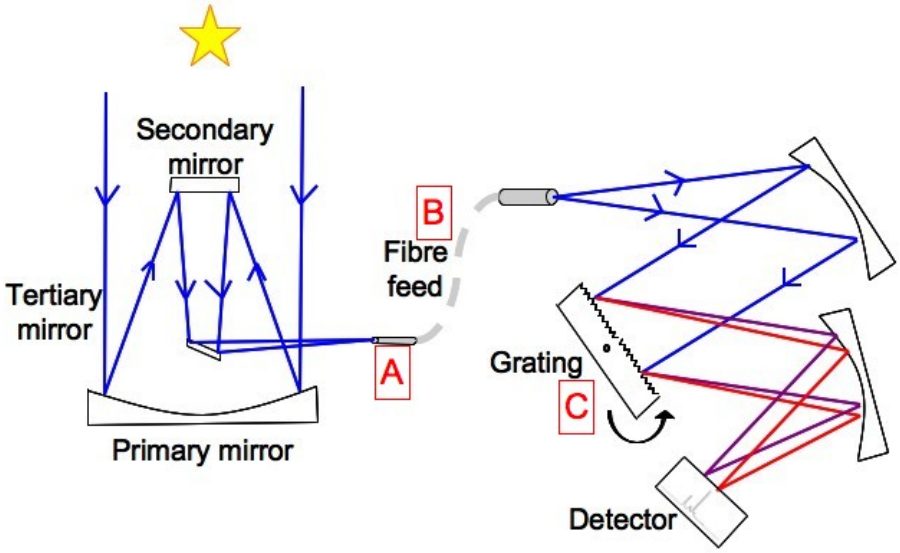

Figure 1.7: Schematic of a classical Cassegrain telescope interfacing with a basic spectrograph via a fibre feed.

lengths, $\nu(\sin\alpha + \sin\beta)$ is an integral number of wavelengths as shown in the grating equation:

$$m\lambda = \nu\left(\sin\alpha + \sin\beta\right), \tag{1.2}$$

or more commonly as:

$$m\Lambda\lambda = \sin\alpha + \sin\beta, \tag{1.3}$$

where α and β are the angles of incidence and diffraction order respectively, $\Lambda = 1/\nu$, is the groove density, ν is the groove spacing, λ is the wavelength and m is the spectral order.

A special case arises when the angle of incidence equals the angle of reflection, achieving maximum efficiency at specific wavelengths. This case is known as Littrow configuration and arises when $\alpha = \beta$ and the grating equation becomes:

$$m\Lambda\lambda = 2\sin\alpha. \tag{1.4}$$

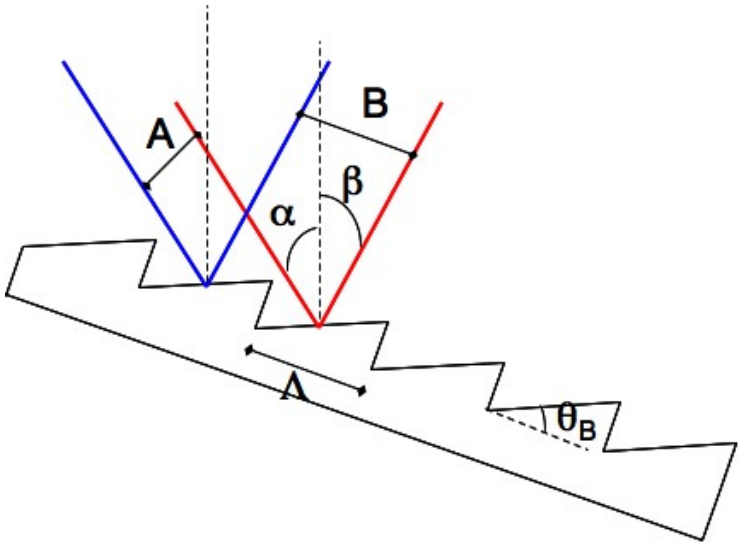

Figure 1.8: Geometry of diffraction, for planar wavefronts. The parallel waves are in phase at A and are only in phase, after diffraction if the difference in their path lengths, $\nu\,(\sin\alpha + \sin\beta)$ is an integral number of wavelengths.

1.3.2 Dispersion

The main purpose of any spectrograph is to separate the incident light into its constituent wavelengths, where each wavelength is diffracted in a different direction. Dispersion is a measure of the separation, both angular and spatial, between different wavelengths. Angular dispersion is expressed as the spectral range per unit angle, and the spatial dispersion is expressed as the spectral range per unit length.

Angular Dispersion The angular dispersion of the dispersing element is defined as the angular spread, $\Delta\beta$, of the spectral order, m, between λ and $\lambda+\Delta\lambda$.

In order to find the angular dispersion of the grating we must assume that the input angle, α, is constant and differentiate the grating equation (1.3) with

respect to β to obtain:

$$\frac{\mathrm{d}\beta}{\mathrm{d}\lambda} = \frac{m}{\nu \cos\beta} = \frac{m\Lambda}{\cos\beta}, \tag{1.5}$$

which shows that as the groove density, Λ increases, the angular dispersion will also increase. In order to find the general form of this equation we must substitute the grating equation back into the angular dispersion to obtain:

$$\frac{\mathrm{d}\beta}{\mathrm{d}\lambda} = \frac{\sin\alpha + \sin\beta}{\lambda \cos\beta}, \tag{1.6}$$

and therefore, for any given wavelengths, the angular dispersion is only a function of α and β.

In Littrow configuration ($\alpha = \beta$) the angular dispersion is expressed as:

$$\frac{\mathrm{d}\beta}{\mathrm{d}\lambda} = \frac{2\tan\beta}{\lambda}, \tag{1.7}$$

and again, for any given wavelengths, the angular dispersion is only a function of β.

Linear Dispersion Linear Dispersion is simply a product of the angular dispersion and focal length, f, of the system:

$$Df = \frac{fm\Lambda}{\cos\beta}. \tag{1.8}$$

1.3.3 Resolving Power

One of the most definitive properties of a dispersing system is the ability to separate adjacent spectral lines of wavelength, λ, and is expressed as:

$$R = \frac{\lambda}{\Delta\lambda}, \tag{1.9}$$

where $\Delta\lambda$ is the difference in adjacent wavelengths.

The theoretical resolving power of a planar diffraction grating is given as:

$$R = mN, \tag{1.10}$$

where N is the total number of grooves illuminated on the surface of the grating. If the grating equation (1.3) is substituted into this equation then

$$\begin{aligned} R &= \frac{N(\sin\alpha + \sin\beta)}{\Lambda\lambda}, \\ &= = \frac{N\nu(\sin\alpha + \sin\beta}{\lambda}). \end{aligned} \tag{1.11}$$

This equation shows that the resolution of a grating is dependent on both the number of illuminated grooves and the angle of the incident light. It can also be shown that both the slit width and diameter of the telescope are inversely proportional to the resolution which is detrimental to the photon count of the spectrograph. Different types of grating offer different limits to ruling density and grating efficiency and these options will be further investigated in the following sections.

1.3.4 Grating Efficiencies

High efficiency gratings are particularly desirable in astronomical instrumentation when many instruments are assessed on their cost-per-photon. A grating with high efficiency will be able to measure weak transition lines more easily. This may imply lower instrumental stray light due to other diffracted orders, as the total energy flow for a given wavelength leaving the grating is conserved.

There are various types of diffraction gratings which have different efficiencies for different wavelengths. Standard ruled gratings usually peak with high efficiency at specific wavelengths but this efficiency drops rapidly as the wavelength changes.

Classically ruled gratings are normally manufactured by drawing lines with a diamond tool and are characterised by a blaze wavelength and groove density. The standard rule of thumb states that the useful wavelength range of a grating is between $2/3\lambda_{\text{blaze}}$ and $3/2\lambda_{\text{blaze}}$ [10].

Volume Phase Holographic (VPH) gratings are increasingly being promoted in astronomical instrumentation due to their high efficiency and offer a new alternative as a dispersing element. VPH gratings, which are generally used in transmission, are now being used extensively in astronomy because of their high diffraction efficiencies. The diffraction is caused by a harmonic variation in refractive index perpendicular to the fringes, which is currently between 300-6000 lines mm $^{-1}$. For astronomical gratings, the active layer is typically 3-10 μm thick, which is sandwiched between glass substrates of a few millimetres in thickness. VPH gratings with a high blaze angle are tested in chapter 5.

A complete treatment of grating efficiency requires the vector formulation of electromagnetic theory applied to corrugated surfaces [11, 12], however simplifications are useful when making approximate predictions.

In many instances the diffracted power depends on the polarisation of the incident light, since one polarisation will be parallel to the grating grooves and one polarisation will be perpendicular to the grating grooves. If the incident light is unpolarised, the efficiency curve will be exactly halfway between the P and S efficiency curves.

Scalar theories of grating efficiency lead to accurate results in certain cases, such as when the wavelength is much smaller than the groove spacing ($\lambda \ll d$); the vectorial nature of optical radiation is not taken into account in this formalisation.

Vector or Electromagnetic theories can be grouped into two categories. Differential methods start from the differential form of Maxwell's equations for TE (P) and TM (S) polarization states. Integral methods start from the integral form of these equations. Each of these categories contains a number of methods, none of which is claimed to cover all circumstances.

Gratings are most often used in higher diffraction orders primarily to obtain higher dispersion, but also in order to extend the spectral range of a single grating to shorter wavelengths than can be covered in lower orders. For blazed gratings, the second-order peak will be at one-half the wavelength of the nominal first-order peak, the third-order peak at one-third, and so on. Since the ratio λ/d will be progressively smaller as $\mid m \mid$ increases, polarization effects will

become less significant; anomalies are usually negligible in diffraction orders for which $\mid m \mid \geq 2$.

1.3.5 Extremely Large Telescope Instrumentation

There are currently two major plans for Extremely Large Telescopes: The European-ELT (E-ELT) and the Thirty Metre Telescope (TMT). The Giant Magellan Telescope (GMT, 24.5 m diameter) and the Large Binocular Telescope (LBT, two 8.4 m primary mirrors) are also significantly larger than current telescopes, however they are not on the same scale as ELTs. An overview of the E-ELT will now be outlined in order to further illustrate the requirements of ELT instrumentation.

The E-ELT is designed to have a footprint of about 80 m diameter and is about 60 m high. This structure supports the five mirror optical design and accommodates two Nasmyth platforms. Each platform is about the size of a tennis court and can host several instruments.

As was discussed above, atmospheric turbulence prevents all current telescopes from achieving their theoretical resolution, and consequently the E-ELT optical design will include an Adaptive Optics unit. The desire to include Adaptive Optics into the design of the telescope resulted in a five mirror design: a three mirror anastigmat with two flat folding mirrors providing the Adaptive Optics. This novel five-mirror design results in an exceptional image quality, with no significant aberrations in the 10 arcmin field of view.

To date, six instrument concepts have been identified along with two post-focal AO modules (MCAO and LTAO) of high priority and two other instru-

ments to be chosen after an open call to the community for additional concepts. Table 1.1 shows an overview of planned First Generation Instruments and it is expected that two to three instruments will be ready for first light. A full suite of instruments covering a wide parameter space will be built up over the first decade of E-ELT operations, in a similar way to the VLT.

The instruments which are proposed in table 1.1 have addressed, or will need to address, all of the concepts investigated in this thesis. Design studies for CODEX identify the need to limit the grating and the pupil size in order to contain costs. To facilitate the thermal stability of the system, the spectrograph should have a limited volume. OPTIMOS/EVE will use different sized bundles of fibres to provide as much flexibility as possible to sample the focal plane in a similar manner to DFS and will also use VPH gratings in order to maintain high throughput. Finally, the implementation of all of the instruments will have a phased approach in order to operate before the full AO capabilities are realised and the instruments can work at the diffraction limit.

Name	Instrument Type	λ Range (μm)	Spectral Res.	FOV
CODEX	High Resolution, High Stability Visual Spectrograph	0.37-0.71	135 000	0.82"
EAGLE	AO-assisted Multi-integral Field NIR Spectrometer	0.8-2.45	4000 & 10 000	IFU:1.65″ × 1.65″
EPICS	Planet Imager, Spectrograph and Imaging Polarimeter with Extreme Adaptive Optics	0.6-1.65	125, 3000 & 200,00	IFU: 0.8″ × 0.8″, EPOL:1.37″
HARMONI	Single Field Integral-field Spectrograph	0.47-2.45	4000, 10 000 & 20 000	2:1 aspect ratio:10″ × 5″ and 1″ × 0.5″
METIS	Mid-infrared Imager and Spectrograph with AO. Complement by EPICS in NIR	2.9-14	Long slit: 900 ≤R≤ 5000 at L,M,N; IFS: 100000 at L,M	imager: 17.6″ × 17.6″; longslit:17.6″; IFS: 0.4″ × 1.5″
MICADO	Imager and Slit Spectrograph	0.8-2.5	≤3000	up to 53‴
OPTIMOS-DIORAMAS	Wide-Field Imager and Low-Medium Resolution Slit Spectrograph	0.37-1.6	300, 1000, & 2500	6.78′ × 6.78′
OPTIMOS-EVE	Optical-NIR Fibre-based MOS	0.37-1.7	5000, 15 000, & 30 000	Single object fibres: 0.81 − 0.9″;IFU-1:1.8″ × 3″; IFU-2: 7.8″ × 13.5″
SIMPLE	Cross-dispersed Echelle Spectrograph, Long-slit Option	0.8-2.5	1300 00	≤ 4″

Table 1.1: First light instruments proposed on the E-ELT

My job is to turn starlight into rainbows and then photograph them... that's actually a brilliant job isn't it?!

Luke Tyas, 2011

Chapter 2

Optical fibres in astronomical instrumentation

This chapter will provide an overview of the practical applications and considerations when using optical fibres in astronomical instrumentation. Section 2.1 will describe different types of astronomical spectrographs and provide examples of how optical fibres have been successfully utilised. Section 2.2 will introduce the properties and guiding mechanisms of optical fibres which must be fully understood. Both of the theoretical models presented in section 2.3 describe a perfect classical optical system, however, optical fibres can not be treated as such. Section 2.4 will define what considerations must be made when fibres are used in Astronomical Instrumentation, with particular emphasis being placed on their inability to conserve Étendue, which is presented in 2.5.

2.1 Astronomical Spectroscopy

The earliest spectroscopic technique that was employed in Astronomical Instrumentation was Long-Slit Spectroscopy (LSS). LSS involves obtaining the spectrum of light incident upon an aperture defined by the slit, which can be lengthened to include background elements. However, if the object of interest is extended, the spectrum can only be recorded in the 1-dimension defined by the slit. This problem can be overcome if the slit is stepped across the sky, but this is time consuming and prone to errors due to varying atmospheric conditions. Astronomical applications seek more time efficient spectroscopic solutions and the two most popular methods are currently Multi-Object Spectroscopy (MOS) and Integral Field Spectroscopy (IFS).

Multi-Object Spectroscopy (MOS) is used to collect light from many discrete objects over a wide field. MOS only obtains the spectrum of the total light collected within each sampling aperture (usually the core of a positionable optical fibre or a slit-let cut in a mask at the telescope focus). The MOS targets are generally faint objects at the limits of detection such as primeval galaxies. MOS offers a large multiplex gain in terms of the number of objects it is possible to measure in a single observation, but does not record spatial information. In contrast, IFS obtains complete, spatially-resolved coverage over a small field.

Observations made at high redshift show that the universe has a blobby and confused structure [13]. Diverse-Field Spectroscopy (DFS) is an instrument paradigm which combines MOS with IFS in order to allow the observer to select arbitrary combinations of contiguous and isolated regions of the sky to maximise observing efficiency and scientific return.

These three types of spectroscopy and different methods of positioning fibres

at the focal plane will now be described more comprehensively

2.1.1 Multi-Object Spectroscopy

The possibility of obtaining simultaneous spectra of many objects via optical multiplexing of telescopes has been one of the most popular and successful applications of optical fibres to astronomy. The history of the development of Multi-Object Spectroscopy, which in turn was driven by the scientific motivation for large-scale redshift surveys, employing optical fibres is discussed by Hill [14]. Hill was involved in the development of the pioneering instruments such as MEDUSA which obtains simultaneous spectra of 32 objects at the Steward Observatory 2.3 m telescope.

The general structure of a multi-object spectrograph is deceptively simple: numerous single optical fibres are positioned in the telescope focal plane such that each fibre acquires light from a target object; the output ends of the fibres are then arranged along the spectrograph slit as shown in figure 2.1. A two-dimensional detector (normally a CCD) is employed to simultaneously detect the spectra from all objects in the focal plane to which fibres have been employed.

In practice, a small percentage of the fibres are assigned to monitor the sky background and, optionally, some to calibration lamps. Another practicality when using fibres at the focal plane is selecting an appropriate core size to match the telescope plate scale and seeing. The plate scale describes the relation between an angular distance on the sky, u, and a physical distance in the

telescope's focal plane, s. It is calculated as:

$$\text{Plate scale} = \frac{u}{s} = \frac{u}{FDu} = \frac{.206}{f}\text{arcsec } \mu\text{m}^{-1}, \tag{2.1}$$

where u is the angular size of the image in radians, s is the image height, F is the focal ratio of the telescope, f is the focal length, and D is the objective diameter.

For example, when selecting fibres to be used at the Anglo-Australian Telescope (AAT), the plate scale at prime focus is calculated as $0.015''$ μm $^{-1}$ (D=3.9 m and f=3.5 m), which, when matched with an average seeing of $1.5''$ requires that fibres are selected to have a core diameter of around 100-150 μm .

The way in which optical fibres are positioned in the focal plane is unique to each instrument and the various schemes which have been employed in astronomical instrumentation will now be reviewed.

Perhaps the simplest fibre positioning system is that of plug-plates. In this scheme, a sheet of suitable material is drilled with accurate, pre-configured holes into which fibres are inserted. This method has many advantages in terms of versatility and has been successfully implemented in CIRPASS, SDSS, and BOSS instruments. The main advantage of this method is that there are very few positional constraints since there are no magnets, prisms, or crossing fibres. In addition, operation during the night is extremely simple so there is a very low risk of the telescope time being lost compared to systems which reconfigure the fibres on the telescope. However, it is necessary to have many CNC machines at the telescope site in order to enable enough plates to be manufactured for each nights observation and enough fibre pluggers to efficiently prepare the plates. It is proposed that the Dark Energy (DE) and Galactic Archeaology (GA) surveys

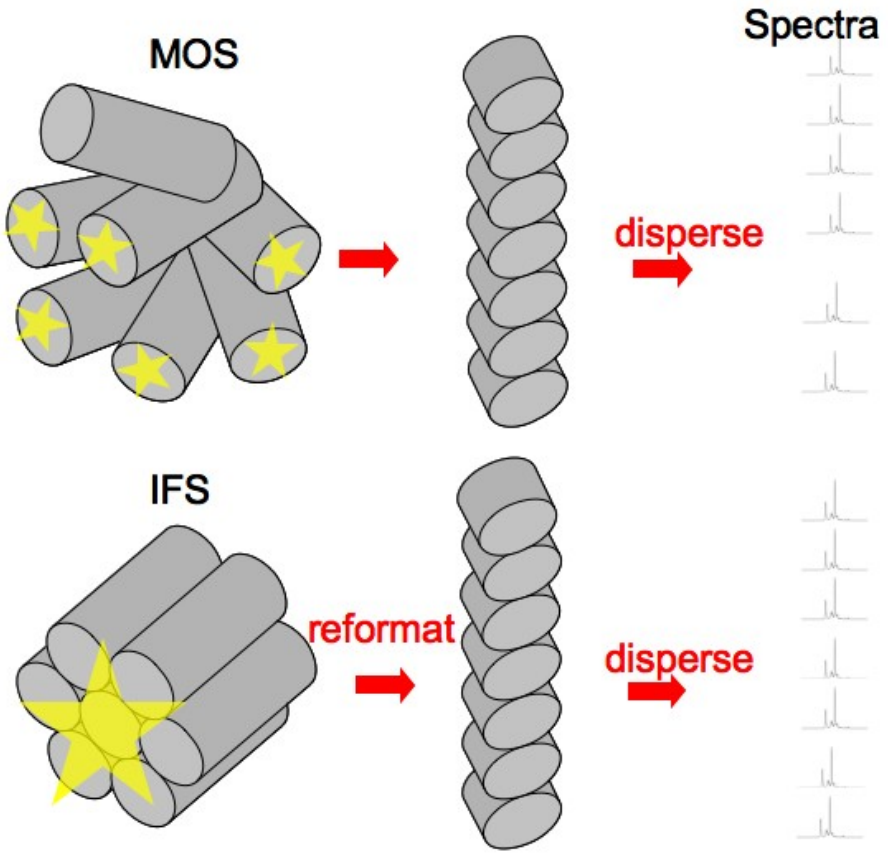

Figure 2.1: A bundle of fibres can be rearranged to form a spectrograph slit. Normally one fibre is used as background subtraction. MOS aims to target one object per fibre whereas IFS aims to obtain spatial information.

which have high target density requirements would benefit from plug-plate fibre positioning [15]. SMIRFS (Spectroscopic Multi-object Infra-Red Fibre System) [16] on UKIRT uses plug-plates and was the first IR multi-object fibre system (J, H, and K (1-2.5 μm) windows).

A more time-efficient solution is to use Pick and Place fibre positioning systems. One of the first pick and place fibre positioning systems, AUTOFIB [17] was a collaborative instrument built at Durham University in 1986 and then developed into Af-1.5 for the 2.1 m telescope at Guillermo Haro [18], Af-2 for the WHT, and finally 2dF on the AAT. 2dF addresses up to 400 objects with a single robot which positions magnetic buttons carrying optical fibres on a flat focal plate as shown in figure 2.2. 2dF was followed by 6dF and OzPoz, which was designed to operate with a curved focal surface. With these 'Pick and Place' systems the configuration time is essentially proportional to the number of deployable fibres since one robot positions each fibre individually, and could potentially lead to unacceptable delays between observations as the field is reconfigured. This problem is overcome, at the expense of mass and mechanical complexity, by using multiple exchangeable field plates allowing one field to be configured while another is being used in an observation. This approach minimises the configuration 'dead time'.

Developments away from a pick and place robot then came in the form of a fibre positioning system on the Fibre Multi-Object Spectrograph (FMOS) on the Subaru telescope. The field of view of FMOS is $30'$, with a physical size of 150 mm diameter at its focus. In order to position 400 fibres within the limited area, ECHIDNA [19] (shown in figure 2.2), was developed. Echidna uses fibres mounted on patrolling spines in a 0.5° diameter FoV to position the fibres as

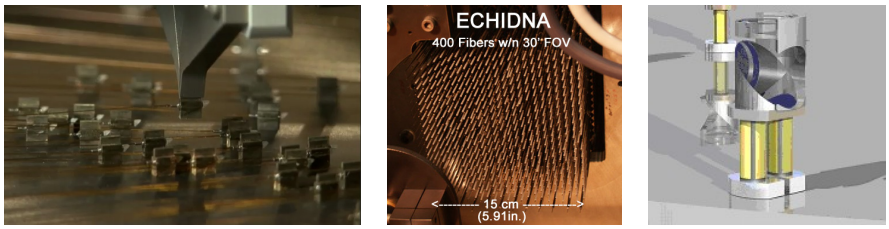

(a) **(b)** **(c)**

Figure 2.2: 2dF, ECHIDNA, and starbugs show the evolution of fibre positioning systems for Multi-Object Spectroscopy.

required. Each spine is separated by 7.2 mm from each of its 6 neighbours and can be tilted up to 7.2 mm radially in any direction. Each spine in the FMOS-ECHIDNA system can be simultaneously and independently moved, effectively freeing its field configuration time from its former proportional dependence on the number of deployable fibres. Fast configuration times eliminate the large 'dead times' between observations without the need for multiple field plates. This can have large savings both financially and spatially, and reduce system complexity. This system can also be of particular value in cryogenic environments since it does not need to be removed prior to configuration.

A new alternative to ECHIDNA positioning systems are Starbugs which employ micro-robotic actuators to independently and simultaneously position multiple small fibres accurately on an arbitrarily large field plate [20]. Starbugs are a dynamic robotic positioning concept for use in future instruments on large telescopes such as the MOMSI instrument. Starbugs can deploy multiple payloads, such as pick-off optics, optical fibres and other possible devices, with micron-level accuracy over a flat or curved focal plane.

2.1.2 Integral-Field Spectroscopy

Integral Field Spectroscopy (IFS) is the technique of obtaining spectra for an array of contiguous spatial samples in a 2-dimensional field of view. Each spatial point gives an individual spectrum hence the resulting data can be considered as a data-cube with 2 spatial dimensions (x, y) and another dimension corresponding to the wavelength, λ.

IFS is used when partially resolved spectroscopic information of an astronomical object is required in. For example, IFS can be used to study resolved stellar populations, active galaxies, groups and cluster of galaxies, and highly redshifted galaxies.

Figure 2.3 shows the three main techniques of IFS in addition to a fourth new type which is a hybrid between a lenslet array and image slicer system [21].

IFS with microlens arrays

Panel (a) shows an IFS which uses a Micro-Lens Array (MLA) to sample the focal field. Lenslet based IFS use MLAs to segment an image formed by the telescope and then forms separate images of the telescope pupil. These images are then dispersed into a number of discrete spectra by the spectrograph. The pupil images therefore form a two-dimensional field which would overlap in the detector plane. To overcome the problem of overlap, the angle of the direction of dispersion is rotated. This solution results in a longer spectrum than would otherwise be achievable and an additional band pass filter is used to isolate the required spectral range. The maximum length of spectrum is determined by the ratio between the size of the pupil image and the spacing between the

sub-images (determined by the element size). A large ratio results in a longer spectrum by decreasing the opportunities for overlap, but this requires a fast lenslet array and spectrograph.

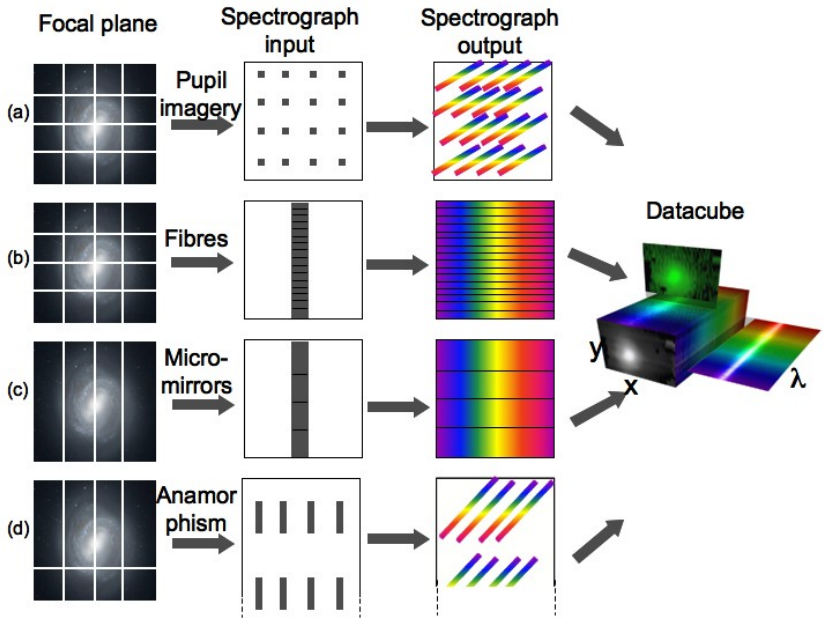

Figure 2.3: The main techniques of Integral Field Spectroscopy(image courtesy of Jeremy Allington-Smith [22])

Lenslet based spectroscopy is best suited to studies of the individual absorption lines in galaxies or the kinematics from single absorption or emission lines where a long spectrum is not required. Because overlaps between adjacent spectra must be strictly avoided, unilluminated pixels between spectra are required which does not make optimal use of the detector surface.

Historically, this technique was among the first to be employed, chiefly by the Lyon group [23] and recent examples include OSIRIS on Keck [24], KYOTO-3D on Subaru [25], SNIFS on the University of Hawaii 2.2 m telescope [26], and

SAURON on the WHT [27].

IFS with optical fibres

Panel (b) of figure 2.3 shows an IFS which uses optical fibres arranged in a close-packed bundle at the telescope focus. Fibres with a high core-cladding ratio are preferred since they minimize the dead space between cores. The fibres are then reformatted into a pseudo-slit so that light emerging from the fibre ends is dispersed by the spectrograph into what resembles a long-slit spectrum. Because of the linear format, the spectrum can be as long as the detector format allows.

Fibre only IFUs have a distinct advantage over lens only IFUs since the field can be easily reformatted into a psuedo-slit. However there are also inherent disadvantages in IFUs which use only fibres. The first is that the filling factor of the focal plane is limited by the ratio of the core diameter of the fibres compared to the cladding thickness. The generally accepted rule of thumb is that the thickness of the cladding must be more than 10λ thick in order to avoid significant light loss via evanescent waves. Fibres used in astronomy, typically have a maximum core diameter of around 100 μm and at operate at optical wavelengths (≤ 1 μm) resulting in a filling fraction of 83 %. In order to achieve even this filling factor, the buffer of the fibre must be removed, making the fibre more susceptible to damage. The second problem with using a fibre only IFU is that the focal ratio must be limited to around f/5 in order to avoid focal ratio degradation which is discussed in more detail in chapter 3. This problem can only be overcome by using solutions which also have inherent problems such as changing the speed of the beam before it enters the fibre, or over-sizing the optics.

Fibre only IFUs are chiefly used for mapping the internal velocity fields of relatively bright galaxies. Recent instruments include 2D-FIS, Hexaflex and INTEGRAL which are all on the WHT [28, 29, 30].

IFS with mirolenses and fibres

In order to utilise the reformatting capabilities of fibres, whilst overcoming the inherent disadvantages, lenslets can be added at the input and (optionally) at the output of the fibres. If the input lenslets form a two-dimensional contiguous array, they can eliminate the problem of filling factor and provide better matching between the fibre and the telescope, thereby efficiency. This technique also means that light is not incident upon the cladding hence the spectrograph has full spatial coverage. Some crosstalk is acceptable since neighbouring spectra are adjacent on the sky and in wavelength, hence larger fields of view can be obtained. This design can then be adapted according to requirements. For example the GMOS instrument on the Gemini telescope trades field of view for spectral coverage by dividing the field into equal sections [31]. Fibres transfer the light from each section to pseudo slits at the spectrograph entrance. When the largest field of view is required, blocking filters must be used to limit spectral coverage and avoid overlap. Conversely, when higher spatial resolution or longer wavelength coverage is required then some of the pseudo slits can be masked off to increase spectral coverage at the expense of FOV. Other examples of IFUs which use both fibres and lenslets are VIMOS and FLAMES on the VLT [32, 33], PMAS on Calar Alto Observatory 3.5 m telescope [34], CIRPASS on Gemini [35], and FALCON which is being designed for the next generation of VLT or future ELT [36].

The main drawback of fibre and lenslet based technology is that the lenses in the micro-lens array must tessellate and are therefore normally either square or hexagonally packed. This geometry causes the beam to be faster in the corners as shown in figure 2.4 and also imposes a balance to be made as there is a finite ratio of fibre aperture to lenslet size. Both of these effects act as sources of FRD. Geometric FRD will be further investigated in section 3.3 as the same issues arise when using fibres with a non-circular core.

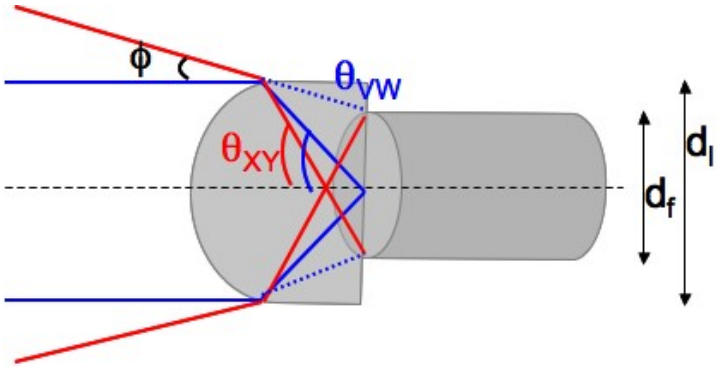

Figure 2.4: Geometric FRD induced by square lenslets.

As is shown in figure 2.4 the non-circular shape of the lenslets results in a larger angle of rays from the corners of the lens, θ_{VW}, than from the edges of the lens, θ_{XY}. In addition to this, although the size of the lens is matched as closely as possible to the dimensions of the fibre core, the diameter of the lens, d_{l}, will inevitable by larger than the diameter of the fibre core, d_{f}. By conservation of Étendue:

$$\phi d_{\mathrm{l}} = \theta_{\mathrm{XY}} d_{\mathrm{f}}, \tag{2.2}$$

and $\theta_{\mathrm{VW}} \longrightarrow \theta_{\mathrm{XY}}$ when $d_{\mathrm{l}}/d_{\mathrm{f}} \longrightarrow 0$ and the FRD due to the finite size of the pupil image is minimised.

Another possible solution is to use an image slicer as shown in panel (c) of figure 2.3. This technique is especially applicable to wavelengths beyond 1.8 μm , where instruments must be cooled to reduce the thermal background. In this design the image formed by the telescope is incident on a slicing mirror consisting of a number of narrow slices. Each mirror slice is set at a slightly different angle, so that the diverging beam from each slice exits in a slightly different direction. Each beam is then reflected by another mirror which is offset in the direction parallel to the long axis of each slice. The overall effect is to rearrange the rectangular field into a long thin field, made up of all the slices arranged end to end to form the slit of the spectrograph. The advantage of this technique is that FRD is avoided as no fibres are used, chromatic aberrations are eliminated as lenses are not used, and the slicing arrangement gives contiguous coverage of the field due to the fact that only mirrors are used. Slicing also offers higher efficiency that conventional techniques since the mirrors can be coated in order to be optimised for the desired wavelength range. However, the sampling along the slices is the same as that provided naturally by the telescope, so there is reduced scope to optimise for use with a spectrograph that must also work in a normal slit-spectroscopy mode.

Image slicing was pioneered by the Max-Planck-Institut für extraterrestrische Physik (MPE) with the 3D spectrograph [37]. GNIRS on Gemini adapted the design in order fit in with existing spectrographs as did SINFONI on VLT(UT4) [38], SWIFT on the 200 inch Hale Telescope [39], and FRIDA on the GTC [40]. NIRSPEC on the JWST [41] showed the compact size and cryogenic capability makes these IFUs particularly suitable for space based instrumentation.

The final IFS design, shown in panel (d) of figure 2.3 is being developed as

part of a feasibility study of the spectrograph MEIFU for the VLT [42]. The new concept of transparent microslice IFUs, permits 2-3 orders of magnitude more spatial elements at a reasonable cost and uses lenslet arrays to divide the field in 2D. The properties of crossed-cylindrical arrays are then exploited, in order to allow each pupil image to be replaced by a slice which contains spatial information along its length. This provides many of the benefits of the image slicer in terms of reducing dead space between spectra, but not to the same extent because the spectra are distributed over a 2D field, and overlaps must be avoided since the wavelengths are not continuous between slices (although they are within a slice).

2.1.3 Diverse-Field Spectroscopy

Diverse-Field Spectroscopy aims to combine the techniques of Multi-Object and Integral Field Spectroscopy in order to efficiently sample the large focal planes which will be accessible with ELT's. One of the problems of producing spectrographs for Extremely Large Telescopes (ELTs) is that the beam size is required to scale with telescope aperture if all other parameters are held constant, leading to enormous size and implied cost. It is therefore not possible to sample the entire focal plane, so regions of interest (ROIs) must be selectively routed to the entrance of the spectrograph.

Figure 2.5 shows an image of a Lyman Alpha Blob (LAB) in the SSA 22 protocluster region, obtained with SAURON on the WHT. LABs are some of the largest known individual objects in the universe, and are effectively a huge concentration of gas emitting the Lyα emission line. The Lyα line is produced by the recombination of an electron with ionised H atoms. These objects are not easily observed since the earth's atmosphere is very effective at filtering out

UV photons. Lyα photons must therefore be highly red-shifted in order to be transmitted through the atmosphere. It is expected that this is the kind of faint object which will be readily accessible to ELTs.

Instruments such as DAZLE (Dark Ages 'Z' Lyman Explorer) on the VLT [44] also use red-shifted Lyα lines in order to detect emission from hydrogen gas ionised by young stars in galaxies at very high redshifts. These faint emission lines will be much more accessible with the larger collecting areas available with ELTs. As is shown in this figure, there are both contiguous and non-contiguous regions of interest (ROIs) on the detector. To take full advantage of the size and light gathering capability of ELTs we must be able to take spectroscopic data of both these types of fields. DFS allows arbitrary distributions of target regions to be addressed to optimize observing efficiency when observing complex, clumpy structures. A DFS type instrument concept will be presented in chapter 6.

2.1.4 Other Applications

It is important to note that whilst optical fibres have primarily been used in astronomical spectrographs, they have also been used in other applications such as high precision radial-velocity work, interferometry, and photometry.

The scrambling ability, which will be described in section 2.4 results in any structure at the input end of the fibre becoming uniform at the output given a sufficiently long length of fibre. This makes fibres potentially extremely useful to high precision radial-velocity measurements. The HARPS instrument is one such instrument which takes advantage of this property, and has re-

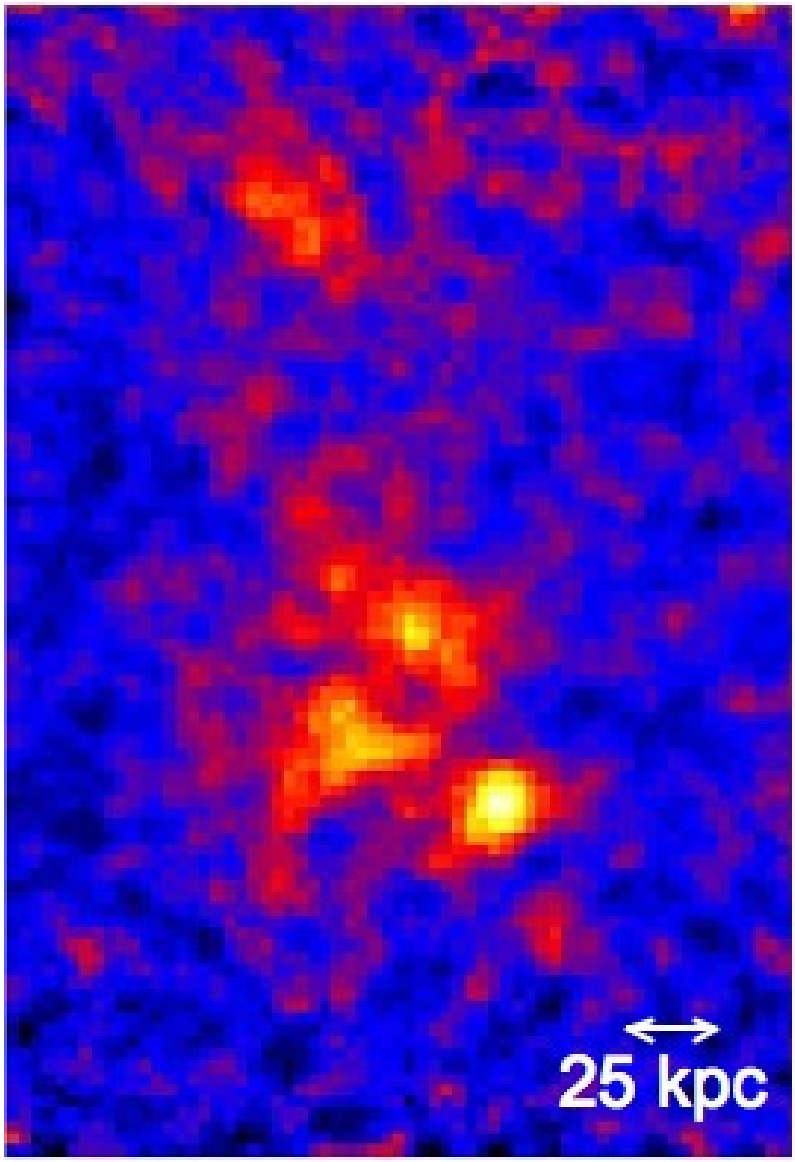

Figure 2.5: Continuum-subtracted Lyα emission region LAB1 in the SSA 22 protocluster region at z = 3.09 [43]. This image was obtained by collapsing the SAURON spectra over a narrow wavelength range centred on the emission line. These objects are not easily observed since the earth's atmosphere is very effective at filtering out UV photons so Lyα photons must be highly red-shifted in order to be transmitted through the atmosphere. It is expected that this is the kind of faint object which will be readily accessible to ELTs (Image courtesy of Weijmans 2009)

cently reported the discovery of a planetary system comprising of at least five Neptune-like planets with minimum masses ranging from 12 to 25 M_J, orbiting the solar-type star HD 10180 at separations between 0.06 and 1.4 AU [45].

The GRAVITY [46] instrument for the second generation of Very Large Telescope Interferometry (VLTI) instrumentation shows how fibres are used to combine beams from different telescopes providing high-precision narrow-angle astrometry and phase-referenced interferometric imaging. The optical fibres provide single-mode filtering of the incoming wave-front and transport the light to the integrated optics beam combiner. The optical path length of the fibres can be adjusted by stretching the fibres, which are wrapped around a piezo ceramic cylinder. This method of changing the path length is simple and convenient compared to mirror-based path-length compensator's.

As the study of Exoplanets gains momentum, multi-fibre photometry is becoming an increasingly useful technique since a large number of objects spread over a large FOV need to be monitored for variability. Since the amount of light transmitted down a fibre is strongly dependent on the position of the stellar image on the fibres input face, and since typical fibres used in astronomy are much bigger than a stellar image, Borucki *et al.* [47] concluded that optical fibres would not be able to carry out this type of work with sufficient precision. However, it was shown by Parry [48] that the photometric capability of fibres was adequate if it was possible to obtain a large amount of dedicated observing time on a large Schmidt telescope.

2.2 Optical Fibre Theory

Traditional optical fibres used in Astronomical Instrumentation are cylindrical dielectric waveguides with a cross sectional diameter of a few hundred microns and a step index type gradient, as shown in figure 2.6.

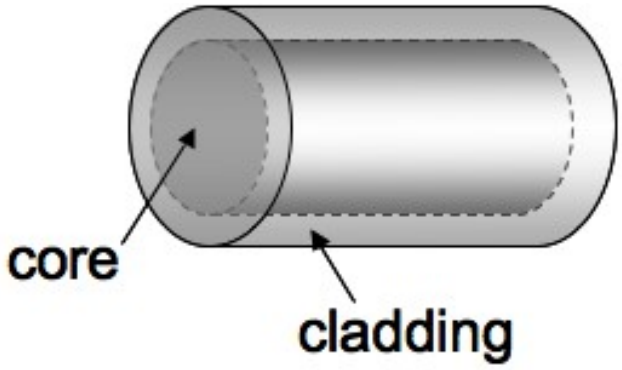

Figure 2.6: The structure of a basic optical fibre

The core of an optical fibre is composed of a dielectric material surrounded by a cladding made up of a dielectric material of lower refractive index. For fibres used in the optical and IR regime, the core will normally be made of high purity fused silica which, with such small cross sections, means that the fibre will be fairly flexible. It is due to this flexibility that optical fibres form the basis of Multi-Object Spectroscopy, by which a substantial fraction of the world's large telescopes have been multiplexed to great advantage as discussed above. The multiplexing capability could also be performed by conventional optical waveguides, but the small size and flexibility of fibres make the task far simpler and less expensive.

Electromagnetic waves do not generally propagate through optical fibres as

simple plane waves and consequently, any description of guided waves in fibres is inherently approximate. However, in order to gain a basic understanding, the description of propagation via rays is sufficient as a starting point and the following section (section 2.3.1) explains some of the basic theory. The physically correct description of guided waves as modes is discussed in section 2.3.2. This guided mode theory is especially important in the context of this thesis since it is the transfer of energy from lower to higher order modes which manifests as the focal ratio degradation which is investigated in chapter 3.

2.3 Wave Propagation Theory

2.3.1 Ray theory of propagation of light

Standard Ray theory relies on the principle that EM waves are guided via Total Internal Reflection (TIR) in the type of traditional optical fibres shown in figure 2.6. The active core, which is of uniform index of refraction n_1, is coated with a cladding of lower refractive index n_2.

If a ray enters a fibre at an angle ϕ with respect to the normal at the core-cladding interface, then that part of the ray which has entered the core gets reflected into the core from the core-cladding boundary at an angle θ_1, and the other part gets transmitted into the cladding at an angle of θ_2. From Snell's law we know that:

$$n \sin \phi = n_1 \cos \theta_1; \tag{2.3}$$

$$n_1 \sin \theta_1 = n_2 sin \theta_2. \tag{2.4}$$

Where n is the refractive index of the medium outside of the fibre. Substituting for θ_1 from equation 2.4 into equation 2.3 leads to the following expression for ϕ:

$$\phi = \sin^{-1}\left(\frac{n_1 cos\left(\sin^{-1}\left(\frac{n_2}{n_1}\sin\theta_2\right)\right)}{n}\right). \tag{2.5}$$

Using the trigonometric identity $\cos x = \sqrt{1-\sin^2 x}$, equation 2.5 can be re-written as:

$$\phi = \sin^{-1}\left(\frac{n_1\sqrt{1-\left(\frac{n_2}{n_1}\sin\theta_2\right)^2}}{n}\right). \tag{2.6}$$

If the ray at the core-cladding interface makes the critical angle, then $\theta_2 = \pi/2$ radians and hence

$$\phi = \sin^{-1}\left(\frac{\sqrt{n_1^2 - n_2^2}}{n}\right). \tag{2.7}$$

The physical significance of this value of ϕ is that any ray of light which enters the core at an angle less that that of ϕ would undergo Total Internal Reflection (TIR) at the core-cladding interface. It would therefore become trapped in the core as it propagates through the fibre. Thus, the value of ϕ as evaluated using equation 2.7 for a given fibre is referred to as the maximum acceptance angle of that fibre. The numerical aperture (NA) is now derived from equation 2.7 and is expressed as

$$NA = n\sin\phi = \sqrt{n_1^2 - n_2^2}. \tag{2.8}$$

The numerical aperture can also be expressed in terms of the focal ratio as

$$\text{NA} \approx \frac{1}{2F}, \tag{2.9}$$

where $F = f/D$, f is the focal length and D is the diameter of the aperture.

The numerical aperture is often quoted when describing fibres since the number of bound modes, M, is proportional to the NA squared.

2.3.2 Electro-Magnetic wave theory of propagation of light

As discussed above, an understanding that EM radiation propagates through fibres in a set of discrete modes helps to explain the phenomenon of focal ratio degradation.

Any description of EM theory must begin with a definition of Maxwell's equations. In a dielectric medium wherein there are no stored charges and hence no electric current flowing, Maxwell's equations can be written as:

$$\bigtriangledown \times \mathbf{E} = -\frac{\partial \mathbf{B}}{\partial \mathbf{t}}; \tag{2.10}$$

$$\bigtriangledown \times \mathbf{H} = -\frac{\partial \mathbf{D}}{\partial \mathbf{t}}; \tag{2.11}$$

$$\bigtriangledown \cdot \mathbf{B} = 0; \tag{2.12}$$

$$\bigtriangledown \cdot \mathbf{D} = 0. \tag{2.13}$$

with the constitutive relations:

$$\mathbf{D} = \varepsilon \mathbf{E}; \tag{2.14}$$

$$\mathbf{B} = \mu \mathbf{H}. \tag{2.15}$$

Where **E** and **H** are the electric and magnetic field vectors, **D** and **B** are the electric and magnetic flux densities, t is time, and ε and μ are the permittivity and permeability of the dielectric medium respectively.

The EM theory of propagation of light through optical fibres is based on solving the wave equation in electric or magnetic fields, subject to certain boundary conditions. A substantial amount of literature deals with this theory [49], however since FRD is the transfer of power between modes, this section will only consider the resulting modal fields.

When dealing with many variable equations it is important to reduce the number of variables at every stage. The following description aims to derive a formula for the Electric field which only depends on r, so that the shape of the mode can be described. This equation can then be solved in terms of Bessel functions.

If we take the curl of the curl of the electric field

$$\bigtriangledown \times (\bigtriangledown \times \mathbf{E}) = -\frac{\partial}{\partial \mathbf{t}} (\bigtriangledown \times \mathbf{B}), \tag{2.16}$$

and substitute in the curl of B, we obtain

$$\bigtriangledown \times (\bigtriangledown \times \mathbf{E}) = -\frac{\partial^2 \mathbf{E}}{\partial \mathbf{t}^2} \times \frac{1}{\varepsilon_0 \mu_0}. \tag{2.17}$$

Using the identity$\bigtriangledown \times (\bigtriangledown \times \mathbf{A}) = \bigtriangledown (\bigtriangledown \cdot \mathbf{A}) - \bigtriangledown^2 \mathbf{A}$ and the fact that $c^{-2} = (\varepsilon_0 \mu_0)$, we obtain the standard electromagnetic wave equation that describes the propagation of electromagnetic waves through a medium:

$$\bigtriangledown^2 \mathbf{E} = \frac{1}{c^2} \frac{\partial^2 \mathbf{E}}{\partial t^2}. \tag{2.18}$$

We then make an ansatz as to how the field will look in space, using an

exponential term which separates both a decaying and oscillatory propagation constant with distance [50]:

$$\mathbf{E} = \mathbf{E}\,(r)\, e^{-\beta z - inkz} \frac{\cos l\phi}{\sin l\phi}, \tag{2.19}$$

where β is the imaginary part of the axial propagation constant, integer l is the azimuthal index of the mode, $n(r)$ is the refractive index at radius r, and k is the free-space wave number, where $k = 2\pi/\lambda$, where λ is the wavelength. The periodic dependence on ϕ following $\cos l\phi$ or $\sin l\phi$ gives a mode of radial order l and hence the fibre supports a finite number of guided modes.

Substituting equation 2.19 into equation 2.18 it is possible to obtain a second order differential equation of the form:

$$\frac{\mathrm{d}^2\mathbf{E}}{\mathrm{d}r^2} + \frac{1}{r}\frac{\mathrm{d}\mathbf{E}}{\mathrm{d}r} + \left[\left(n_1 k^2 - \beta^2\right) - \frac{l^2}{r^2}\right]\mathbf{E} = 0. \tag{2.20}$$

Since the cylindrical form of the Laplacian was used to obtain equation 2.20, the solutions are only valid for a waveguide with cylindrical geometry. Furthermore, due to the strict boundary conditions imposed, equation 2.20 is only valid for a step index fibre, with a constant refractive index core and takes the form of a Bessel differential equation. The solutions of the Bessel function are cylindrical. In the core region these functions are of the first kind and take the form J_l. If the field is finite at $r = 0$, it may be represented by the zero order Bessel function J_0. However, the field vanishes as r goes to infinity and the solutions in the cladding are therefore modified Bessel functions denoted by K_l. These modified functions decay exponentially with respect to r. The

electric field may therefore be given by:

$$E(r) = GJ_l(UR); \quad \text{for} \quad R \leq 1 \quad (core) \tag{2.21}$$

$$= GJ_l(U)\frac{K_l(WR)}{K_l(W)}, \quad \text{for} \quad R \lesneq 1 \quad (cladding) \tag{2.22}$$

where G is the amplitude coefficient and $R = r/a$ is the normalised radial coordinate when a is the radius of the fibre core; U and W are the eigenvalues in the core and cladding respectively defined as [50]:

$$U = a\left(n_1^2K^2 - \beta^2\right)^{1/2}; \tag{2.23}$$

$$W = a\left(\beta^2 - n_2^2k^2\right)^{1/2}. \tag{2.24}$$

The normalised frequency parameter, V, is defined via the sum of the squares of U and W so that

$$V = \left(U^2 + W^2\right)^{1/2} = ka\left(n_1^2 - n_2^2\right)^{1/2}. \tag{2.25}$$

Using the equation for the numerical aperture defined by equation 2.8, the V parameter can be defined as:

$$V = \frac{2\pi}{\lambda}a(NA). \tag{2.26}$$

The V parameter is important since Gloge showed [51] that the total number of guided modes, or mode volume M_S, for a step-index fibre is related to V by the approximate expression [52]:

$$M_S \backsimeq \frac{V^2}{2}. \tag{2.27}$$

Figure 2.7 shows the electric field profiles of the guided modes of a step

index fibre at a particular wavelength. There is a fundamental mode (LP01) with an approximately Gaussian intensity distribution, and a number of higher-order modes with more complicated spatial profiles. Each mode has a different propagation constant β. Any guided field distribution can be considered as a superposition of the guided modes. For example, a multimode fibre with NA=0.22, d_{core}=50 μm , would guide 258 modes at a wavelength of 1500 nm.

2.4 Considerations when using optical fibres in astronomical instrumentation

There are three main characteristics of fibres which need to be considered when designing an astronomical instrument:

1. Image scrambling - Optical fibres scramble light both azimuthally and radially. Whilst azimuthal scrambling is almost perfect in step index fibres, radial scrambling is not. This effect increases for slower input beams. As the position of the target changes on the input of the fibre due to atmospheric turbulence, and the fibre does not perfectly scramble, the radial input position of the dispersed spectrum will be shifted in wavelength (as incident angle on grating is changed), as shown in figure 2.8;

2. Spectra transmission - Losses in fibres occur due to scattering, absorption or macro-bending. The amount of attenuation, in dB per unit length, is calculated as

$$\text{attenuation} = \frac{10}{L} \log_{10} \frac{P_{\text{in}}}{P_{\text{out}}}, \tag{2.28}$$

where L is the length of the fibre in metres and P is the power in Watts. Figure 2.9 shows a typical attenuation curve for both a low-OH (or 'dry')

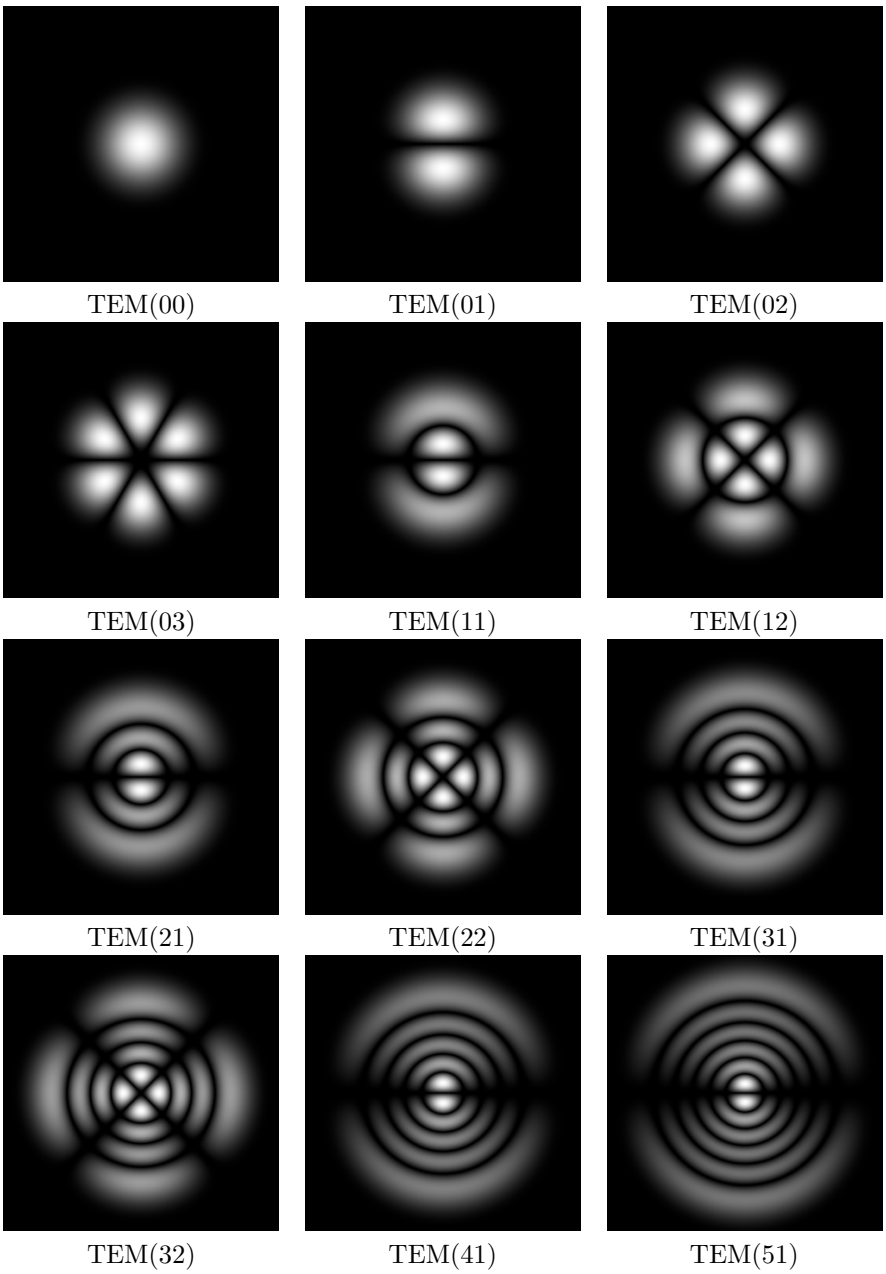

Figure 2.7: Electric field amplitude profiles for the cylindrical Transverse Mode Patterns TEM(pl). In general, light launched into a multimode fibre will excite a superposition of different modes.

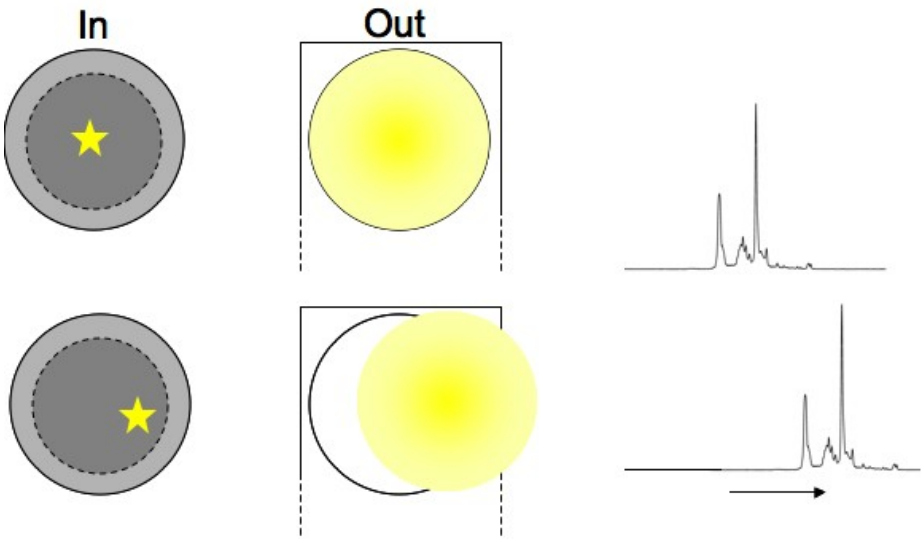

Figure 2.8: As the position of the target changes on the input of the fibre due to atmospheric turbulence, and the fibre does not perfectly scramble, the radial input position of the dispersed spectrum will be shifted in wavelength (as incident angle on grating is changed)

and high-OH (or 'wet') fibres made by Polymicro. Wet fibres contain OH impurities within the silica and lead to many absorption bands between 7200-20000 Å, however, for ultraviolet transmission where the losses approach the Rayleigh scattering limit these fibres are most suitable. Most astronomical applications require high transmission throughout the optical region and in J (1.25 μm) and H (1.65 μm) bands in the near infra-red. Consequently, dry fibres are most commonly used. Unfortunately, Si - O bonds are broken during the fibre drawing process which remain broken and introduce material defect absorption blue-ward of 6300 Å.

3. Focal ratio degradation - This effect occurs due to energy being transferred between modes in the fibre and is fully discussed in the remainder of this chapter.

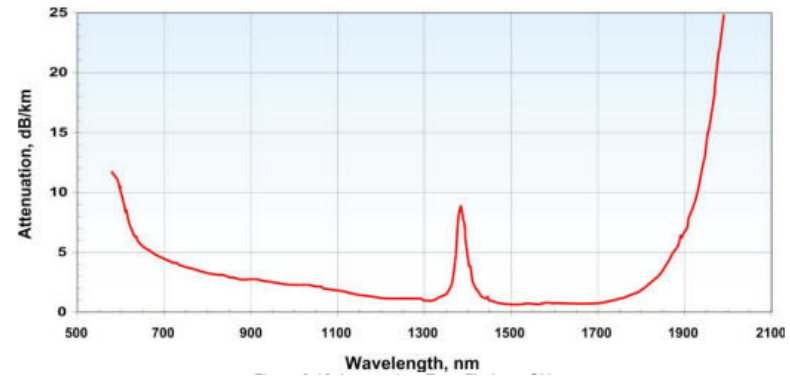

(a)

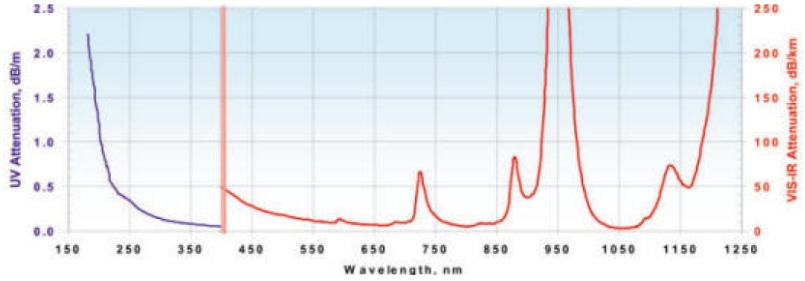

(b)

Figure 2.9: A typical attenuation of a (a) low-OH and (b)high-OH fibre.

2.5 Focal Ratio Degradation

The description of mode propagation given in the preceding sections apply only to a perfect dielectric waveguide. In practice, waveguides suffer from perturbations such as variations in the core diameter with length, irregularities at the core-cladding interface and refractive index variations. These perturbations change the propagation characteristics of the fibres by coupling energy travelling in one mode to another depending on the specific perturbation. This transfer of energy between modes gives rise to focal ratio degradation (FRD).

Practically, FRD means that the focal ratio of light coming out of the fibre will be faster than the light that was injected as shown in figure 2.10 and Étendue will not be conserved in the optical system. A loss of Étendue results in an increase in entropy, and this limits the information which can be obtained from an optical system. The degradation worsens for slower input beams in a similar manner to the radial scrambling. It is extremely important to understand this process since so much is being invested into ELT instrumentation, both theoretically and financially, and if these problems are not well understood at the outlet, greater problems will be encountered at a later stage.

2.6 Causes of Focal Ratio Degradation

FRD has been described as an exchange of power between high and low order modes and with this model of modes in mind, fibre loss mechanisms can be considered as two types; Mode Independent which are intrinsic factors, and Mode Dependent which are extrinsic factors.

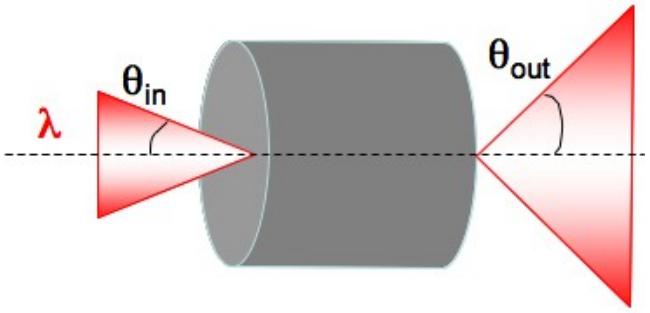

Figure 2.10: Focal Ratio Degradation occurs when $\theta_{in} \lesssim \theta_{out}$.

2.6.1 Mode Independent - Intrinsic Factors

Intrinsic factors are well characterised by manufacturers and it has been shown that the major contributions are from scattering. FRD as a result of scattering is due to Raman, Brillouin, and Rayleigh scattering. Rayleigh scattering is the only mechanism which is considered in this section, since, as is shown by figure 2.11, discounting the OH^- peak, it is the dominant intrinsic factor contributing to the total FRD between the UV and IR absorption tails.

Rayleigh Scattering: Rayleigh scattering is caused by microscopic non-uniformities, which cause rays of light to partially scatter as they travel along the fibre, as is shown schematically by figure 2.12.

Inhomogeneities manifest themselves as refractive index fluctuations and arise from density and compositional vibrations which are frozen into the glass on cooling. Clearly these can be reduced by improving the fabrication process but can never be eliminated by the techniques used at present.

Rayleigh scattering becomes important when the size of the structures in the glass are comparable to the wavelength of light travelling through the glass, and

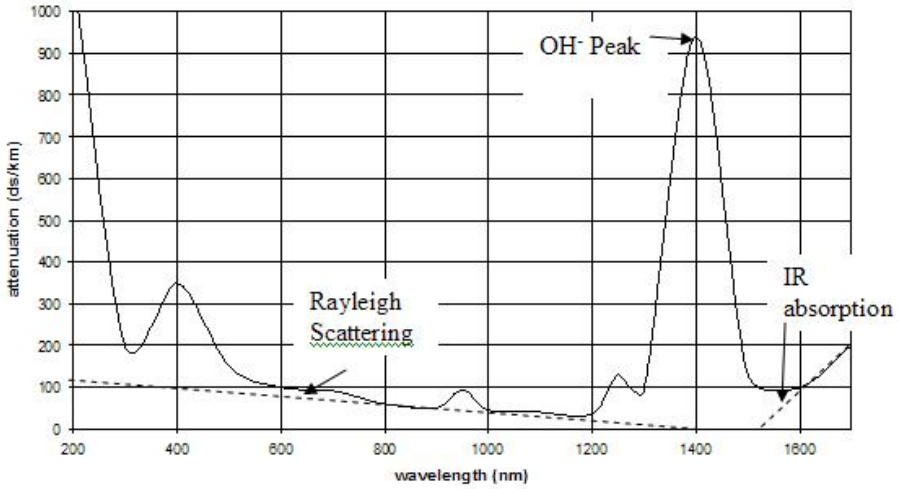

Figure 2.11: Sources of attenuation at wavelengths of operation for a silica fibre

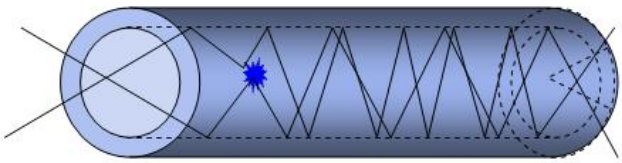

Figure 2.12: Non-uniformities in the geometry or refractive index profile of the fibre, cause light to scatter and the geometry of the beam is changed.

therefore long wavelengths are less affected than short wavelengths. The subsequent scattering due to the density fluctuations, which is in almost all directions, produces attenuation proportional to λ^{-4} following the Rayleigh scattering formula given by:

$$\gamma_R = \frac{8\pi^3}{3\lambda^4} n^8 p^2 \beta_c k_B T_F \propto \frac{1}{\lambda^4} \ , \tag{2.29}$$

where γ_R is the Rayleigh scattering coefficient, λ is the optical wavelength, n is the refractive index of the medium, p is the average photo-elastic coefficient, β_c is the isothermal compressibility at a fictive temperature T_F defined as the temperature at which the glass can reach a state of thermal equilibrium, and k_B is the Boltzmann constant.

Mode Dependent - Extrinsic Factors

Extrinsic factors are rarely addressed by manufacturers and consequently there has been a significant amount of research in this area. A number of factors have been identified as causing and increasing the FRD produced on a fibre. The most relevant of these include :

- micro and macrobending
- alignment
    - i) perpendicularity between the fibre surface and fibre axis
    - ii) polishing errors
- stability of the light source and movable mechanical parts

Microbending It has been shown that mechanical deformation causes FRD by the formation of microbends in the fibre [53]. These microbends scatter the

axial angles of incidence of guided rays, causing a net decrease in the focal ratio of the guided beam. If they are sufficiently large, such beam-spreading can cause the NA of the fibre to be exceeded which ultimately results in light loss from the beam. Microbends are primarily created when the fibre is being drawn and depend upon the type of cladding used and how it is applied. It is intuitive that fibres made from different materials will be affected by FRD induced by microbends differently. Glass and quartz are generally considered as the most favourable material from which to make an optical fibre when considering surface quality, homogeneity and light transmission.

Microbending becomes a problem in fused silica when the fibre core is stressed, which is induced by cladding and consequently fibres clad with a material of low elastic modulus show relatively lower beam spreading. Furthermore Avila *et al.* [54] have shown that the difference in FRD between fibres clad with Polyimide and acrylate protective coverings is minimal. The model used in chapter 3 to describe the experimental results assumes that the main factor that contributes to the total FRD is microbending. The number of microbends per unit length is defined via the parameter, d, and this allows different fibres to be quantitatively compared.

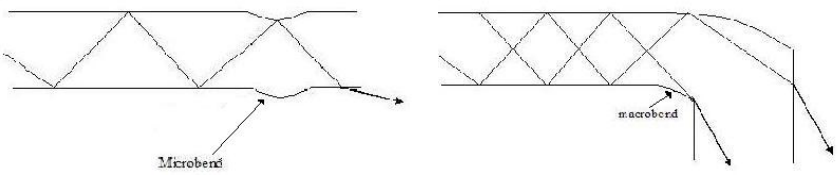

Figure 2.13: Microbending and macrobending are a major source of FRD

Macrobending In astronomical instrumentation, fibres are often wound around a large coil when they are being transported or when they are used to

transport light from the focal plane to the spectrograph slit. More generally, whenever a fibre is bent on a scale larger than would induce micro-bending, it is defined as macrobending, and this alters the angle with which guided rays hit the total internal reflection interface. This in turn increases the angle of propagation, and results in increasing the angle of the output beam. In specific cases the rays arrive at the core cladding interface at an angle that can no longer be totally internally reflected and are consequently lost to the cladding.

Engelsrath [55] *et al.* have shown that macro-bends are not a major loss mechanism. Kapany [56] predicted that for an incident cone of light with a half-angle of 40°, meridional rays begin to escape through the walls of an unclad fibre when $R \leq 3.5d$, where R is the bending radius and d is the fibre diameter. This work was extended by Powell [57] who showed that macro-bends are not a major factor in FRD except in extreme cases. Consequently, when it appears that macro-bends do cause some FRD, it is not so much due to the curvature of the fibre, as the microbends induced by the stress of the large scale bend.

Alignment There are two issues relating to alignment that are known to increase FRD. Firstly the alignment of the fibre with respect to the input beam must be accurately known and secondly the end of the fibre must be polished perpendicular to the optical axis. In Chapter 6, figure 6.8 shows the extra FRD which is induced for varying degrees of misalignment for instruments fed at different focal ratios.

The following chapter aims to determine how physical influences affect the FRD performance of optical fibres and develop a theoretical model in order to predict the behaviour.

I think that in the discussion of natural problems we ought to begin not with the Scriptures, but with experiments, and demonstrations

Galileo Galilei

Chapter 3

Experimental and Theoretical Investigation of Focal Ratio Degradation

The ability to accurately predict the focal ratio degradation (FRD) performance of optical fibres, which places constraints on the performance of fibre-fed spectrographs used for multiplexed spectroscopy, is paramount. In this chapter the dependence of FRD on wavelength, temperature, and length is investigated. Results show that when the fibre is warm, FRD increases as wavelength decreases, as predicted by the theoretical model proposed by Carrasco and Parry [58]. Analysis of the experimental data shows that when the fibre is at room temperature the change in enclosed energy at f/5 varies by as much as 2% within the wavelength range. When the fibre is cold, this trend is reversed. This unexpected behaviour may relate to frozen-in stress. The theoretical model also predicts a strong dependence on FRD with length that is not seen experimentally. By adapting the single fibre model to include a second fibre, the amount of FRD due to stress caused by the method of termination is quantified.

3.1 Introduction

In the preceding chapters a physical description of focal ratio degradation (FRD) was given along with its implications for practical applications. In this chapter, experimental results will be presented which investigate various properties which affect FRD. In section 3.2 a standard theoretical model is described which is then used as a measure against the experimental data. The theoretical model described in this section is a model first proposed by Gloge [59] and later adapted by Gambling *et al.* [60] and Carrasco and Parry [58] in order to define a single parameter, D, which can be used to quantify the FRD. In section 3.3 the model will be used to explain the properties of fibres with different shaped cores in order to test the model and experimental procedures. This model predicts a number of trends, such as FRD being dependent on wavelength (investigated in section 3.4) and on length (investigated in section 3.5). In the final section 3.6 the original Gloge model is modified in order to eliminate the dependence on FRD with length which is predicted theoretically but not seen experimentally. By modelling the fibre as two separate lengths with different amounts of scattering defects it can be shown that most of the FRD is caused by stress frozen in at the fibre ends during end-preparation.

3.2 Theoretical model

3.2.1 Power Spectrum

When determining the power spectrum in an optical fibre it is assumed that mode coupling only takes place between next neighbours since the mode coupling strength decreases rapidly with mode spacing. The power variation, $\mathrm{d}P_m$ of the power P_m of the m^{th} mode is considered along an increment $\mathrm{d}L$ of the

waveguide.

Figure 3.1 shows how the parameters are defined within the fibre.

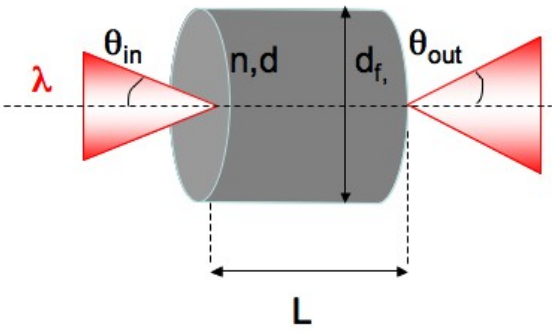

Figure 3.1: Schematic diagram of how parameters are defined within the fibre.

If the coupling is considered statistically, and the individual mode fields are ignored, the power rate equation depends only on the scattering, represented by the term $-\alpha_m P_m \mathrm{d}L$ and d_m is the coupling coefficient between the modes of order m and $m+1$ is defined as:

$$m\frac{\mathrm{d}P_m}{\mathrm{d}L} = -m\alpha_m P_m + m d_m \left(P_{m+1} - P_m\right) + \left(m-1\right) d_{m-1} \left(P_{m-1} - P_m\right), \quad (3.1)$$

where α_m is the loss due to dissipation and scattering to the outside.

In the limit of closely spaced modes, increments can be replaced by differentials, such that $\Delta\theta = \theta_{m+1} - \theta_m$, and thus we set:

$$\frac{P_{m+1} - P_m}{\theta_{m_1} - \theta_m} = \frac{\mathrm{d}P_m}{\mathrm{d}\theta}, \quad (3.2)$$

and equation 3.1 can be rewritten as:

$$\frac{\mathrm{d}P_m}{\mathrm{d}L} = -\alpha_m P_m + \frac{\Delta\theta}{m}\left(md_m\frac{\mathrm{d}P_m}{\mathrm{d}\theta} - md_{m-1}\frac{\mathrm{d}P_{m-1}}{\mathrm{d}\theta}\right). \tag{3.3}$$

If an analogous transition is made, the power spectrum can be obtained in terms of the m^{th} mode

$$\frac{\mathrm{d}P_m}{\mathrm{d}L} = -\alpha_m P_m + \frac{\Delta\theta^2}{m}\frac{\delta}{\delta\theta}\left(md_m\frac{\delta P_m}{\delta\theta}\right). \tag{3.4}$$

Finally, since all of the variables are a function of θ, when the coefficients are expanded, it is found that in $\alpha(\theta) = \alpha_0 + A\theta^2$, the second order term dominates as it represents the loss at the cladding/core boundary. Consequently, only d_0 is retained and this is the parameter which represents microbending. The power spectrum is therefore defined as:

$$\frac{\mathrm{d}P}{\mathrm{d}L} = -A\theta^2 P + \frac{D}{\theta}\frac{\delta}{\delta\theta}\left(\theta\frac{\delta P}{\delta\theta}\right), \tag{3.5}$$

where A is an absorption coefficient and D is a parameter that depends on the constant d_0 that characterises microbending:

$$D = \left(\frac{\lambda}{2d_f n}\right)^2 d_0, \tag{3.6}$$

where λ is the wavelength of light, d_f the fibre core diameter and n the index of refraction of the core.

Equation 3.4 has been solved by Gambling, Payne, and Matsumure [60] for the case of a collimated input beam of angle of incidence θ_{in}. The solution is

found through the separation of variables:

$$P(\theta_{\text{in}}, L) = Q(\theta_{\text{in}}) \exp(-rL), \tag{3.7}$$

$$x = (A/D)^{1/2} \theta^2, \tag{3.8}$$

where $Q(\theta) = G(x) \exp(x/2)$.

Substituting these parameters into the equation 3.5 yields a solution which can be expressed through Laguerre polynomials,

$$P = \sum_{n=1}^{\infty} K_n L_n \exp(x/2) \exp(-r_n L). \tag{3.9}$$

The modal cut-off distributions are characterized by plane wave fields in the cladding which contain practically all the mode power. Gambling *et al.* have shown that if a plane wave approach is adopted along with orthogonal relations for the Laguerre polynomials, the expansion coefficients, K_n can be calculated. Substituting the coefficients into equation 3.9 and using the formula for summation of Laguerre polynomials, the solution is found:

$$P(\theta_{\text{out}}, \theta_{in}) = \exp\left\{-\left(\frac{\chi_i + \chi}{2}\right)\left[\frac{1+\exp(-bL)}{1-\exp(-bL)}\right]\right\} \times \left[\frac{\exp(-bL/2)}{1-\exp(-bL)}\right] I_o\left[\frac{(4\chi_i\chi)^{\frac{1}{2}}\exp(-bL/2)}{1-\exp(-bL)}\right], \tag{3.10}$$

where $\chi = (A/D)^{1/2} \theta_{in}^2$, $b = 4(AD)^{1/2}$, and I_0 is the modified Bessel function of zeroth order. For $bL \ll 1$, $\exp(-bL) \approx 1 - bL$, and so:

$$P(\theta_{\text{out}}, \theta_0) \approx \frac{1}{bL} \exp\left(\frac{\theta_{\text{out}}^2 + \theta_0^2}{4D}\right) I_0\left(\frac{\theta_{\text{out}}\theta_0}{2D}\right). \tag{3.11}$$

Carrasco and Parry have shown that the approximated solution P when in

equation 3.10 may be generalised using a function, G, which represents the standard beam, to the case of an input beam with any aperture as follows:

$$F(\theta_{\text{out}}, \theta_0) = \int_0^{2\pi} \int_0^{\pi} G(\theta_{in}, \phi, \theta_0) P(\theta_{\text{out}}, \theta_{in}) \sin\theta_{in} d\theta_{in} d\phi, \tag{3.12}$$

where $\sin\theta_{in} d\theta_{in} d\phi = d\Omega$ is the differential of solid angle, ϕ is the azimuthal angle measured around the optical axis, and G is a function that represents the input beam. For the case of a solid angle input beam, G is described as a top hat function.

For a fibre illuminated by a single input ray, the output intensity distribution takes the form of a ring with rms width

$$\sigma = \sqrt{2DL} = \sqrt{\frac{Lq}{2}} \left(\frac{\lambda}{d_f n} \right). \tag{3.13}$$

Carrasco and Parry have shown that when the value of D is found for the asymptotic focal ratio of a specific fibre, the results of other experiments where the far field output beam is recorded for input pencil beams of varying focal ratio can be successfully predicted.

Once the validity of the model has been confirmed, various trends shown in figure 3.2 can be predicted using equation 3.6.

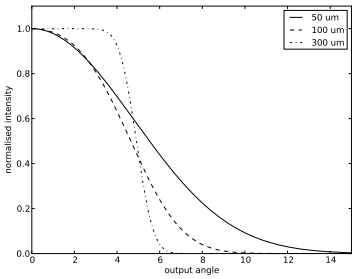

(a) FRD is worse for small core fibres

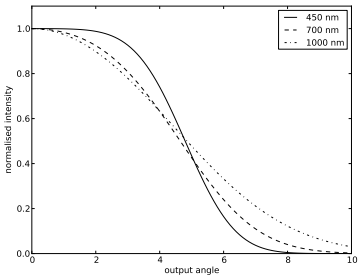

(b) FRD is worse at long wavelengths

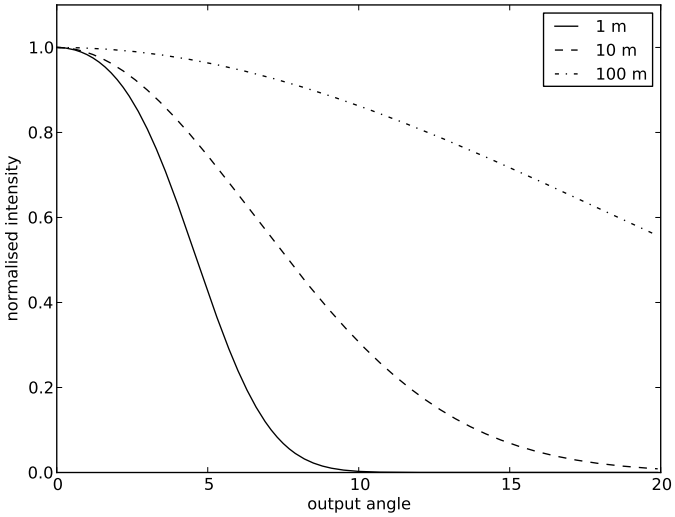

(c) FRD is worse for long fibres

Figure 3.2: Normalised theoretical results to show how the output power distribution will be affected by changing the input parameters. All results are for a solid input beam of angle 5° and unless otherwise stated for a fibre of length 1 m, $d_f = 100\ \mu m$, and $d_0 = 100$.

Figure 3.2 can be summarised by the following statements:

1. **More FRD is predicted for smaller core fibres than for larger core fibres**;

   When it is assumed that FRD arises due to microbends between the core and cladding interface, it is intuitive to predict that larger core fibres would suffer from less FRD than small core fibres since the light will hit the boundary fewer times per unit length. This prediction was tested experimentally by Ramsey [61] who found that FRD did indeed increase as the core diameter decreased. This trend is tested experimentally in section 3.3. This test is not definitive since different types of fibres are used (FBP and FIP), however both fibres had a polyimide buffer and were from the same manufacturer.

2. **More FRD is predicted at long wavelengths than at short wavelengths;**

   Modal diffusion occurs in multimode fibres when light is coupled to neighbouring modes via Rayleigh scattering, Mei scattering, microbending and macrobending [59, 62, 63, 64]. When the light is coupled to higher order modes through this process, an increase in focal ratio is observed. All of these processes have a wavelength dependence for example, surface scattering theory scales as $\delta^2\lambda^{-2}$ (where δ is the rms surface roughness and λ is the wavelength of light) and Rayleigh scattering scales as λ^{-4}. Published results show many discrepancies between observed trends with Poppett *et al.* and Haynes *et al.* [65, 66] observing a strong wavelength dependence, whilst other authors observe only a very weak wavelength dependence or none at all [67, 68, 69]. One possible source for the discrepancies in the observed trends is that the measurements are not being made at the asymptotic focal ratio since many measurements are performed at

the focal speed at which the fibres will operate. Figure 3.3 shows the output light distributions at $\lambda = 450$ nm and $\lambda = 700$ nm for a fast and a slow beam. This result clearly demonstrates the need to observe the trends at slow focal ratios. This effect is further investigated in section 3.4.

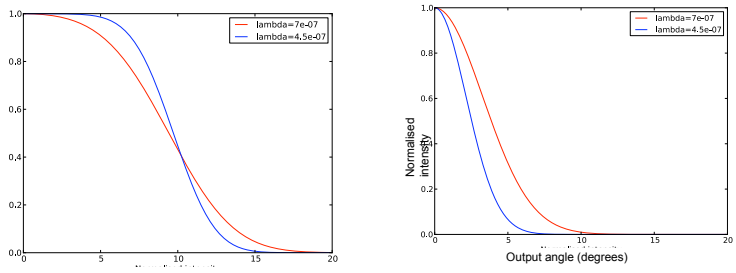

(a) (b)

Figure 3.3: For a fibre with a core diameter of 100 μm and $d_0 = 148.1\text{m}^{-1}$ if the wavelength is varied between $\lambda = 450 - 700$nm, for (a) a slow input angle of $\theta = 10°$ the output angle varies between 10.5 and 11.7, for (b) a slow input angle of $\theta = 1°$ the output angle varies between 4.1 and 6.4. Clearly the dependence with wavelength must be investigated at slow input angles.

3. **More FRD is predicted for long fibres than for short lengths of fibre.**

   The only trend whereby all of the published literature agree is that FRD does not depend on the length of the fibre. The most extreme case being Avila *et al.* [66] who found no FRD difference between fibres that were 1, 3, and 74 m long. Avila *et al.* show that a dependence with length only occurs in very short fibres ($\sim$ 1 m) and small apertures ($\geq F/8$) or when the fibre is wound onto a transportation wheel which introduces macrobending. Gambling *et al.* did report a length-dependence, however this result was for liquid-core fibres. This result has never been reproduced for monolithic fused silica fibres. In section 3.5 this length dependence will

again be tested and in section 3.6 a theoretical description of the method of eliminating this length dependence will be presented.

3.3 Experimental procedures and testing non-cylindrical core fibres

As stated in section 1.2, optical fibres have been used in astronomical instrumentation for more than 30 years. As a general rule, whenever fibres are used, their FRD performance is assessed. However, there have been some inconsistencies in the results reported by different researchers even for fibres from the same manufacturer and of the same type due to experimental procedures or end preparation techniques.

Most FRD measurements are relative in nature; that is, they assume that all light is transmitted at some lower limit of the output f-ratio. The measurements of Powell [57] are an exception to this as they are absolute. The scheme compares the light in the input beam to that emanating from the fibre by way of a simple 90° flip of two separate mirrors.

In the majority of cases when relative FRD measurements are taken, two main techniques are used. Namely, the cone technique [70, 71, 72, 73], shown in figure 3.5, and the parallel laser beam technique [58, 74, 75], shown in figure 3.4. Neither method is considered superior to the other, although one method will be more suited to the task depending on the outcome requirements.

The cone technique gives a good estimate of the total light loss that might be expected when employing the fibre in a optical setup, however it can be

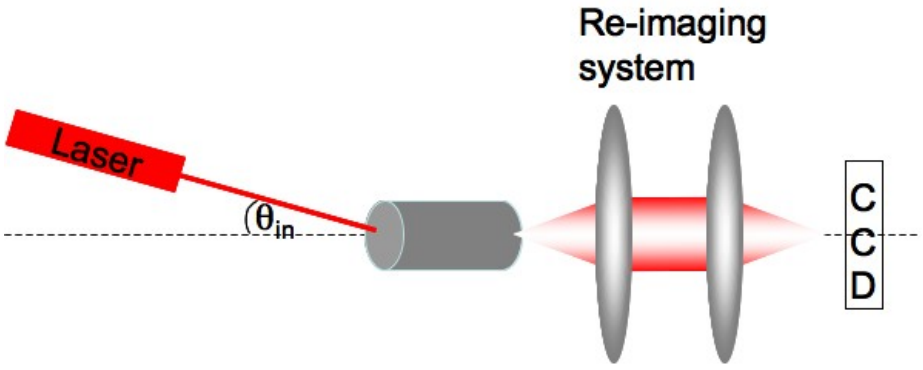

Figure 3.4: Schematic setup for the laser beam technique. A collimated input beam is launched at an angle θ_{in} into a test fibre. The far field output pattern, consisting of an angular ring at a mean angle θ_{in}, is projected on to a screen which is imaged by a CCD camera.

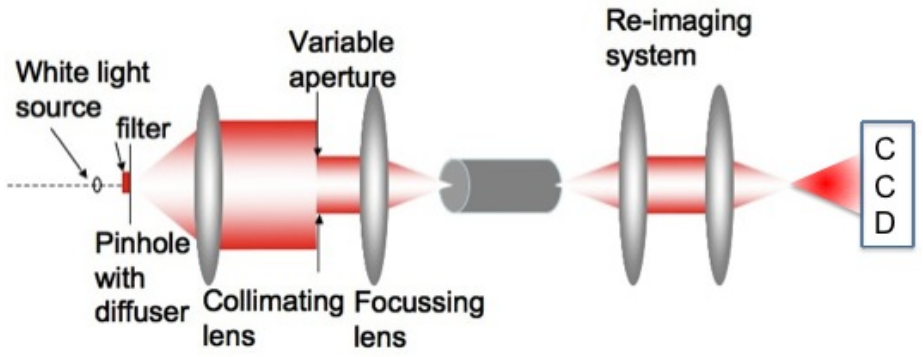

Figure 3.5: Schematic setup for the cone technique. A solid cone of input light is injected into the fibre along the optical axis. The focal ratio is determined by the size of the variable aperture.

highly sensitive to alignment errors and does not provide information about the possible sources that may be contributing to the observed FRD. The parallel laser beam technique is highly sensitive to small changes in FRD and is commonly used as a 'quick look' technique, however, in order to quantify the FRD it assumes that the radial profile of the FRD distribution has a Gaussian profile and measures FRD in terms of the FWHM.

Throughout this chapter, the cone method was used in all experimental setups in order to be able to compare experiential results to the Gloge theoretical model. The following sections describe this experimental method in more detail and describe how the data was reduced, before presenting experimental data.

3.3.1 Experimental method

The equipment used throughout this chapter is illustrated in figure 3.5. Incoherent broad-band visible light is injected into the fibre in a filled cone such that the far-field distribution of specific intensity with angle is constant for angles of θ, where $-\theta_{\text{in}} \leq \theta \leq \theta_{\text{out}}$, which is set by an adjustable iris placed in the collimated input beam. The light source is used to illuminate a pinhole and diffuser. Light entering the fibre is first passed through a bandpass filter. The position of the fibre is adjusted as required for the change in focus caused by the different thicknesses and refractive indices of the different filters used, although this should not affect the angular distribution striking the fibre face. The complete fibre core is illuminated by matching the pinhole size to the fibre diameter and using a 1:1 magnification system. The focal ratio is calculated from this

angle using the relationship:

$$f/\# = \frac{1}{2\tan\theta}.. \tag{3.14}$$

Light exiting the fibre is intercepted by a CCD from which the distribution of specific intensity with angle (i.e. the far-field pattern) is measured. A laser beam denotes the optical axis to which all components were aligned. A viewing system allows the end of the fibre to be examined in-situ by means of a beam splitter and microscope.

Data reduction

The CCD images (in FITS format) were processed using the Psfmeasure task of the IRAF [76] astronomical data reduction software package to obtain the energy encircled within a specified radius measured from the image barycentre. The images were first processed to remove background illumination by subtracting images taken at the same time without illumination. However, the software also removes residual background which is estimated from a specified annulus centred on the image barycentre chosen to be outside the maximum radius for the encircled energy calculation. The resulting encircled energy curves were inspected to ensure that they smoothly approached unity asymptotically. The focal ratio (input and output) was defined by θ_{95} , the half-angle of the cone that encircles 95 per cent of the energy, using equation 3.14. Once the optimum set of input parameters had been determined, they were used throughout to ensure consistency of results. In addition, the throughput of the system was estimated by summing over the distribution of light and normalizing by the angular extent of the input cone, $\theta_{\rm in}$ and comparing to the amount of power detected when the fibre was replaced by pinhole of the same diameter.

3.3.2 Core size and shape effects

As a first test of the experimental method, fibres were tested that were subject to no external FRD sources such as bending, or stressing which might affect different fibres in unpredictable ways. In order to test the assumption of a cylindrical waveguide (resulting in Bessel functions for the modes), these tests were expanded to include multimode step-index fibres which did not have a cylindrical core.

Non-Cylindrical fibres have recently begun to be investigated for use in astronomical spectroscopy due to their image scrambling ability. In chapter 2 one of the main limitations in using traditional cylindrical core optical fibres in astronomical instrumentation is their relatively poor ability to completely scramble the input image, as shown in figure 2.8. Scrambling prevents the optical fibre from carrying any information on the star's radial position at the fibre input. If position information were preserved, it would affect the optical geometry inside the spectrograph, and a shift in the star's radial position on the fibre (such as from atmospheric refraction) would result in a shift of the spectrum's position on the CCD sensor. Analogous to focal ratio degradation, the amount of image scrambling a fibre exhibits increases with increasing f number. We therefore undertook a number of tests to investigate their FRD performance

Specifications of the fibres tested are given in table 3.1.

The fibres were mounted in stainless steel ferules with EpoTek 301-2 and then manually polished using a polishing chuck and abrasive paper with grit

Table 3.1: Details of the fibres tested for FRD.

Name	Core diameter (μm)	Cladding diameter (μm)	NA	Manufacturer
FBP140168198	140	169.7	0.22	Polymicro
FIP100110125	100	110	0.22	Technologies
OCT WF 100/187 P	100	187	0.22	CeramOptec
SQ WF 200x200	192x192	218x21	0.22	

sizes ranging from 5-0.3 μm . The fibres were mounted into ferules in order to ensure that they each experienced the same amount of stress throughout the polishing process.

Figure 3.6 shows the polished, non-circular fibre surfaces at a 100x magnification.

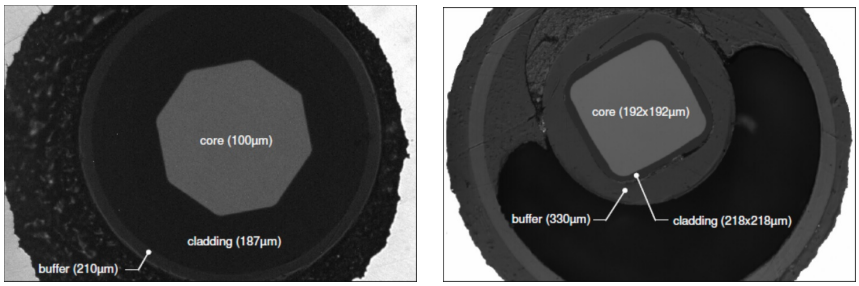

(a) **(b)**

Figure 3.6: Image of the octagonal and square fibres after they had been hand polished to 3 μm .

Focal ratio degradation measurements were made in the far field region for different input focal ratios in the range from f/4 to f/16. Figure 3.7 shows the results for the four fibres tested under the same conditions ($L = 3\ m, \lambda = 632$ nm). Dashed lines represent experimental results and solid lines show the best fit of

the Gloge model. The varying d_0 parameter indicates different levels of microbending per unit length for each of the fibres.

As is shown by figure 3.7 the CeramOptec octagonal fibre showed the best result, whereas the CeramOptec square core fibre showed a poor FRD performance. A possible explanation for this result may lie in the thickness of the cladding layer of the square fibre. A larger cladding layer would help to stabilize the fibre against mechanical deformations resulting from fibre termination and mounting. As expected from equation 3.6 which shows that $D \propto d_f^{-1}$, the 100 μm circular core fibre showed a larger amount of FRD than the 140 μm circular core fibre.

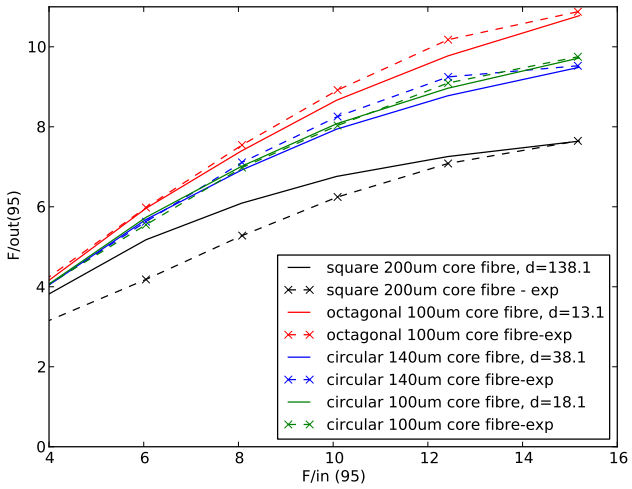

Figure 3.7: Comparison of theoretical modelled curves (solid lines) with experimental performed results (dashed lines) where the output focal ratio is displayed as a function of input focal ratio. The parameter d_0 which characterizes the affect of microbending is displayed for each theoretical curve.

These results show that a sufficient experimental technique has been devel-

oped for the requirements of these investigations and also that the model is able to predict experimental results at different focal ratios.

When comparing the FRD curves of different shaped core fibres it is not immediately obvious as to what trends would be expected. From a purely theoretical perspective, it may be expected that circular fibres should show the best performance since they are not subject to geometric FRD effects, unlike non-circular core fibres as shown in figure 3.8.

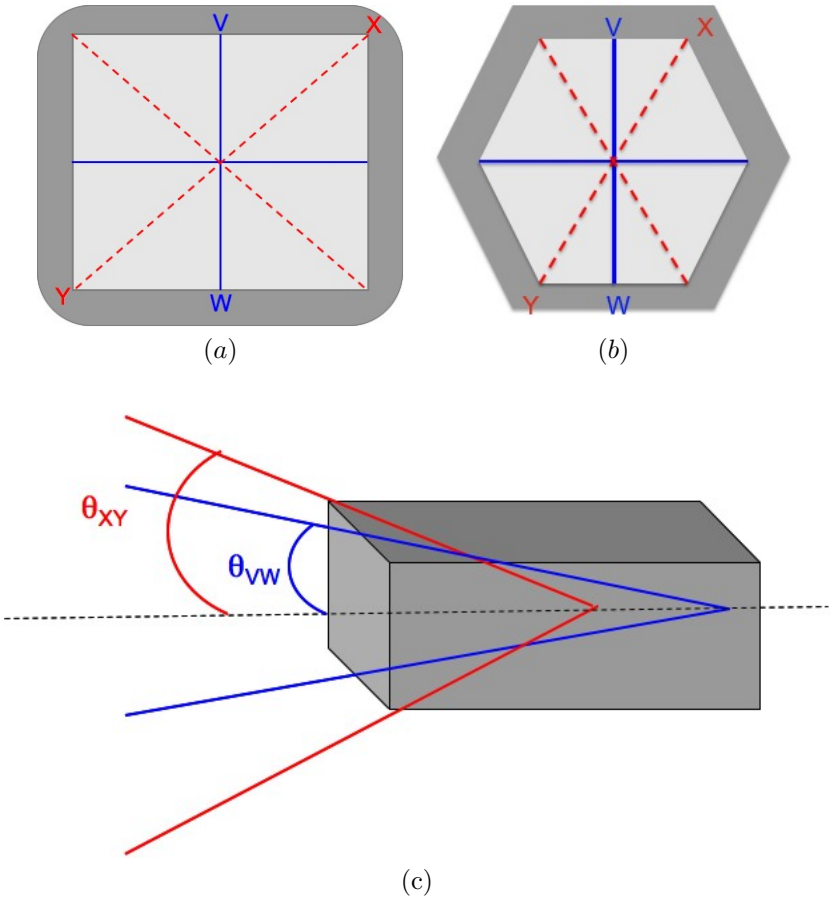

Figure 3.8: Geometic FRD of non-circular core fibres. As shown in (a) and (b) for square and hexagonal core fibres respectively, light entering from the VW axis with have a smaller angle than light entering from the XY axis.

Geometric FRD arises in non-circular core fibres due to θ_{XY} defined in the figure being greater than θ_{VW}, and the greater the difference, the more FRD can be expected (from geometric sources) meaning that, considering only this argument, circular fibres should perform better than octagonal fibres, which should in turn perform better than square fibres. However, as is shown in figure 3.7, the octagonal fibre shows a better FRD performance than either of the circular fibres. This can be attributed to the manufacturing process. Since octagonal core fibres are a relatively new development it is possible that more care is taken during the drawing process and the core/cladding boundary suffers from fewer microbends.

In the following sections, the FRD properties of fibres will be further investigated as external influences are applied which should worsen the FRD performance. These experimental results will again be compared to the theoretical model in order to provide a more robust description.

3.4 Temperature and wavelength effects

The increase in telescope aperture means that increasing numbers of targets are highly cosmologically redshifted so that diagnostic ionic bound-state transitions are observed in the near-infrared. To reduce the thermal background, the instrument must be cooled to 100-200 K while the telescope focus stays at 260-290 K; therefore, fibres must be able to tolerate a difference of 100-200 K along their length (1-100 m). A further requirement is for broad-band performance which will allow the same fibres to feed separate wavelength-optimized spectrographs.

Previous studies by Lee *et al.* [64] of the dependence of FRD on temperature concluded that fibres remain flexible at 80 K temperature and, after a brief equilibration period, show only a slight degradation in performance. This is true of fibres mounted without encapsulation. For the more realistic case where fibres are mounted in ferrules and matrices of holes using adhesives, a variety of effects are seen depending on the thermal mismatch between fibre and mount. However, this can be ameliorated by designing the system to eliminate differences in thermal properties. One method of doing this is to mount silica fibres in glass ferules rather than the traditional option of stainless steel.

Several authors have studied the wavelength dependence of FRD at room temperature in the visible regime [58, 67, 73, 69] and have found it to be small or unmeasurable. However, as this effect is not expected to be large it must be tested at the asymptotic f-number in order to be observable. Schmoll *et al.* [67] tested the fibre at f/3 and Crause [69] tested the fibre at a slightly slower beam of f/4.2, at these focal ratios only a small amount of FRD is observed and the dependence on wavelength is smaller than the experimental errors.

These results are broadly consistent with the picture of fibres where light is scattered by small defects (microbends) presumably introduced during the drawing process and modelled as a modal diffusion process by Gloge [59]. Any wavelength dependency in this process, depending on the typical size and number density of the defects and, possibly, on their internal properties and contrast with the surrounding material may manifest itself as a dependency of FRD on wavelength.

3.4.1 Experimental setup

As described in the section 3.3.1, FRD measurements were made using the cone technique. The fibres used in the experiment were of doped step-index construction made from fused silica with core diameter of $d_F = 100$ or 280 μm and length 2 m as shown in table 3.2.

Table 3.2: Details of the fibres tested for FRD-temperature effects.

Name	Core diameter (μm)	Cladding diameter (μm)	Buffer material material	NA	Manufacturer code
FMOS-a FMOS-b	100 ± 3	140 ± 3	polymide	$.22 \pm 0.02$	FBP100140170

The fibres were prepared by mounting them in a polishing jig and manually wet-polishing using a figure-of-eight motion on abrasive sheets with progressively smaller grit sizes down to 0.3 μm . The fibres were mounted in a chuck designed for this purpose taking care not to stress the fibres. For geometrical calibration, the fibre was replaced by a pinhole matched to the fibre diameter and the distance between the fibre input and output eliminated so that light propagated directly into the receiver stage. The relationship between the output and input focal ratios was found to have a slope of 1.02 ± 0.003 with intercept -0.2 ± 0.0004 indicating a maximum error of 2 per cent over the entire range of focal ratios measured. However, some of this may be due to diffraction which broadens the beam with an equivalent focal ratio of half the ratio of the pinhole diameter and the illumination wavelength (typically F/100).

Variation of temperature and wavelength

The temperature of the middle section of the fibre (≈ 1 m) was varied between $T \approx 290$ K (warm) and 80 K (cold) by immersing it in liquid nitrogen and allowing a few minutes for the output beam to stabilize. The fibre was long enough that the input and output ends could be left undisturbed in the apparatus while the rest was subjected to variation in temperature with minimal physical disturbance.

The wavelength of the incident light was altered by changing the colour filter. The filters had a bandpass of 40 nm with central wavelengths between 450 and 700 nm.

3.4.2 Results

Table 3.3 shows the results of all three fibres tested at the extremes of the wavelength range and the d_0 parameter that has been fit to the results. Figure 3.9-3.10 show the FRD curves for each of the fibres and the theoretical predictions that have been fit to them.

The two main sources of uncertainty are as follows:

1. Deviations in angle between the normal to the fibre face and the optical axis of the fibre - this was investigated by measuring the axial distance at which features on the polished face were in focus at various points over the core. The angular error was estimated as 10 mrad for the FMOS fibres;

2. Determining the value of θ_{95} - this was calculated from the scatter in results obtained when the program was run starting from different initial

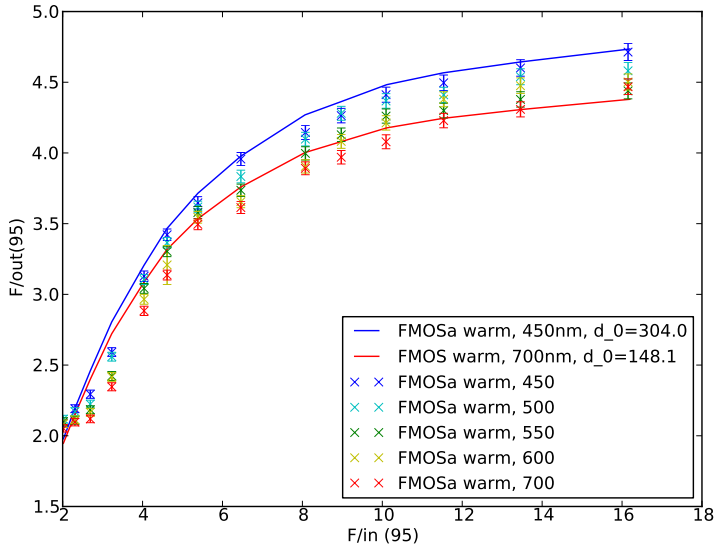

(a)

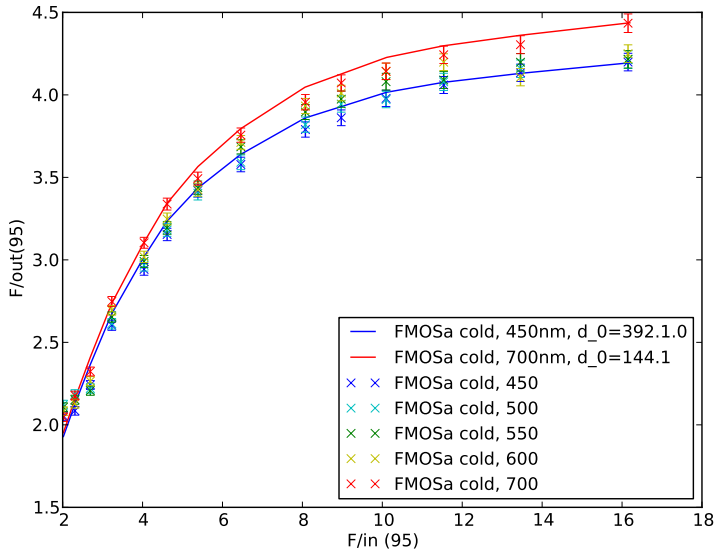

(b)

Figure 3.9: Results for the FMOSa fibre at different wavelengths when (a) warm and (b) cold, with theoretical curves shown as solid lines

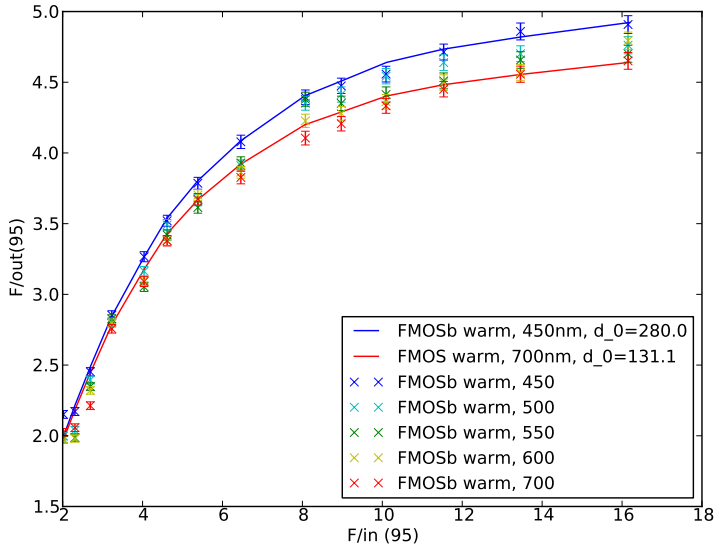

(a)

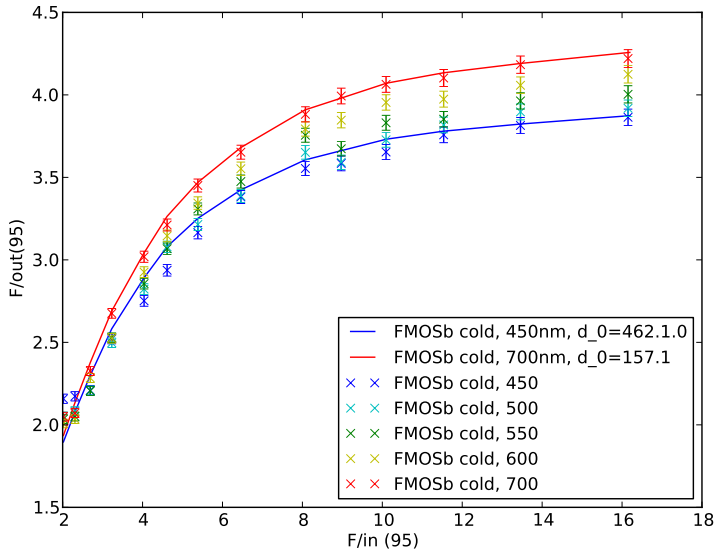

(b)

Figure 3.10: Results for the FMOSb fibre at different wavelengths when (a) warm and (b) cold, with theoretical curves shown as solid lines

Table 3.3: Summary of results for FMOS fibres at different wavelengths and temperatures

Fibre	temperature	λ (nm)	$\theta_{\rm in}$ (deg)	$\theta_{\rm out}$ (deg)	% enc. energy	% enc. energy at f/5	d_0 ($\rm m^{-1}$)	DL
FMOSa	warm	450	1.35	5.95	35.1	82.5	304.1	1.37×10^{-3}
		700		6.45	32.6	80.7	148.1	1.61×10^{-3}
	cold	450	1.35	6.73	31.3	79.7	392.1	1.76×10^{-3}
		700		6.34	33.0	81.0	144.1	1.57×10^{-3}
FMOSb	warm	450	1.35	5.72	36.4	83.3	280.1	1.26×10^{-3}
		700		6.07	34.5	82.0	131.1	1.43×10^{-3}
	cold	450	1.35	7.29	29.1	77.7	462.1	2.08×10^{-3}
		700		6.62	31.8	80.0	157.1	1.71×10^{-3}

estimates of the barycentre and by changing the parameters defining the annuli involved in the summation.

The error bars are generally quite small and are consistent with the systematic differences between the data obtained at different wavelengths.

The main trends observed are:

1. at room temperature, FRD increases at longer wavelengths;
2. when the fibre is cryogenically cooled, FRD increases at shorter wavelengths.

The first result is predicted by the theoretical model. When warm, the output beam approaches an asymptote of $F_{\rm out} = 5.2$ for the two FMOS fibres. This behaviour spans that typically encountered in fibres used in astronomy. The results for the two FMOS fibres are very similar (difference is 2 per cent in the mean and 4 per cent in rms over the range of $F_{\rm in}$) which is consistent with the typical size of error bar (average 4 per cent in $F_{\rm out}$). This validates our error estimation and the consistency with which the fibres have been prepared, aligned and measured.

As discussed above, the Gloge model predicts that FRD will depend on the wavelength of the input light, however, the model should be able to predict the amount of FRD at any wavelength, once the d_0 parameter for the fibre has been determined. In other words, the d_0 parameter should be the same for a specific fibre at any wavelength at any focal ratio. Figure 3.11 shows the enclosed energy at a range of input focal ratios. The solid lines show the theoretical predictions when the d_0 parameter is found using the experimental result at 450 nm, in this case d_0=304.1 m^{-1}. The red solid line shows the model prediction at 700 nm and the dashed lines show the experimental results at this wavelength. Clearly, the model is predicting more FRD at longer wavelengths than is observed experientially.

The second result is not predicted by the model since there is no temperature dependence. When cold, the asymptotic F_{out} is slightly faster than at room temperatures. The scale of these results is consistent with previous results [64], however, the sign of the wavelength dependence is reversed. Figure 3.12 shows the enclosed energy at a range of input angles for the different fibres. It is clear from this figure that the temperature of the fibre affects the FRD at shorter wavelengths, much more than at longer wavelengths. This observation may be important when analysing the process behind the results.

The reality of the change in sign with temperature is supported by: the consistency in the trend seen at each input focal ratio; the consistency of the throughput results between fibres of the same type and between those of different construction (even if the general FRD was very different); and the fact that the only difference in the experimental setup was whether the middle portion

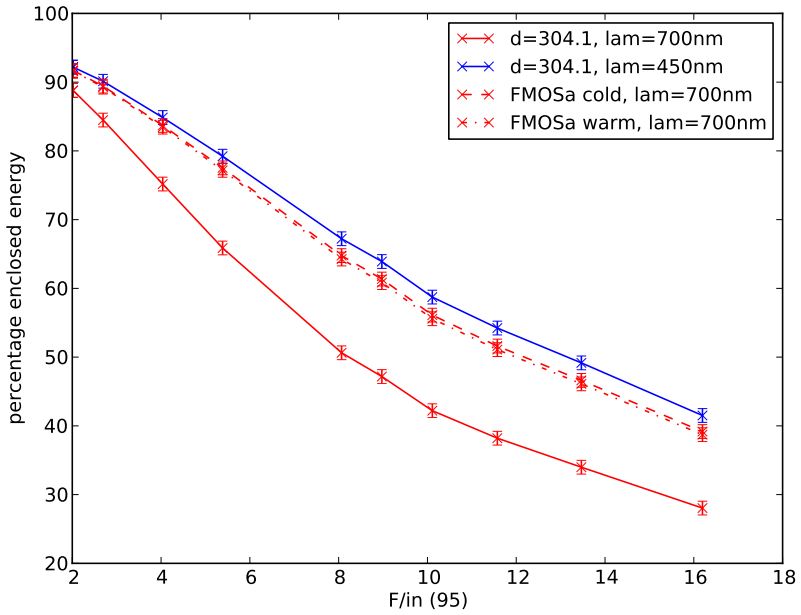

Figure 3.11: If the d_0 parameter is fit for the fibre at 450 nm a value of $d_0 = 304.1$ m^{-1} is obtained. The solid red line shows the model predictions of the enclosed energy using the same parameters at $\lambda = 700$ nm and the dashed lines show the actual enclosed energy obtained experimentally. Clearly, the model is predicting more FRD at longer wavelengths than is experimentally observed.

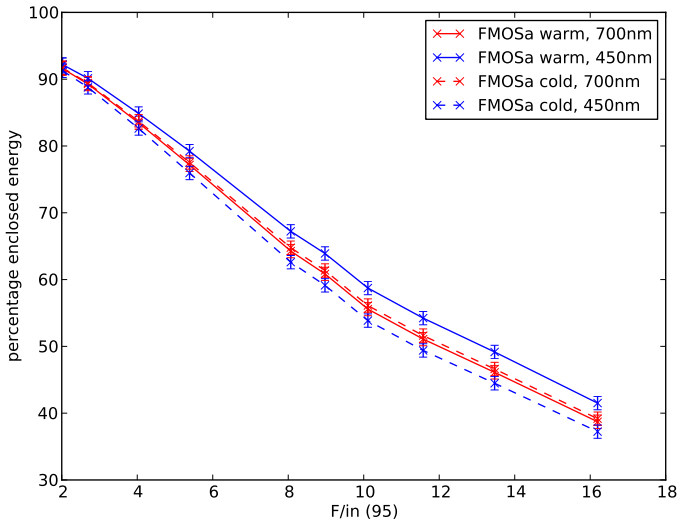

(a)

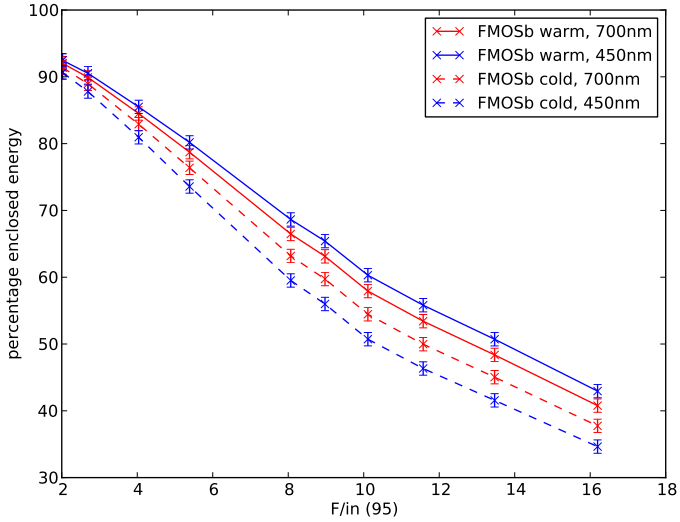

(b)

Figure 3.12: Enclosed energy as a function of input angle for (a) FMOSa, and (b) FMOSb, fibre. The temperature dependence is more dominant at shorter wavelengths.

of the fibre was immersed in the cryostat or not.

In the following sections a number of possible candidates that may explain the experimental results are identified and examined.

3.4.3 Discussion

It is proposed that there are two main processes responsible for the results:

1. the refractive index is kept constant throughout the simulations, whereas in reality it has a dependence on both wavelength and temperature;
2. different scattering processes are affecting the results.

.

The refractive index of a material is dependent on both wavelength and temperature, however it is impossible to obtain a precise value of the refractive index at any given temperature and wavelength since fibres have dopants introduced to change the refractive index between the core and cladding. The refractive index of the buffer material will also be different to both the core and cladding. Figure 3.13 shows how the refractive index would have to vary in order to be able to state a single value of d_0 (in this case, the FMOSa fibre is being modelled with $d_0 = 304.1$ m^{-1}) for the fibre. Figure 3.14 shows the new theoretical FRD curves against the experimental results, for both the warm and cold cases, if the refractive index is varied in this way.

The actual variation in refractive index with wavelength for fused silica is shown in figure 3.15 . It is clear that the variation in refractive index with temperature and wavelength needed to successfully predict the theoretical results is

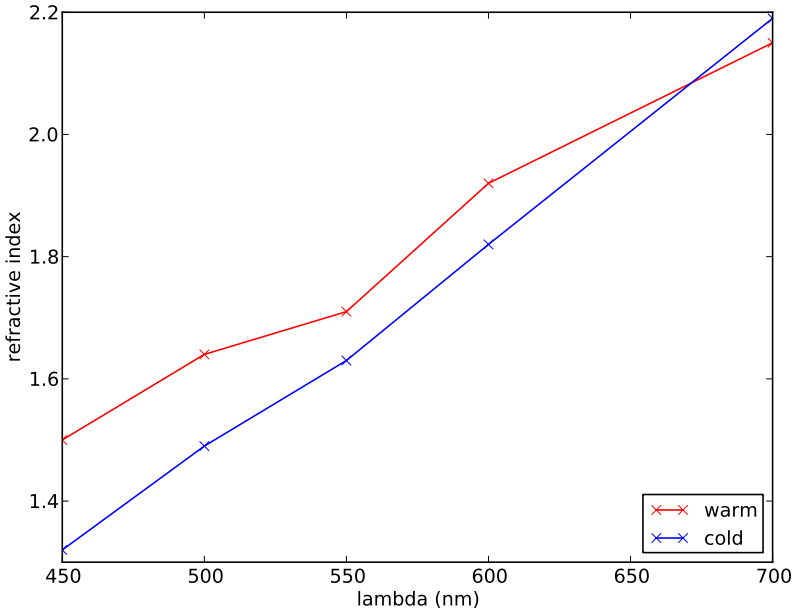

Figure 3.13: Variation of refractive index needed to maintain a constant d_0 for the FMOSa fibre

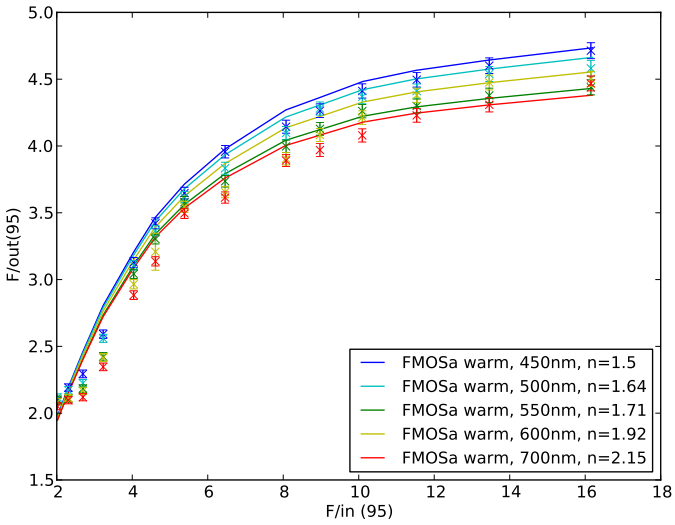

(a)

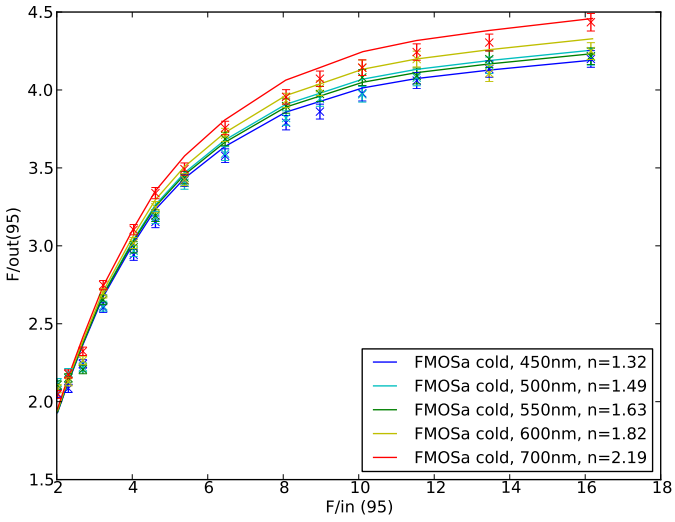

(b)

Figure 3.14: Theoretical FRD predictions for the FMOSa fibre (solid lines) with d_0=304.1 and n varying with wavelength and temperature. Experimental results are shown as points.

much too large to completely account for the experimentally observed results, however, it is possible that it plays a role.

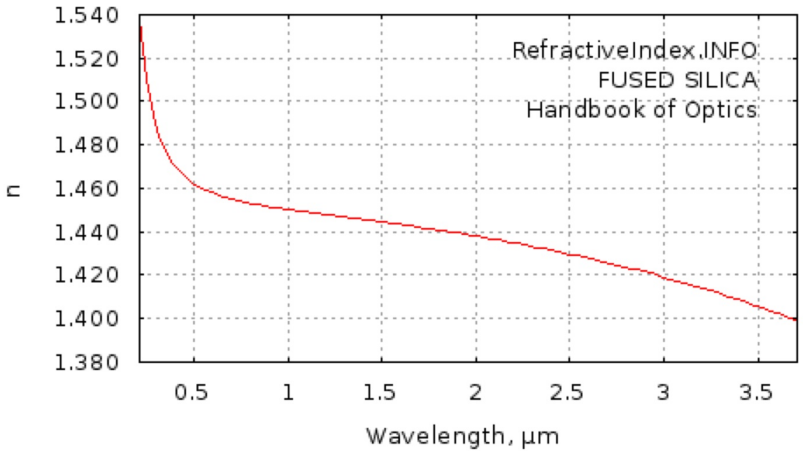

Figure 3.15: Refractive index of fused silica (*Image taken from the handbook of optics [77]*),

The general weakness of the temperature dependence relative to the predictions of Gloge's model might result from the assumption of a continuum of weakly scattering centres whereas the fibre may actually contain a smaller number of strong scatterers at the core/cladding boundary. An extreme example of this argument is if the bulk of the scattering occurs at the fibre ends due to the method of termination (polishing and mounting in a ferrule) which may produce localized stress. This is supported by the weak dependence of FRD on fibre length that is found by many authors and further discussed in section 3.5.

Models of light scattering can be divided into three domains based on a dimensionless size parameter, α which is defined as :

$$\alpha = \frac{\pi D_{\mathrm{p}}}{\lambda}, \tag{3.15}$$

where πD_{p} is the circumference of a particle and λ is the wavelength of incident radiation. Based on the value of α, these domains are:

- $\alpha \ll 1$: Rayleigh scattering (small particle compared to wavelength of light)
- $\alpha \approx 1$: Mie scattering (particle about the same size as wavelength of light)
- $\alpha \gg 1$: Geometric scattering (particle much larger than wavelength of light)

Rayleigh scattering

Rayleigh scattering dominates when the size of the density fluctuation is $\alpha \ll 1$ and is thought to be one of the main source of attenuation in optical fibres since the density fluctuations vary on a microscopic scale.

The coefficient used to define the energy loss due to scattered light is:

$$\alpha_{\mathrm{sc}} = \frac{8\pi^3}{3\lambda^4} \left(n^8 p^2\right) k_B T_f \beta, \tag{3.16}$$

where n is the refractive index, λ is the wavelength of the incident light, p is the photoelastic coefficient, T_f is the fictive temperature and β is the isothermal compressibility. The fictive temperature is the temperature at which the liquid structure is frozen into the glassy state and for silica glass, $T_f = 1200°\mathrm{C}$, however Sakaguchi *et al.* [78] have found that in silica core fibres $T_f = 1600°C$ due to dopants. Since T_f is a resultant temperature from the thermal history of a given glass, the scattering intensity varies depending on T_f. For a typical fibre, $\alpha_{\mathrm{sc}} = 2.53 \times 10^{-28} \lambda^{-4} m^{-1}$ (with p=0.286, $\beta = 7 \times 10^{-11} m^2 N^{-1}$, $n = 1.5$ and $T = 1673$ K.

It is clear from the results above that the dependence of FRD on wavelength is much weaker than the λ^{-4} dependence predicted by Rayleigh scattering, however the value of T_f can be changed by heating the fibre and changing the cooling rate: a slower cooling rate results in a lower T_f and therefore lower $\alpha_{\rm sc}$. The fibres in these tests were not subject to heating and cooling cycles and this did not affect the FRD, however this may be an interesting topic for future research.It is also possible that as the difference between the temperature of the fibre and T_f increases, the scattering would increase.

Mie scattering

Mie scattering dominates when $\alpha \approx 1$, which in the optical regime is too large for a density fluctuation, but it may apply to microbends along the core/cladding interface or indeed to defects caused by end preparation.

As stated above, the warm results observed are consistent with those of Haynes *et al.* [66] who found that when they tested a fibre with ends immersed in index matching gel in order to eliminate surface defects, the scattering component (Lorentzian component) at 532 nm reduced and the enclosed energy (EE) increased. At 1064 nm, the Lorentzian component remained constant with little improvement in the EE. Haynes *et al.* conclude that his result is consistent with surface roughness scattering theory which scales as $\delta^2\lambda^{-2}$ (where δ is the rms surface roughness and λ the wavelength of light) such that long wavelengths are less sensitive to small-scale surface structure. This result may also be explain by Mie scattering which is similarly, weakly wavelength dependent.

Geometric scattering

It is generally accepted that if the fibre is polished to a suitable optical quality, and all dirt is removed from the end face that geometric effects will not contribute to FRD.

In order to further determine which process is likely to be dominating we must find the dependence on lambda in the experimental results.

If the difference in asymptotic F_{out} is calculated, it can be seen from figure 3.16 FRD is inversely proportional to the profile (FRD$\propto$P^{-1}), which is proportional to $D^{1/2}$ as given in equation 3.13. Equation 3.6 shows that $D \propto \lambda^2$ and hence FRD$\propto \lambda$. The results do not show a linear trend.

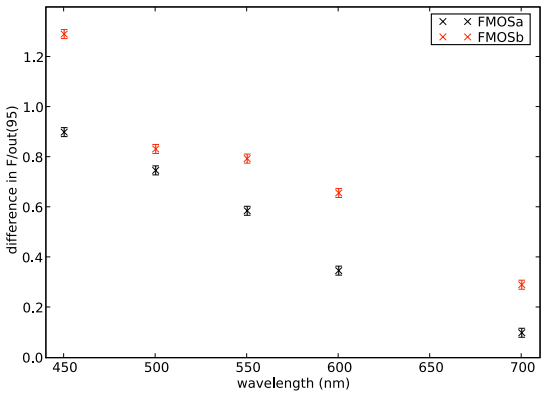

Figure 3.16: Difference in asymptotic value as a function of wavelength.

If σ is adopted as a measure of FRD, from equation 3.13, it would be expected that FRD would scale in direct proportion to the wavelength. Taking the angular width of the input and output beams as the inverse of the respective

focal ratios and deconvolving the distributions, it is true that :

$$\sigma(\lambda) = \left\{ F(\lambda)_{\text{out}}^{-\alpha} - F(\lambda)_{\text{in}}^{-\alpha} \right\}^{1/\alpha}, \tag{3.17}$$

where α=2 for Gaussian functions.

To generalize the wavelength dependency, the FRD is allowed to scale with wavelength as $\sigma \propto \lambda^{\beta}$ where the model prediction has 'colour index' $\beta = 1$. The exponent is then estimated using

$$\beta = \frac{\ln\left[\sigma(\lambda_1)/\sigma(\lambda_2)\right]}{\ln(\lambda_1/\lambda_2)}. \tag{3.18}$$

Estimates of β are shown in figure 3.17 for the three fibres for $\lambda_1 = 450\ nm$ and $\lambda_2 = 700\ nm$. Since the distributions are not strictly Gaussian, α was varied but it was found that a value of 2 gave the least variation in β with F_{in} , so a value of $\alpha = 2$ was adopted.

Although there is some difference between fibres for $F_{\text{in}} \leq 5$, the results are quite consistent from fibre to fibre. The index reaches asymptotic values of approximately +0.2 when warm and -0.2 when cold. Over the full range of input focal ratio excluding the first noisy point, the average values of β are +0.26 and -0.11 at these temperatures. For $F_{\text{in}} \leq 5$, the situation is less clear, but there is still a systematic difference in colour index with temperature, of similar size to the difference at the asymptotes, although at both temperatures the index reaches more positive values, up to $\beta = 0.5$ when warm, but still much less than the model prediction of $\beta = 1$.

Although many possible causes of the behaviour have been explored, the

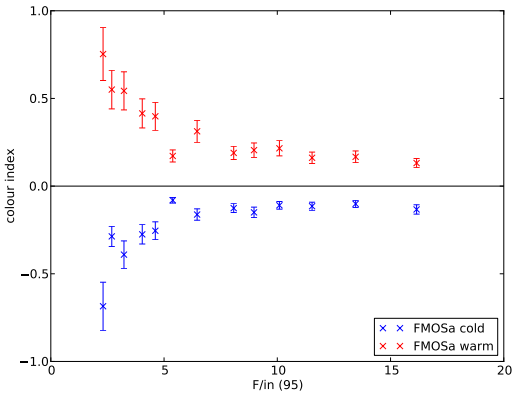

(a)

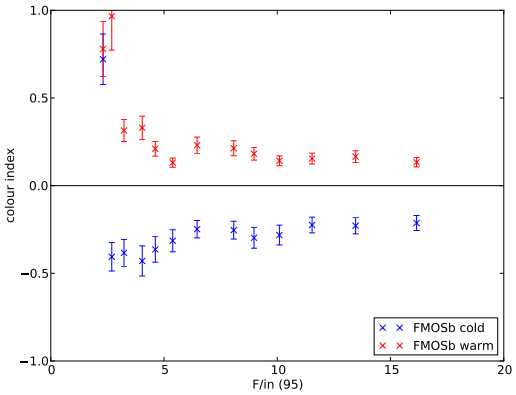

(b)

Figure 3.17: Colour index variations.

complete explanation for the reversal in the wavelength dependence remains unknown. It is noted that the source of the FRD is more effective at lower temperatures where the output focal ratio asymptotes to a faster beam. It is also noted that the refractive index of fused silica is a function of both temperature and wavelength: differing by 0.01 between 450 and 700 nm and 0.003 between 77 and 296 K independent of the other variable (higher at higher temperatures and shorter wavelengths). However, this is unlikely to cause effects more significant than 1 per cent in any measurable property of a fibre on a macroscopic scale, compared with the observed difference of ∼10 per cent in the output beam-speed. The same argument applies to microscopic effects if this difference in refractive index was applicable to the contrast between the scattering centres and the bulk material.

Nevertheless, if the scattering is due to the contrast between defects in the fibre and the bulk of the fibre material in some property that affects scattering, the implication is that this process is more effective at low temperatures. An example of this behaviour would be if the difference in thermal expansion between the defects and the bulk material decreased with increasing temperature. Since the differential expansion would produce localized stresses that affect the refractive index, this could cause more scattering at low temperatures. Another candidate is stress frozen in by the production process as the glass cools below ≈1200 K. A further reduction in temperature by ≈ 220 K from room temperature to ≈ 80 K might increase this stress leading to greater FRD at lower temperatures, as observed experimentally.

If the contrast in the scattering properties does indeed become greater at lower temperatures by one or both of these mechanisms, the wavelength depen-

dence could be explained if it follows Rayleigh theory, for which the scattering scales as λ^4. This could produce an extra component to FRD which increases with decreasing wavelength and dominates over Gloge's process which produces more FRD at longer wavelengths.

3.5 FRD end effects

3.5.1 Introduction

The need for the fibre ends to be flat, smooth, and perpendicular to the axis of the fibre is well documented, although the method of end preparation varies widely depending on various restrictions. The quickest way to prepare a fibre is cleaving, typically by scoring it with a diamond pen or tungsten-carbide-edged blade, although a $C0_2$ laser [79], or spark erosion [80] has also been used. Once the fibre has been scored, it is placed under tension and then bent along the fracture until it snaps. Although this method is relatively quick to perform the results are not always satisfactory and a visual inspection must be performed. In addition to the problem of repeatability, it is extremely difficult to avoid a small defect occurring at the point where the fibre is scored as is shown in panel (a) of figure 3.18. The second method is to polish the fibre on progressively finer grades of abrasive paper and finally on a solution of colloidal silica. This method of polishing the fibre is time-consuming, however visual and interferometric inspection of the end normally shows it to be high quality. Haynes *et al.* [81] have shown that the quality of the polish has a large effect on the FRD by comparing fibres with end face roughness of 245 nm and 6 nm rms.

Figure 3.18 shows the typical finish which can be expected when a fibre is

cleaved or polished. All methods of preparing the ends of the fibre produce stress. The amount of stress and the depth to which it propagates from the end face is currently difficult to measure and methods can only be compared based on the smoothness of the finish as assessed with a microscope or interferometer. The most common rule-of-thumb is that stress propagates to 3 times the depth of the biggest defect on the end face of the fibre although this has never been proven. It has been shown by Craig *et al.* [62] that for the various fibres that they tested, there is no observable difference in FRD between a properly cleaved fibre and a polished fibre.

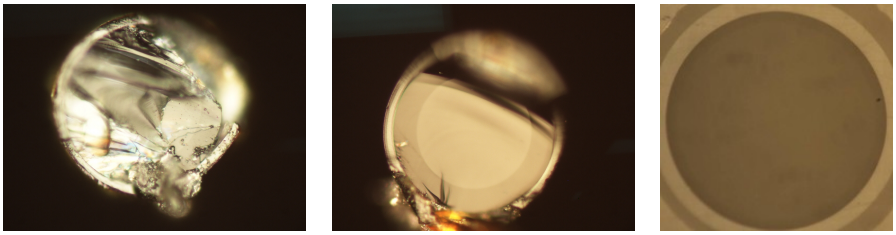

(a) **(b)** **(c)**

Figure 3.18: Results of different methods of end-preparation for a typical fibre with a diameter of 100 μm (a) unprepared (b) after cleaving (c) after polishing. In panel (b) the defect from scoring the fibre is clearly visible

In section 3.6 the Gloge model was modified to include two fibres with different properties in series. This allows us to model the end effect as a short fibre of fixed length with a larger number of scattering defects per unit length, d_0, than the main length of fibre. This parameter, d_0 has different values depending on the termination method used.

It has been shown by Avila *et al.* [54] that FRD is strongly affected by the way in which a fibre is mounted. Avila *et al.* tested UV grade silica fibres and found that, at an input focal ratio of $F_{in} = 8$, F_{out} fell from $F/6.2$ when the

fibre was held gently in a clamp to $F/3.2$ when it was squeezed strongly. This is an important issue because fibres are usually mounted in a ferrule or holder to protect the tip and allow them to be polished in bulk. When the fibres are mounted in this way they must be glued into position and it is extremely important to test the effects of various adhesives on the resultant FRD as shown by Oliveria *et al.* [73]. This model also provides a quantitative measure of these mounting methods which will be independent of the fibre used.

3.5.2 Experimental results

To test the experimental dependence of FRD with length, the cone method described in section 3.3.1 was employed. The fibre used was a typical fibre made by polymicro [1] (FIP100110125) with a core diameter of 100 μm, which has similar characteristics to fibres used in astronomical instruments. Input beams ranging between f/1.7 and f/18.9 (i.e. cone half-angles $16^\circ - 1.5^\circ$) were used to investigate how the FRD evolved with input angle.

Tests were taken for a case of a cleaved fibre of length 10 m immersed via index-matching gel to a smooth flat glass plate and for the same fibre after it had been polished to a 1 μm optical finish. The FRD curve presented in figure 3.19 shows that the fibre has a fairly good FRD performance with an FRD ratio of around 1.1 at $F_{in} = 4.5$. The rationale for testing a cleaved fibre with index matching gel was to make sure that the effect of stress was isolated from any scattering caused by imperfections in the topography of the end face. The use of index-matching gel for the cleaved fibre should eliminate the effect of surface roughness and the smoothness of the finish would do the same for the polished

[1] Polymicro Technologies, A Subsidiary of Molex Incorporated, 18019 N. 25th Avenue, Phoenix, AZ 85023-1200

fibre. Furthermore, it is reasonable to expect that cleaving would result in relatively low stress and therefore provide a baseline against which the results of the polishing could be compared.

The test was repeated after the fibre had been cut to a length of 1 m for both the cleaved and polished case. These two lengths of fibre will be referred to as 'long' and 'short' for the remainder of this chapter.

The measured FRD for all scenarios under which the fibre was tested are shown in figure 3.19. From this, the D parameter for the fibre has been estimated in each of the specific cases (Table 3.4). The FRD ratio is the ratio of $F_{\text{in}}/F_{\text{out}}$ and is often used when describing the FRD performance of fibres. Theoretical predictions using these parameters are also shown in figure 3.19. From this it is estimate that the difference in FRD due to the different fibre lengths for the cleaved fibre at the asymptotic value was 0.15 ± 0.7, and hence is clear that within our experimental uncertainty, no length dependence is observed.

Table 3.4: Parameters need to produce theoretical curves which match experimental results for the fibre preparation methods.

preparation method	fibre length	FRD ratio (at $F_{in} = 4.5$)	d_0 (m^{-1})	D (m^{-1})	D×L
cleave	long	1.07	5.0	2.1×10^{-5}	2.10×10^{-4}
cleave	short	1.09	52	2×10^{-4}	2×10^{-4}
polish	long	1.19	9.1	4×10^{-5}	4×10^{-4}
polish	short	1.15	85	3.7×10^{-4}	3.7×10^{-4}

In order to explain these results, we hypothesise that the fibre does not contain the same number of scattering centres along it's entire length. Instead, the fibre must be modelled as two separate sections: the first being the end of

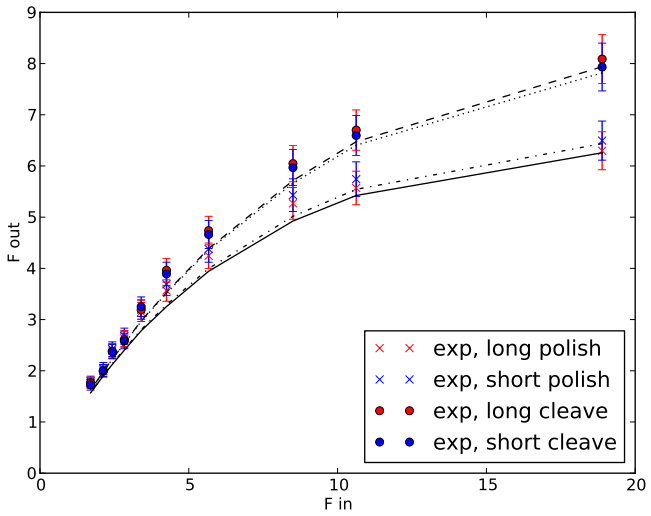

Figure 3.19: FRD curves where experimental results are shown by crosses and theoretical results produced by the original one-fibre model are given by a smooth line

the fibre which is subject to large amount of stress and will therefore have a large d_0 parameter, and the second being the main length of the fibre which will have a much smaller number of microbends per unit length.

3.6 Two fibre theoretical model

In order to add a second fibre into the model it is assumed that for a single input ray at angle θ_{in} to the fibre axis, the output surface brightness at angle θ_{out} is given by the Gloge model as $F(\theta_{out}, \theta_{in})$.

For a solid input angle defined by unit surface brightness for $\theta_{in} < \theta_0$, the

total output surface brightness is given by:

$$F_1(\theta_{\text{out},1}, \theta_0) = \int_0^{\theta_0} F(\theta_{\text{out},1}, \theta_{\text{in},1}) 2\pi\theta_{\text{in},1} \mathrm{d}\theta_{\text{in},1}, \tag{3.19}$$

where numerical subscripts denote the fibre being described as shown in figure 3.20.

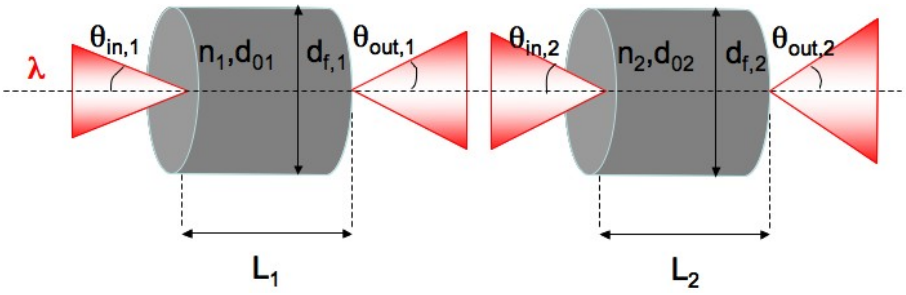

Figure 3.20: Schematic diagram of how parameters are defined within the two fibre model.

If a second fibre is added to receive light from the first fibre, the equivalent number of single rays it sees at the input is given by:

$$\mathrm{d}N(\theta_{\text{out},1}) \propto F_1(\theta_{\text{out},1}, \theta_0) 2\pi\theta_{\text{out},1} \mathrm{d}\theta_{\text{out},1}, \tag{3.20}$$

and hence the output surface brightness in terms of the angle at the exit of the second fibre, $\theta_{\text{out},2}$, is:

$$\begin{aligned} F_2(\theta_{\text{out},2}, \theta_0) &= \int_0^{\infty} F(\theta_{out,2}, \theta_{\text{out},1}) \mathrm{d}N(\theta_{\text{in},2}), \\ &= \int_0^{\infty} F(\theta_{\text{out},2}, \theta_{\text{out},1}) F_1(\theta_{\text{out},1}, \theta_0), \\ &\quad \times 2\pi\theta_{\text{out},1} \mathrm{d}\theta_{\text{out},1}. \end{aligned} \tag{3.21}$$

The coupling between fibres is achieved by setting $\theta_{\text{in},2} = \theta_{\text{out},1}$.

Figure 3.21 shows curves for the output power distribution produced by both the one-fibre and two-fibre model. In this figure, the results from the two-fibre model are offset by 0.03 in the ordinate in order to show the two separate lines. Since we can't determine $d_{0,2}$ and L_2 independently, we use the product $S = d_{0,2}L_2$ to characterise the second fibre. This parameter essentially quantifies the total number of scattering centres (microbends) present in the second fibre. The value of S was chosen to produce the same amount of FRD at the asymptotic value as the one-fibre model. This figure shows that the two-fibre model agrees well with the predictions made by the one-fibre model (itself rigorously tested against experimental data here and elsewhere). Indeed the difference in the 95% enclosed energy values of the one- and two-fibre models differ by the same amount as the experimental error bars (see below). We use the angle which encloses 95% of the energy to define the output focal ratio since this reduces sensitivity to stray light in the experimental setup.

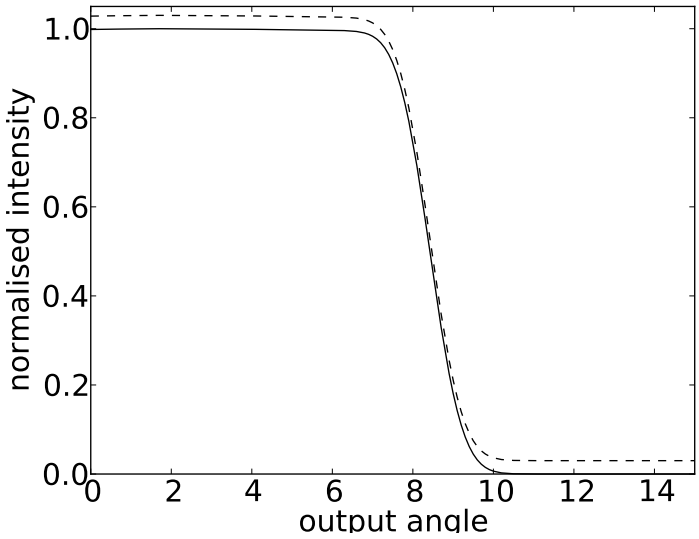

(a) fibre with good FRD performance

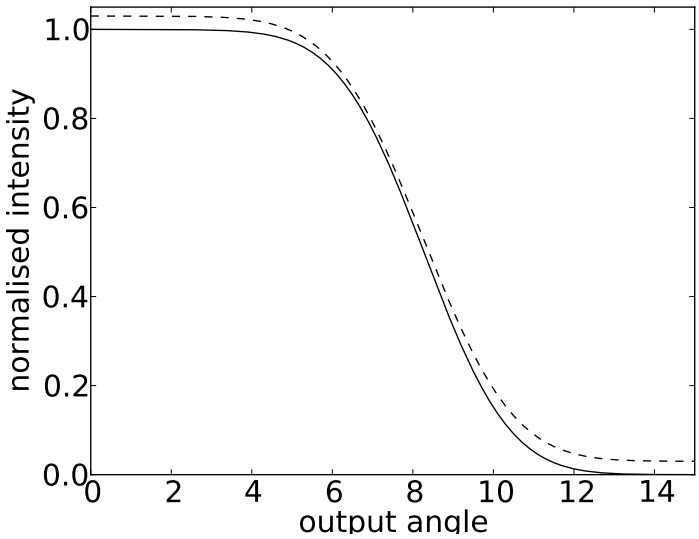

(b) fibre with bad FRD performance

Figure 3.21: Output power distributions predicted by the one fibre (dashed) and two fibre models (solid, with an offset of 0.03 in order to be able to show both curves) which should predict the same output power distribution as a check of the new, two fibre model.

3.6.1 Using the two-fibre model with the experimental results

The experimental results are now used to eliminate the length dependency and compare stress induced by different end preparation techniques. To this end the model can be run for various combinations of $d_{0,1}$ and S to find a single set of values which predict the experimentally-observed FRD curves. In order to find this set of values, a number of constraints can be applied to the two-fibre model, such that it is required that:

1. $d_{0,1}, S$ combinations where the difference in asymptotic F_{out} for the long and short fibres is less than the experimental errors;

2. $d_{0,1}, S$ combinations which give an F_{out} which agrees with the experimental data at the asymptote for both the cleaved and polished fibres ;

3. $d_{0,1}$ value less than that determined from the one-fibre model, and the same for both the cleaved and polished fibres.

As is shown in section 3.5.2, the length dependence was less than $F/0.15 \pm 0.67$ for the cleaved fibre. The contour plot shown in panel (a) of figure 3.22 shows the difference in asymptotic F_{out} between L=1 m and L=10 m with contours shown in increments of 0.7. This plot defines the upper limit on allowable ΔF, and all values within the 0.7 contour region give acceptable solutions for specific values of $d_{0,1}$ and S. Panel (b) shows the difference in asymptotic F_{out} between experimental and theoretical results for the cleaved fibre. The asymptotic F_{out} must be the same as the experimental data within the error bars. For the case of the cleaved fibre, the error in F_{out} was determined to be 0.46. All values within this 0.46 contour region give acceptable solutions for specific $d_{0,1}$ and S. Figure 3.23 shows how these graphs can be combined to find a single solution, marked by the large cross. A solution for the cleaved fibre is found

at $d_{0,1} = 0.1\ m^{-1}$ and $S = 25$. Using these constraints for the polished fibre produces a solution at $d_{0,1} = 0.1\ m^{-1}$ and $S = 48$.

Figure 3.24 shows the FRD curves for various lengths of fibre using these parameters. From this figure it is clear that the length dependence of the model has been removed within the lengths for which it was constrained. The small discrepancies between the theoretical and experimental results arise due to misalignments within the experiment and the fact that it was assumed that G was a perfect step function rather than measuring it explicitly.

The second objective of the two fibre model is to provide a method of comparing stress induced by various end preparation techniques. Comparison of the parameter S between the polished and cleaved cases gives a quantitative assessment of the induced stress. The relative values show that there are twice as many microbends per unit length when polishing the fibre, compared to when it is cleaved. The high absolute values of S make a very strong argument for taking great care to eliminate stress in the end-preparation process.

Currently, there is no method of determining the depth to which stress in the end of the fibre extends. The rule-of-thumb that the stress propagates to 3 times the depth of the largest defect on the end face of the fibre implies that the stress only affects a few μm of the length of the fibre and forces $d_{0,2}$ to be extremely large. Thus, assuming that the defect size is determined by the smallest grit size, implies $L_2 = 3\ \mu m$ and $d_{0,2} = 8.3 \times 10^6\ m^{-1}$ and $d_{0,2} = 16.0 \times 10^6\ m^{-1}$ for the polished and cleaved fibres respectively.

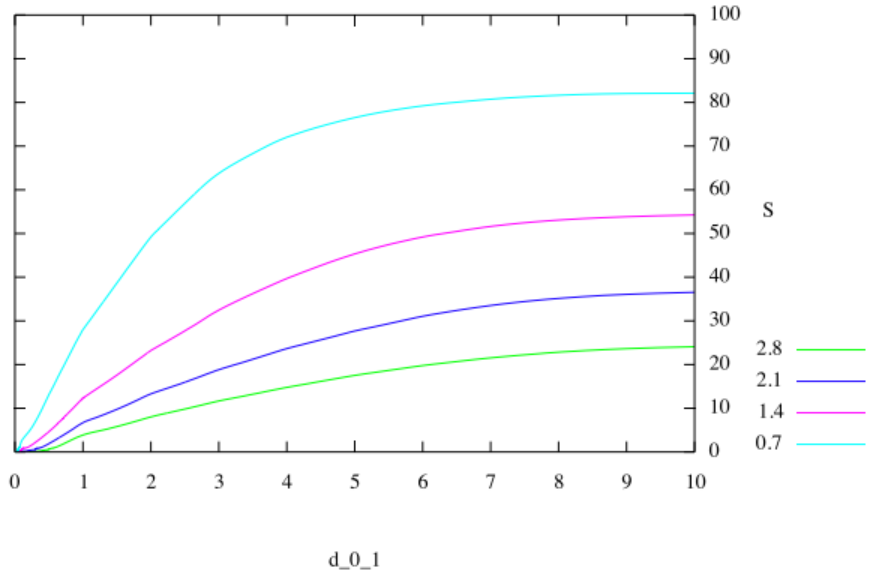

(a)

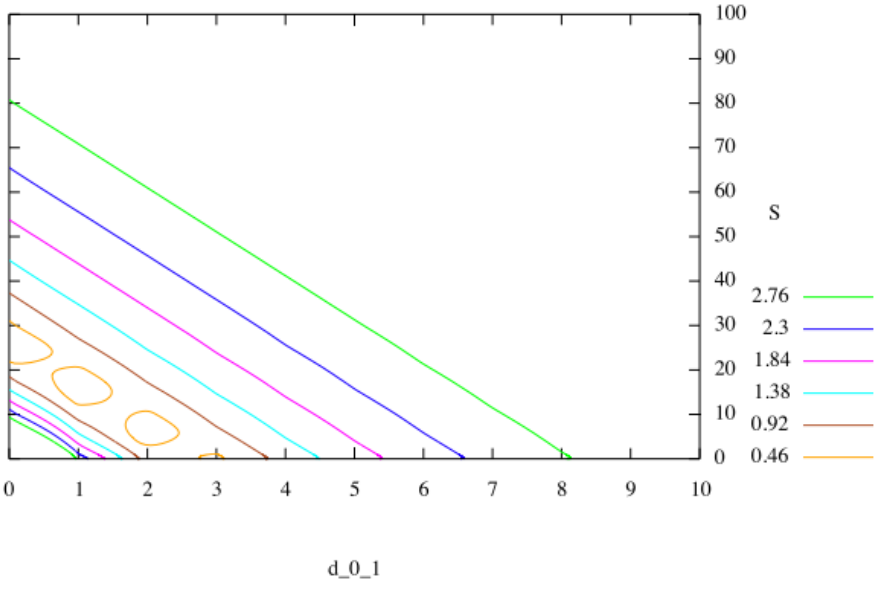

(b)

Figure 3.22: The two fibre model was run for various combinations of $d_{0,1}$ and S (where $S = d_{0,2}L_2$) . Panel (a) shows the difference in asymptotic F_{out} between L=1 m and L=10 m with contours shown in increments of 0.7. Panel (b) shows the difference in asymptotic F_{out} between experimental and theoretical results for the cleaved fibre.

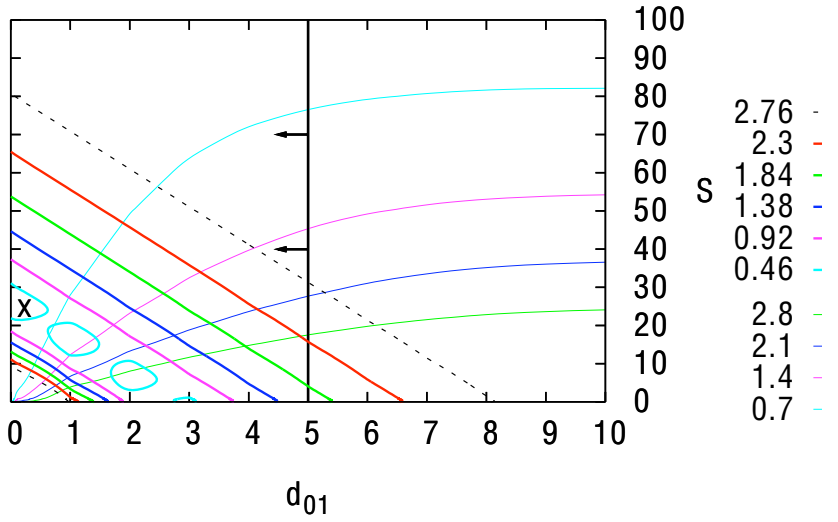

Figure 3.23: The two fibre model was run for various combinations of $d_{0,1}$ and S (where $S = d_{0,2}L_2$). Panel (c) shows how these graphs can be combined to find a single solution, marked by the large cross, for $d_{0,1}$ and S which satisfies experimental data. The black vertical line in panel (c) shows the $d_{0,1}$ parameter predicted by the one fibre model for the cleaved fibre.

3.7 Conclusions

In this chapter, factors which affect the focal ratio degradation (FRD) in optical fibres have been investigated. It has been shown that the shape and size of the core, the temperature of the fibre, and the wavelength of the incident light, all affect the FRD performance, however the length of the fibre does not.

In Section 3.3 an experiment was designed in order to test the fibre preparation, experimental procedure, and data reduction techniques. Results on a standard circular fibre showed that preparation procedures were sufficient to test the fibres and the experimental procedure was established. In this section the idea of using non-circular fibres in astronomical instrumentation was presented and it was shown that the theoretical model, which is designed to predict

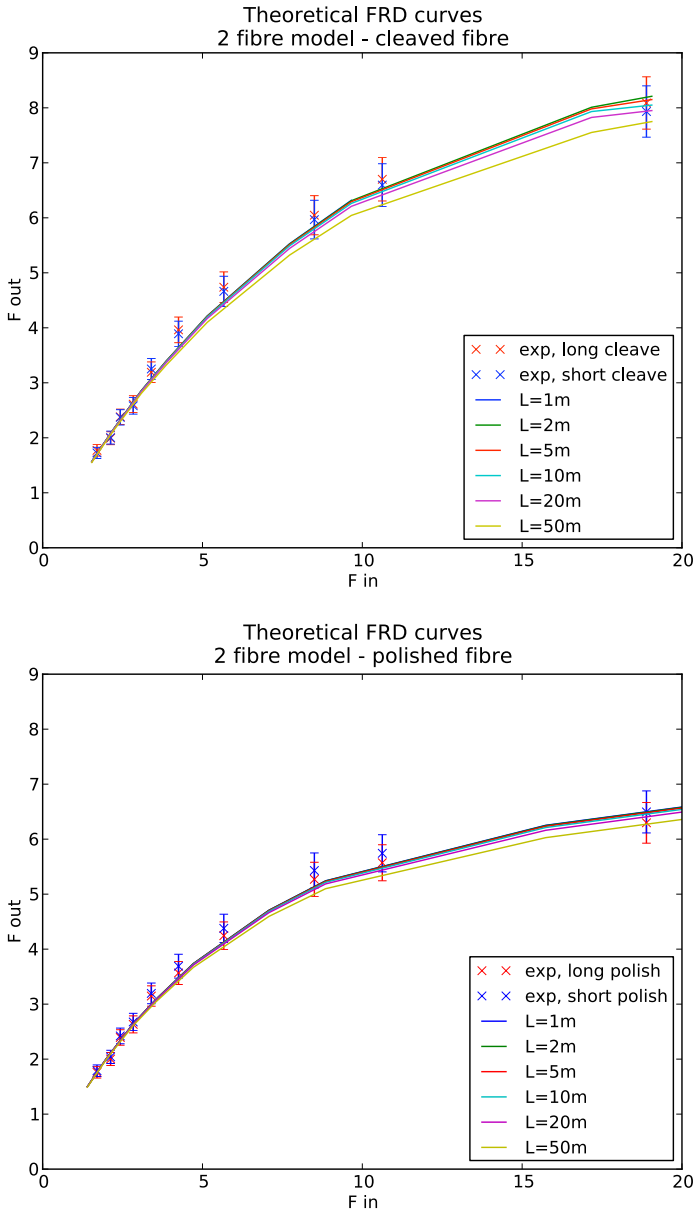

Figure 3.24: 2 fibre model results with $d_{0,1} = 0.1\ m^{-1}$ and $d_{0,2}L_2 = 25$ for the cleaved fibre and $d_{0,2}L_2 = 48$ for the polished fibre. It is clear that within the errors the length dependence of the original model has been removed.

the behaviour of circular fibres, must be further modified in order to be able to accurately predict the behaviour of non-circular core fibres. This result was expected but it is useful to ascertain the limits of the current model.

In section 3.4 it was determined that a qualitative understanding of the anomalous wavelength dependency may be obtained if the scattering follows Rayleigh theory and is dependent on the contrast between the scattering centres. One candidate for this is frozen-in stress resulting from the production process or end preparation techniques. If it is due to frozen in stress when the fibre is terminated, a two fibre model may be necessary to explain the experimental results.

The results presented in section 3.6 agrees with results presented by other authors who have found that the dependency of FRD on fibre length is much weaker than predicted. Since FRD is a function of the number of microbends per unit length, it may be expected that FRD would scale with length. However, results have shown that FRD is only worse in longer fibres when they are wound onto a bobbin and therefore this effect is due to microbends induced by macrobending. In this section it was assumed that the weak dependence on FRD with length is due to the end effects of the fibre dominating over the FRD from the middle section of the fibre.

In order to test this theory, the power distribution model described by Gloge was adapted and a new model has been produced which eliminates the length dependence on FRD. This model was tested against the original one-fibre model, and with experimental data, showed good agreement. As a result of trying to quantify the amount of stress within the end of the fibre it has been shown that

the end-effect is extremely powerful.

If it is assumed that the $d_{0,2}$ parameter characterizes the FRD induced in the end of the fibre then it is possible to compare how the FRD produced in the majority of the length of the fibre is affected. In the case of the cleaved fibre the d_0 parameter (which quantifies the amount of microbending) calculated using the one fibre model was reduced from 5 m^{-1} for a 1 m fibre and 52 m^{-1} for a 10 m fibre to 0.1 m^{-1} independent of length using the two-fibre model. This significant reduction is testament to the strength of the end effect and clearly shows how much FRD is generated in the end of the fibre.

It was initially assumed that cleaving the fibre would produce very little stress, however this was not shown to be the case. This model is therefore extremely useful when comparing various end preparation techniques. For example, our results show that cleaving the fibre halves the strength of the end effect compared with polishing. The model can also provide an upper limit on the FRD performance of any length of fibre and will therefore prove to be very useful when building instruments for Extremely Large Telescopes.

Each fresh peak ascended teaches something.

Sir William Martin Conway, 1856-1937.

Chapter 4

Using Photonic Crystal Fibres in astronomical instrumentation

Photonic crystal fibres (PCFs) offer the possibility of new applications in astronomy with important benefits to interferometry and multiplexed spectroscopy. In this chapter the optimum method of preparation and maintenance of the PCF face is investigated and the near-to-far field intensity distribution of the propagating mode predicted and observed. This study is extended to investigate the practical applications of using a Multicore-PCF (M-PCF) in astronomical instrumentation. M-PCFs are essentially bundles of fibres of low multiplicity (≤ 100) integrated within a single substrate. These devices are likely to be important as building blocks for future astrophotonic instruments aimed at spectroscopy with very high multiplex gains. The M-PCF is currently being tested in order to obtain quantitative loss measurements, however it is shown that it is possible to eliminate crosstalk between cores. It is also shown that standard theoretical models can be used to predict the power intensity distribution.

4.1 Introduction

Astrophotonics lies at the interface of astronomy and photonics and aims to offer a solution to some of the problems of building instruments for the next generation of telescopes through the use of photonic devices to miniaturise and simplify instruments.

The field of astrophotonics has emerged over the past decade and early successes include:

- planar waveguides to combine signals from widely spaced telescopes in stellar interferometry;
- broadband Fibre-Bragg gratings to suppress unwanted background;
- Photonic Lanterns that convert multi-mode light into multiple single-modes;
- arrays of waveguides to miniaturize astronomical spectrographs;
- Photonic Crystal Fibres

This chapter investigates the suitability of a Multicore-Photonic Crystal fibre (M-PCF) for use in astronomical spectroscopy. However, before specific applications are considered, section 4.2 provides a description of how the field of PCFs has developed and how different types of fibre are classified. Another requirement for using PCFs is for theoretical models to be developed which are able to predict the behaviour of the fibres and these are outlined in section 4.2.3. Required also are the technical skills such as end preparation techniques since the normal methods used for optical fibres are not entirely suitable. In section 4.4 a standard type of PCF, a highly non-linear PCF, is experimentally tested in order to prove the robustness of the theoretical model and the suitability

of the end preparation techniques developed. After the preparation techniques have been established and the theory tested, the M-PCF is studied in section 4.5.

4.2 Photonic crystal fibres

One of the most classical examples of photonic band-gap structures in nature are the colourful spots on certain butterfly wings which can be observed to change colour as the wings move. If this highly periodic structure is observed, it seems like an obvious source of inspiration for a research device. However, despite its broad application in nature [82], it is only recently that the principles have been brought into use in optical components considered to operate by the photonic band-gap effect.

The possibility of modifying the guidance properties by introducing a micro-structure in the refractive index profile of optical fibres was first suggested by Kaiser and Astle in 1974 [83], and in 1991 the idea emerged [84] that light could be trapped inside a hollow core fibre by creating a periodic wavelength-scale lattice of microscopic holes in the cladding glass - a photonic crystal. By further manipulation of the fibre geometry the fibre can be designed to display a variety of properties such as endlessly-single-mode behaviour or highly non-linear dispersion.

Since the realisation of the first PCFs in the mid 1990s interest has grown both in the academic and industrial communities and this has led to the development of a wide range of different types of fibre. Photonic crystal fibres are also referred to as Micro-structured Fibres (MSF), or Micro-structured Optical fibres (MOF), and all of these terms refer to the type of fibre in the broadest

description. This broad description can be further refined by placing fibres in two groups depending on whether the light is guided via modified total internal reflection (MTIR) or via the photonic band-gap (PBG) effect. Fibres which guide light via MTIR are often referred to as either High-Index Core (HIC) fibres, Index Guiding (IG) fibres, or Holey Fibres (HF). Fibres which guide light via the PBG effect are generally referred to as PBG fibres or Band-gap-Guiding (BG) fibres.

These two divisions of MTIR and PBG guiding fibres can be further divided into a number of sub classes, which are primarily determined by the dimensions of the fibre structures, and their specific properties. Within the subset of index-guiding fibres, three subclasses have emerged so far: High-numerical-aperture (HNA) fibres, Large-Mode-Area (LMA) fibres, and Highly-Non-linear (HNL) fibres. Within the subset of PBG fibres, a further three subclasses have emerged: Low-Index Core (LIC) fibres, Air-Guiding (AG) or Hollow-Core (HC) fibres, and Bragg fibres (BF). In this chapter, HIC fibres are investigated. The following section discusses these fibres in more detail.

4.2.1 Properties of High-Index Core Fibres

As discussed above, high index core fibres guide light via a process of modified total internal reflection (MTIR) since the effective refractive index of the core is higher than the surrounding cladding material. These effective refractive indices are typically obtained through the introduction of air-holes which may be ordered in different patterns, and which have different shapes, as shown in figure 4.1. Current fabrication techniques allow the relative size of the cladding holes, d, to the centre-to-centre hole spacing (Δ =1-20 μm), to range from

1-90%.

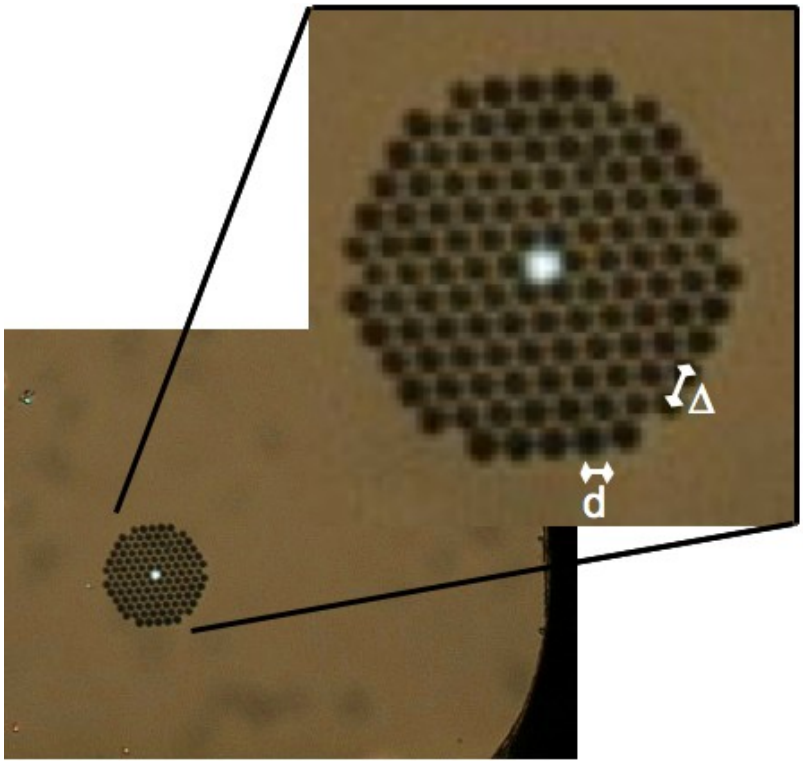

Figure 4.1: Image taken, using a Nikon CFI Plan Fluor microscope with 100x magnification, of a HNLPCF after it has been sliced using a Thorlabs X140 slicer. It clearly shows the holey structure which characterise PCFs and the extremely small core sizes and large d/Δ ratios specific to non-linear fibres. The fibre was illuminated with diffuse white light at the input and the mode area can clearly been seen in the solid core region

.

As with traditional optical fibres, it is useful to characterise PCFs by their ability to confine and conserve modal structure within the fibre.

The design of HIC fibres supports confined modes with a β/k-ratio that obeys the relation:

$$n_{\mathrm{cl,eff}} \leq \frac{\beta}{k} \leq n_{\mathrm{co}}, \tag{4.1}$$

where β is the propagation constant of the guided mode, k the free-space wave-number defined as $k = 2\pi/\lambda$, $n_{\text{cl,eff}}$ is the effective refractive index of the cladding structure and n_{co} is the refractive index of the core. This relation is, in principle, similar to that of traditional optical fibres. However, Knight *et al.* [85] report a PCF which supports only a single mode over an extraordinarily large wavelength range. This behaviour is not observed in traditional optical fibres, and is explained due to the strong wavelength dependence of the cladding refractive index. The number of index-guided modes, N_{PCF}, is approximated as:

$$N_{PCF} \approx \frac{(k\rho)^2(n_{\text{co}}^2 - n_{\text{cl,eff}}^2)}{4}, \tag{4.2}$$

where ρ is the effective core radius. Since $k \propto \lambda^{-1}$, it follows that $N_{PCF} \propto \lambda^{-2}$ and in the high frequency limit ($\lambda \to \infty$) an infinite number of guided modes may not be a feature of PCFs due to the vanishing core-cladding index difference.

In traditional fibre theory, a normalized frequency, V, is commonly used to describe the properties of optical fibres. In order to use an expression similar to that of equation 2.26 for PCFs, the cladding refractive index should be replaced with β_{fsm}/k, where β_{fsm} is the propagation constant of the lowest order mode in the cladding structure. Hence the equivalent expression for an effective V parameter for index guiding PCFs becomes:

$$V_{eff} = \rho\sqrt{k^2 n_{\text{co}}^2 - \beta_{\text{fsm}}^2} \tag{4.3}$$

One of the main concerns regarding the replacement of optical fibres with photonic fibres is the coupling efficiency. However Corbett *et al.* [8] have demonstrated that an atmospheric coupling comparison of large mode area (LMA) and step-index fibres shows that for $\lambda/\lambda_{\text{cut-off}} \leq 1.35$, LMA fibres can

be used as a drop in replacement for single step-index fibre.

4.2.2 Highly Non Linear PCFs

The high non-linear coefficient and designable dispersion properties make HNL-PCFs attractive for many non-linear applications and have been investigated most intensively for their application to super-continuum generation using optical pulses. This phenomena was first observed in 1970 by Alfano and Shapiro [86, 87] , and is due to an interplay of non-linear effects such as self-phase modulation (SPM), Raman scattering, and four wave mixing (FWM). It has been shown by Ranka *et al.* [88] that an extremely broadband super-continuum can be generated covering more than two octaves from low energy ($\sim$ 1 nJ) pulses with an initial duration $\tau_0 = 100$ fs.

In optics, non-linear effects arise from the dependence of material properties on the electric and magnetic fields associated with the light beam. These effects are due to the intensity having a non-linear dependence. For example, self focussing of the beam arises due to the non linear dependence of refractive index on intensity, whereas Second Harmonic Generation (SHG) arises due to the non-linear dependence of polarisation on the electric field [89].

Photonic crystal fibres have a major advantage over traditional optical fibres in this regime since their geometry can be tailored. HNL-PCFs are characterised by having extremely small core sizes ($\sim 1\mu m$) and large d/Δ ratios as shown in figure 4.1 where Δ is the pitch (distance between the centre of two adjacent holes). Small core sizes and a large core/cladding index contrast result in small effective areas and high non-linear coefficients. The effective index difference

between the core and cladding is a strong function of wavelength since at longer wavelengths, the modal field extends further into the airholes, thereby reducing the effective cladding index. Photonic crystal fibres have revitalised the area of non-linear fibre optics since they can have non-linear coefficients three orders of magnitude more than standard fibre [90]. Modifying the geometry of PCFs changes the mode size of the field, which in turn alters the effective non-linearity by either increasing or decreasing the intensity. Altering the intensity alters the non-linear phase change that is experienced by light during propagation [91]. The result is that a wide range of non-linear processes can be observed with a short piece of fibre and a modest laser power available in most optical laboratories.

4.2.3 Theory and Modelling of Microstructured Fibres

Since the field of PCF fibre theory is relatively new, attempts have been made to adapt existing wave-guide or fibre analysis. Although this method is not robust enough to fully predict the behaviour of a PCF, it is still possible to use some elements from standard-fibre modelling. For the index-guiding PCFs, it is possible to apply an approximate scalar model, based on an effective index of the cladding [92, 93]. However, this approximation approach has a limited application range and in order to be able to design and accurately predict the behaviour of new PCF structures, more powerful tools must be employed such as those described in table 4.2.

The experimental results described in section 4.4.2 and 4.6.2 which show the far-field power distribution of a highly non-linear PCF and a multi-core PCF respectively, are described by a model which assumes that a discrete set

Method	Summary	Advantages	Disadvantages
Effective Index, [93, 94, 95]	Evaluates the periodically repeated hole-in-silica structure of the cladding and then replaces the cladding by a properly chosen effective index.	Simple, Low computation time,	No polarisation propagation, accurate modal propagation, No PBG analysis possible
Localized functions, [96]	based on the direct solution of Maxwell's equations,using a representation of the refractive index and field distributions as sums of their localized basis functions	Solutions may be adapted to finite size structure, May describe random hole distributions	Needs great care on result interpretation,Rel. complex method, Inefficient PBG analysis
Bi-orthonormal-basis method, [97, 98]	Takes into account the full vector character of light propagation in PCFs	Vectorial mode repressed, Flexible and efficient, highly accurate	Demanding formulation
Plane-Wave, [99, 100]	Utilizes the periodicity of photonic crystals to solve the Schrdinger equation to predict electronic band-gaps	Well suited for PBGs, Good agreement with experiment, Widespread approach	Large super-cells needed for complex structures, Very demanding for full fibre analysis
Multipole, [101, 102, 103]	Uses many expansions, one based on each of the holes in the structure	Describes the effects of a finite cladding region, No false birefringence errors, suited for symmetry studies, predicts leakage loss	Cannot analyse arbitrary cladding configurations
Fourier-decomposition, [104]	Takes point of reference in a basis function expansion technique to determine confinement loss	Predicts leakage loss	Requires a scalar formulation, Requires adjustable boundary conditions
Finite Difference, [105, 106, 107]	Assumes that the propagation constant along the z-direction is fixed	General approach, describes arbitrary structures, well established and tested	Non-modal approach, numerically intensive, requires detailed treatment of boundaries
Finite Element, [108]	Solves the classical Maxwell differential equations for a large set of properly chosen elementary subspacess	Well tested and accurately describes the modal structure	Complex definition of a calculation mesh
Beam-propagation, [109, 110]	Propagates a launched field profile within a wave-guide	Well tested, commercially available, may use a complex propagation const.	Computationally inefficient
Equivalent averaged index, [104]	Scalar method which takes advantage of symmetry to minimize calculation times	Simple to implement and numerically efficient	Scalar approximation which provides only qualitative results

Table 4.2: Overview of advantages and disadvantages concerning different numerical methods used for analysis and design of photonic crystal fibres. Adapted from Bjarklev [111]

of Gaussians at the end face of the fibre add up in the near-field, similar to the multipole method. This model was developed by Mortensen *et al.* [112] and is described in the following section.

Mode Propagation in the far-field

Mortensen *et al.* proposed a semi-empirical model based on characterising the near-field as a sum of seven Gaussian distributions: one Gaussian in the guiding core and suppressing Gaussians from the nearest air-holes. This model has been successfully used to predict the far-field intensity distribution observed experimentally [113, 114].

As was the case with optical fibres, any description of mode propagation begins with a description of Maxwell's equations (equations 2.10:2.13). The photonic crystals are assumed to be constituted of linear, isotropic and non-magnetic materials, hence the constitutive equations are:

$$\mathbf{D} = \varepsilon_r \varepsilon_0 \mathbf{E}, \tag{4.4}$$

$$\mathbf{B} = \mu_r \mu_0 \mathbf{H}, \tag{4.5}$$

where ε_r is the relative dielectric constant, ε_0 is the free-space permittivity, μ_0 is the free-space permeability, and μ_r is the relative permittivity (which for dielectric waveguides is usually set to $\mu_r = 1$). If we ignore the time dependence and assume that the field only varies in z, the **E** and **H** fields of angular frequency

inside the fibre, ω, may be expressed as:

$$\mathbf{E}(x,y,z) = \mathbf{e}(x,y)\exp\left[i\beta(\omega)z\right], \tag{4.6}$$

$$\mathbf{H}(x,y,z) = \mathbf{h}(x,y)\exp\left[i\beta(\omega)z\right]. \tag{4.7}$$

Using standard Fresnel diffraction transforms we know that the electric field diffraction pattern at a point (x,y,z) outside of the fibre is given by:

$$E(x,y,z) = \frac{z}{i\lambda}\iint A(x',y',0)\frac{\exp\left[ikr\right]}{r^2}dx'dy', \tag{4.8}$$

where $r = \sqrt{(x-x')^2+(y-y')^2+z^2}$.

This transform basically adds together the amplitude of the spherical waves at the end of the fibre and propagates in the z-direction.

Mortensen *et al.* take the form of the field as

$$I(\mathbf{s}) = \mid \mathbf{h}(\mathbf{s}) \mid^2 = \mid \sum_j A_j u(\mathbf{s}-\mathbf{s}_j,\omega_j) \mid^2, u(\mathbf{s},\omega) = \exp(-s^2/\omega^2), \tag{4.9}$$

where $\mathbf{s} = (x,y)$ is a position vector on the end of the fibre, and the summation runs over the guiding core and the six nearest air-holes.

For the radiation in free space this gives a linear combination of expanding Gaussian beams, which is a well studied problem [89, 115]. Neglecting the small back-scattering from the end-facet, the Gaussian $u(\mathbf{s},\omega)$ at finite $z \geq 0$

transforms as

$$u(\mathbf{s},\omega) \rightarrow u(\mathbf{s},z,\omega) = \left(1 - i\frac{2z}{k\omega^2}\right)^{-1} \exp\left[-ik\left(z + \frac{s^2}{2R(z)}\right) - \frac{s^2}{W^2(z)}\right], \tag{4.10}$$

where $R(z) = z(1 + k^2\omega^4/4z^2)$ and $W(z) = \omega(1 + 4z^2/k^2\omega^4)^{1/2}$. The intensity is now calculated as a particular simple linear combination at a distance z away from the end face of the PCF;

$$I(\mathbf{s},z) = \left| u(\mathbf{s},z,w_c) - \gamma \sum_{j=1}^{6} u(\mathbf{s} - \mathbf{s_j}, z, w_h) \right|^2, \tag{4.11}$$

where $\mathbf{j}$ is the number of air-holes being summed over, z is the position of the output along the z-axis and u defines the Fresnel transformation of the Gaussian function centred on $\mathbf{s_j}$ and of standard deviation w_h. The amplitude of the Gaussian function representing the holes is smaller than the Gaussian function representing the core by a factor of γ. The first term gives the overall Gaussian intensity profile of the mode and, with $\gamma \approx u(R-c, w_c)$, the additional six terms of opposite sign suppress the intensity at the six air-holes nearest to the core at finite $z > 0$.

Before this theory can be further tested, a fibre must be prepared and an experimental setup designed which will allow the power distribution in the far field to be observed.

4.3 Fibre preparation

To date, a great deal of work has been published regarding the termination of conventional optical fibres, however the literature regarding PCFs is less abun-

dant. There are many methods to prepare a PCF, however all have significant disadvantages. This section discusses the three main methods of fibre preparation; polishing, cleaving, and slicing.

4.3.1 Polishing

With regard to optical fibres, polishing the fibre is the preferred method of termination since it usually produces a near perfect finish. There are two main reasons for polishing an optical fibre. Firstly, dirt must be removed as this could either refract the ray or absorb it completely which would cause anomalies in the final result. Secondly, surface imperfections such as scratches or micro-pits should be eliminated as they may also refract the light or indicate frozen in stress. It is difficult to quantitatively measure stress, and the amount of stress as a result of polishing cannot be determined. However it is a reasonable assumption that a rough end has more stress than a smooth end. When a fibre is polished, any protrusions removed by the abrasive paper will cause a shock to the surrounding material. However, when it comes to photonic crystal fibres, this method is not as suitable since the debris collects in the holey structure. This problem can be overcome by holding the end of the fibre in ultra-sonicated water for 2-3 seconds. It has been found empirically that if the debris is removed from the holes between different polish grades then the damage to the air-holes is minimized. This technique then requires a final step to remove the water which has collected in the holes via capillary action using an alcohol such as acetone or isopropanol. However there is a risk that although the water has been removed from the end of the fibre, it may remain at some point inside the fibre. The final problem with this method is that due to the different hardness of materials over the end of the fibre, material is removed at a differential rate

resulting in a slightly concave facet as shown by figure 4.2.

4.3.2 Cleaving

A fibre is cleaved by scoring using a diamond scribe by hand and then bending the fibre until it snaps along the fracture. This method is quick to execute however the finish must be inspected carefully and repeated until the desired result is achieved as optimum results require a high level of skill. It is extremely difficult to achieve a perfectly flat facet which is perpendicular to the length of the fibre as is shown by figure 4.3. The working depth of the microscope objective was 0.3 mm so the out of focus region in figure 4.3(b) shows that the end is not flat to within 0.3 mm. Consequently this method is not suitable for systems involving numerous fibres such as those being proposed for the next generation telescopes when efficient and reliable methods of end preparation will be paramount.

4.3.3 Slicing

There are many commercial fibre slicers available which provide a quick and easy method of preparing the end of a fibre with repeatable and reliable results. In order to slice a fibre, the buffer must first be stripped. When working with bare fibres in a non-clean room environment, dust and other contamination might deteriorate the performance of the fibre and result in an unpredictable performance. As a result of this and since the fibre facet cannot be cleaned, re-cleaving the fibre is necessary before any measurements can be taken. Re-cleaving can be avoided by using a connectorized fibre with sealed, cleanable end facets although this is not practicable for many applications. If the fibre is used in a cryogenic environment for example, differences in the coefficient of thermal expansion between the fibre and the holder may result in misalignment

and other undesirable effects.

4.4 Results of testing an HNL-PCF

In order to test the end preparation techniques and theoretical model described above a 30 cm length of a highly non-linear PCF (HNL-PCF) of which little was known, was selected. The dimensions of this fibre were measured and are shown in table 4.3.

Table 4.3: Dimensions of the fibre measured from the microscope image (see figure 4.1) where d=diameter of air-holes, Δ=pitch(distance between the centre of two adjacent air-holes), R_c=radius of solid silica core

d (μm)	d/Δ (μm)	R_c (μm)	Percentage of cladding which is holey
0.97 ± 0.07	0.74 ± 0.09	0.7 ± 0.03	13.1 ± 0.4

4.4.1 Comparing preparation methods

The various preparation methods were outlined in section 4.3 and figures 4.2-4.4 show results achieved using these preparation techniques.

Table 4.4 shows a summary of the results obtained using the different methods of termination. The results for the flatness gained by polishing the fibre look the most promising, however debris and liquid remained trapped in the holes and consequently the light was not guided sufficiently. Cleaving the fibre resulted in a smooth but not flat end and although the light was guided, the process must be repeated many times before a desirable result is achieved. Slicing the fibre using a X140 slicer from Thorlabs proved to be an extremely reliable process.

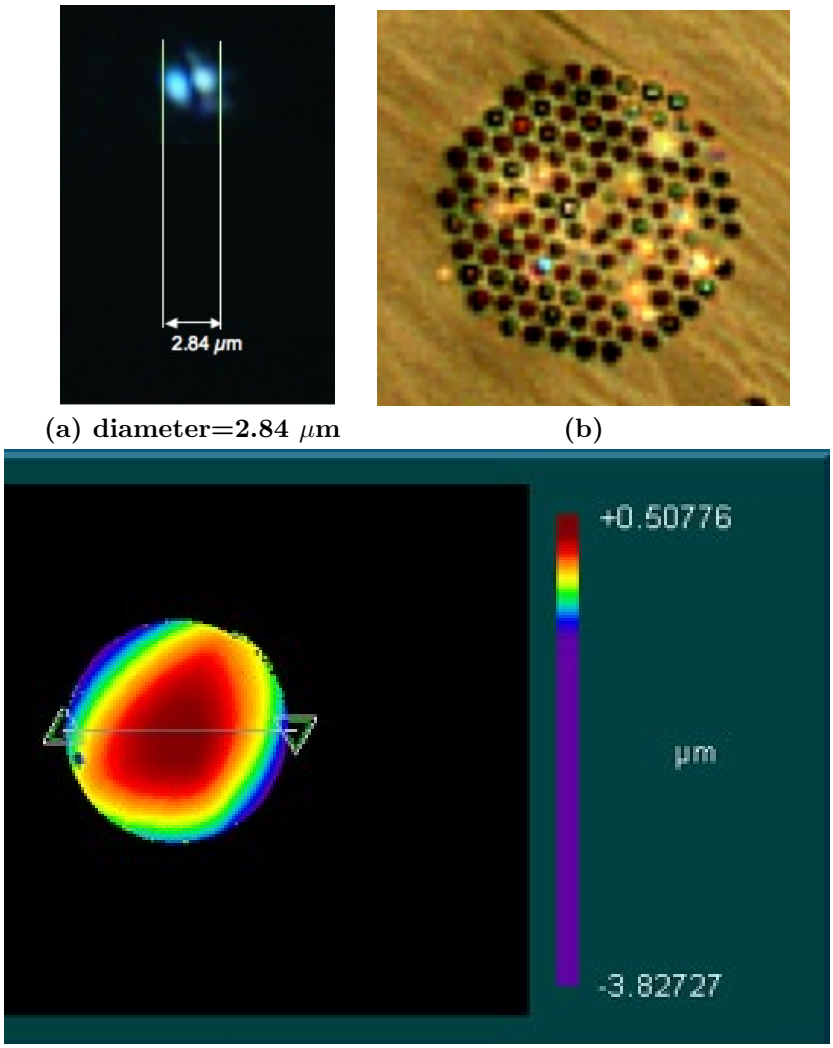

(a) diameter=2.84 μm **(b)**

(c)

Figure 4.2: Results of polishing a PCF. (a) Output distribution when uniform white light is incident on the input end of the fibre. As a result of air holes becomming blocked during the polishing process, the light is not guided 'cleanly' and the output is not a smooth Gaussian spot. (b) Microscope image of the end of the fibre. Black holes are holes which are free of debris, coloured holes are those which are filled with liquid, and holes which are the same colour as the solid silica cladding are those which are blocked with debris, (c) Map of surface height of the end of the fibre showing a slightly concave end face due to differential hardness over the surface. Although the difference is only a few microns this may be important for some applications.

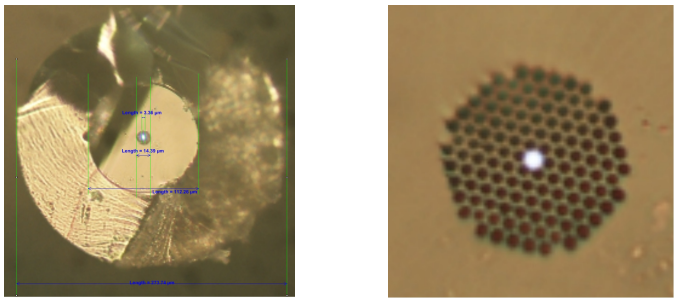

(a) **(b)**

Figure 4.3: Results of cleaving a PCF. (a) a good finish can be achieved with a high level of skill (dimensions: holey region diameter = 14.9μm, cladding diameter = 121μm, buffer diameter = 277μm, (b) Microscope image of the end face shows that all of the holes are clear and undamaged, however the out of focus regions around the outer ring of holes shows that the end is not flat. The fibre was illuminated with diffuse white light at the input and is well guided at the output however it may not be aligned with the optical axis due to the end not being perpendicular to the length of the fibre.

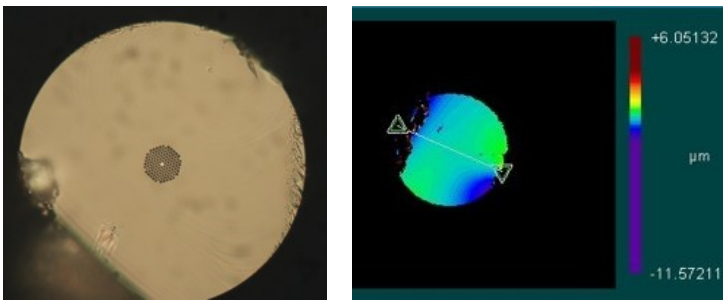

Figure 4.4: Results of slicing the fibre using a Thorlabs X140 slicer. (a) Microscope image of the end face of the fibre after it has been sliced. The end is flat, and the holes are not damaged during the slicing process. The damage to the silica cladding is a result of the initial scoring before the fibre is bent and snapped and does not affect the confinement of the light in the core. The cladding has been stripped which results in an extremely fragile strand of glass. (b) Surface map of the end of the fibre showing that the end of the fibre is flat to within 0.3 μm.

Table 4.4: Summary of quality of the end face after it had been prepared by the methods discussed in section 4.3

Method	PV (μm)	rms (nm)	RA (nm)	light
Polish and Ultrasonicate	4.4	256	206	not guided very well
Cleave	342.4	896	246	guided
Slice (1)	17.6	662	298	guided
Slice (2)	8.0	266	179.	guided
Slice (3)	17.9	360	180	guided

4.4.2 Near-field to far-field transition

As a test of the end finish the fibre was mounted in an optical system as shown by figure 4.5. Both the throughput and the near to far-field transition of the modal distribution were investigated.

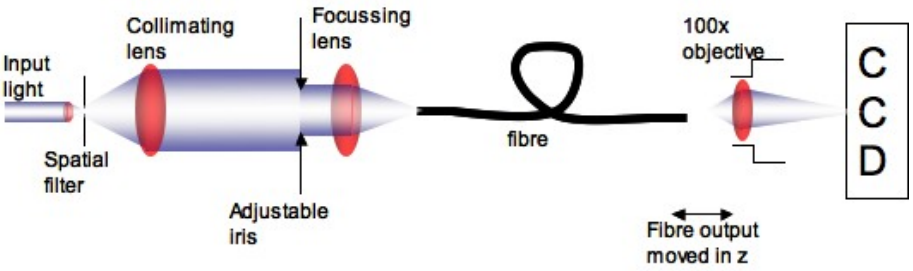

Figure 4.5: Experimental set-up to view the near to far-field transition of the output of the fibre

The fibre was fed with light propagating at a free space wavelength of $\lambda =$ 635 nm and an input ratio of f/2.5 so as not to exceed the numerical aperture of the fibre. Throughput measurements were take in order to determine how much of the light incident on the cladding at the input was guided by the fibre. Results were compared to a pinhole image in order to provide a calibration. The smallest available pinhole had a radius of 5 μm so these results were scaled to the size of the guiding region in the fibre ($R_c = 0.7 \pm 0.03$). Figure 4.6 shows the average throughput as the output of the fibre is moved along the z-axis.

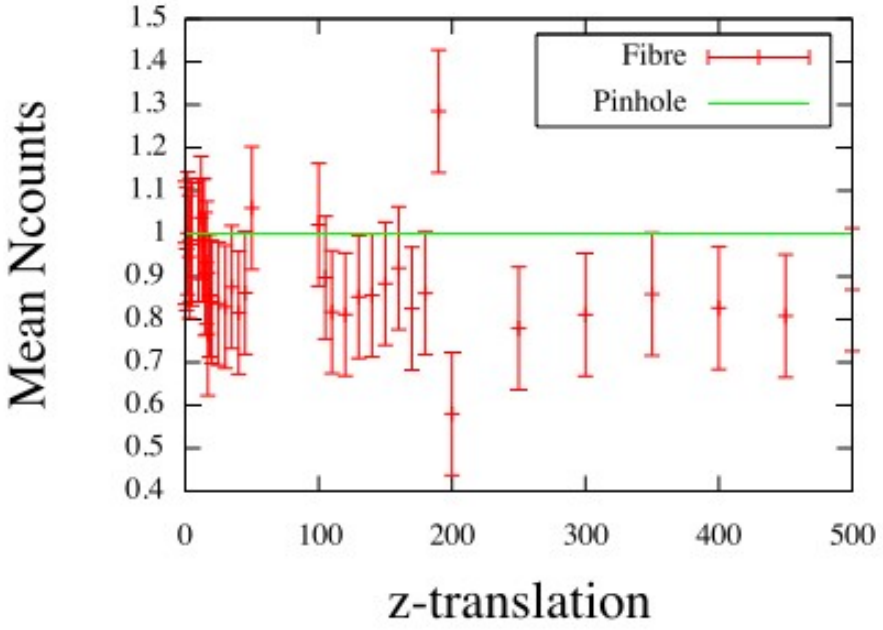

Figure 4.6: $89\% \pm 2\%$ of the incident light was guided by the fibre. Since $\sim 4\%$ will be lost at each air-glass interface, this shows that only $\sim 3\%$ of the incident light was lost within the fibre.

It is expected that a PCF would guide around $\sim 92\%$ of incident light since $\sim 4\%$ will be lost at each air-glass interface. It is clearly shown by figure 4.6 that the fibre does not guide all of the light and by taking an average of the fibre data, the percentage of incident light which was guided by the fibre was calculated to be $89\% \pm 2\%$. This means on average $\sim 3\% \pm 2\%$ of the light was lost within the fibre. The greatest source of error was the read noise of the CCD since the number of counts was relatively low.

After it had been established that the fibre was guiding a sufficient proportion of light incident on the input, the near-field distribution was measured using a microscope objective in order to magnify the modal power distribution

onto a CCD. By translating the fibre away from the focal plane, the intensity distribution was imaged at different distances between the near and far-field as shown by figure 4.7.

It can be seen that at certain z-translations the mode propagates as would be expected from any standard PCF, transforming from a single Gaussian and then developing satellites resulting from the innermost ring of air-holes. However at certain positions, the intensity distribution suffers from a dip in the centre. In order to verify these distributions, the results were compared to a model proposed by Mortensen *et al.* [112] described in section 4.2.3. Using γ=0.1 provides an acceptable fit by eye to the model of Mortensen *et al.* and these results are shown in figure 4.8.

Comparison of the experimental data with the Mortensen model shows qualitative agreement and suggests the fibre is guiding light as expected. Figures 4.7 and 4.8 show that in the extreme near-field the intensity distribution is circular and becomes progressively hexagonal as z increases. At $z = 6\ \mu m$ the Gaussian function in the holes dominate over the central Gaussian function resulting in a bright ring with no peak in the centre. At $z = 8\ \mu m$ the central peak returns with a large contribution from the air-holes since structure can be seen in the ring. As z increases further the distribution returns to a smooth Gaussian. The most important result is that the pattern produced by the air-holes profoundly modifies the overall Gaussian function and this result is in agreement with the model. It is proposed that this is due to the extremely high d/Δ ratio combined with the extremely small core size which results in the air holes having a large influence over the far field distribution. This result was also found by Mortensen *et al.* [112].

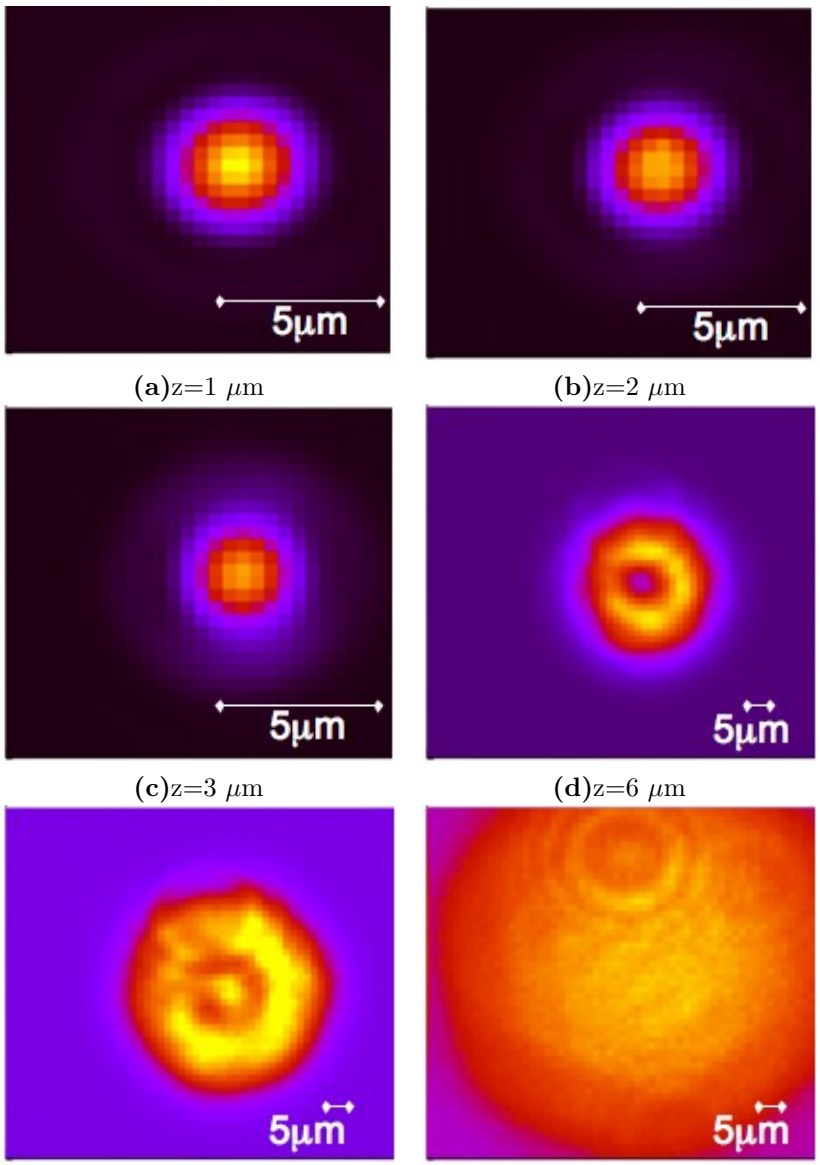

(a)z=1 μm **(b)**z=2 μm

(c)z=3 μm **(d)**z=6 μm

(e)z=8 μm **(f)**z=13 μm

Figure 4.7: Experimental intensity distribution as the fibre is translated away from the focal plane. (a) to (b) In the extreme near-field the mode is circular with a Gaussian profile,(c) an airy disk develops as the diffraction limit is approached, (d) and (e) air holes modify the overall Gaussian distribution sufficiently to produce higher order spots, (f) the distribution returns to a smooth, circular Gaussian in the far-field.

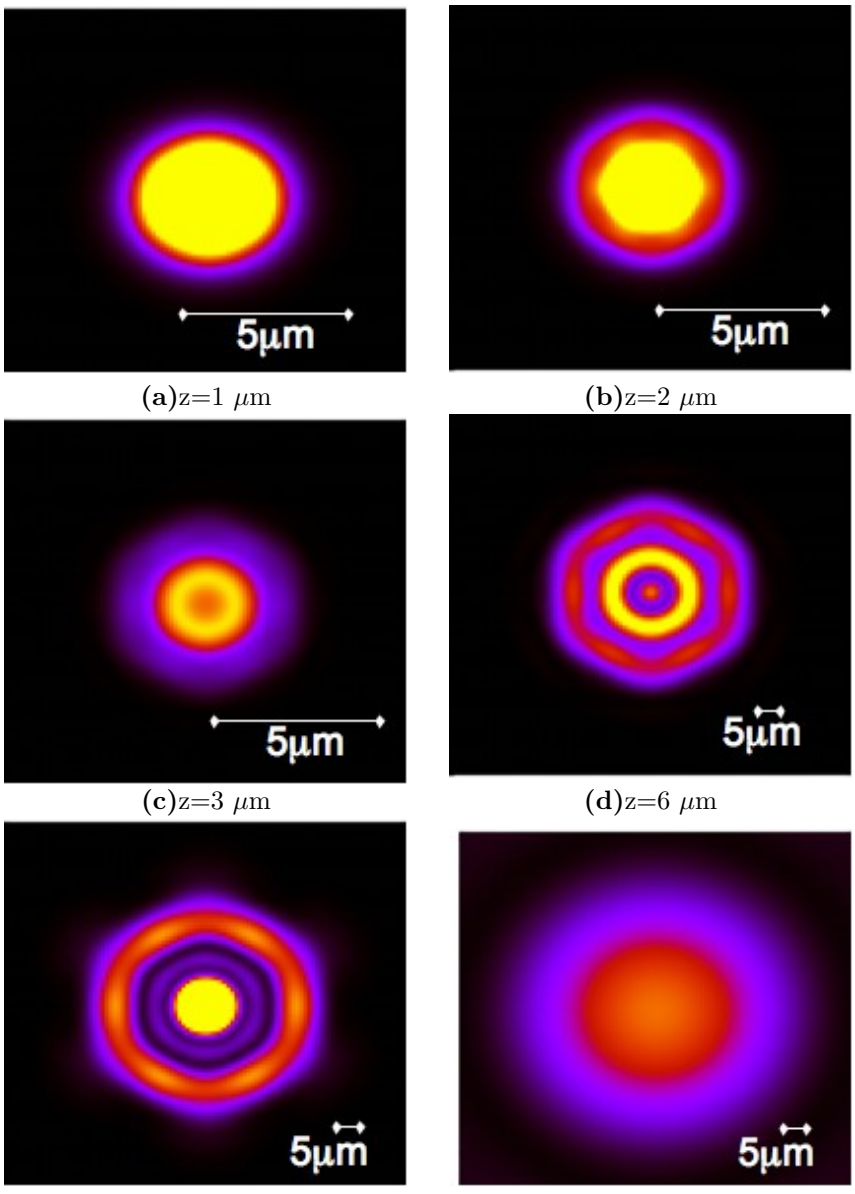

(a)z=1 μm **(b)**z=2 μm

(c)z=3 μm **(d)**z=6 μm

(e)z=8 μm **(f)**z=13 μm

Figure 4.8: Theoretical intensity distribution as the fibre is translated away from the focal plane. In the extreme near-field the mode is circular with a Gaussian profile,an airy disk develops as the diffraction limit is approached, the mode transforms to hexagonal intensity distribution, air holes modify the overall Gaussian distribution sufficiently to produce higher order spots, and finally the distribution returns to a smooth, circular Gaussian in the far-field.

4.5 Assesment of Multicore-Photonic Crystal fibres for astronomical instrumentation

Multi-core-Photonic Crystal Fibres (M-PCFs) contain multiple photonic cores which guide light analogously to small fibre bundles, but are contained within a single substrate to form a single integrated component. This is an emerging technology of significance to several areas of astronomical spectroscopy, especially highly-multiplexed spectroscopy where very large numbers of fibres can be used to target individual points in the field and guide the light to a set of spectrographs. These are astrophotonic devices, originally developed for telecommunications, that exploit photonic properties to provide new types of behaviour which are not available from the bulk material properties alone [116]. For this reason, we are investigating the performance of research devices to assess their suitability for use in the next generation of astronomical instrumentation. The main areas where M-PCFs are relevant are briefly outlined below.

1. Diverse-field spectroscopy (DFS) [117] is a generalisation of integral field and multi-object spectroscopy which allows arbitrary distributions of contiguous or non-contiguous spaxels to be routed to an optimised set of spectrographs. The DFS paradigm requires hardware of various levels of sophistication. One important component of the system is a fibre bundle that guides light from the whole field into a set of optical switches for routing into the restricted number of locations within the spectrograph slits. The fibre bundle needs to contain very large numbers of fibres, designed and manufactured in a highly structured and modular way. The fibre system would have, at its lowest level in the hierarchy, small bundles

of fibres capable of targeting individual objects, using the small multiplex gain in each unit bundle to improve spectroscopic accuracy by eliminating aperture effects, guiding errors and maximising throughput. Although the main focus of this application is on multi-mode devices, the performance of single-mode M-PCFs is highly relevant.

2. Multicore-PCFs could be used as a multichannel transmission line with minimal crosstalk if the holes between the cores are enlarged. The resulting large refractive index step would effectively isolate the cores from each other. The cores may then become multimode, but it may be sufficient to filter off the higher modes over a short length by partly collapsing the holes using a heat source such as a fibre fusion splicer.

3. Fibre bundles, as described in 2.1, can be modified to provide spatially-resolved spectra. This requires that the input field is reformatted into a 1-D linear distribution so that the bundles perform as an integrated small integral field unit (IFU), or for image slicing to boost the product of throughput and resolving power. This can be achieved either by post processing (as is the case for the hexabundles described below) if it does not disrupt the internal light-guiding properties, or by the addition of a fan-out (2D or 3D) wave-guide structure [118]

4. Although most photonic devices work only with single-moded light, the input from most telescopes is likely to be multi-moded (with mode multiplicity 10-100). The ability to convert multi-mode light to single-mode light is an essential function. There are various ways to tackle this, for example by using photonic lanterns [119], however, this relies on adiabatic transitions which are not trivial to realise in a PCF with a solid silica outer cladding. The outer cladding acts as a large ring-shaped waveguide (with lower-index material inside and outside), to which light can couple and

become lost inside. It may be possible to support an adiabatic transition if most of the holes were gradually collapsed along a length of the fibre, while one or two layers of holes immediately adjacent to the outer cladding were instead kept open or indeed enlarged[1]. Such a transition would end in a large central solid core optically isolated from the outer cladding by a holey layer, i.e. a multimode PCF and has been demonstrated by Chen *et al.* [120].

4.5.1 Multi-core fibres

A lot of work has been done with multiple core optical fibres working in single mode. However, most of these fibres are limited to 4 cores with a pitch of around 50 μm . These have been used to measure strain, by interferometry between any two cores. Flockhart *et al.* [121] have successfully demonstrated the use of multi-core optical fibre containing three fibre Bragg gratings for curvature measurement about two axes simultaneously. Silva-Lopez *et al.* [122] show similar results but also investigated how load affects inter-channel crosstalk. They find that cores directly under the load point suffer from peak splitting more than cores located at an angle to the load. Rosinksi *et al.* [123] coupled light into a multi-core fibre (4 cores) using vertical cavity surface emitting lasers and test for efficiency. No cross-talk was observed.

The M-PCF shown in figure 4.10 is a fibre where multiple sites within the structure act as solid guiding cores, and was initially created for use in an optical interconnection system. Similar issues to those facing astronomical instrumentation are also facing those working in the telecommunications industry. Electronic processors are becoming faster and more compact, able to handle more data, and the data interconnections between them will, within the next

[1] private communications with Prof Tim Birks

few years present a significant technological barrier. Taylor *et al.* [124] report results from fifteen fibre samples produced by Crystal fibre A/S all with the same preform, but at slightly different pitches. They report a maximum coupling efficiency of 40 % from a vertical cavity surface emitting laser (VCSEL) to core. Also an optical power coupling between adjacent cores, including fibre-end and evanescent coupling, of -44 dB over 1 m was measured: this is equivalent to a coupling constant of 0.006 dB m^{-1}, which is as low as expected from modelling.

Roberts *et al.* [125] have shown that the guiding properties of Multi-core PCFs can be efficiently calculated following a cluster multiple-scattering (CMS) approach [126]. Roberts *et al.* show that the beat length, l_{beat}, which provides a good measure of the length scale, over which interaction between cores takes place, rapidly increases with decreasing wavelength, λ, and increasing hole separation, a. They note that if the hole sizes are kept at a fixed fraction of the hole spacing;

$$l_{\text{beat}} \propto \frac{a^2}{\lambda}; \qquad \text{for } \lambda \leq a. \tag{4.12}$$

The hybridization length thus increases markedly with core separation, resulting in independent core separation.

4.5.2 Implementation

In 2007 Thomson *et al.* [127] demonstrated that ultra-fast laser inscription could be used to fabricate 3D wave-guide interconnects which facilitate the reformatting of the two-dimensional array of guiding cores into a one dimensional array of guiding cores. Recently, this concept has been extended to multi-core fibres which consist of ≥ 100 guiding cores for astrophotonic applications [128].

Although the insertion losses of this proof-of-concept device were high (≥ 5 dB), the authors believe that this can be greatly improved. If these fibres were to be used in a spectrograph, it may be necessary to couple the M-PCF to a planar arrayed wave-guide grating (AWG) where the light is dispersed and projected onto a two-dimensional detector array. To solve this coupling issue it would be possible to utilise a three-dimensional fan-out device similar to the device developed by Thomson *et al.* shown in figure 4.9.

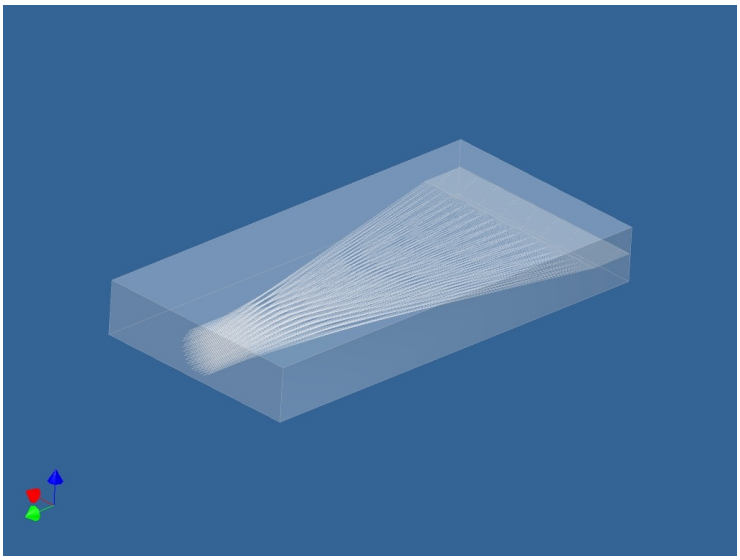

Figure 4.9: Conceptual diagram of the integrated three dimensional fan-out device developed by Thomson *et al.* [128]

4.5.3 Performance metrics for astronomical spectroscopy

As described in section 4.5, M-PCFs are key to several areas of modern astronomy, by providing an extra degree of versatility and the potential performance advantage of photonic behaviour (although this might be considered to be a double-edged sword since there is also a requirement to convert multi-mode

celestial light into single-modes). Even without the photonic advantage, multi-core fibres are likely to be of great benefit to multiplexed spectroscopy because of their flexibility and small size.

The key parameters that we need to measure for astronomical applications are: throughput, cross-talk and the distribution of light at the output. These may all be affected by the accuracy of spatial registration between the input light and the cores, so it is important to determine the tolerances on spatial registration between the M-PCFs and the feed optics. Cross-talk is also critical to their use as mini-IFUs in order to avoid degrading the spatially-resolved spectral information as it emerges from adjacent cores. Similar arguments apply to their potential use as mode filters. Since these are single-mode devices, the distribution of light at the output should be predictable using standard single-mode wave-guide theory without the complication of focal ratio degradation [129].

4.5.4 Fibre Preparation

As was discussed in section 4.3, cleaving the fibre is accepted as the best way to prepare any type of PCF since slicing produces variable results and polishing results in air holes being filled with debris and a concave surface on the end of the fibre due to material being removed at different rates [113]. The usual methods of cleaving the fibre is to remove the buffer material from the end of the fibre, stretch it, score it and bend it until it snaps along the fracture. However, when the buffer was removed from this multi-core fibre it was extremely brittle (which may be due to the excess of holes, or the large size of the cladding diameter). In order to overcome this problem, buffer material was only removed from the

middle section of the end of the fibre and then scored and snapped. The results obtained using this method of cleaving are shown in panel (a) of figure 4.10.

An image of the end face of the fibre is show in panel (a) of figure 4.3. Panel (b) shows how the parameters are defined.

The fibre is a M-PCF which has 37 cores, the dimensions are summarised in table 4.5. The value of d/Δ is often quoted when PCFs are described since this gives an indication of the number of modes the fibre can support. It is interesting to note that the geometry of each individual channel is similar to the geometry of the individual air-holes and the value of d/Δ is extremely close to that of D_C/Δ_C .

Table 4.5: Dimensions of the M-PCF fibre

	airholes d, μm	airholes pitch Δ, μm	d/Δ	eff. core D_C, μm	holey region H, μm	eff. core pitch Δ_C, μm	length m
diameter	2.3	6.1	0.4	12.7	25.6	31.9	2
error	0.14	0.18	0.07	0.41	0.20	0.41	0.1

4.5.5 Experimental setup

The experimental setup used throughout the investigation is shown in figure 4.11. The pinhole was mounted in such a manner as to allow it to be easily removed and replaced with pinholes of different sizes. A laser operating at $\lambda = 632$ nm was used for all tests. The first lens system gave us the flexibility of magnifying the input spot. The beam splitter combined with a viewing microscope allowed us to inspect the light being injected into the individual cores. The input face of a 2 m length of M-PCF was mounted onto two micrometer

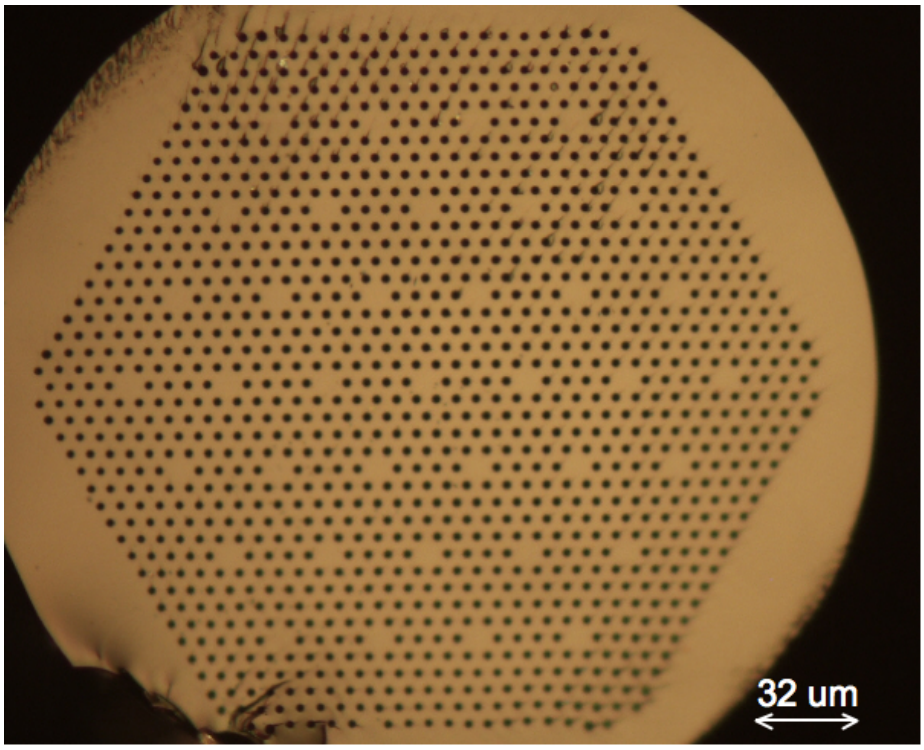

(a)

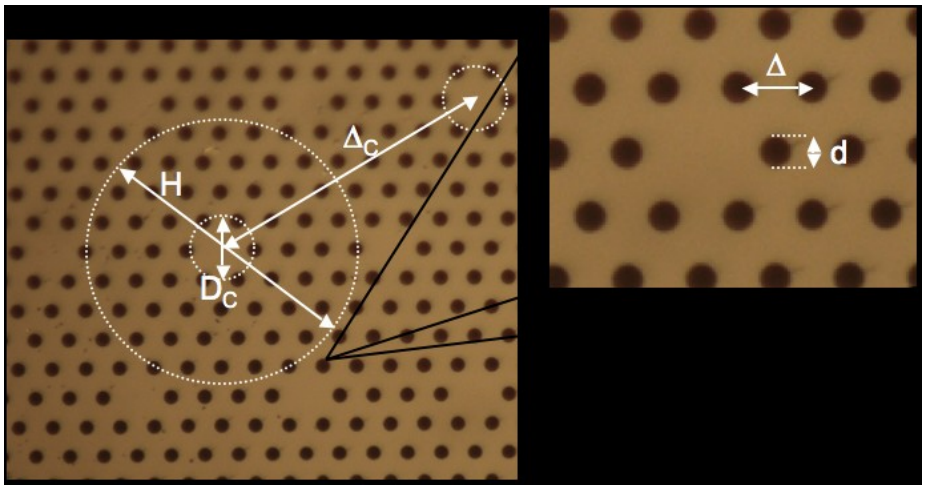

(b)

Figure 4.10: (a) Image of the end face of the fibre after it has been cleaved, (b) Definition of parameters. The dimensions of the fibre are given in table 4.5.

stages in order to allow us to position the input beam at the desired location. A Q-imaging CCD with a pixel size of 6.45 μm was used to record the output image.

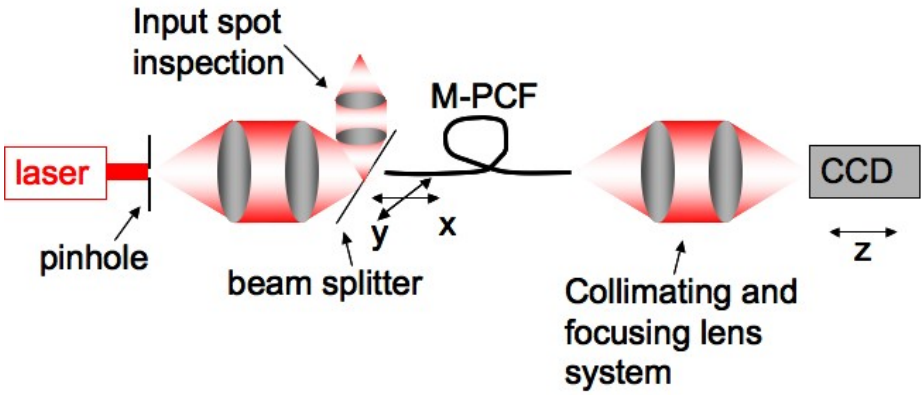

Figure 4.11: Basic layout of experimental setup with $\lambda = 632$ nm and a 2m length of M-PCF.

4.6 Experimental Results of M-PCF Testing

As described in section 4.5.3 we set out to investigate the following parameters:

1. To quantify the amount of crosstalk observed between cores since we need to avoid contamination of the signal from one object by other objects in the field. To this end, illuminating spots of varying sizes was positioned onto an arbitrary core and the output was recorded in the form of a FITS file;

2. To determine the accuracy to which the input spot must be positioned on a core guiding area whilst still maintaining a satisfactory efficiency. This is determined once the optimum input spot size has been established.

3. To determine if the distribution of light at the exit of a single core could be modelled using existing PCF theory.

4.6.1 Crosstalk

Taylor *et al.* [124] have tested similar fibres and reported low crosstalk at λ =850 nm. Taylor *et al.* also modelled the PCFs structures using an equivalent step index method and coupled wave theory to calculate the coupling constant for different fibre geometries as shown in figure 4.12.

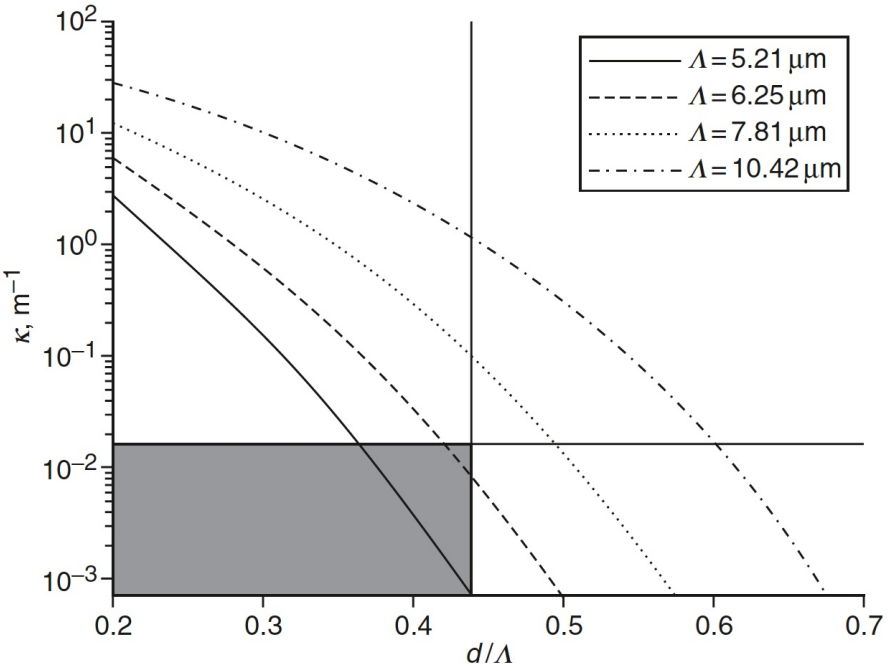

Figure 4.12: Coupling constant κ against diameter of airholes, d, for cores 31.25 μm apart and different periodicity as calculated by Taylor *et al.* [124]. The shaded area shows the single-mode regime.

In order to further investigate the crosstalk and determine the accuracy to which the input spot must be positioned on the endface of the fibre, qualitative measurements were made.

Figure 4.13 was obtained by illuminating the input face uniformly. The im-

age was used to define the location of the cores so that the cross talk could be assessed accurately as a function of position with respect to the cores. The pitch was found to be 37.0 ± 4 μm , hence a small amount of defocus was inherent in the optical system which could affect the magnification and therefore the position of the cores. For the remainder of the analysis, pitch measurements were compared to this value.

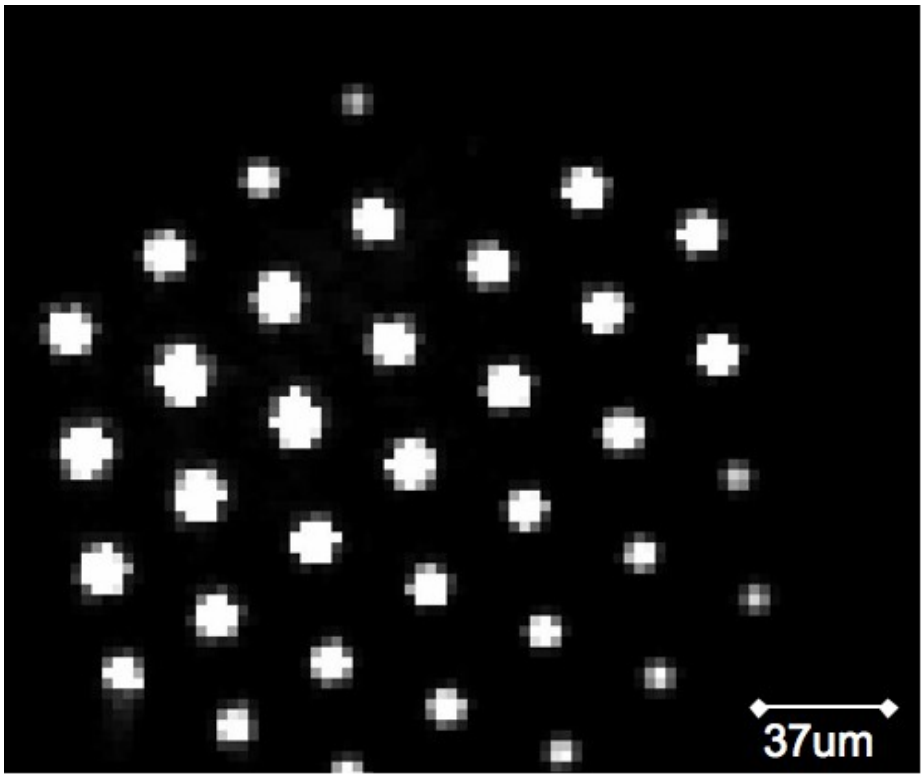

Figure 4.13: Image of the end face of the fibre after the entire input face is illuminated. A small amount of defocus is inherent in the optical system and this image is used as a reference to confirm that crosstalk is indeed power in adjacent cores and not light in air-holes, or satellites in the far-field.

Since the mode field diameter of the fibre was not known, tests were initially performed with a 20 μm spot placed at various positions on the end face of the

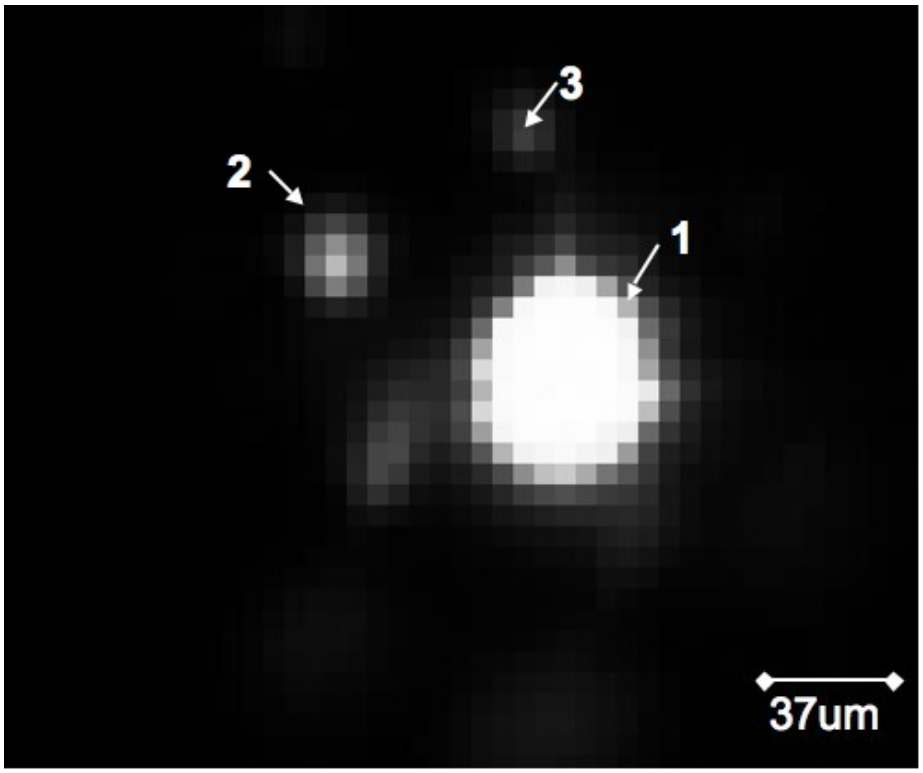

Figure 4.14: Output image when a 20 μm spot of $\lambda = 632$ nm light is focussed onto the centre of an arbitrary core at the input. Cross talk can be seen in 3 neighbouring cores. (Core 1 is the target core and cores 2 and 3 are neighbouring cores).

fibre. Figure 4.14 shows the near-field pattern when a 20 μm spot is focused onto the centre of a guiding core. The first analysis aimed to determine whether these spots were in a position consistent with the measured dimensions of the fibre or whether they were ghosts or stray light. The distance between the cross talk spots is 37.4 ± 0.4 μm compared with a measured pitch of 37.0 ± 0.4 μm . From these measurements it is clear that light is leaking into neighbouring cores and that the mode field area of the fibre has been exceeded.

It is clear that by comparing the pattern of spots in figure 4.13 and figure 4.14 that light is guided, in varying degrees, in 5 of the surrounding cores. As the input spot is moved away from the centre of the first core, the amount of light in the adjacent cores increases. Figure 4.15 shows how the percentage of light in the surrounding cores changes as the input spot is moved in micrometer steps.

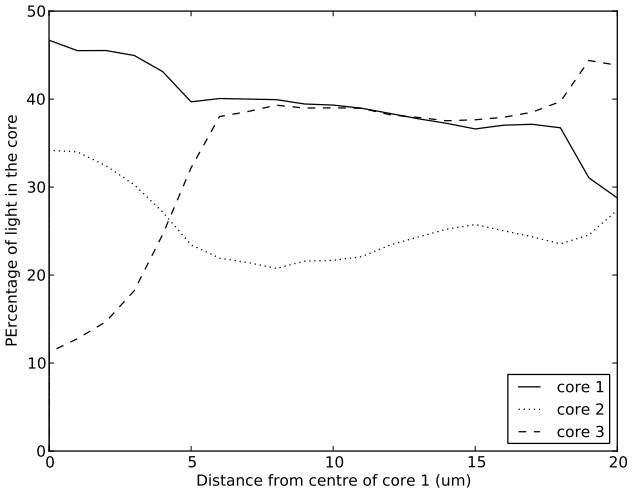

Figure 4.15: If a spot larger than the mode field diameter is injected into a single core, crosstalk is observed in neighbouring cores. As the input spot is moved, the percentage of light in the 'main' core decreases as the spot is translated away from its centre.

The 20 μm pinhole was then replaced with a smaller pinhole and figure 4.16 shows the results of moving a 5 μm spot around the input end of the fibre. The spot was initially positioned on an arbitrary core by optimising light intensity at the output. When the input spot was in a position that gave the maximum power intensity at the output, this was recorded as being the centre of one of the cores. The input spot was then moved in micrometer steps away from the center of the core until no light was guided. Figure 4.17 shows how the intensity at the peak falls as the spot is moved away from the centre of the core. Also shown in figure 4.17 is how the total intensity in the M-PCF decreases as the input spot is moved away from the centre of the guiding core. This allows us to see if light is being lost or simply redirected into an expanded output spot. This figure suggests that the light is not being transmitted by the fibre but is lost (presumably the light is being reflected back towards the source). This is consistent with the behaviour of endlessly single mode PCFs where the throughput depends on the position with respect to the mode area [8].

4.6.2 Far-field results

Figure 4.18 shows the results of translating the CCD away from the focal plane, and imaging the intensity distribution at different distances between the near and far-field.

A good fit is obtained by assuming a value of $\gamma = 0.5$.

The far-field distribution follows the trend predicted by the theoretical model considering the small size of the air holes compared to the large solid guiding region. Since the air holes are comparatively small, the contribution from the

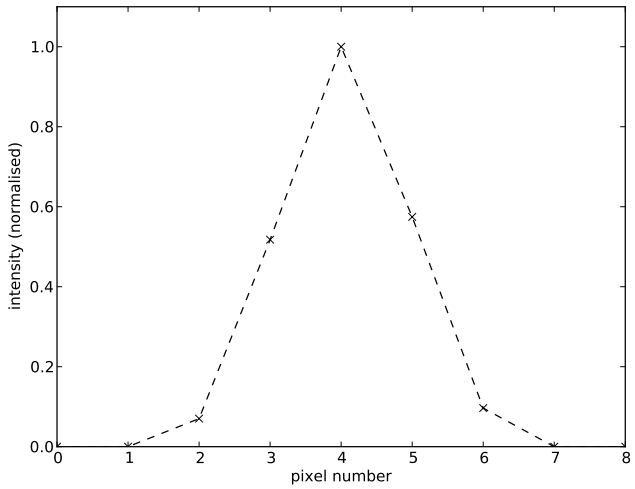

Figure 4.16: Plot through the centre of the image if a 5 μm spot is injected into a core. The spot shows a distinct maximum spot and no crosstalk is observed in any other part of the image

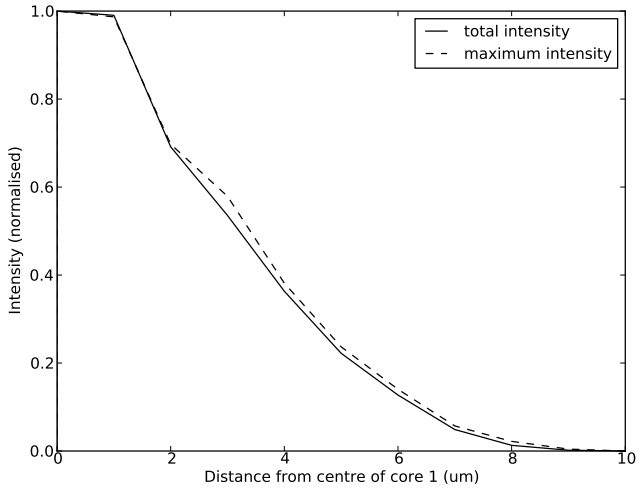

Figure 4.17: Graph to show how the amount of guided light decreases as the input spot is moved away from an arbitrary core. The dashed line shows the normalised peak intensity and the solid line shows the total number of counts. This clearly shows that light is being lost, into the cladding, or by reflection or scattering.

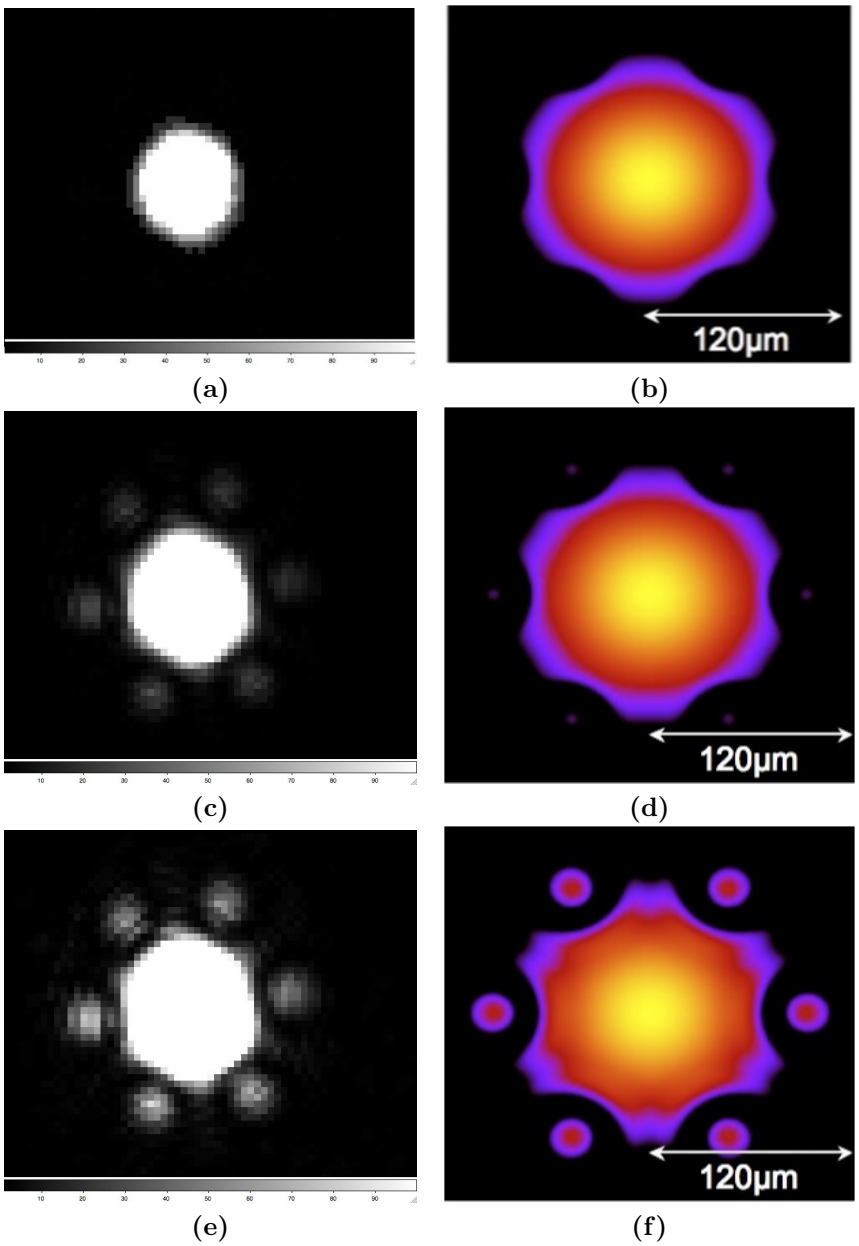

Figure 4.18: Experimental far-field intensity distribution as the CCD is translated away from the focal plane by (a) 1 μm , (c) 5 μm , (e) 9 μm . Theoretical far-field intensity distribution as the CCD is translated away from the focal plane by (b) 1 μm , (d) 5 μm , (f) 9 μm . a value of $\gamma = 0.5$ was empirically fit.

satellites is relatively small. Indeed it is clear that the central spot in the experimental M-PCF is saturated in order to gather enough power from the satellites. When the M-PCF were not saturated, only a central spot with a Gaussian power distribution was detected. The theoretical plots shown in figure 4.18 are plotted on a logarithmic colour scale in order to show the satellites. By comparing the theoretical and experimental power distributions it can be seen that the mode propagates as would be expected from a standard, single core PCF. As predicted the mode transforms from a single Gaussian and then 6 satellites develop at a $\pi/6$ rotation compared to the orientation of the air holes.

4.7 Conclusions

In this chapter photonic crystal fibres (PCFs) have been investigated with a view to their application as astrophotonic devices. Astrophotonics is defined as 'the use of materials to manipulate light for the purpose of improving our understanding of the universe through astronomy and astrophysics using optical systems to collect and process light.'

Three different aspects of PCFS have been discussed in this chapter:

1. how to prepare PCFs;
2. how their behaviour can be modelled;
3. how they can be used in astronomical instrumentation.

The quality of the end face of a fibre is extremely important to the propagation of light in terms of both throughput and intensity distribution. The standard practice of preparing normal optical fibres is to polish using progressively finer grades of abrasive paper. However, if this method is used to prepare a PCF,

debris can become trapped in the air-holes and consequently affect the confinement of light into the core. A further problem arises due to the differential hardness of materials over the face of the fibre resulting in a slightly concave surface. It has been found experimentally the best method for preparing a PCF fibre is to slice using a fibre slicer such as the X140 from Thorlabs. This method is quick to execute and relatively reproducible. The only possible problem results from the necessity of the the fibre to be stripped prior to slicing, leaving a fragile strand of glass which is susceptible to damage.

As a test of the quality of the end face after slicing, throughput measurements were taken which showed that the fibre guided $89\% \pm 2\%$ of the light incident on the end face. This result shows that only 3% of the incident light is being lost within the fibre since 4% will be lost at each air-glass interface.

Once it had been established that a sufficient proportion of the light was being guided by the fibre, the evolution of the mode shape was then investigated in the transition from the near to the far-field. The observations were reproduced theoretically, by approximating the near-field distribution by a main Gaussian peak from which six narrow Gaussians located near the centre of the six inner holes have been subtracted as proposed by Mortensen *et al.* [112]. It was found that due to the extremely high d/Δ ratio combined with the extremely small core size, the air-holes modified the overall Gaussian profile sufficiently and higher order spots are visible away from the center of the intensity distribution.

In the last section of this chapter, skills learnt in the preceding sections were used to asses the suitability of a multicore-PCF for use in astronomical instrumentation. The main performance parameters were identified as throughput

and crosstalk.

The fibre was prepared by cleaving and then mounted in an experimental setup which allowed an input spot to be moved around the end face. The results show that crosstalk can be eliminated if the input spot size is small enough. For a 5 μm spot size, the input position needs to be aligned to within 2 ± 0.5 μm in order to obtain 50% of the maximum signal. Light is still guided within 6 ± 0.5 μm .

If M-PCFs are to be used as part of a mini-IFU, we require an insertion loss of $\leq$ 0.5dB from the optics feed which might be a micro-lens array or a fan-out device. In order for this level to be achieved, the fibre would need to be aligned to within 2 μm .

Finally, it has also been demonstrated that the power distribution at the output is well modelled using existing theory for single core PCFs and therefore it is likely that models which are entirely new will not need to be developed.
aa

Muse, sing of Hermes, the son of
Zeus and Maia...For it was
Hermes who first made the
tortoise a singer.

Homeric Hymn to Hermes

Chapter 5

Volume Phase Holographic Gratings for HERMES

HERMES is a High Efficiency and Resolution Multi-Element Spectrograph which aims to unravel the history of the Galaxy from detailed elemental abundances for about 1.2 million individual stars down to magnitude V=14. The highest risk component of the instrument design has been identified as the volume phase holographic gratings which must have both a high blaze angle and a large footprint in order to achieve a high resolution. Tests on the gratings have shown that the first prototype gratings do not meet the design requirements, however it is hoped that the analysis of the data contained within in this chapter will enable the manufacturers to improve upon their current techniques.

5.1 Introduction

In order to exploit all aspects of ELTs we must investigate each feature of the instrument design. The previous chapters have investigated the fibre component of the instruments, but if we are to achieve the maximum efficiency of the instrument in a larger area of the EM spectrum, we must also use highly efficient gratings. In section 5.2, a thorough analysis of Volume Phase holographic (VPH) gratings is given. These gratings are proposed to be used in the HERMES instrument on the Australian Astronomical Telescope (AAT) and section 5.4 describes this instrument and the science it will be used to investigate. Finally, in section 5.5, prototype VPH gratings designed specifically for the HERMES instrument are tested against their design specifications.

5.2 Volume Phase holographic Gratings

Holographic surface-relief gratings (SRGs) have revolutionized ultraviolet astronomy through the fabrication of curved gratings with built-in aberration correction [130]. Diffraction gratings based on volume holograms rather than surface relief holograms have also been developed over the past few decades and Barden *et al.* [131] proposed their use in astronomical instrumentation in 1998 through the analysis of a 613 line mm^{-1} VPH grating. The advantages of using VPH gratings in astronomical Instrumentation are discussed in section 5.3.

In VPH gratings the diffraction is due to a periodic variation of the refractive index of a film with a constant thickness as is shown schematically in panel (a) of figure 5.1 for two types of VPH gratings.

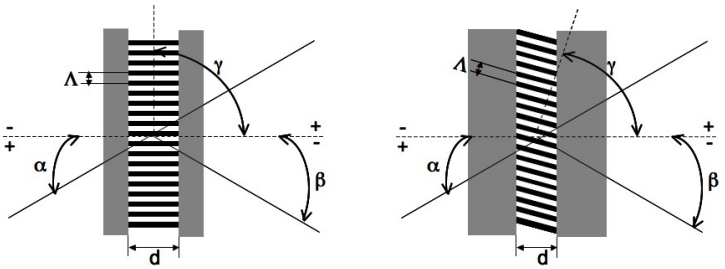

(a) (b)

Figure 5.1: Some possible VPH grating configurations showing Bragg condition diffraction. (a) Transmission grating with fringes perpendicular ($\gamma = 90$ degrees) to the grating surface (unslanted fringes). In this case the magnitude of α equals that of β for the Bragg condition. (b) Transmission grating with tilted fringes may reduce ghost images [132].

As is shown in figure 5.1, the spacing of the fringe planes is defined as Δ or $1/\nu$ and this dictates the grating dispersion. The grating equation for a transmissive VPH grating is given by the standard grating equation:

$$m\nu\lambda = \sin(\alpha) + \sin(\beta), \tag{5.1}$$

where m is the order of diffraction, ν is the grating frequency, λ is the wavelength of light in free space, α is the angle of incidence in air, and β is the angle of diffraction in air (according to the sign convention for transmission, shown in both figures).

Light traversing a VPH grating is also affected by interaction with the fringes as it travels through the bulk or volume of the grating material. The depth of the grating volume, the intensity or contrast of the fringe structure, and the angular and spectral relationship of the incident light to the Bragg condition determine how much light goes into which order.

The Bragg condition for a plane, parallel grating with fringes that are normal

to the grating surface (the case shown in Figure 1a) is given by:

$$m\nu_g\lambda = n_g 2\sin(\alpha_g), \tag{5.2}$$

where ν_g is the frequency of the index modulation within the grating volume (where $\Delta = 1/\nu_g$), n_g is the average refractive index of the grating material, and α_g is the Bragg angle within the grating.

The Bragg condition for VPH gratings follows the same conditions as traditional gratings, so as the incident angle changes, the Bragg condition changes, and the peak efficiency moves in wavelength. Baldry *et al.* [133] have shown that the Kogelnik efficiency [134] versus Bragg angle depends only on one parameter, given by $P_{\text{tune}} = (\Delta n d)/(n\Lambda)$, where Δn is the semi-amplitude of the refractive index modulation, n is the average index, d is the thickness of the active layer, and Λ is the grating period. Baldry *et al.* also showed it is theoretically possible to obtain 100% diffraction efficiency with one linear polarization at any angle, or to obtain 100% efficiency with unpolarised light at specific angles.

There are two main methods that are generally employed to theoretically model the diffraction efficiency of a VPH grating: the Rigorous Coupled Wave Analysis (RCWA)[135] and modal analysis [12, 136]. Both of these methods involve complex computations, however, Kogelnik [134] developed a two-wave, first order coupled wave analysis that can be used to estimate the first order efficiency of a VPH grating. This approximation is valid when

$$Q = \frac{2\pi\lambda d}{n_g\Delta^2} > 10, \tag{5.3}$$

where d and n_g are the depth and index modulation contrast of the grating structure.

Kogelnik shows that the peak diffraction energy is achieved when the angle of incidence and the wavelength satisfy the Bragg condition (equation 5.2) and when the following relationship between wavelength, index modulation, and grating depth is nearly satisfied:

$$\Delta n_g d \approx \frac{\lambda}{2}. \tag{5.4}$$

This relationship provides the starting point in the design of most VPH gratings.

5.3 VPH Gratings in Astronomy

There are many advantages to using VPH gratings in astronomical spectroscopy and these include, but are not limited to:

1. VPH gratings can have potentially higher peak diffraction efficiency approaching 100% in many cases.;
2. Polarization effects in most VPH gratings are not as severe as in surface-relief (SR) gratings and also have fewer grating anomalies;
3. VPH gratings can be generated with higher line densities (up to 6000 lines mm^{-1}) than can SR grating;
4. Holographic technology is capable of producing very large VPH grating structures, up to and larger than 800 mm in diameter;
5. Robustness since the grating is encapsulated within the glass.

Since VPH gratings have the active grating material encapsulated between two pieces of glass, they are extremely attractive to applications where the grating will be installed in a harsh environment or a location with limited access. Many authors have tested the VPH gratings after they have achieved a steady state of operation at cryogenic temperatures [137, 138, 139] and have have reported favourable or manageable outcomes. Arns *et al.* [140] tested 2 gratings in BK-7 and fused silica substrates, cycled between room temperature and 100 K and reported no significant change in transmission or diffraction energy between 300-2000 nm.

Arns *et al.* [141] have also investigated the feasibility of using slanted fringe VPH gratings, similar to those shown in panel (b) of figure 5.1. Arns *et al.* have shown, in theory, these slanted fringe VPH gratings can achieve anamorphic magnifications as high as a factor of 4 whilst continuing to take advantage of the high diffraction efficiency. However, although it is possible to theoretically design these gratings, no prototypes to date have met the requirements since the tolerances in the fabrication process are so high [142].

VPH gratings are currently employed in EFSOC2 on the New Technology Telescope (NTT), and FORS1, FORS2, and VIMOS on the Very Large Telescope (VLT). It is also planned to use VPH gratings on the 2nd generation MUSE instrument on the VLT. VPH gratings are being used in the MUSE instrument for two reasons: Firstly, it was possible to consider high line density VPH gratings without the efficiency penalty of classical grisms. For the same efficiency, the camera focal length and pupil size can be almost half of what would be required to achieve the same linear dispersion at the CCD with a classical grism. This leads to important cost savings due to the smaller over-

all size of each of the 24 unit spectrographs and is a key feature to make this still massive instrument a realistic proposition. Secondly, the optical design optimization includes the VPH grating and has led to a design where the VPH grating is combined with a lens. This not only diminishes internal ghosts, but improves the overall image quality, reduces the number of optical elements in the camera, and has led to further cost savings. It is also planned to use VPH gratings in the CODEX instrument for the E-ELT.

5.3.1 Design considerations

The resolution of a spectrograph was given in chapter 1 by equation 1.11 and shows the relationship between the size of the grating and the angle of the incident light. In order to maximise the resolution the grating must have as many grooves as possible illuminated at the highest angle possible.

Pazder *et al.* [143] have presented a surprising result that a larger incident angle also decreases the efficiency of the grating due to polarisation effects. A consequence of this result is that larger gratings are even more desirable.

The availability of very large VPH gratings is limited by the manufacturer's ability to coat and process high quality holographic emulsions on large optical substrates and the size of the optics installed in the interferometer used to make the holographic exposure. Film coating and processing quality has steadily improved in anticipation of larger size requirements. Large exposure optics represent a significant investment but the total cost of scaling up production capability is much greater and large-sized gratings with acceptable quality remain to be demonstrated. An alternative approach is to develop a grating

mosaic of multiple exposures that would, for all practical purposes, perform as a single, monolithic grating.

Large gratings have already been designed, produced, and tested by Arns *et al.* [144], for the Apache Point Observatory Galactic Evolution Experiment (APOGEE) spectrograph. The gratings in the APOGEE instrument have been manufactured by Kaisor who can make gratings up to a maximum width of 298.7 mm. Since the gratings are illuminated at an angle of 54 degrees, the width of the grating needs to be 475 mm - much larger than can be produced in a single exposure and therefore it was decided to mosaic the exposures.

The technique of mosaicing classical surface relief gratings has been established for many decades [145]. This is not true of VPH gratings, however VPH grating mosaics are a similar challenge to ruled reflection gratings.

To-date, three methods have been identified for building VPH mosaics: framed, common bonded, and step and repeat [143] as shown in figure 5.2. The gratings used in the HERMES spectrograph use the step and repeat procedure and more details including experimental testing results are given in section 5.5.5.

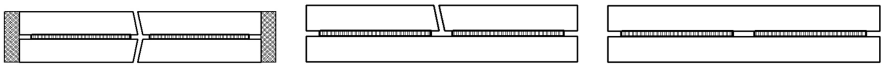

Figure 5.2: Cartoon to show how VPH gratings can be mosaiced. (a) framed mosaic where four independent gratings are held in place by a frame around the edges, (b) common bonded method where VPH gratings are fabricated independently and bonded to a common substrate, (c)Step and Repeat where a monolithic substrate is exposed in sub-sections.

5.3.2 VPH grisms

In addition to VPH gratings, VPH grisms are also being used in astronomical instrumentation. A VPH grism is the high dispersion device which consists of a VPH grating sandwiched between two prisms, and are easier than VPH gratings to incorporate into existing spectrograph designs since they disperse, but do not deviate, the light. The first example of the use of a VPH grism in an existing spectrograph was in the LDSS++ instrument for the AAT [146]. Other instruments that have VPH grisms are Taurus++ on the AAT [147], FORS-1 on the VLT[148], and MARS on the Mayall 4 m at Kitt Peak National Observatory (KPNO) [149]. Ebizuka *et al.* [150] used the RCWA method to evaluate VPH grisms for FOCAS on Subaru and found that the measured diffraction efficiency was in good agreement with the theory.

The design of the High Efficiency and Resolution Multi-Element Spectrograph (HERMES) spectrograph on the AAT is pushing the development of VPH technology in both Bragg angle and size. The following sections will give an overview of the instrument design and the performance of 4 prototype gratings.

5.4 HERMES

HERMES is a High Efficiency and Resolution Multi-Element Spectrograph. The primary goal of the HERMES survey is to unravel the history of the Galaxy from detailed elemental abundances for about 1.2 million individual stars down to magnitude V=14. The spectrograph will normally operate at a resolution of $R = 28,000$, and the high resolution mode will operate at $R = 45,000$. At

a resolving power of $R = 28,000$, the chemical tagging survey will concentrate on wavelengths between $\lambda = 500 - 900$ nm in order to identify dissolved star formation aggregates and ascertain the importance of mergers throughout the history of the Galaxy. In addition to chemical tagging, a smaller subset of stars will be selected for further investigation and the radial velocities of these stars will be combined with the transverse velocities from GAIA. This will enable the complete spatial motion for each star to be known and it will be possible to identify spatially mixed stars with a common origin.

Figure 5.3 shows the basic design of the spectrograph. HERMES will make use of the existing 2dF fibre positioner, discussed in section 2.1.1, whereby each 140 μm fibre covers 2 arcseconds on the sky and their F/3.65 output is optically relayed at F/6.3 to the HERMES slit. The slit is 230 mm in length and its spatial scale matches that of the fibres. Light from the slit exits at F/6.3, and then hits the off-axis collimator at 9.3 degrees giving a 195 mm diameter parallel beam. As is shown in figure 5.3 the basic layout of HERMES is a 4-arm design, obtained by large dichroic beam splitters feeding 4 separate channels, and is based on high dispersion VPH gratings. The VPH gratings, which are further discussed in section 5.5 have a high blaze angle of 68 degrees and a large physical size of 220×580 mm.

5.5 HERMES VPH gratings

The grating parameters required for the Galactic archaeology (GA) survey described above are given in table 5.1.

Since the VPH gratings are technically challenging and are one of the most

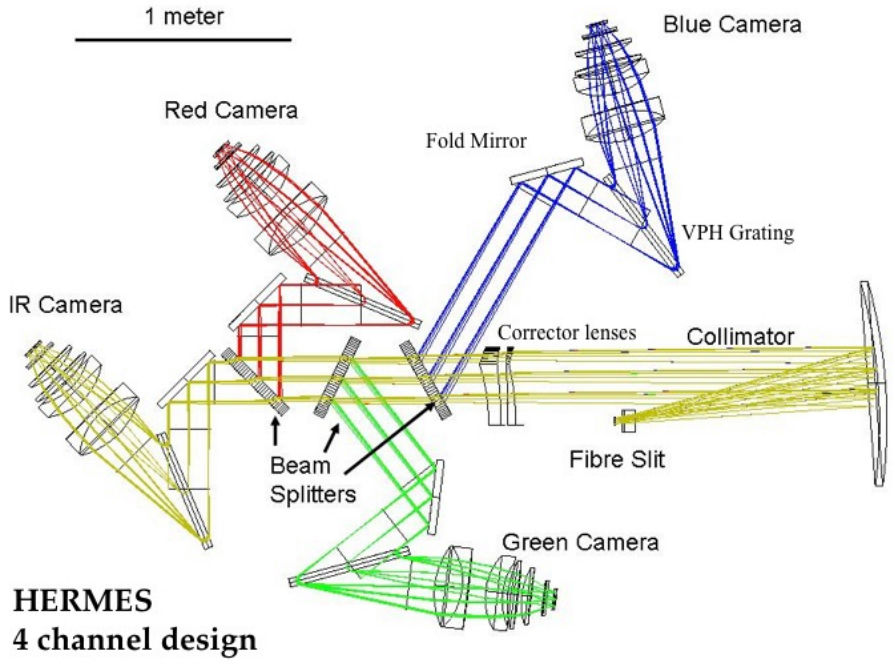

Figure 5.3: Optical configuration of the HERMES instrument (*image courtesy of Luke Gers)*

Table 5.1: HERMES gratings for the 4-channel Galactic Archaeology survey.

Grating	Line freq. (lmm^{-1})	Bragg angle (deg)	Bragg λ (nm)	Camera angle (deg)	Central λ on detector (nm)	λ band (nm)	Band width (nm)
Blue	3857	67.2	478	68.1	478.5	468.1-486.6	18.5
Green	3196	67.2	576.9	68.1	577.4	564.9-587.3	22.4
Red	2785	67.2	662	68.1	662.6	648.1-673.9	25.8
IR	2379	67.2	775	68.1	776	759-789.0	30

high risk aspects to the HERMES project, prototype gratings were requested from several different vendors in order to be evaluated using the following criteria:

- Measurement of the 1st order diffraction angle with respect to the design incident angle (section 5.5.3);
- Measurement of the VPH mosaic co-alignment (section 5.5.5);

5.5.1 Fabrication Specifications

Wasatch Photonics [1] are one of the leading vendors of high quality VPH gratings and were able to provide four prototypes to be tested. The specifications of the prototype gratings are given in table 5.2 . As is shown in figure 5.4 the efficiency of the gratings is a function of the thickness of the gel. Therefore, two gratings were manufactured (proto-1 and proto-2 in table 5.2) which had a gel thickness of 4.2 μm which would, in theory, obtain the first peak in efficiency of 58%, and two gratings were manufactured (proto-3 and proto-4 in table 5.2) which had a gel thickness of 12.3 μm which would, in theory, obtain the second peak in efficiency of 90%. The thin layer substrates are manufactured via a 'scraping' process, and the thick layer substrates are manufactured via a 'spin' process. It is not necessary to describe the details of these processes, however it is important to note that different processes are used to obtain different gel thicknesses.

Table 5.2: Prototype HERMES gratings.

Name	Bragg λ (nm)	Line frequency (lmm-1)	Bragg angle (in air) (deg)	Index modulation (Δng)	Depth (d)	Mosaic alignment (arcsec)
Proto-1	632.7	2914 0.1	67.2 0.1	0.06	4.2	3
Proto-2	632.7	2914 0.1	67.2 0.1	0.06	12.4	3

[1] Wasatch Photonics, 1305 North 1000 West Suite 120, Logan, UT 84321

5.5.2 Theoretical predictions

The theoretical efficiency of the gratings for various gel depths has been calculated by Sam Barden whilst he was at the AAO and is shown in figure 5.4. The theoretical efficiencies are calculated using the RCWA method which was mentioned in section 5.2, and show predictions for both polarised and unpolarised light. Also shown in this figure is the highest efficiency which was measured with the prototype gratings and will be further discussed in section 5.5.3.

It should be noted that although the efficiency for polarised light was theoretically calculated, it was not measured experimentally since polarised light is not fed from the telescope.

5.5.3 Testing the Blaze angle

Gratings were tested using the setup shown in figure 5.5. Monochromatic light is collimated using two large lenses in order to provide a beam diameter which will illuminate as much of the grating as possible. The collimated beam passes through the grating and is refocussed by two further large lenses onto a radiometer. The radiometer and focussing lenses are mounted on a rotating arm and allow the power to be measured in the $m = 1, 0, -1$ orders.

The requirement of the setup was to enable us to determine the blaze angle and to calculate the percentage of power that was being sent to the $m = -1, 0, 1$ orders ($m = -1$ is the reflected light). In order to perform this test the grating was set to an arbitrary angle and the power in the various orders was recorded (minus the background at each position). The angle of the grating was then altered and the measurements repeated, until a peak in the first order was

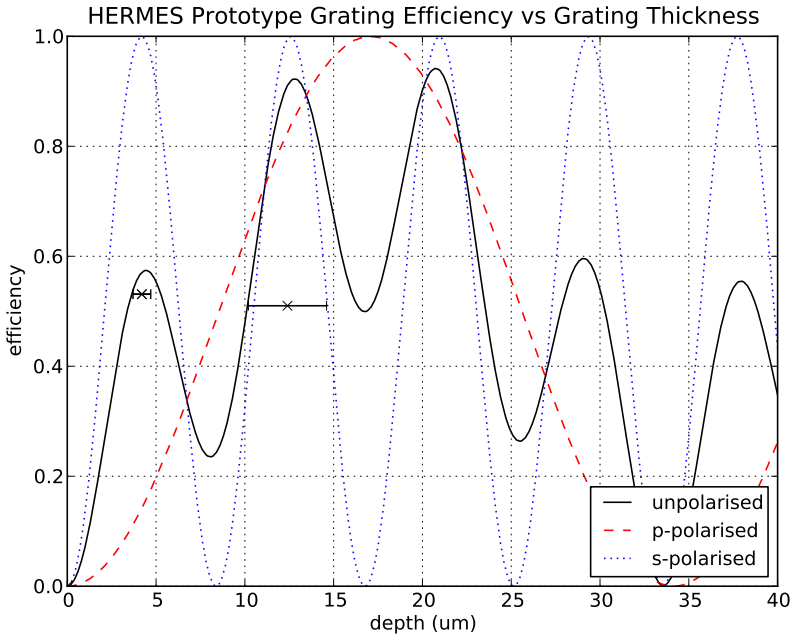

Figure 5.4: Theoretical efficiency of the prototype gratings with points to show the highest efficiency which was measured with the prototype gratings. The experimental results are presented in section 5.5.3.

found.

Results The results of the blaze angle tests at various grating angles are shown in figures 5.6-5.9 and summarized in table 5.3. The power in each of the orders was recorded and is shown as a percentage of the total light in all 3 orders. The throughput efficiency is the total power in the three orders, compared to the power recorded by the radiometer with the grating completely removed so provides an absolute efficiency.

All substrates showed that both the grating frequency of 67.2° and the design requirement of $\geq$ 40% of the light being in the $m = 1$ mode has been achieved. However, the results shown in table 5.3 show that the efficiency of the thick gratings did not meet the theoretical maximum of 90% in the first order as shown in figure 5.4. Further tests were required in order to determine whether this was because the thickness of the gel varied over the substrate, or whether the thickness was well controlled but wasn't sufficiently thick.

Table 5.3: Summary of results for all substrates with unpolarised light

grating	gel thickness (μm)	angle (deg)	relative % of power in order			absolute throughput efficiency (%)
			1	0	-1	
Proto-01	4.2	67.2	53.1	34.5	12.4	89.5
Proto-02	4.2	67.2	51.8	36.3	11.9	87.1
Proto-03	12.4	67.2	51.0	35.8	13.2	82.6
Proto-04	12.4	67.2	47.4	36.6	16.1	82.6

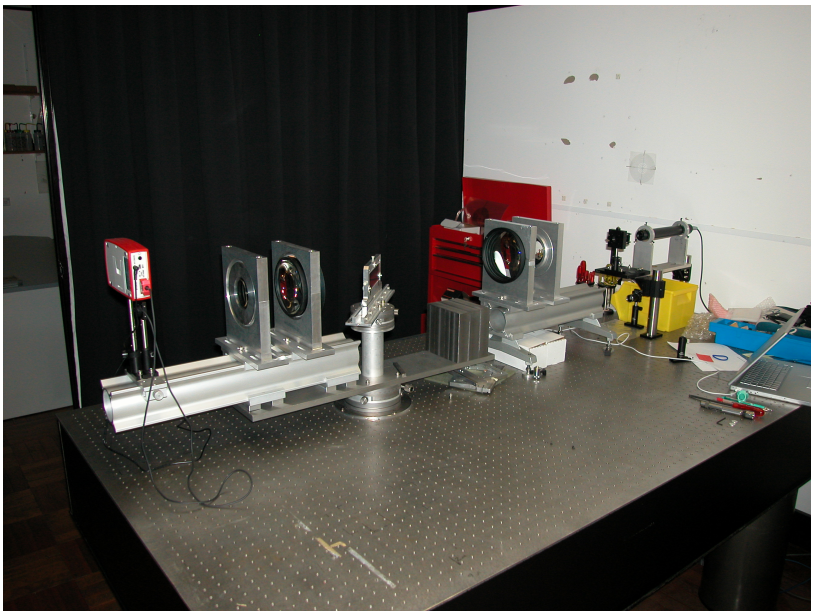

(a) measuring power in the m=0 order

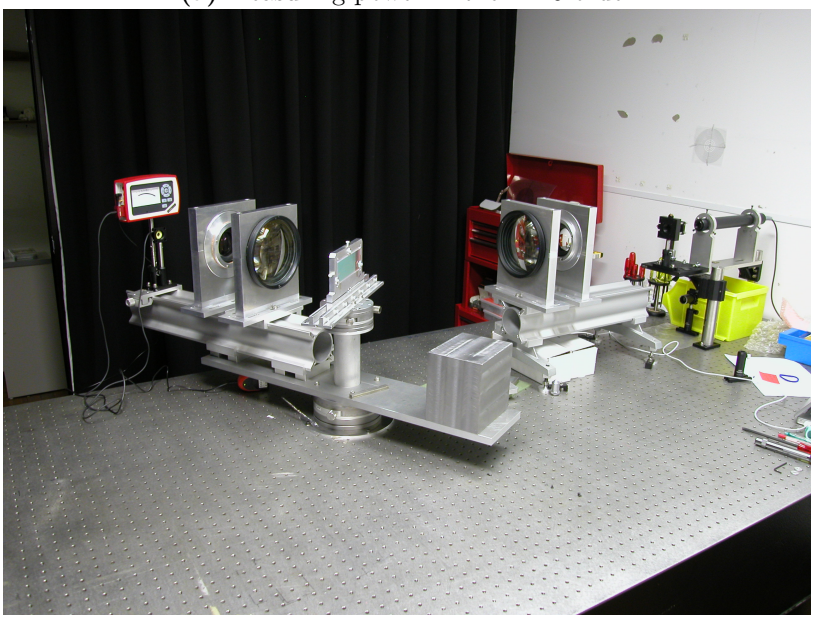

(b) arm is rotated to measure power in the m=1 order

Figure 5.5: Optical setup used to test the gratings. A laser operating at $\lambda = 632$ nm is expanded using a spatial filter and collimated using the first two lenses. This collimated beam then passes through the VPH grating. The light is then focussed onto a radiometer using the second two lenses.

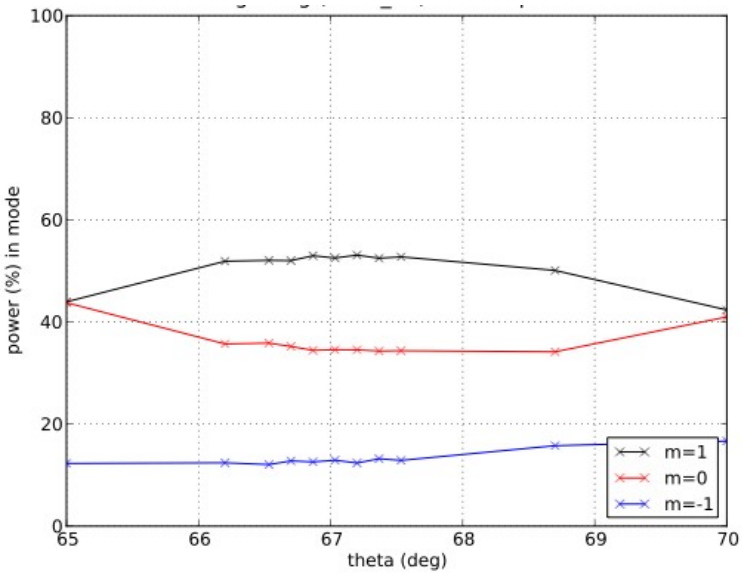

Figure 5.6: Percentage of light in the m=-1,0,1 orders for Proto-1 which has a gel thickness of 4.2 μm and therefore obtain 58% of power in the first order. Errors on values are below 1%.

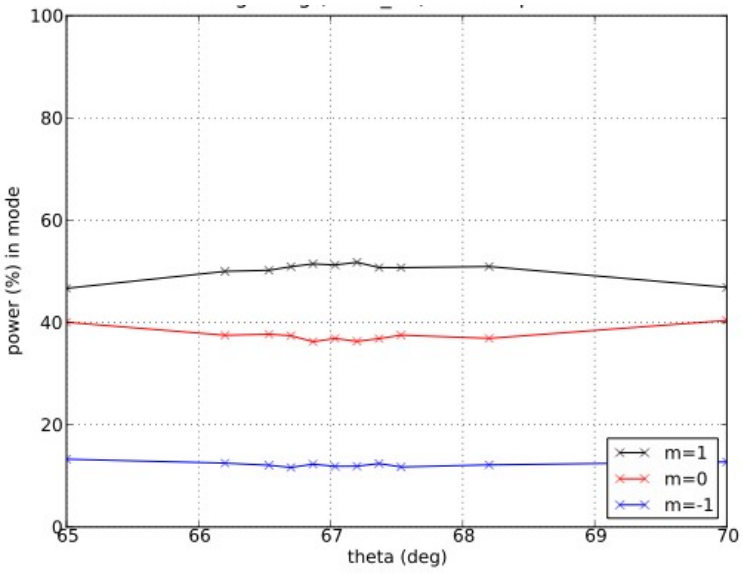

Figure 5.7: Percentage of light in the m=-1,0,1 orders for Proto-2 which has a gel thickness of 4.2 μm and therefore obtain 58% of power in the first order. Errors on values are below 1%.

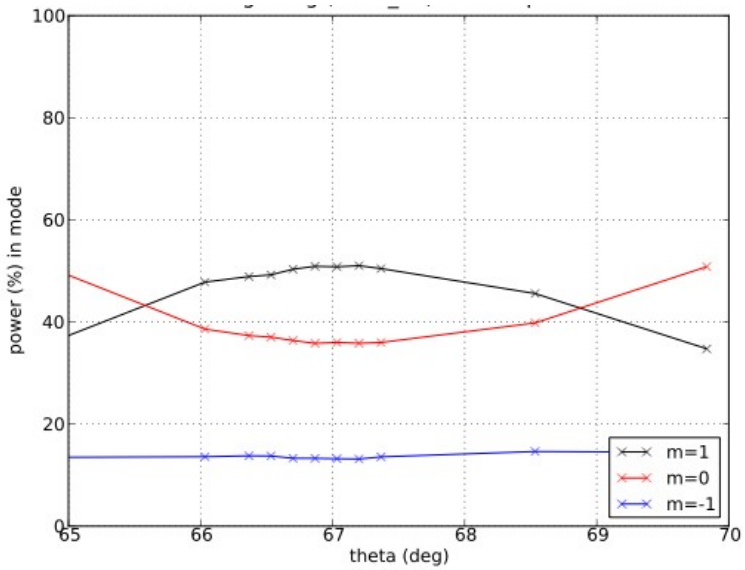

Figure 5.8: Percentage of light in the m=-1,0,1 orders for Proto-3 which has a gel thickness of 12.4 μm and therefore obtain 90% of power in the first order. Errors on values are below 1%.

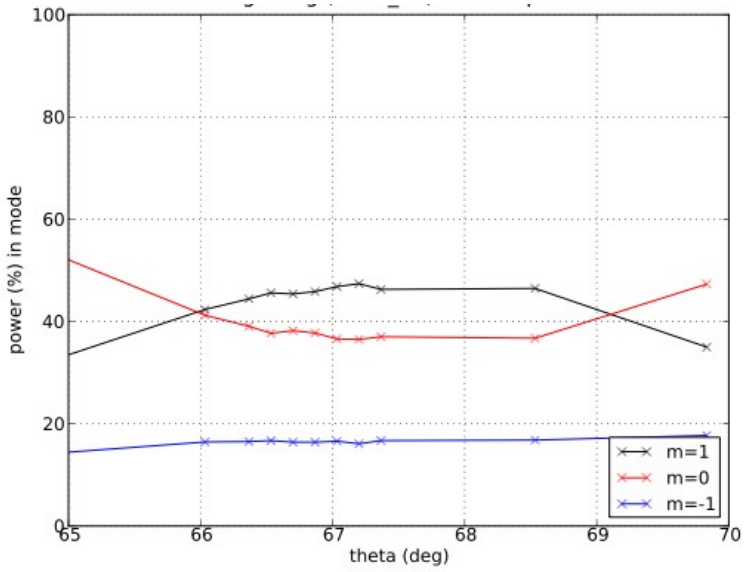

Figure 5.9: Percentage of light in the m=-1,0,1 orders for Proto-4 which has a gel thickness of 12.4 μm and therefore obtain 90% of power in the first order. Errors on values are below 1%. .

5.5.4 Testing the homogeneity of the gratings

In order to ascertain the cause of the low efficiency, a small aperture with $d = 10\ mm$ was placed after the beam was collimated in order to illuminate only a small section of the grating as shown in figure 5.10. This spot was moved in 5mm increments along the length of the grating in order to obtain the power in each of the orders through different parts of the gratings. The results of the tests are shown in figures 5.11-5.14. The results show that the thin gratings are fairly homogeneous (as would be expected since they are reaching the theoretical maximum shown in figure 5.4), however, the thicker gratings show that the percentage of light in the first order is slightly lower at one side of the grating than the other.

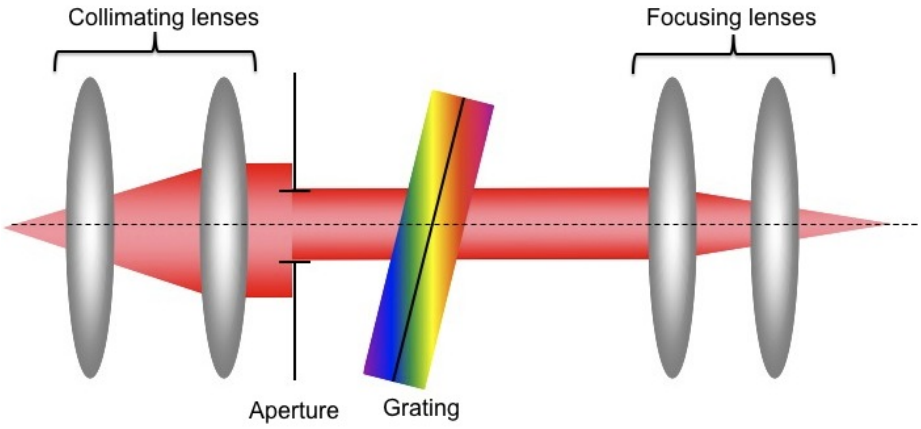

Figure 5.10: Experimental setup used to test the homogeneity of the gel thickness of the gratings. The collimated beam is stopped down in order to illuminate a small section of the grating. This spot is then moved around the grating in order to measure the efficiency in the first order at different points.

The results shown in figures 5.13 and 5.14 suggest two things. Firstly, the thickness of the gel is not 12.4 mm since if it was, then the efficiency in the first order should have been much higher. Secondly, the thickness of the gel over the

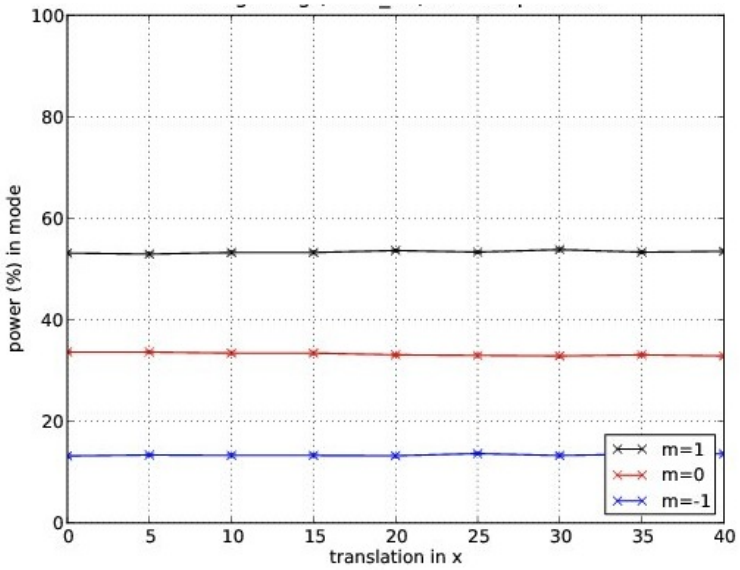

Figure 5.11: The homogeneity of Proto-1 was tested by creating a smaller aperture and testing the efficiency in each of the orders at different positions on the substrate. Errors on values are below 1%

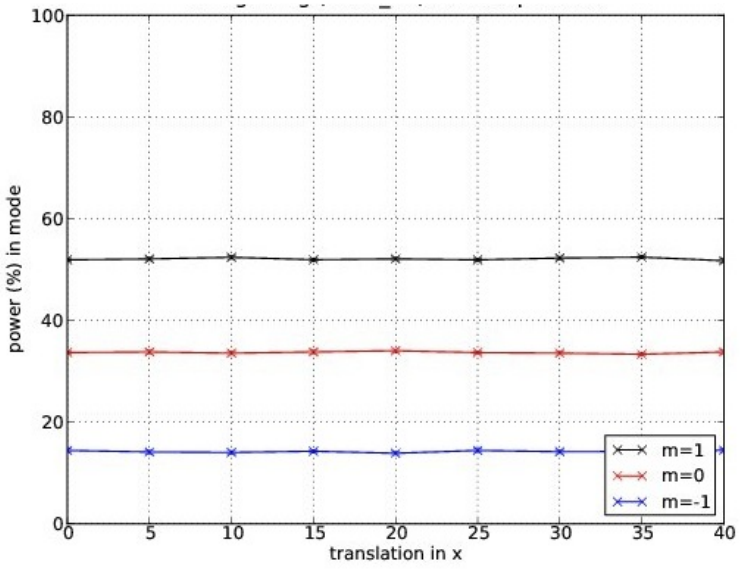

Figure 5.12: The homogeneity of Proto-2 was tested by creating a smaller aperture and testing the efficiency in each of the orders at different positions on the substrate. Errors on values are below 1%

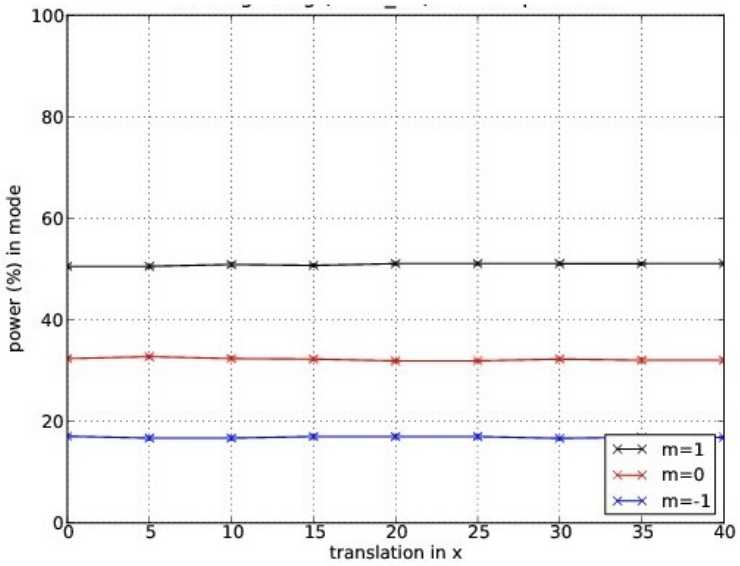

Figure 5.13: The homogeneity of Proto-3 was tested by creating a smaller aperture and testing the efficiency in each of the orders at different positions on the substrate. Errors on values are below 1%.

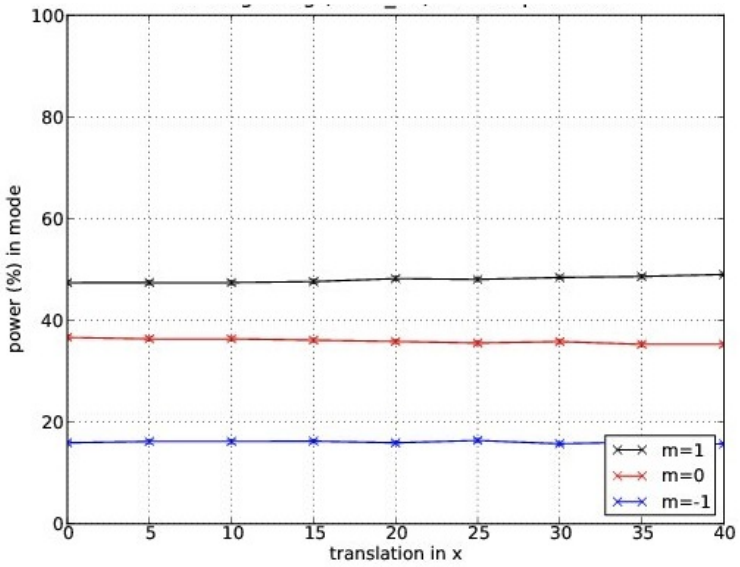

Figure 5.14: The homogeneity of Proto-4 was tested by creating a smaller aperture and testing the efficiency in each of the orders at different positions on the substrate. Errors on values are below 1%

entire substrate is not constant since if it was, then the efficiency in the first order would not vary.

5.5.5 Mosaic Alignment

As was discussed in section 5.3.1, the resolution of the spectrograph is proportional to the width of the illuminated grating. Since the gratings are illuminated at a large angle, the size of the grating is larger than can be manufactured in a single exposure and therefore, a step and repeat procedure is required. If the mosaics are sufficiently aligned to each other as shown in panel (a) of figure 5.15, the dispersion at the output will appear as if it was formed with a single grating. However, if the gratings are not sufficiently aligned as shown in panel (b), the dispersion will form separate footprints at the output.

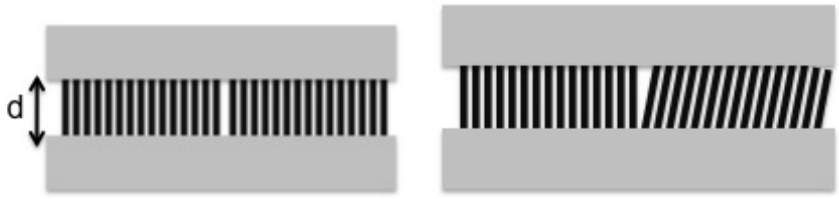

Figure 5.15: Cartoon to show possible misalignment between the VPH grating mosaics.

It was determined that the gratings need to be aligned to within $3''$ in order to obtain a single dispersion footprint at the output of the instrument, and a lens system was designed which was able to resolve these angles. In order to guarantee these angles were resolved, a tighter constrain of $1''$ was demanded of the lens system. The prototype gratings consisted of two mosaics in order to be able to determine the alignment accuracy.

Lens system In order to be able to distinguish the separate dispersions which would be evident if the mosaics were misaligned, a minimum separation of 2 pixels between angle misalignment was required. Hence the focal length, f, required to resolve $1''$ is calculated. An SBIG CCD with a pixel size of 9 μm was available for the tests and this meant a focal length of 4123 mm was required. Due to this large focal length, a magnification system was designed.

Figure 5.16 shows the final lens design, which has been optimized for $\lambda =$ 632 nm. Using this lens design, the spots are diffraction limited and separated by around 20 μm This meets the initial requirement of having a minimum separation of 2 pixels for a resolution of $1''$.

Lenses are numbered from left to right as L1-L4 and a summary of the lenses is given in Table 5.5.

Table 5.4: Summary of results for all substrates with unpolarised light

Lens	Manufacturer	Focal length (mm)	Diameter (mm)	Glass	Product code
1 2	Edmund Optics	76.6	849.9	BK7, DF2	NT54-567 (mounted)
3	Sigma Koki	-50.7	34	S-BSL7	SLB-40-50N
4	Archer Optics	1000	50.8	BK7, SF6	DP-50.8-1000A

Table 5.5: Lens data for the VPH alignment system

Results This lens system should produce a full field spot with geometric radius=42.465 μm . The separation of $1''$ spot is 9 μm and the separation of $3''$ spot is 25 μm . Calculations made using Zemax [151] predict that the system

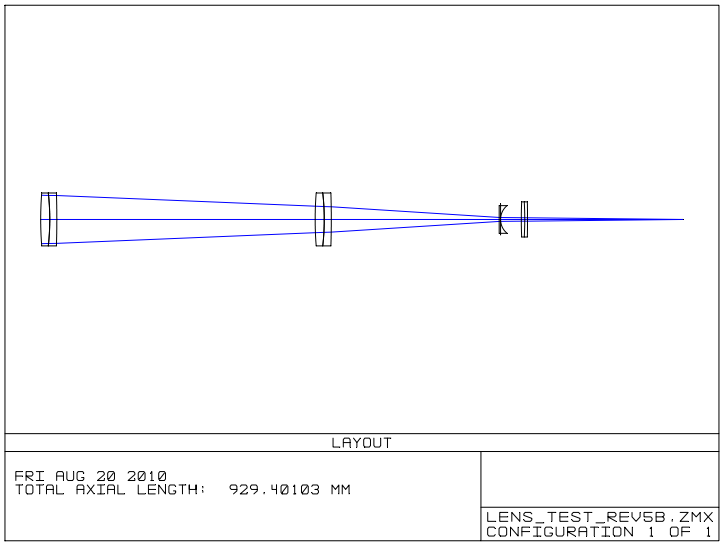

Figure 5.16: Layout of the 4 lens telescope system

should have an effective focal length (EEFL) of 1692.321 mm.

We have measured the effective focal length of our physical system by focusing a spot on a fixed CCD and then moving the lens system radially. We find that for a $5'$ rotation, the spot moves by 279 pixels, or 2511 μm . Using these measurements, we calculate our EEFL=1739 $\pm$13.5 mm, in close agreement to the Zemax prediction.

We next need to calculate what the dispersion of the laser should be when it diffracts through the grating in the first order. In order to calculate this we use equation 5.2 which gives the Bragg condition for a plane, parallel grating with fringes that are normal to the grating surface and rearrange to find α_g for

the first order :

$$\alpha_g = \sin^{-1}(\frac{\lambda\nu}{2}) \tag{5.5}$$

In the case of our grating, ν=2914 l mm^{-1} (or 2.914 l μm $^{-1}$), λ = 633.05 nm, and hence α_g=67.04 deg μm $^{-1}$.

We now use the EEFL that we calculated above to work out the extent of the dispersed laser that we would expect to observe.

$$\frac{h}{2} = \tan\left(\frac{\mathrm{d}\alpha_g}{2}\right) \times \mathrm{EEFL}. \tag{5.6}$$

Therefore, the length of the dispersion is calculated as h = 36 pixels or 327 μm .

Results Figure 5.17 shows a schematic of the image we obtain when diffracting laser light through the grating. The actual image suffers from aberrations but this has been ignored in the analysis.

The bar on the right is from one half of the grating and the bar on the left is from the other half of the grating. Dimensions a-d give the physical size of the bars to ensure we are obtaining the dispersion we expect. Dimensions e and f give the angular misalignment.

In order to calculate what this separation means in terms of physical offset we take the inverse tangent of this distance and divide it by the focal length, as shown in equation 5.7

$$\mathrm{offset} = \tan^{-1}\left(\frac{e}{\mathrm{focal\ length}}\right) \times \mathrm{arcseconds} \tag{5.7}$$

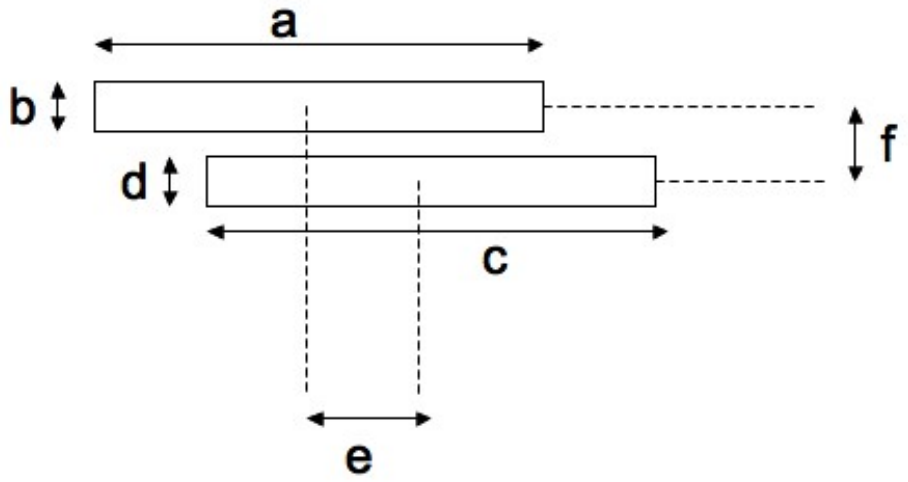

Figure 5.17: Schematic of our dispersed images

The measured dimensions are shown in the following table:

Table 5.6: Dimensions of the dispersed images

grating	a (μm)	b (μm)	c (μm)	d (μm)	e (arcsec)
1855 01	396	171	297	162	19.2
1855 02	675	234	864	243	21.4
1855 03	558	180	702	189	22.4
1855 04	783	198	873	216	17.1

The dimensions 'a' and 'c' in this table should equate to the extent of the dispersed laser from the grating which was calculated as 327 μm . These values show that more dispersion is observed than was expected. Dimension 'e' indicates the amount of misalignment between the mosaics. The misalignment between the mosaics was specified as less than $3''$, however, the results show that there is both a lateral and a rotational misalignment between the mosaics.

5.6 Conclusion

Volume Phase Holographic gratings provide unique advantages over traditional dispersive elements. For this reason they are used in many astronomical instruments are being considered for instruments on large telescopes. However, before their full potential can be realised on these large instruments many technological obstacles must be overcome. The VPH gratings required in the HERMES instrument push the boundaries of the size of the blaze angle and size of the gratings and are a pathfinder for future instruments.

The HERMES instrument must maximise it's resolving capabilities in order to fulfil it's chemical tagging ambitions. It has been shown that resolution is increased for larger gratings operating at large angles. These two properties are the focus of the experimental work performed in this chapter and demonstrate that progress is being made.

Since the VPH gratings were identified as the highest risk component in the instrument design, four prototype gratings were procured in order to test the manufacturing capabilities of Wasatch Photonics.

Since it was understood that the grating efficiency is a function of the thickness of the gel layer, two gratings were manufactured that had a gel thickness of 4.2 μm which would reach the first theoretical peak in efficiency of 58% in the first order and two gratings were manufactured that had a gel thickness of 12.4 μm which would reach the second theoretical peak in efficiency of 90%.

Experimental tests showed that the blaze angle of all of the gratings met the design specification of 67.2°, however the theoretical efficiency of light in the

first order was not met.

Further investigations regarding the homogeneity of the gratings showed that the depth of the gel layer was well controlled over the entire substrate since the efficiency through different sections of the grating did not vary within the experimental errors. It was therefore concluded that the gel was not the correct thickness.

The second test focussed on testing the mosaic alignment within the gratings since the size of the grating is larger than can be manufactured in a single exposure and therefore, a step and repeat procedure is required. Results showed that the mosaics were misaligned by more than 17 arcseconds which exceeded the design specifications of 3 arcseconds.

The prototype gratings tested in this chapter had both the largest blaze angle and the largest footprint that had ever been manufactured by Wasatch Photonics so it is perhaps unsurprising that the first attempt was not completely successful. However, the results obtained as a result of this work have allowed the vendors to identify which aspects of the manufacturing process need to be improved and it is hoped that the second attempt at manufacture will prove to be more successful.

There's no limit to how much
you'll know, depending how far
beyond zebra you go.

Dr. Seuss

Chapter 6

Spectroscopy with Extremely Large Telescopes

Smart focal plane technologies are currently being promoted to enable efficient sampling of the focal plane of ELTs [152]. In this chapter the concept of Diverse Field Spectroscopy (DFS) using highly multiplexed monolithic fibre systems (MFS) is explored. DFS allows arbitrary distributions of target regions to be addressed in order to optimise observing efficiency when observing complex, clumpy structures such as protoclusters which will be increasingly accessible to extremely large telescopes. After the theoretical case has been presented, practical ways in which the systems would be built are examined. Since it is not currently possible to access the entire input field with a single switching unit, it is shown that when the field is divided into smaller 'cells', the ability to address every region of interest in sample images increases by around 80% if the input field is randomised prior to down-selection.

6.1 Introduction

To image a diffraction limited, $2'$ field with the E-ELT ($D = 42$ m) , in the infra-red range ($\lambda = 1.5$ μm) would require ∼26,700 pixels if the field was being sampled at the Nyquist-Shannon limit. The largest CCD format currently available from e2v [1] is 4096×4112 and has a pixel size of 15 μm . To cover the entire focal plane would require 7×6 detector arrays and the focal plane would be 0.43×0.37 m in size. If this is compared to the detector focal plane of the Gemini Multi-Object Spectrograph which is 0.08×0.06 m, the technological challenges are obvious.

Figure 6.1 shows the Celestial Selector: a proposed ELT type instrument concept which illustrates the technique of Diverse Field Spectroscopy. The Celestial Selector may be conveniently implemented with a monolithic fibre system, discussed in section 6.2 followed by a layer of optical switches that route to a number of spectrographs.

The most obvious way to reduce the amount of data is to only route regions of interest (ROIs) to the spectrograph. Section 6.3 describes how optical switching systems could be designed to realise this. However, there are currently no practical technological solutions able to implement this option on the scales required. In order to overcome this problem we present data in section 6.4 that demonstrates the statistical advantages that will be gained by randomising the input field before a down-selection is implemented.

[1] e2v ltd., 106 Waterhouse Lane, Chelmsford, Essex, CM1 2QU

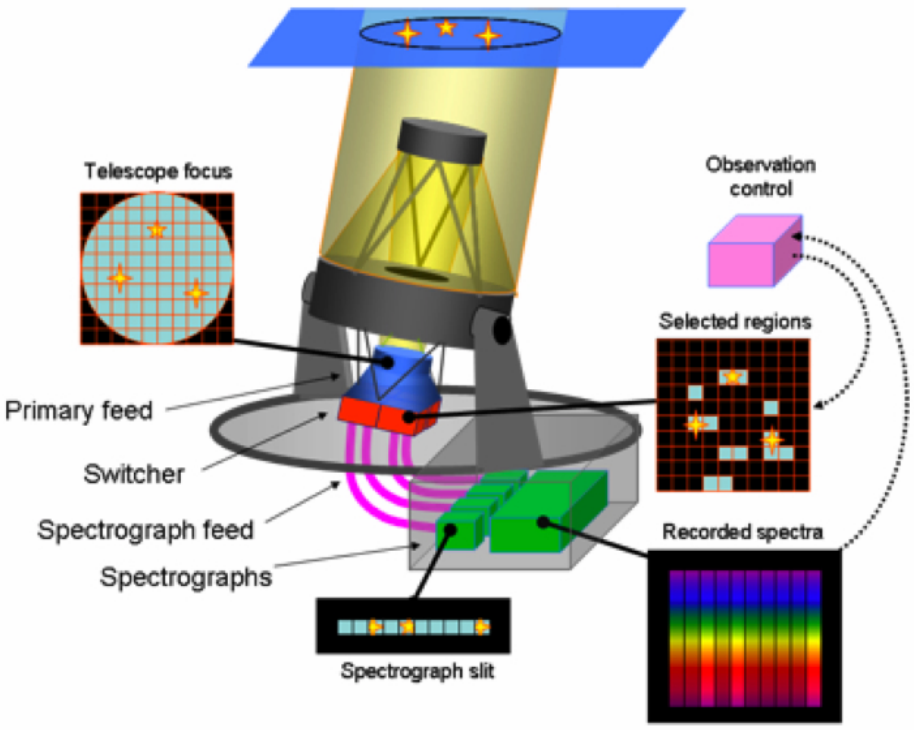

Figure 6.1: Celestial selector concept showing a large input fibre bundle and a switching unit which selects ROIs to be routed to the spectrograph *(Image courtesy of Jeremy Allington-Smith)*

6.2 Accessing the entire focal plane of an ELT

Table 6.1 shows a number of instruments which have successfully used a coherent fibre bundle to re-format a 2-D field into a 1-D array, suitable for coupling into a spectrograph. This table does not provide a comprehensive list of instruments, but serves as an indicator of how fibre bundles used in astronomical instrumentation has progressed since 1986. The basic requirements of the fibre system are to:

- Minimise focal ratio degradation (this has been discussed extensively in chapter 3);
- Minimise losses by maximising the fill-factor at the input of the fibre bundle;
- Retain a high degree of spatial precision at the input and output ends.

Figure 6.2 shows the input ends of the DensePak, CIRPASS and GMOS integral field units. DensePak was one of the first instruments to use a coherent fibre bundle, however, the filling-factor was only 54%. The GMOS IFU uses one of the largest fibre bundles in astronomical instrumentation. The GMOS IFU uses two bundles of fibres, one with 1000 fibres and one with 500 fibres for background subtraction. The fibres are mounted in ferrules for support and are then attached to a lenslet array which increases the filling factor since all incident light is focussed onto the fibre cores. One of the main disadvantages to using lenslet arrays is that tighter requirements are imposed on the spatial precision or a loss in throughput will result. A more thorough discussion of the implications of using a microlens at the input of a fibre bundle was given in section 2.1.2.

A high spatial precision is difficult to achieve when building large fibre bundles since, although the ferrules have tight tolerances on their dimensions, there

Instrument	Year	number of fibres	core diameter (μm)	on-sky coverage	Notes
DensePak [153],Kitt-Peak	1986	49	100	$16'' \times 19''$	no microlenses
Hexaflex [154],WHT	1991	{2 units× 61	200, 320	$13''$, $1'$	allows a change in spatial and spectral resolution without modifying the spectrographs configuration
2D-FIS[155],WHT	1997	125	200 μm	($0.9''$ on sky)$9.2'' \times 12.2''$	includes a ring of fibres for sky subtraction
CIRPASS [156],Gemini	2002	499	104	$13.3'' \times 4.8''$, $9.3'' \times 3.3''$, $4.4'' \times 1.6''$, $1.9'' \times 0.7''$	variable lenslet
GMOS [157], Gemini	2002	1 unit ×1000 1 unit ×500	67 μm	$5'' \times 7''$	large monolithic bundle
VIMOS [158], VLT	2002	6400	100 μm	4 units 7×8 $'^2$ $54\times54''^2$	pitch required: $\pm$ 5 μm achieved: $\pm$ 30 μm at edges spherical lens used to compensate
VIRUS-132 [159], HET	planned	132 units ×247	undecided	29 sq$'$	first demo of replicable system

Table 6.1: The number of fibres in fibre bundles used in astronomical instrumentation has increased since they were first developed. The efficiency of some of the instruments have been improved via the addition of microlenses.

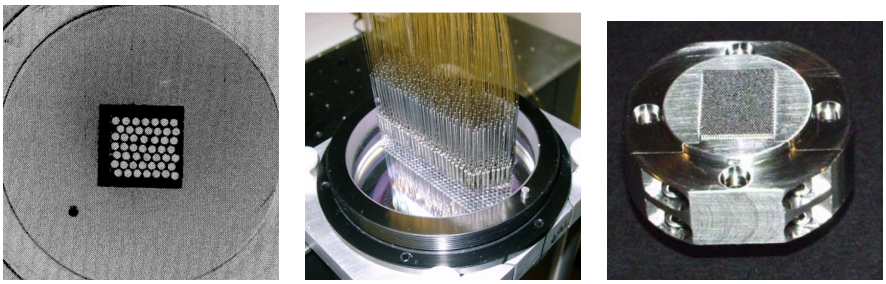

(a) (b) (c)

Figure 6.2: The development of building fibre bundles has progressed from a simple fibre design (a - DensePak) to a larger bundle which includes microlenses (b - CIRPASS) to a massive bundle of 1000 fibres (c - GMOS).

will inevitably be some deviation in the diameter size. The other problem inherent to building a bundle using ferrules, is that a smaller variation in pitch is achieved if the packing is hexagonal, whereas microlens arrays are usually square.

Figure 6.3 schematically shows the effect of using different sized ferrules when making a fibre bundle. The dashed lines show an evenly spaced grid over which the centres should lie if the ferrules were all exactly the same size, with red ferrules at the minimum of the size tolerance and blue ferules at the maximum of the size tolerance.

The maximum systematic error on the position of the n^{th} centre in one dimension is given by:

$$\alpha c_n = \frac{\alpha}{2} + (n-1)\alpha, \tag{6.1}$$

where αc_n is the error on the n^{th}core, α is the error on the diameter of the ferrule and n is the number of ferrules. Hence, if ferrules were being used which had a diameter of 100 ± 3 μm , then the maximum difference of the centre of the 30^{th} ferrule compared to if there was no variation in sizes, would be 88.5 μm .

The range of tube sizes can be refined by measurement and selection from a substantially larger batch, however the error within the entire bundle will always scale with the size of the bundle.

This systematic error shows the most extreme case where all of the ferrules are at the maximum of the accepted tolerance dimension. In reality the random assortment of ferrule sizes (which are still within the tolerance) will result an a random error which may be much smaller. However, as was discovered with the VIMOS instrument described in table 6.1, additional lenses may be required to compensate for the offset, and this makes this method of holding fibres a less desirable option for building large bundles for ELTs.

6.2.1 Laser-Cut Hole Arrays

Laser-cut hole arrays have been investigated as an alternative to packing the fibres in ferrules. The advantages of this method are:

- The error on the pitch will be absolute over the entire bundle;
- Any packing pattern can be achieved;
- The array material can be selected so that the material characteristics (hardness, coefficient of thermal expansion, etc..) match the characteristics of the fibre.

Although laser-cut hole array type holders have been used in instruments such as SPIRAL [160] and the SOAR IFU [161] , no literature has been published. Consequently many aspects need to be investigated and understood.

Manufacturing methods There are two main manufacturing methods which produce a large price difference for different arrays. This is a result of the type

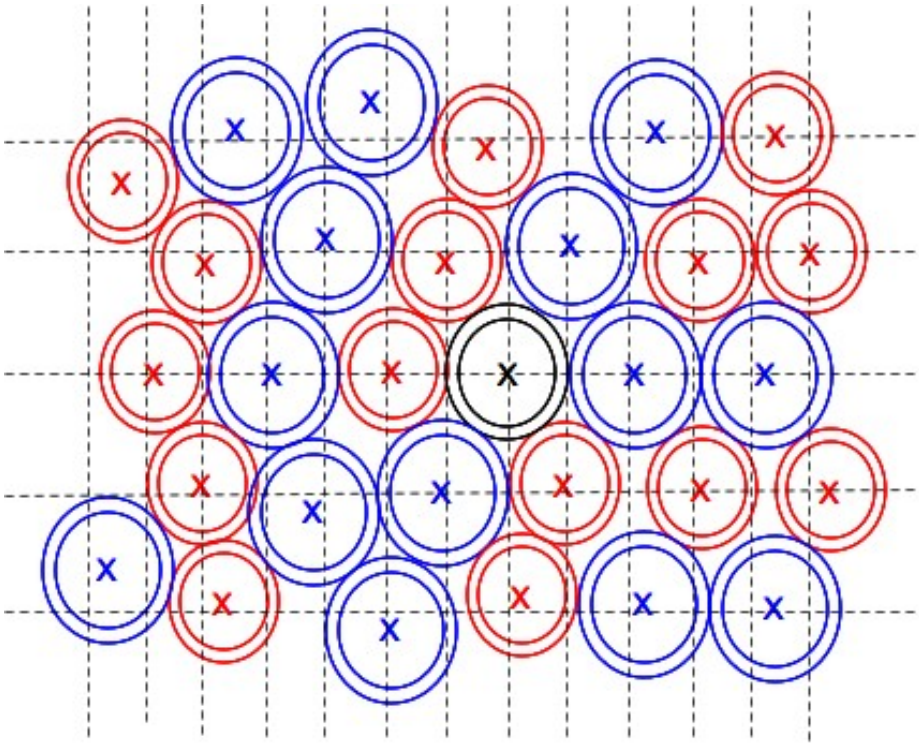

Figure 6.3: Deviations in the size of ferrules used to build fibre bundles result in a systematic error which propagates throughout the bundle. The dashed lines show a regularly spaced grid upon which the centre of the ferrules (shown in blue black and red) should align.

of laser being used and does not affect the quality of the array.

1. The first method is to use a precision laser tuned to the wavelength specific to the material and draw the pattern for each hole separately. This method is extremely expensive and is time consuming.

2. The second method is to place a mask in front of a large planar excimer laser and photo-ablate the entire array in one go. After the initial cost of the mask, this method is inexpensive and produces replicable arrays. This method has been adapted from the semiconductor industry where many cheap chips are required.

Array material The array material determines the maximum thicknesses of each array as thicker arrays result in poorly defined hole profiles. However, the main limitation to array material is decided by the laser that each manufacturer uses. Each material is suited to a particular wavelength so a balance must be made between selecting a manufacturer which uses the second manufacturing method described above, and one which produces a hole array in a desirable material.

A number of hole arrays in different materials have been obtained from various manufacturers and table 6.2 gives an overview of the measured geometry of a selection of these. The holes in the cirlex array looks the 'cleanest' (figure 6.4), however the error in the dimensions was larger than for the other arrays. The paper array (figure 6.5) is made of a laminated stiff cardboard, which has poorly-defined holes. The variation in the size of the holes was acceptably small however, it is possible, but difficult, to apply epoxy to the bundle since the paper is absorbent. The ceramic arrays (figure 6.6) have funnelled holes which

is useful when building the array as it allows the fibres to be guided in, however the ceramic is extremely brittle and will have a poorly matched coefficient of thermal expansion (CTE) with the fibres.

material	diameter				pitch			
	x	s. d.	y	s. d.	x	s. d.	y	s. d.
cirlex	148.4	10.3	147.0	8.1	248.2	5.8	249.0	5.8
paper	142.3	5.3	133.8	6.2	251.0	5.5	248.2	4.0
ceramic	138.9	5.1	139.5	4.9	250.2	6.4	248.3	5.2

Table 6.2: Metrology of the arrays. Arrays were designed to have a diameter of 142±5 μm with a pitch of 250±5 μm .

Designing the bundle Once the options for different types of hole arrays have been established, a device must be designed. Due to the manufacturing methods, the arrays can only be made from relatively thin wafers of material. If the fibre is only constrained by a guide which is a few millimetres thick, the fibres may not be parallel to the optical axis as shown in figure 6.7. The maximum deviation in angle will occur when the end of the fibre is at the far edge of the front of the array and at the opposite edge at the back of the array. This angle is calculated by simple trigonometry and the effects of different wafer thicknesses is shown in figure 6.7.

If the fibres are not sufficiently aligned to the optical axis, unnecessary focal ratio degration will be introduced into the system. Figure 6.8 shows the FRD that occurs due to varying amounts of fibre misalignment with respect to the optical axis for instruments that are fed at different focal ratios. This figure clearly shows that the effects are more pronounced for slower input beams, but in general substantial degradation occurs for misalignments above 0.1-0.6°. Bershady *et al.* [162] have performed similar calculations and found that a

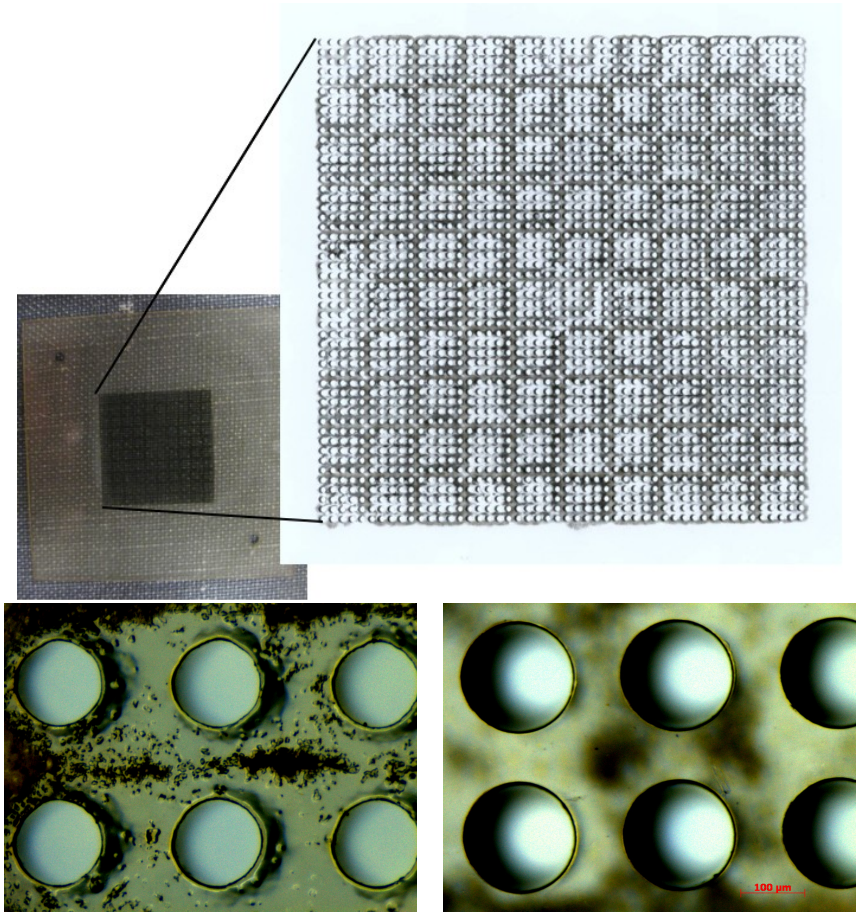

(a) (b)

Figure 6.4: Images of the Cirlex array. The top panel shows a stitched view of the entire array with a $\times 8$ magnification. Bottom panels show alternate sides of the array with $\times 100$ magnification (design diameter is 142 μm).

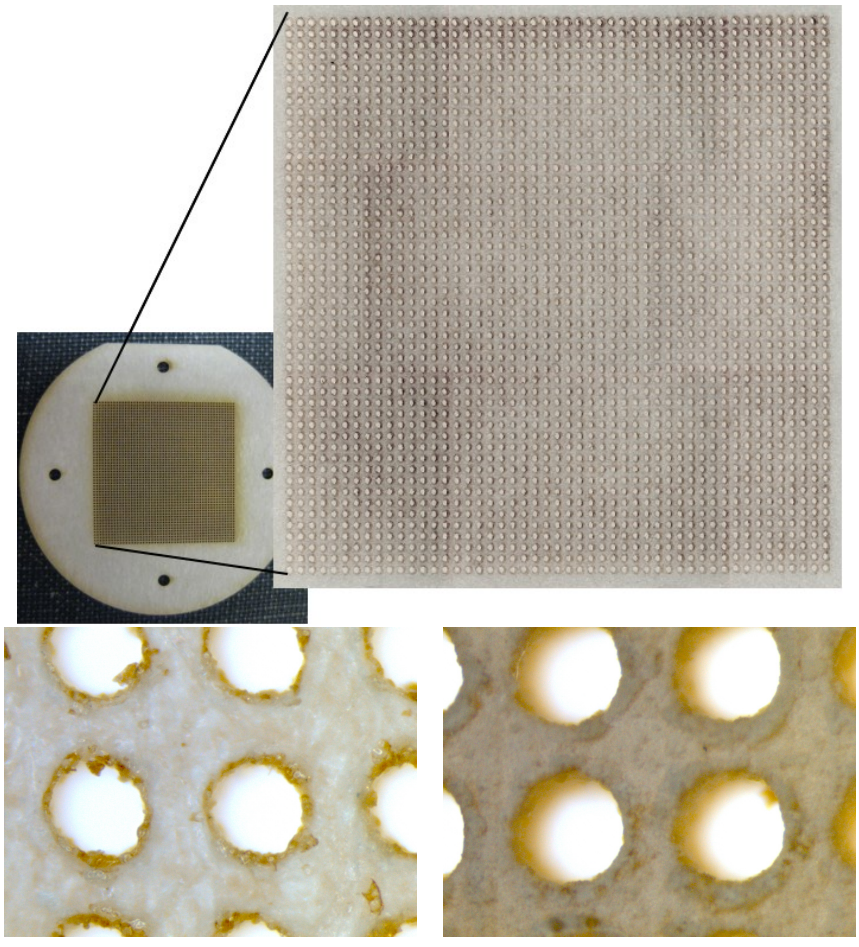

(a) (b)

Figure 6.5: Images of the Paper array. The top panel shows a stitched view of the entire array with a $\times 8$ magnification. Bottom panels show alternate sides of the array with $\times 100$ magnification (design diameter is 142 μm).

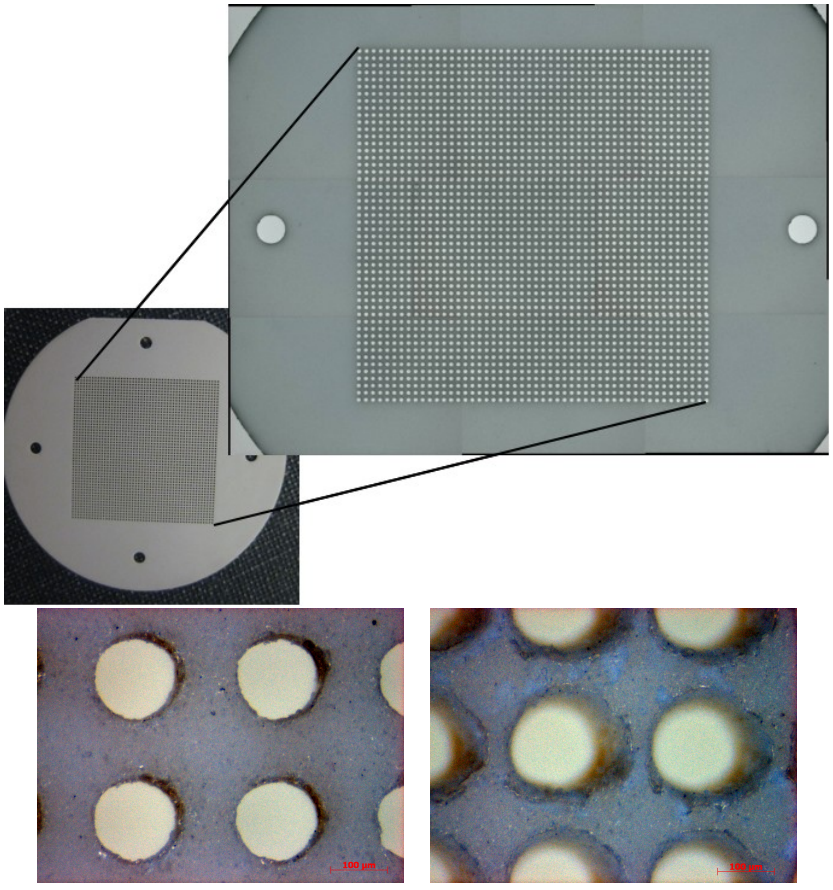

(a) (b)

Figure 6.6: Images of the Ceramic array. The top panel shows a stitched view of the entire array with a ×8 magnification. Bottom panels show alternate sides of the array with ×100 magnification (design diameter is 142 μm).

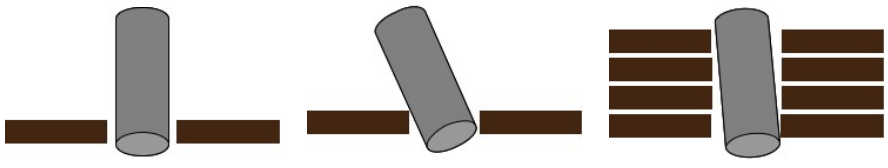

(a) (b) (c)

Figure 6.7: If the fibre is only constrained by a guide which is a few mm thick, the fibres may not be parallel to the optical axis. Panel (a) shows the ideal case, panel (b) shows the extreme case of a thin stack and panel (c) shows how a thicker array can constrain the angle of the fibre with respect to the optical axis.

misalignment of 0.41° would reduce the focal ratio of SALT from f/4.2 to f/4.1, but if the input focal ratio was much slower, a f/13.7 input would degrade to f/12.6.

The hole arrays that have been sourced to date have a tolerance of ±5 μm . It is necessary to oversize the holes by 4 μm (2 μm either side of the edge of the fibre) in order to ensure that the fibre was not damaged during the building process. This resulted in the diameter of the hole being a maximum of 20 μm larger than the minimum diameter of the fibre. Therefore, in order to constrain the fibre to within 1°, the stack must be 850 μm in depth. A stack which is 0.9 cm in depth will constrain the fibre to within 0.1°, and a stack which is 2 cm in depth will constrain the fibre to within 0.04°. This results in an f/5.5 beam being degraded to f/4.6, f/5.4, and f/5.5 respectively. If the error budget dictates that 2% focal ratio degradation is acceptable, a stack of 9 arrays is required if each array is 1 mm thick.

There are two solutions to this problem, as shown in figure 6.9. The first solution is that a second array could be placed at some distance behind the first array, and the intermediate space filled up with epoxy. However, this may stress the fibres as the epoxy dries and contracts. The second solution, which was utilised in the final fibre design, is to stack multiple arrays in order to control the angle of the fibre with respect to the optical axis.

6.2.2 Building the fibre bundle

Fibre bundles that use laser-cut hole-arrays have not been built in Durham, hence a prototype was produced in order to establish an effective building and

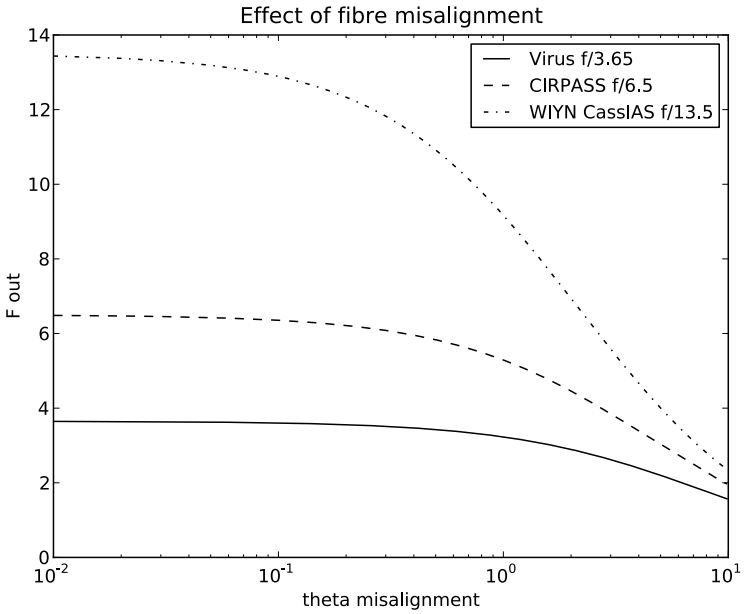

Figure 6.8: FRD that occurs due to varying amounts of fibre misalignment with respect to the optical axis for instruments that are fed at different focal ratios.

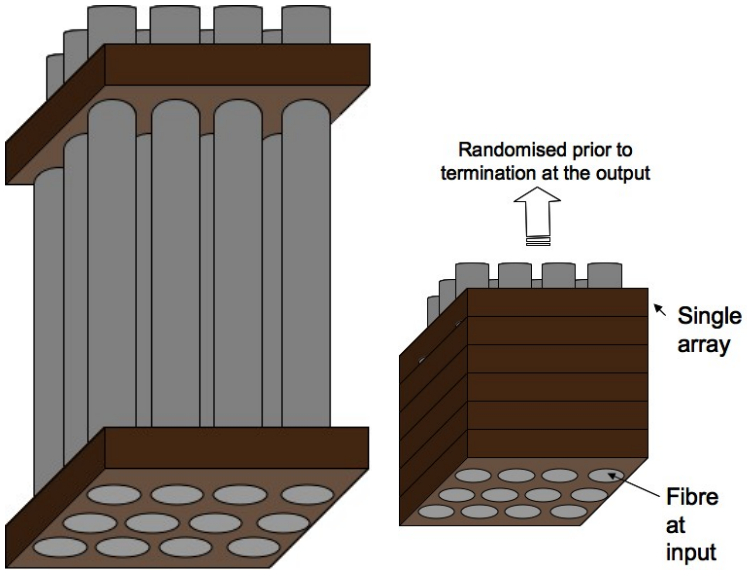

Figure 6.9: Due to the manufacturing methods, the arrays can only be made from relatively thin wafers of material and must be stacked in order to ensure that all fibres are able to be aligned to the optical axis.

termination procedure. The first bundle was built using small hole arrays with 23 holes and was used to establish a building method. The building process is shown in figure 6.10 and described below.

First, the hole arrays are stacked, using the guiding pins to provide a sufficiently tight alignment. Then the fibres are fed sequentially into the stacked arrays. The array is then placed into the holder which is covered in masking paint in order to prevent the epoxy from adhering to undesirable areas. Polyimide tubing is used as guiding pins since they have tightly toleranced outer dimensions and the CTE is well matched to the polyimide buffer fibres. The whole array is then held in a pot of epoxy such that the epoxy will wick up the fibres and bond the entire stack. When the epoxy is tacky, it is removed from the pot. When the epoxy is completely hardened the excess is removed

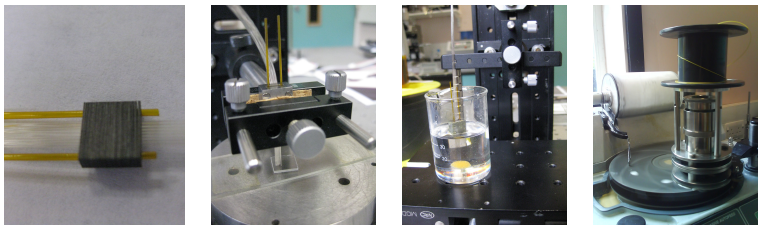

(a) (b) (c) (d)

Figure 6.10: The process of building a fibre bundle. In (a) the wafers are stacked using the guiding pins and the fibres are inserted. In (b) the ends of the fibres are glued to ensure that they remain in place before being enclosed in the housing and (c) potted in epoxy which is allowed to wick up into the bundle. Finally the entire bundle is polished as shown in (d).

from the array and is then polished using finer and finer colloidal silica particles suspended in purified water.

Once the building method had been established, the large bundle which had 2304 (48×48) fibres was built and this is shown in figure 6.11

The main difficulties encountered when building the bundle were in polishing it. This is because of the large surface area over which material was being removed and the different hardnesses of the fibres, cirlex arrays and stainless steel housing.

After the input end of the large bundle had been successfully made and polished, a program was written which randomised the bundle and a robot was used to move a laser around the input plane to randomly select fibres to be placed successively at the output.

Although a suitable array material has yet to be sourced, the work presented in this chapter has shown that the technique is feasible and could easily be scaled

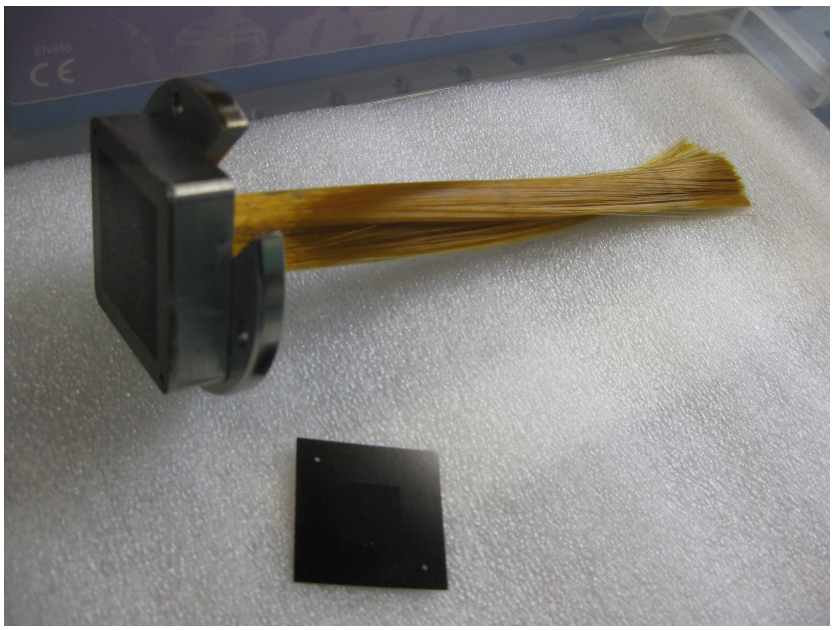

Figure 6.11: A 2304 bundle which has been built and polished. The bundle is built using fibres with a core size of 100 μm in diameter and a pitch of 200 ± 5 μm .

up to larger bundle sizes. A number of parameters, such as the necessary depth of the stack, have been constrained, and a method of building the bundles has been established. A process to randomise the bundle has been developed and the completed bundle has been polished to a satisfactory optical quality.

The randomised mapping was recorded for future reference and the advantages in randomising the bundle prior to down-selection will be demonstrated in section 6.4. However, the ideal solution to DFS would be to have an optical switch which could address the entire bundle and this will now be considered.

6.3 Optical switch networks

As was discussed in section 6.1, 26,700 pixels would be required to sample a $2'$ field with the E-ELT ($D = 42$ m), in the infra-red ($\lambda = 1.5$ μm). The most obvious way to reduce the amount of data is to only route regions of interest (ROIs) to the spectrograph which would require some kind of optical switch network.

Developments in optical switching have predominantly been driven by the telecommunications industry where single mode fibres are used in order to avoid modal dispersion. When the fibre core diameter is of the order of the wavelength of the light, only one mode of propagation is allowed and the fibre is single-moded. If optical switches were to be useful in astronomical instrumentation, they would need to be able to handle multimoded light. The next problem is that current fibre optic switches generally switch from a small number of inputs, N, to one output, $M = 1$ using rotary[163] or translational [164] switches. However, DFS relies on $N \times M$ switching, where N is large and $M \gtrsim 1$.

Table 6.3: Number of switches and interconnects necessary for a two layer switch of the type shown in figure 6.12

N (inputs)	M (outputs)	number of interconnects	number of switches
100	10	2,510	210
529	23	27,002	1081
2500	50	262,550	5,050
10000	100	2,050,100	2,100

Although there are inherent problems with implementing an effective optical switch system, optical switches remain the only way that a fully diverse system can be implemented. The basic concept states that for a given number of inputs, N, any subset, M may be selected to be routed to the spectrograph. The most efficient switching system will only have two layers of switches as shown in figure 6.12 where any 25 inputs can be down-selected to 5 outputs, however, this is only possible when $M = \sqrt{N}$. As discussed above, a single switch must have only one input, however to simplify the ideas presented in this section, the 'sub switches' (shown in the bottom right of figure 6.12) do not contribute to the number of layers but are necessary to build the switch and must be taken into account when considering the number of interconnects in a given system.

In order to have the most flexible switch (i.e. $M \neq \sqrt{N}$), it is necessary to have 3 layers of switches as shown in figure 6.13 where any 25 inputs can be down-selected to 8 outputs. This configuration only works when $M = 4a$, where a is an integer, however different configurations can be found when $M \neq 4a$. When a manufacturing solution becomes available, it will be possible to assess each configuration based on losses within the method.

Now that possible configurations have been identified, technological solutions

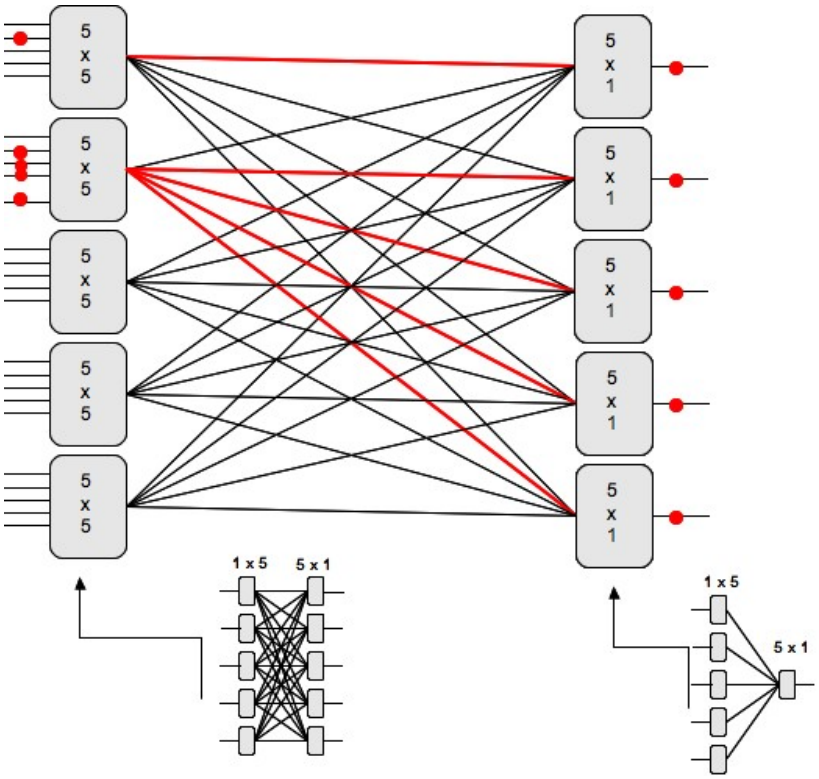

Figure 6.12: 2 layer switching used to create a $N \times M$ switch where N is the number of inputs, M is the number of outputs, and $M = \sqrt{N}$.

Table 6.4: Number of switches and interconnects necessary for a three layer switch of the type shown in figure 6.13

N (inputs)	M (outputs)	number of switches	number of interconnects
2304	40	341,576	9,032
2304	100	584,546	12,962
2304	200	1,183,496	21,512
2304	600	6,004,296	80,712
2304	1000	14,705,096	179,912

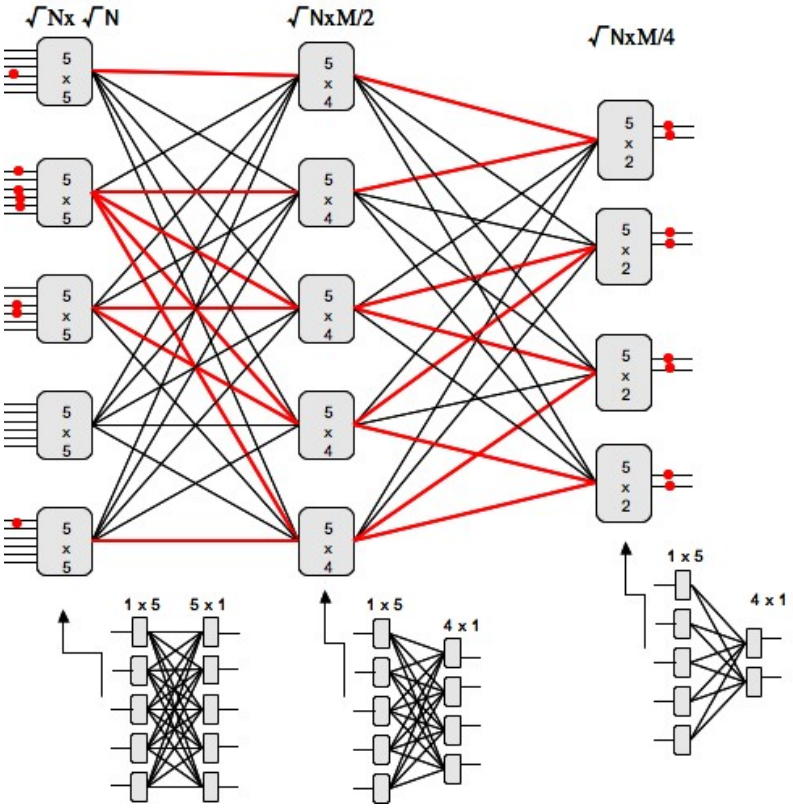

Figure 6.13: 3 layer switching used to create a $N \times M$ switch where N is the number of inputs, M is the number of outputs, and $M \neq \sqrt{N}$.

must be found to implement these design rules. The numbers shown in tables 6.3 and 6.4 clearly show that the huge number of switching units and interconnects mean that any technological solution must be extremely efficient, whilst still being able to be mass produced. Switching technology has advanced rapidly in recent years in order to meet the growing demand for such devices in the telecommunications sector, however the needs are very different to the needs presented here. Assuming any such system would be possible, three distinct approaches have currently been studied[165]:

1. Plug-in fibres;
2. Arrays of tilt-able micromirrors;
3. Movable lenses.

Plug-in fibres These devices differ widely in design and many systems display a high degree of ingenuity. They are also potentially highly efficient. A good example is the switching technology developed by Polatis Inc. [2] where lensed fibres are steered directly by means of piezoelectrically driven fingers via a central optical relay shown in figure 6.14. The single-mode commercial products available from this company have switching speeds of ≤ 10 ms and the bandwidth is limited only by the fibre, so they can function throughout the optical spectrum. The number of optical interfaces is small (six including the fibrelens interfaces), so the insertion losses are low, $\sim$1 dB. There is to-date no plan to commercialize a multi-mode system however. Interesting as such schemes are, they are more suited to low fibre counts because the positioning actuators tend to be bulky and elaborate, incorporating relatively large mechanisms. Therefore they are not currently an ideal DFS solution.

[2]Polatis, Inc., 332/2 Cambridge Science Park, Cambridge CB4 OWN, United Kingdom

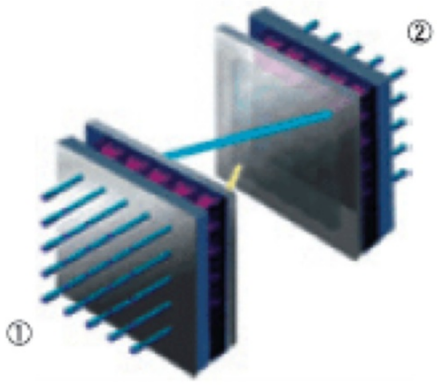

Figure 6.14: A Polatis switch: an optical beam is collimated and steered from an input array ("send" side) to an output array ("receive" side). In reconfigurable port configurations, a single fold mirror provides the ability to return light back to a single array. Voltage signals to the piezoelectric elements control the pointing, while accurate position feedback provides continuous closed loop precision.

Movable lenses The most promising commercial solution so far seems to be one which uses moveable lenses. This idea is currently being investigated jointly with CrossFiber Inc [3] and it is hoped that an effective solution will be forthcoming, however at present, the information is proprietary. The basic idea is that the switches will use movable lenses to feed fibres in a circular bundle. The lenses must be small enough to make it possible to produce a large number of switches at a reasonable cost, and still limit the total size of the instrument.

Arrays of tilt-able micromirrors The simplest solution which uses micromirrors is shown in figure 6.15 and utilises two micromirror arrays. The first micromirror array can be used to direct regions of interest (ROIs) to output fibres and the second array is used to ensure that light being fed into the fibres is on-axis. The micromirror arrays used in this design can be tilted along two

[3]CrossFiber Inc., 10455 Pacific Centre Court, San Diego, CA 92121-4339

axes, unlike other micromirror arrays, so these mirrors can be given any intermediate tilt between their extreme inclinations.

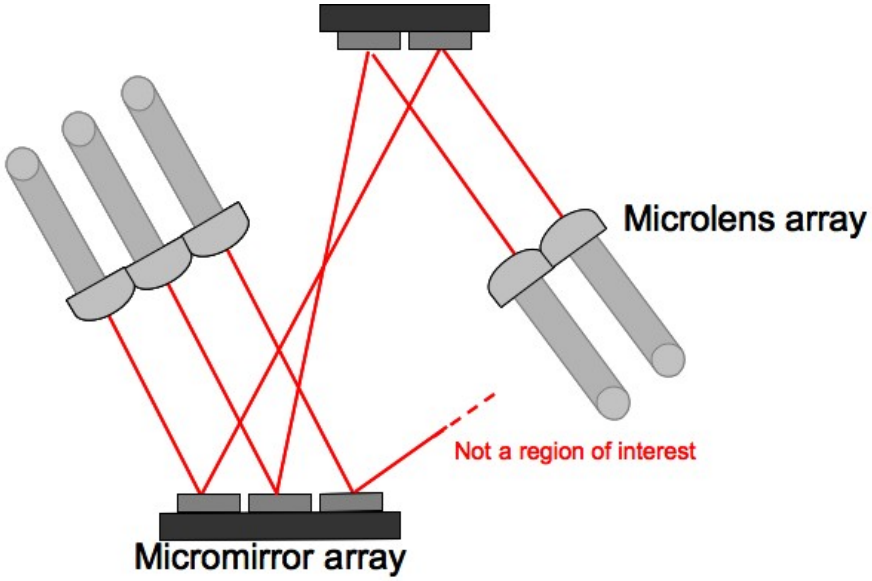

Figure 6.15: Simple switch using micromirror arrays

Current design studies by Content *et al.* [165] using a Crossfibre array used for telecommunications optical switches, similar to those shown in figure 6.16, imply that intermediate optics would be necessary to limit the chromatic aberrations, however the Étendue will still be small at 0.01 mm which gives 0.5″ on a 4 m telescope. If a Fourier optic is introduced (a lens is placed between the micromirrors which has a focal length equal to its distance to the micromirror arrays so the intensity distribution on one micromirror array is the Fourier Transform of the distribution on the other) the Étendue is increased.

All of the systems for switching discussed above would, if a technological solution was found, enable the entire field to be arbitrarily down-selected to a smaller field which would be sent to the spectrograph. However, since the solu-

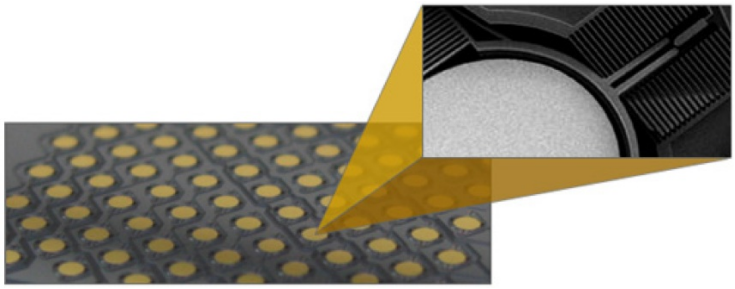

Figure 6.16: A fully steerable MEMS-based MMA (courtesy of CrossFiber Inc.).

tion is currently not forthcoming, it is necessary to investigate the slightly easier problem of breaking the field into smaller sections prior to down selection. The way in which the efficiency of such a system is maximised will now be discussed.

6.4 Remapping switched fibre systems

6.4.1 The advantage

The Celestial Selector concept that was shown in figure 6.1 may be conveniently implemented with a monolithic fibre system (i.e. a fibre bundle) followed by a layer of optical switches that route selected fibres to a number of spectrographs. Ideally the switch array allows N input spaxels to be down-selected to M output ($\lesssim N$) but this is infeasible using current switching technology, especially on the scales needed where $N \sim 10^5$ and $M \sim 10^4$.

The capabilities of optical switches in the telecommunication industry is generally $N \geq 100$ and $M \leq 10$. Therefore the inputs must be divided between many switches. For the remainder of this chapter, these divisions will be termed 'cells' and input cells will be defined as N_C whereas the total number of inputs remains as N.

The major problem with only being able to access one output from any given cell is that it is not possible to address contiguous ROIs. This is a consequence of fibres which are adjacent in the field being routed to the same cell, from which only one can be routed onwards to the slit. Only if the ROI is at the edge of two cells or at the corner of four cells can this problem be overcome. However, if the mapping between the field and the switch array is incoherent, i.e. randomising or re-ordering in other ways, there will be a finite chance that two or more spaxels which are adjacent in the field will be mapped to a spectrograph since they now occupy different cells as shown in figure 6.17. The different types of mapping are outlined in the following sections.

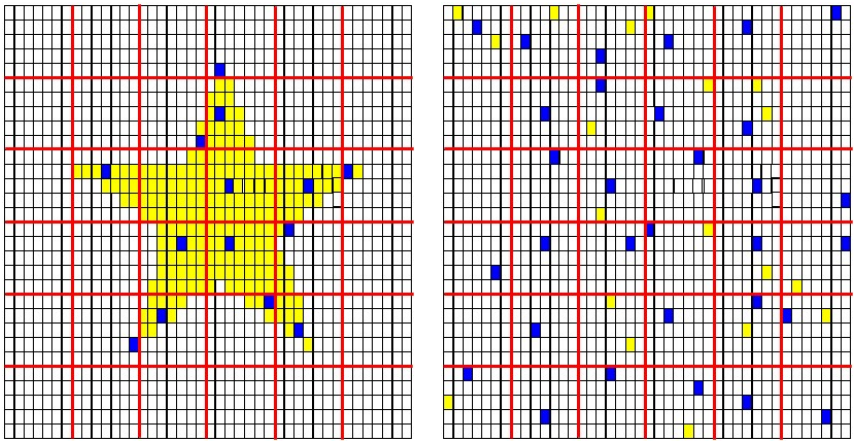

(*a*) (*b*)

Figure 6.17: Illustration of how remapping affects the success of a switching network. Panel (a) shows the regions of interest in yellow where spaxels which will be successfully routed to the spectrograph are shown in blue, if M=1 with direct mapping. Panel (b) shows the improved success rate if M remains equal to 1 but the field is randomised prior to down-selection.

6.4.2 Remapping Schemes

Various remapping schemes are possible. In all cases, although the remapping may be arbitrary, it is known, either by design or through post-manufacture calibration. In the following sections, descriptions of different remapping schemes will be presented where N is defined as the number of input spaxels, and N_C is the total number of cells in the entire switch.

Direct mapping

Regular one-to-one correspondence between input and output so that the two patterns are identical. Contiguous groups of spaxels will not be routed to the slit unless they span the boundary between different cells of the Spatial Light Modulator array. This can be overcome if the field is repositioned (or dithered) to position one contiguous group on the boundary between 4 cells. The maximum field repositioning required is equivalent to one cell or $\sqrt{N_C}$ in both directions or $N_C = N/M$ choices. This is clearly an inefficient solution.

Ordered mapping

Each spaxel in an input cell is routed to a different output cell. Thus it can be ensured that groups of contiguous spaxels will be routed to different output cells and hence to the slit. This solution is optimal for creating constellations containing groups of contiguous spaxels of size similar to that of the cell.

Random mapping

The mapping is randomised so that there is a finite probability that spaxels which are adjacent in the field will be routed to different cells and so have the potential to be routed to the slit. This solution has the same theoretical success rate as for ordered mapping although the pattern must be determined either by design or through post manufacture calibration.

6.4.3 Simulating mapping schemes with real astronomical objects

The different remapping techniques are now applied to a selection of real astronomical objects using a switch format that is commercially available for single mode fibres which switches from 48 inputs to 11 outputs. As previously discussed, design efforts are currently in progress to modify this switch to be compatible with multimode fibres.

Figure 6.18 shows the different stages required to calculate the success rate of different mapping strategies for the SAURON observation of a Lyman-alpha (LAB) emitter shown in panel (a) and described more fully in section 2.1.3. Firstly, these images were binned into 48×48 spaxels containing unit value if the intensity exceeded a specified threshold or zero otherwise in order to identify the 200 brightest spaxels, shown in panel (b). Next the field is subdivided into cells. In this example the input array is arranged into $N_C = 48$ cells each of $N = 6 \times 8 = 48$ spaxels, of which M may be routed to the output. The success rate is then calculated as the percentage of ROIs which are successfully routed to the spectrograph compared to the total number of ROIs. Due to the switch architecture, down-selection is limited within cells, so if there are no

ROIs within a cell, the switches cannot be reallocated to another cell. In order to minimise this problem, the field is randomised prior to down-selection, as shown in panel (c), in order to redistribute the ROIs over the entire field. The success rate is again calculated and compared to the original, unrandomised, result.

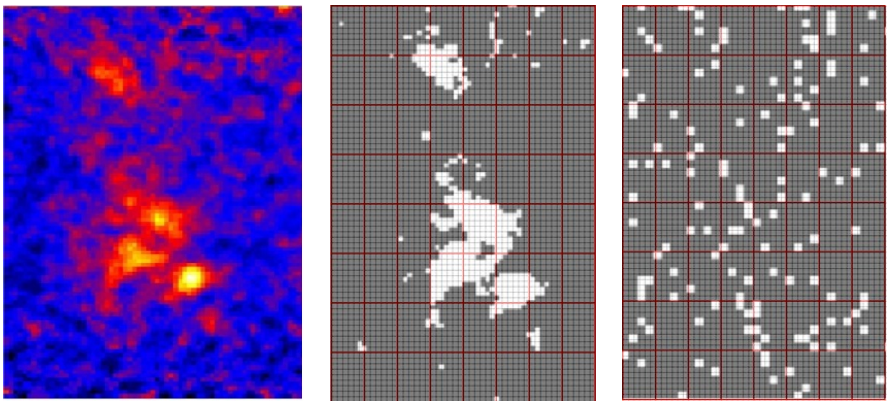

(a) (b) (c)

Figure 6.18: Process to calculate the success rate of random mapping strategies. In (b) the image is binned into 48×48 spaxels arranged into $N_C = 48$ cells each of $N = 6 \times 8 = 48$ spaxels, of which M may be routed to the output. Spaxels are defined to contain unit value if the intensity exceeded a specified threshold or zero otherwise in order to identify the 200 brightest spaxels. Due to the switch architecture, down-selection is limited within tiles, so if there are no ROIs within a cell, the switches cannot be reallocated to another cell. Hence, the field is randomised, as shown in panel (c) so as to redistribute the ROIs over the entire field.

In addition to the tests on the LAB object, 10 Objects were also taken from the Messier catalogue [166] at random and, as shown in figure 6.19, this includes both galaxies and star clusters. As such it provides an illustrative selection of different types of association, clustering and contiguity, and shows the relative benefits of randomising the field, prior to down-selection, for different types of fields.

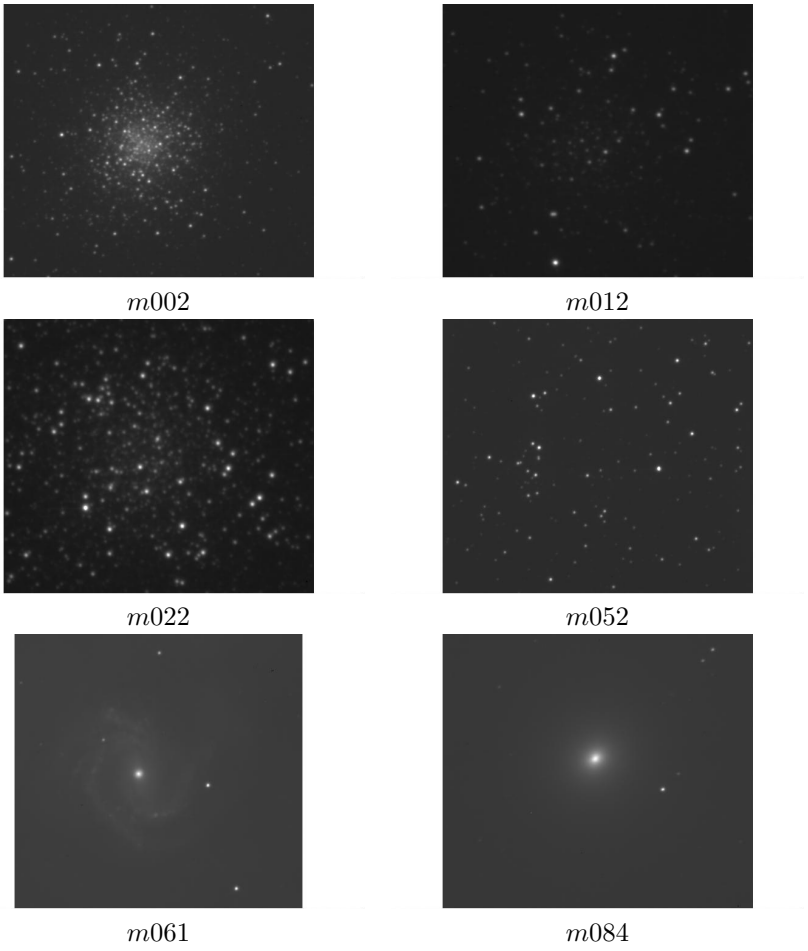

Figure 6.19: The first 6 Messier objects with various amounts of clustering, used to test different remapping schemes.

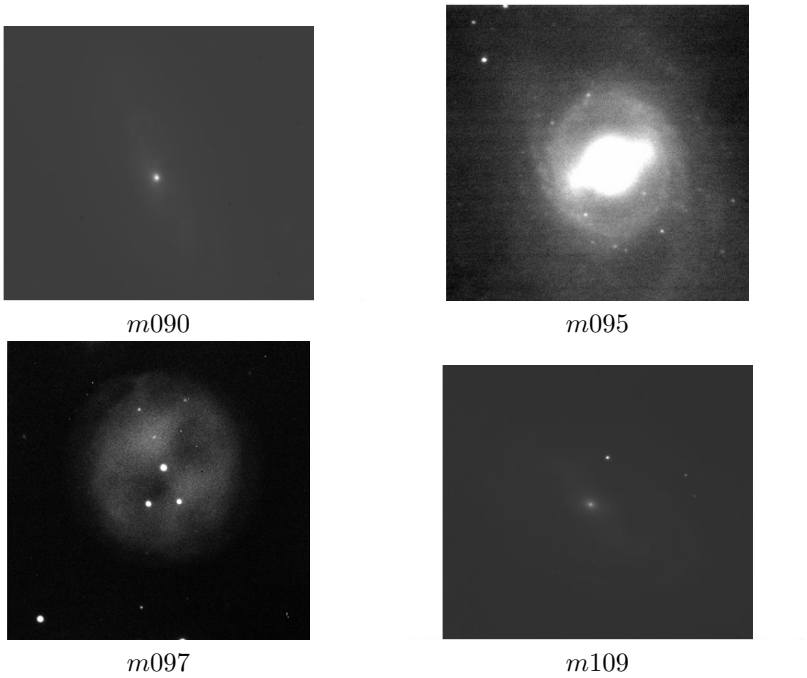

$m090$ $m095$

$m097$ $m109$

Figure 6.19: (Continued)The final four Messier objects with various amounts of clustering, used to test different remapping schemes.

Table 6.5 gives the success rate for the design value, $M = 11$, and also the value of M required to obtain a specified success rate. For the design value of $M = 11$, the down selection factor, G, is equal to $G = 4.4$, since $N = 2304$ and $M = 528$ and $G = N/M$. Without random mapping, the value of M needed to obtain a 100% success rate shows a large scatter ranging from $M = 14$ for fields with sparsely distributed ROIs such as an open star cluster like M52, to $M = 48$ for a heavily concentrated distribution of ROIs such as M84.

With random mapping, all the fields show similar results with $10 \leq M \leq 13$ being optimal (i.e. giving the greatest improvement when random remapping is used). Figures 6.20-6.21 shows the success rate as a function of M for the unrandomised case and the improvement in success rate with the randomised mapping. The improvement is greatest for values of $7 \leq N \leq 25$ which is close to the value needed to maximise the success rate with random mapping in an absolute sense and similar to the number of outputs provided in the commercial device.

Similar results were obtained when the success rate of the LAB objected were simulated. These results are shown in figure 6.22.

In order to compare the ordered remapping and random remapping schemes, multiple realisations were used to estimate the statistical uncertainty in random remapping. These results are shown in figure 6.23, and show that the typical RMS scatter in the abscissa is $\sim$5%.

It is also important to understand how the effect of building the fibre bundle in smaller tiles will affect the estimated success rate since the scope for randomi-

Table 6.5: Success rate for M with 100 ROIs and the value of M required to obtain the specified success rate for randomly-selected objects from the Messier catalogue

Image	Rank	Success Rate (%) for M=11		original mapping M which gives success rate=						Random mapping M which gives success rate=					
		original	random	50%	60%	70%	80%	90%	100%	50%	60%	70%	80%	90%	100%
M84	1	22	97	22	27	33	38	43	48	4	5	6	7	9	13
M95	2	28	99	20	26	32	37	43	48	4	5	6	7	9	13
M109	3	29	100	19	25	34	37	43	48	4	5	6	7	8	11
M2	4	31	99	24	29	34	39	44	48	4	5	6	7	8	12
M90	5	28	99	17	22	29	35	42	48	4	5	6	7	9	12
M97	6	32	98	16	20	24	29	37	48	4	5	6	7	8	13
M61	7	31	100	10	14	19	22	36	48	4	5	5	6	8	11
M12	8	57	100	8	12	16	23	35	48	4	5	5	6	7	10
M22	9	70	98	7	9	12	17	23	31	4	5	6	7	8	12
M52	10	96	99	4	5	6	7	9	14	4	5	6	7	9	13
LAB-1	-	43	98	12	15	25	37	47	48	4	5	6	7	9	12

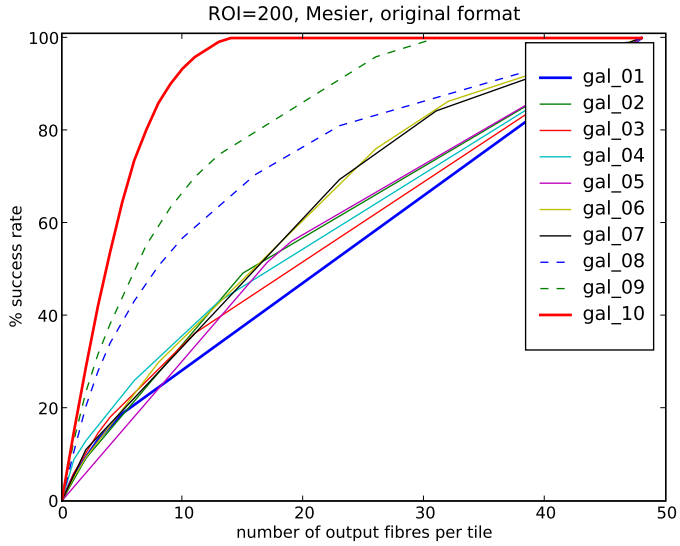

(a)

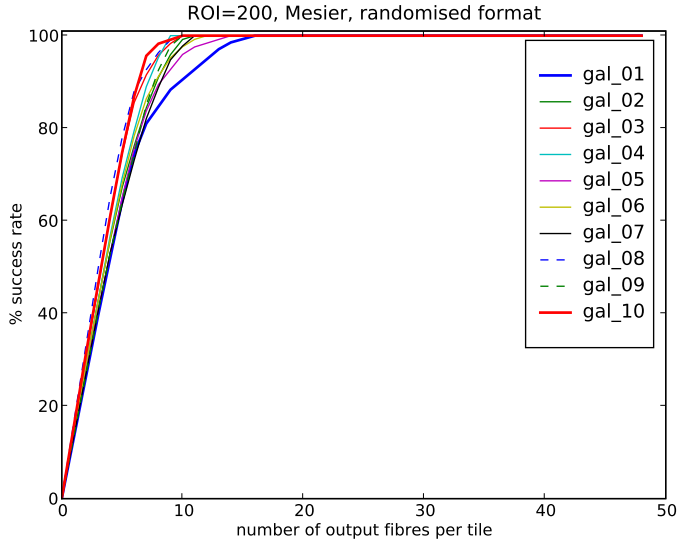

(b)

Figure 6.20: Success rate as a function of the number of outputs per cell, M for the 10 Messier objects with (a) no randomisation prior to down selection and (b) the improvements with randomisation prior to down selection.

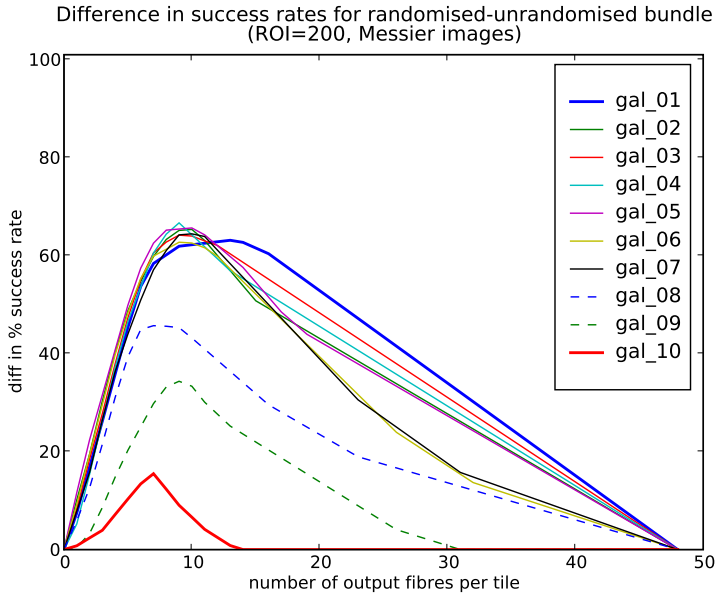

(c)

Figure 6.21: The improvements that can be made by randomising prior to down selection for the Messier objects

sation will be limited. In table 6.1 the details of the planned VIRUS instrument are given. This instrument is a pathfinder for ELT instrumentation and is one of the first to use replicable units to increase the multiplexing in an efficient way. In a similar way to this instrument, the input bundle of the celestial selector will be divided into tiles, so that it can be built up from standardised units made on a production line. However, the introduction of tiles does have an important consequence when incoherent mapping is used because the incoherence can only apply within each tile: it will not be possible to incoherently map between tiles. To this end the images were divided into 4 equal quadrants and randomised only within each quadrant. Figure 6.24 shows that this requires a higher number of outputs to achieve a given success rate depending on the amount of clustering of ROIs already present.

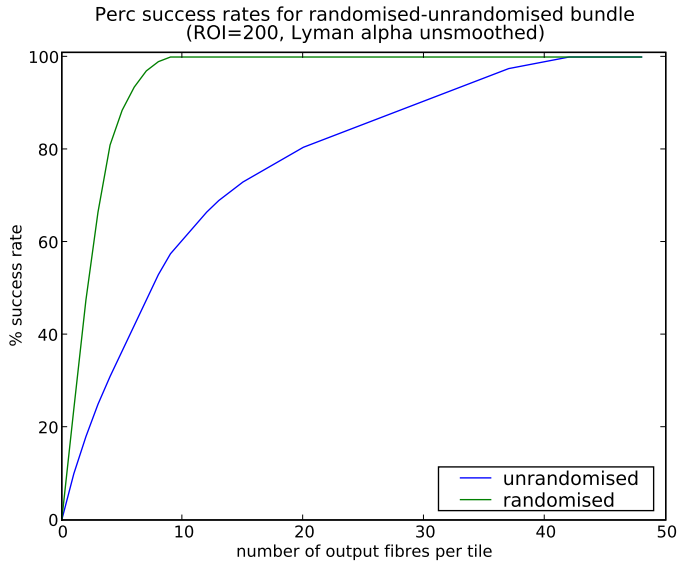

(a) unrandomised

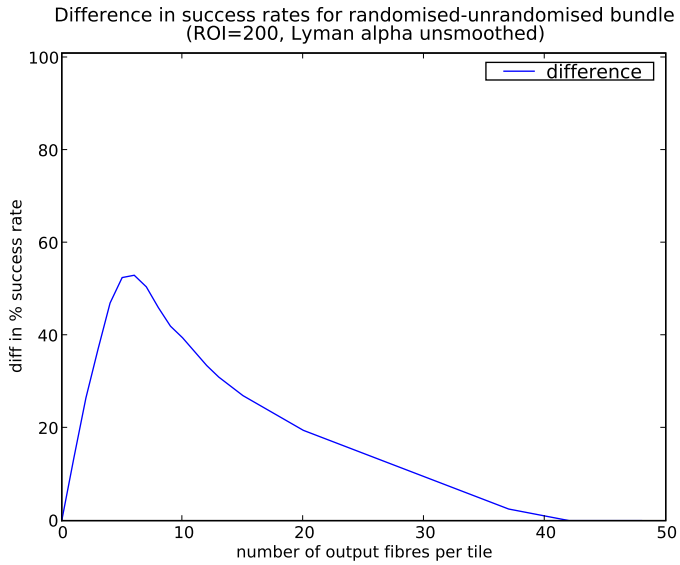

(b) randomised prior to down selection

Figure 6.22: Success rate as a function of the number of outputs per cell, M for the LAB objects, (a) with and without randomisation prior to down selection and (b) the improvements gained by randomising prior to down selection.

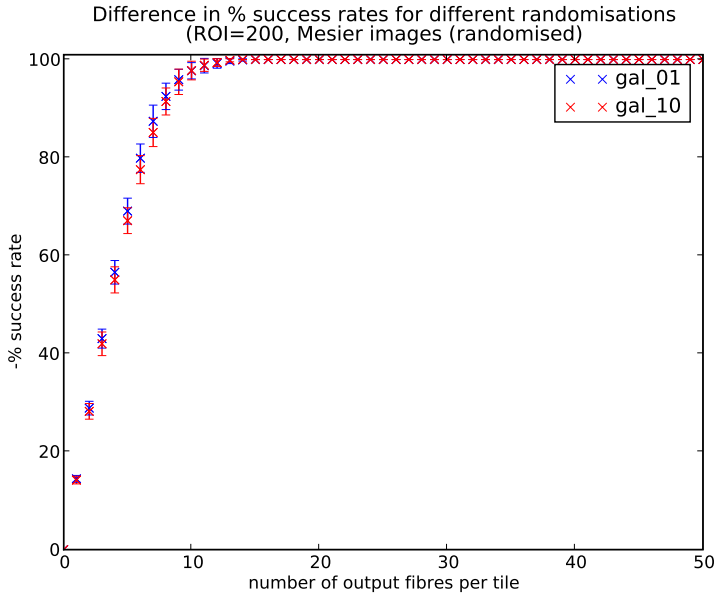

Figure 6.23: Multiple realisations of randomised remapping

As a final test, a catalogue of images was created with increasing correlation index values (i.e. progressively 'clumpier images'). Figure 6.25 shows the advantages which can be achieved when using DFS with random mapping compared to single IFUs, multiple IFUs and MOS.

6.5 Conclusion

This aim of this chapter was to explore methods which would provide efficient and affordable spectroscopic instrumentation on Extremely Large Telescopes with a particular study of techniques for highly-multiplexed spectroscopy; both the strategies and their implementation.

The focus of this chapter was the implementation of Diverse field spec-

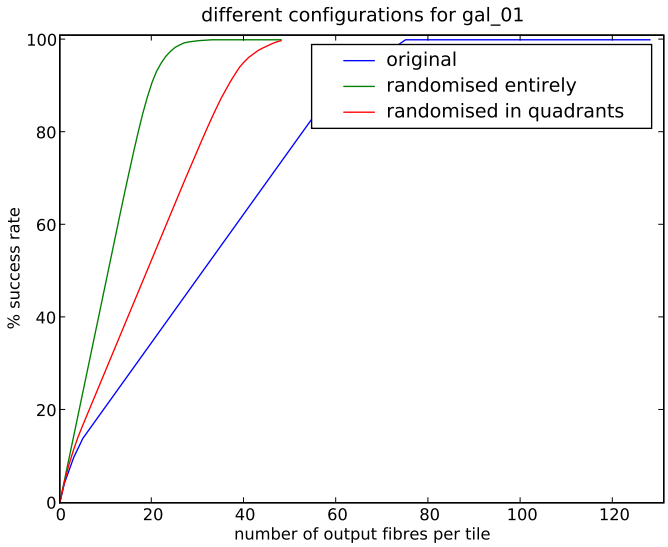

m81

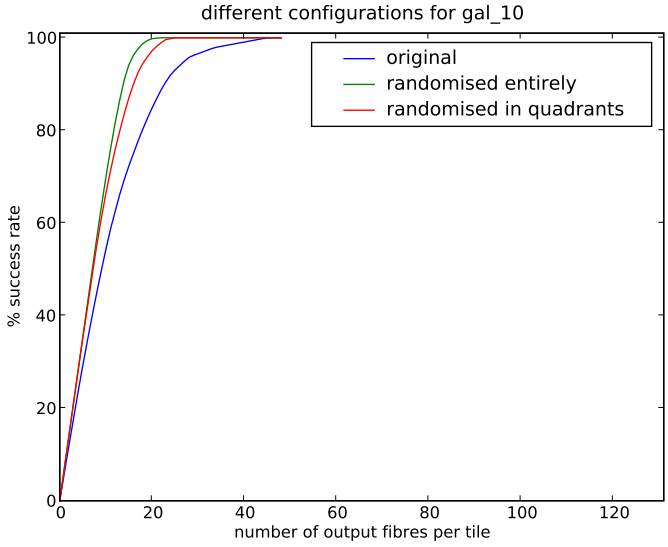

m52

Figure 6.24: Effect of randomising in quadrants for m81 and m52 compared to randomising the field in its entirety. These figures clearly show that randomising the entire field provides the greatest success rates, and fields which are 'clumpier' will suffer more from randomising in quadrants that fields which have a more even distribution of ROIs.

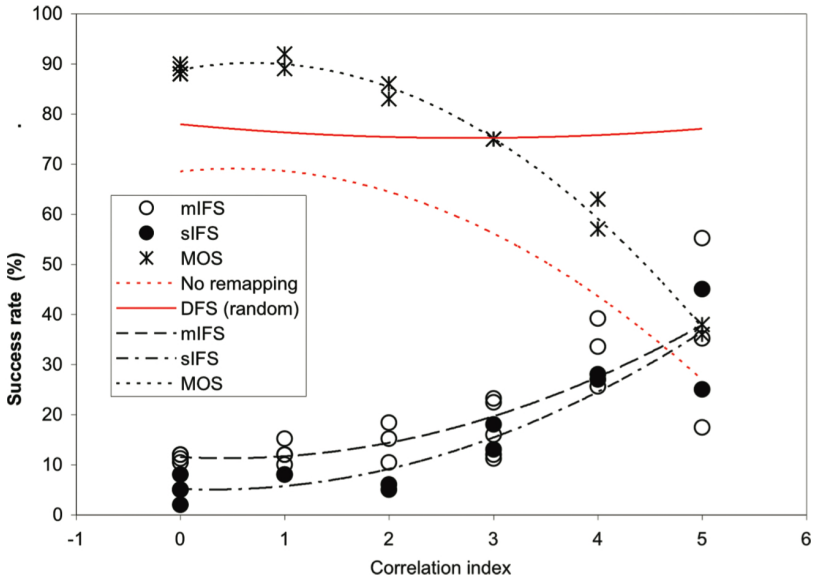

m81

Figure 6.25: Plot of success rate (i.e. occupancy) against correlation index for different types of remapping and without remapping (control). Data points for different realizations are shown together with trend lines (dashed curves).

troscopy. Observations made at high redshift show that the universe has a blobby and confused structure [13] and DFS allows the observer to select arbitrary combinations of contiguous and isolated regions of the sky to maximise observing efficiency and scientific return. However, before DFS can be implemented a large fibre bundle must be available and the ability to select any of the input fibres must be established.

In section 6.2 the practical considerations which must be made when building a large fibre bundle were outlined. Work presented in this section showed that laser cut hole arrays provided a viable alternative to stacking fibres in ferrules and would not suffer large deviations in pitch at the edge of the bundle. Building methods were established and a successful 2,500 fibre bundle was produced.

The limitations of mechanical field-selector deployment in delivering sufficient stability was reported by Allington-Smith *et al.* [167], Therefore, a number of options without large-scale mechanisms to down-select from a fibre system covering a large field of view to a smaller number of fibres which can be fed into a number of spectrographs have been explored.

A number of possible technologies which may be able to implement the down-selection have been indicated although a definitive solution is still being sought. As a preliminary step, different switching configurations have been examined which has emphasised the number of interconnects which will be necessary when implementing the switches. This is an important realisation since it will affect the design of the individual switch and also place a higher importance on its ability to be built by a robot.

Since the switching unit has been identified as the highest risk component of the DFS concept, it has been shown that smaller switches could still provide a high success rate (defined as the number of ROIs that are successfully routed to the spectrograph compared to the total number of ROIs in the field) if the input field is randomised prior to down-selection.

In section 6.4 different mapping strategies were examined. Detailed simulations of their performance for different degrees of clustering of the regions of interest to be addressed were presented. The simulations use real catalogues of objects to define regions of interest and calculate the success rate in targeting as a function of degree of clustering and the geometry of the switching system used, especially the number of outputs per cell.

Using these catalogues the advantage of the remapping is shown for clustered distributions. In addition, the superiority of the Diverse Field Spectroscopy approach over single large-field IFUs and multiple single fibres or small groups in such cases is shown. Depending on how clustered the distribution of ROIs is before randomisation, increases in success rate of up to 80% may be obtained for a down-selection factor of 10, although a range of 5 to 20 would be optimal for different distributions. Devices of this type are currently available for single-mode fibres.

In the future, solutions to the down selection will continue to be sought via a collaboration with CrossFiber Inc. and further hole array materials will be tested.

To finish a work? To finish a picture? What nonsense! To finish it means to be through with it, to kill it, to rid it of its soul, to give it its final blow the coup de grace for the painter as well as for the picture

Pablo Picasso, 1881-1973.

Chapter 7

Conclusions

7.1 Introduction

The work in this thesis is a combination of both theoretical models and experimental data. This is a reflection of the nature of instrumentation development which must be approached both via a 'ground up' and 'bottom down' approach. The first half of the thesis explores the 'bottom up' approach of studying the characteristics of optical fibres used for astronomy and investigating new photonic devices. The second half of the thesis relates to the 'top down' approach of proposing new techniques to be used in possible future instrument designs.

7.2 Thesis synopsis

This thesis has dealt with a range of issues surrounding the use of traditional and new technologies in astronomical instrumentation.

As was shown in chapter 2 optical fibres are extremely popular in astronomical instrumentation in order to optically multiplex telescopes. However,

the main disadvantage of using optical fibres is that they do not conserve the Étendue of the system due to focal ratio degradation (FRD).

Focal ratio degradation is an important property of optical fibres that determines the design and cost of instruments using fibres. Motivated by the importance of fibres in feeding instruments on Extremely Large Telescopes, the need for cryogenic-cooling to reduce thermal background and the desire for broad-band performance, the dependency of focal ratio degradation (FRD) on both temperature and wavelength has been investigated in chapter 3. Also investigated in chapter 3 was the dependence of FRD on the length of the fibre. Whilst the trends shown for the fibre core and d_0 parameter dependence have been demonstrated experimentally as well as theoretically, the extent to which the length affects the FRD has not.

In chapter 4 the use of astrophonic devices in astronomy was explored. Photonic crystal fibres (PCFs) were the focus of this chapter and both the practical implications in using them and the way in which their behaviour could be predicted theoretically was investigated. In the last section of this chapter, skills learnt in the preceding sections were used to asses the suitability of a Multicore-PCF for use in astronomical instrumentation. The main areas where M-PCFs are relevant were identified as integrated mini-IFUs and the main performance parameters were identified as throughput and crosstalk.

Instruments for ELTs must be extremely efficient with the highest resolution possible in order to take full advantage of the light gathering capabilities of the large primary mirror. Volume Phase Holographic gratings provide unique advantages over traditional dispersive elements as was discussed in chapter 5.

In the final chapter, the concept of the celestial selector was presented which aims to explore methods which would provide efficient and affordable spectroscopic instrumentation on Extremely Large Telescopes with a study of techniques for highly-multiplexed spectroscopy; both the strategies and their implementation.

7.3 Contribution

The original contributions in this thesis are as follows:

1. There is a small but significant reduction in performance when the fibres are cooled to 77 K as expected from previous work. It is also shown that the increase in FRD with wavelength is broadly consistent with theory at room temperature but this dependency reverses in sign when the fibres are cooled to 77 K, contrary to existing theory. In order to explain this behaviour the wavelength dependency is parametrised by an ad hoc extension to an existing model. This unexpected behaviour, which may relate to frozen-in stress from the manufacturing process, will need to be taken into account when designing future fibre systems;

2. The FRD within a fibre does not depend on its length. The results presented in chapter 3 show that the difference in FRD due to the different fibre lengths for the cleaved fibre at the asymptotic value was 0.15 ± 0.7, and hence is clear that within our experimental uncertainty, no length dependence is observed. In order to develop the existing model, the power distribution model described by Gloge has been adapted and a new model produced which will eliminate the length dependence on FRD and hence

provide a better agreement with the experimental data. As a result of trying to quantify the amount of stress within the end of the fibre it has been shown that the end-effect is extremely powerful. This significant reduction in the amount of microbending in the end of the fibre compared to the amount of microbending within the middle section is testament to the strength of the end effect and clearly shows how much FRD is generated in the end of the fibre;

3. Photonic crystal fibres (PCFs) are increasingly being exploited in astronomical instrumentation. So far in astronomy, single-mode fibres have been used mainly for interferometry. Multimode PCFs are also available, whereby the core is a very large homogeneous region surrounded by a cladding PCF. This promises extremely high numerical apertures which would be well matched to the fast primary foci of ELT class telescopes. Other more advanced PCF types include, non-linear fibres who's most studied application area to date is in the generation of supercontinua, which might find use in spectroscopic calibration in the lab or even on instrument. The quality of the end face of a fibre is extremely important to the propagation of light in terms of both throughput and intensity distribution, however no work has been published on this topic. In chapter 4 it was shown that the best method for preparing a PCF fibre is to slice using a fibre slicer. This method is quick to execute and relatively reproducible. Once it had been established that a sufficient proportion of the light was being guided by the fibre, the evolution of the mode shape was then investigated in the transition from the near to the far field. The observations were reproduced theoretically, by approximating the near-field distribution by a main Gaussian peak from which six narrow Gaussians located near the centre of the six inner holes have been subtracted as proposed by

Mortensen *et al.* [112];

4. It was shown that if M-PCFs are to be used as part of a mini-IFU, an insertion loss of $\leq$ 0.5dB from the optics feed would be required. Results show that this level could be achieved if the input spot was aligned on any core to within 2 μm .

5. In chapter 5, gratings were tested which were a prototype of the gratings which would be used in the High Efficiency and Resolution Multi-Element Spectrograph (HERMES) on the Australian Astronomical Telescope. These gratings are both the largest VPH gratings which have ever been made and have the highest blaze angle. The resolution of this instrument is extremely high due to the large footprint of the gratings and high blaze angle at which they operate. However, it was shown that the gratings were not performing to their maximum theoretical potential and the smaller mosaics which made up the large substrate were not sufficiently well aligned. Nevertheless, the results obtained as a result of this work have allowed the vendors to identify which aspects of the manufacturing process need to be improved and it is hoped that the second attempt at manufacture will prove to be more successful;

6. One of the major implementation methods discussed was Diverse Field Spectroscopy (DFS). DFS allows the observer to select arbitrary combinations of contiguous and isolated regions of the sky to maximise observing efficiency and scientific return. However although DFS only routes regions of interest to the spectrograph, the entire focal pane must still be sampled and this required a large fibre bundle;

7. It was also shown that laser-cut hole arrays enable any size fibre bundle to be built without incurring large deviations in fibre position at the end of

the array so that a lens-array could be used without intermediate optics. In addition to the large input bundle, different schemes to select regions of interest were identified and possible configuration methods were explored. It was shown that intermediate solutions could be found if a large enough optical switch could not be built and if this was the case, randomising the input bundle prior to down selection would dramatically increase the success rate of the instrument.

7.4 Proposals for future work

Each of the sections presented has suggested further lines of research which could be undertaken to take the subject forward. Work is currently afoot to develop a model which will predict the FRD behaviour of non-circular core fibres. The M-PCF is being tested in order to obtain a quantitative understanding of the crosstalk at different wavelengths. Wasatch are manufacturing new prototype VPH gratings with more attention being paid to accurately controlling the thickness of the gel layer. It is hoped that these will be delivered to the AAO for testing in October 2011. Finally, many aspects to the celestial selector concept can be further investigated. Since this work has been reported, two further hole arrays have been obtained and will be measured in order to determine their dimensions. CrossFibre are developing a multimode switch which can be manufactured and has low insertion losses. Until then, if DFS was employed on an instrument, randomising the bundle would provide a viable alternative to the problem.

7.4.1 Final Words

Innovative instrumentation will continue to be essential for future large telescopes. This thesis has addressed several technological issues which must continue to be investigated in order to advance astronomical instrumentation design. With this in mind, and the original contributions noted in the previous section, I submit this work to the Centre for Advanced Instrumentation at Durham University, as my proposed doctoral thesis.

Further reading

Pierre-Yves Bély, 2003, *The design and construction of large optical telescopes*, Springer

R. M. Kitchin, 1995, *Optical astronomical spectroscopy* , Institute of Physics Pub.

Jonathan Tennyson, 2005, *Astronomical spectroscopy: an introduction to the atomic and molecular physics of astronomical spectra*, Imperial College Press

Ray N. Wilson, 2004, *Reflecting Telescope Optics: Basic design theory and its historical development*, Springer

M. Sathish Kumar, 2005, *Fundamentals of Optical Fiber Communication*, PHI Learning Pvt. Ltd.

John M. Senior and M. Yousif Jamro, 2009, *Optical fiber communications: prin-*

ciples and practice, Pearson Education

Allan W. Snyder and John D. Love, 1983, *Optical Waveguide Theory*, Springer

Anders Bjarklev, 2003 *Photonic Crystal Fibres*, Springer

Federica Poli *et al.* , 2007, *Photonic crystal fibers: properties and applications, Volume 102 of Springer series in materials science*, Springer

Susumu Noda and Toshihiko, 2003, *BabaRoadmap on photonic crystals, Volume 1 of European Heritage in Economics and the Social Sciences Series* , Springer

Newport Diffraction Grating Handbook, 6th Edition, Richardson Gratings

Tarek Sayed and Ahmed El-Bawab, 2006, *Optical switching*, Springer

Martin Maier, 2008, *Optical switching networks*, Cambridge University Press

Bibliography

[1] Astronet. Astronet infrastructure roadmap: a strategic plan for european astronomy. `http://www.astronet-eu.org/`, May 2011.

[2] C. Huygens. Fasc. 1: Dioptrique. *Oevres Completes*, 13:345–345, January 1666.

[3] M. Hugens de Zulechem and Mr. Hook. Some communications, confirming the present appearance of the ring about saturn, by m. hugens de zulechem and mr. hook. *Philosophical Transactions (1665-1678)*, 5:p. 2093, 1670.

[4] G.E. Hale. *A study of the conditions for solar research at Mt. Wilson, California*. 1905.

[5] P.Y. Bély. *The design and construction of large optical telescopes*. Astronomy and astrophysics library. Springer, 2003.

[6] S. C. Barden, editor. *Fiber optics in astronomy; Proceedings of the Conference, Tucson, AZ, Apr. 11-14, 1988*, volume 3 of *Astronomical Society of the Pacific Conference Series*, 1988.

[7] J. M. Hill, J. R. P. Angel, J. S. Scott, D. Lindley, and P. Hintzen. Multiple object spectroscopy - The Medusa spectrograph. *Ap. J*, 242:L69–L72, December 1980.

[8] Jason C.W. Corbett. A brief introduction to photonic crystal fibres for astronomical instrumentalists. *New Astronomy Reviews*, 50(4-5):305 – 312, 2006. Integral Field Spectroscopy: Techniques and Data Production.

[9] B.D. Guenther and D.G. Steel. *Encyclopedia of Modern Optics, Five-Volume Set*. Elsevier Science, 2004.

[10] Erwin Loewen. *DIFFRACTION GRATING HANDBOOK*. Newport Corporation. Newport Corporation, 2004.

[11] M. G. Moharam, Drew A. Pommet, Eric B. Grann, and T. K. Gaylord. Stable implementation of the rigorous coupled-wave analysis for surface-relief gratings: enhanced transmittance matrix approach. *J. Opt. Soc. Am. A*, 12(5):1077–1086, May 1995.

[12] C. B. Burkhardt. Diffraction of a Plane Wave at a Sinusoidally Stratified Dielectric Grating. *Journal of the Optical Society of America (1917-1983)*, 56:1502–+, November 1966.

[13] R. S. Ellis. *Observations of the High Redshift Universe*, pages 259–364. January 2008.

[14] J. M. Hill. The History of Multiobject Fiber Spectroscopy. In S. C. Barden, editor, *Fiber Optics in Astronomy*, volume 3 of *Astronomical Society of the Pacific Conference Series*, pages 77–+, 1988.

[15] I. R. Parry. Very Large Spectroscopic Surveys with the VLT. In A. Moorwood, editor, *Science with the VLT in the ELT Era*, pages 417–+, 2009.

[16] R. Haynes and I. R. Parry. SMIRFS: an infrared multifiber spectroscopic coupler for UKIRT. In D. L. Crawford & E. R. Craine, editor, *Society of Photo-Optical Instrumentation Engineers (SPIE) Conference Series*, volume 2198 of *Society of Photo-Optical Instrumentation Engineers (SPIE) Conference Series*, pages 572–577, June 1994.

[17] I. R. Parry. *Some new techniques for faint object spectroscopy in astronomy*. PhD thesis, University of Durham, 1986.

[18] B. E. Carrasco, S. Vazquez, D. Ren, R. M. Sharples, R. Langarica, I. J. Lewis, and I. R. Parry. Multi-Fiber Spectroscopy at the Observatorio "Guillermo Haro". In S. Arribas, E. Mediavilla, & F. Watson, editor, *Fiber Optics in Astronomy III*, volume 152 of *Astronomical Society of the Pacific Conference Series*, pages 117–+, 1998.

[19] M. Kimura, T. Maihara, F. Iwamuro, M. Akiyama, N. Tamura, G. B. Dalton, N. Takato, P. Tait, K. Ohta, S. Eto, D. Mochida, B. Elms, K. Kawate, T. Kurakami, Y. Moritani, J. Noumaru, N. Ohshima, M. Sumiyoshi, K. Yabe, J. Brzeski, T. Farrell, G. Frost, P. R. Gillingham, R. Haynes, A. M. Moore, R. Muller, S. Smedley, G. Smith, D. G. Bonfield, C. B. Brooks, A. R. Holmes, E. Curtis Lake, H. Lee, I. J. Lewis, T. R. Froud, I. A. Tosh, G. F. Woodhouse, C. Blackburn, R. Content, N. Dipper, G. Murray, R. Sharples, and D. J. Robertson. Fibre Multi-Object Spectrograph (FMOS) for the Subaru Telescope. *PASJ*, 62:1135–1147, October 2010.

[20] Roger Haynes and Andrew McGrath. Wide field astronomy with starbug. *New Astronomy Reviews*, 50(4-5):329 – 331, 2006. Integral Field Spectroscopy: Techniques and Data Production.

[21] Robert Content. Transparent microslices ifus: From 200,000 to 5 millions spectra at once. *New Astronomy Reviews*, 50(4-5):267 – 270, 2006. Integral Field Spectroscopy: Techniques and Data Production.

[22] Jeremy Allington-Smith. Basic principles of integral field spectroscopy. *New Astronomy Reviews*, 50(4-5):244 – 251, 2006. Integral Field Spectroscopy: Techniques and Data Production.

[23] G. Courtes, J. Boulesteix, J. P. Sivan, H. Petit, and I. Karachentsev. Use of large telescopes in fast focal ratio mode - Application to the 6m telescope /BTA/. In C. M. Humphries, editor, *IAU Colloq. 67: Instrumentation for Astronomy with Large Optical Telescopes*, volume 92 of *Astrophysics and Space Science Library*, pages 67–71, 1982.

[24] J. Larkin, M. Barczys, A. Krabbe, S. Adkins, T. Aliado, P. Amico, G. Brims, R. Campbell, J. Canfield, T. Gasaway, A. Honey, C. Iserlohe, C. Johnson, E. Kress, D. Lafreniere, K. Magnone, N. Magnone, M. McElwain, J. Moon, A. Quirrenbach, G. Skulason, I. Song, M. Spencer, J. Weiss, and S. Wright. OSIRIS: A diffraction limited integral field spectrograph for Keck. *New Astronomy Reviews*, 50:362–364, June 2006.

[25] H. Sugai, A. Kawai, T. Hattori, S. Ozaki, G. Kosugi, A. Shimono, and Y. Okita. The Kyoto tridimensional spectrograph II. *New Astron. Rev.*, 50:358–361, June 2006.

[26] Y. Copin and The Nearby Supernova Factory Collaboration. The nearby supernova factory. *Astronomische Nachrichten*, 325:116–119, February 2004.

[27] R. Bacon, Y. Copin, G. Monnet, B. W. Miller, J. R. Allington-Smith, M. Bureau, C. M. Carollo, R. L. Davies, E. Emsellem, H. Kuntschner, R. F. Peletier, E. K. Verolme, and P. T. de Zeeuw. The SAURON project - I. The panoramic integral-field spectrograph. *MNRAS*, 326:23–35, September 2001.

[28] R. F. Peletier, F. Prada, S. Arribas, E. Mediavilla, C. Del Burgo, C. Guttiérez, B. Garcia-Lorenzo, and A. Vazdekis. Integral field spectroscopy on the WHT. *IEEE Spectrum*, 15:16–17, September 1997.

[29] J. L. Rasilla, S. Arribas, E. Mediavilla, and J. L. Sebastian. Two-dimensional spectroscopy by optical fibres at the WHT telescope. *Astrophys. Space Sci.*, 171:301–303, September 1990.

[30] B. García-Lorenzo, S. Arribas, and E. Mediavilla. INTEGRAL: A Simple and Friendly Integral Field Unit Available at the WHT. *The Newsletter of the Isaac Newton Group of Telescopes*, 3:25–28, September 2000.

[31] J. Allington-Smith, G. Murray, R. Content, G. Dodsworth, R. Davies, B. W. Miller, I. Jorgensen, I. Hook, D. Crampton, and R. Murowinski. Integral Field Spectroscopy with the Gemini Multiobject Spectrograph. I. Design, Construction, and Testing. *PASP*, 114:892–912, August 2002.

[32] O. Le Fevre, G. Vettolani, D. Maccagni, D. Mancini, J. P. Picat, Y. Mellier, A. Mazure, M. Arnaboldi, S. Charlot, J. G. Cuby, L. Guzzo, R. Scaramella, L. Tresse, and G. Zamorani. The VLT-VIRMOS Deep Survey. In S. Colombi, Y. Mellier, & B. Raban, editor, *Wide Field Surveys in Cosmology*, pages 327–+, 1998.

[33] L. Pasquini, G. Avila, E. Allaert, P. Ballester, P. Biereichel, B. Buzzoni, C. Cavadore, H. Dekker, B. Delabre, F. Ferraro, V. Hill, A. Kaufer, H. Kotzlowski, J.-L. Lizon, A. Longinotti, S. Moureau, R. Palsa, and S. Zaggia. FLAMES: a multi-object fiber facility for the VLT. In M. Iye & A. F. Moorwood, editor, *Society of Photo-Optical Instrumentation Engineers (SPIE) Conference Series*, volume 4008 of *Presented at the Society of Photo-Optical Instrumentation Engineers (SPIE) Conference*, pages 129–140, August 2000.

[34] M. M. Roth and U. Laux. The PMAS Fiber Spectrograph. In S. Arribas, E. Mediavilla, & F. Watson, editor, *Fiber Optics in Astronomy III*, volume 152 of *Astronomical Society of the Pacific Conference Series*, pages 168–+, 1998.

[35] I. R. Parry, A. J. Dean, R. S. Ellis, D. King, C. D. Mackay, R. G. McMohan, S. R. Medlen, J. M. Pritchard, and A. N. Ramaprakash. CIRPASS: A Near-IR Integral Field Spectrograph. In W. van Breugel & J. Bland-Hawthorn, editor, *Imaging the Universe in Three Dimensions*, volume 195 of *Astronomical Society of the Pacific Conference Series*, pages 191–+, 2000.

[36] M. Puech, F. Sayède, F. Hammer, M. Marteaud, E. Gendron, F. Assémat, P. Laporte, J.-M. Conan, T. Fusco, F. Zamkotsian, and A. Liotard. FALCON: a new concept to extend adaptive optics corrections to cosmological fields. In F. Combes, D. Barret, T. Contini, & L. Pagani, editor, *SF2A-2003: Semaine de l'Astrophysique Francaise*, pages 347–+, 2003.

[37] A. Krabbe, N. A. Thatte, H. Kroker, L. E. Tacconi-Garman, and M. Tecza. 3D: a new generation imaging spectrometer. In A. L. Ardeberg, editor, *Society of Photo-Optical Instrumentation Engineers (SPIE) Conference Series*, volume 2871 of *Presented at the Society of Photo-Optical Instrumentation Engineers (SPIE) Conference*, pages 1179–1186, March 1997.

[38] F. Eisenhauer, R. Abuter, K. Bickert, F. Biancat-Marchet, H. Bonnet, J. Brynnel, R. D. Conzelmann, B. Delabre, R. Donaldson, J. Farinato, E. Fedrigo, R. Genzel, N. N. Hubin, C. Iserlohe, M. E. Kasper, M. Kissler-Patig, G. J. Monnet, C. Roehrle, J. Schreiber, S. Stroebele, M. Tecza, N. A. Thatte, and H. Weisz. SINFONI - Integral field spectroscopy at 50 milli-arcsecond resolution with the ESO VLT. In M. Iye & A. F. M. Moorwood, editor, *Society of Photo-Optical Instrumentation Engineers (SPIE) Conference Series*, volume 4841 of *Presented at the Society of Photo-Optical Instrumentation Engineers (SPIE) Conference*, pages 1548–1561, March 2003.

[39] N. Thatte, M. Tecza, F. Clarke, T. Goodsall, L. Fogarty, R. Houghton, G. Salter, N. Scott, R. L. Davies, A. Bouchez, and R. Dekany. The Oxford SWIFT Spectrograph: first commissioning and on-sky results. In *Society of Photo-Optical Instrumentation Engineers (SPIE) Conference Series*, volume 7735 of *Presented at the Society of Photo-Optical Instrumentation Engineers (SPIE) Conference*, July 2010.

[40] S. Cuevas, J. A. López, S. Eikenberry, B. Sánchez, A. Watson, F. Garzón, A. Prieto, J. Fuentes, J. J. Díaz, C. Espejo, R. Flores, V. Bringas, and O. Chapa. FRIDA: The infrared imager and integral field spectrograph for the adaptive optics system of GTC. *New Astronomy Reviews*, 50:389–391, June 2006.

[41] A. Boccaletti, P. Riaud, P. Baudoz, D. Rouan, J. Baudrand, and P. O. Lagage. Observation of exoplanets with JWST/MIRI. In *35th COSPAR Scientific Assembly*, volume 35 of *COSPAR, Plenary Meeting*, pages 2123–+, 2004.

[42] R. Sharples, S. Morris, and R. Content. MEIFU - A Million Element Integral Field Unit for Deep Ly-α Searches. In M. J. I. Brown & A. Dey, editor, *Next Generation Wide-Field Multi-Object Spectroscopy*, volume 280 of *Astronomical Society of the Pacific Conference Series*, pages 125–+, 2002.

[43] A.-M. Weijmans, M. Cappellari, R. Bacon, P. T. de Zeeuw, E. Emsellem, J. Falcón-Barroso, H. Kuntschner, R. M. McDermid, R. C. E. van den Bosch, and G. van de Ven. Stellar velocity profiles and line strengths out to four effective radii in the early-type galaxies NGC3379 and 821. *MNRAS*, 398:561–574, September 2009.

[44] J. Bland-Hawthorn and The Dazle Team. DAZLE: the Dark Ages Redshifted Lyman alpha Explorer. *Anglo-Australian Observatory Epping Newsletter*, 103:16–+, November 2003.

[45] C. Lovis, D. Ségransan, M. Mayor, S. Udry, W. Benz, J.-L. Bertaux, F. Bouchy, A. C. M. Correia, J. Laskar, G. Lo Curto, C. Mordasini, F. Pepe, D. Queloz, and N. C. Santos. The HARPS search for southern extra-solar planets. XXVIII. Up to seven planets orbiting HD 10180: probing the architecture of low-mass planetary systems. *AAP*, 528:A112+, April 2011.

[46] S. Gillessen, F. Eisenhauer, G. Perrin, W. Brandner, C. Straubmeier, K. Perraut, A. Amorim, M. Schöller, C. Araujo-Hauck, H. Bartko, H. Baumeister, J.-P. Berger, P. Carvas, F. Cassaing, F. Chapron, E. Choquet, Y. Clenet, C. Collin, A. Eckart, P. Fedou, S. Fischer, E. Gendron, R. Genzel, P. Gitton, F. Gonte, A. Gräter, P. Haguenauer, M. Haug, X. Haubois, T. Henning, S. Hippler, R. Hofmann, L. Jocou, S. Kellner, P. Kervella, R. Klein, N. Kudryavtseva, S. Lacour, V. Lapeyrere, W. Laun,

P. Lena, R. Lenzen, J. Lima, D. Moratschke, D. Moch, T. Moulin, V. Naranjo, U. Neumann, A. Nolot, T. Paumard, O. Pfuhl, S. Rabien, J. Ramos, J. M. Rees, R.-R. Rohloff, D. Rouan, G. Rousset, A. Sevin, M. Thiel, K. Wagner, M. Wiest, S. Yazici, and D. Ziegler. GRAVITY: a four-telescope beam combiner instrument for the VLTI. In *Society of Photo-Optical Instrumentation Engineers (SPIE) Conference Series*, volume 7734 of *Society of Photo-Optical Instrumentation Engineers (SPIE) Conference Series*, July 2010.

[47] W. J. Borucki, E. B. Torbet, and P. C. Pham. High precision photometry with fiber optics. In S. C. Barden, editor, *Fiber Optics in Astronomy*, volume 3 of *Astronomical Society of the Pacific Conference Series*, pages 247–260, 1988.

[48] I. R. Parry, E. Carrasco, and F. G. Watson. Multifiber photometry: a technique for detecting extrasolar planets. In D. L. Crawford & E. R. Craine, editor, *Society of Photo-Optical Instrumentation Engineers (SPIE) Conference Series*, volume 2198 of *Society of Photo-Optical Instrumentation Engineers (SPIE) Conference Series*, pages 1315–1323, June 1994.

[49] E. Snitzer. Cylindrical dielectric waveguide modes. *J. Opt. Soc. Am.*, 51:491–498, 1961.

[50] D. Marcuse. *Theory of Dielectric Optical Waveguides*. Academic Press, 1974.

[51] D. Gloge. Weakly guiding fibres. *Appl. Opt.*, 10:2252–2258, 1971.

[52] B.E.A. Saleh and M.C. Teich. *Fundamentals of photonics*. Wiley series in pure and applied optics. Wiley-Interscience, 2007.

[53] C. A. Clayton. The implications of image scrambling and focal ratio degradation in fibre optics on the design of astronomical instrumentation. *Astronomy and Astrophysics*, 213(502-515), 1989.

[54] G. Avila. Tests of optical fibres for astronomical instrumentation at ESO. In S. C. Barden, editor, *Fiber Optics in Astronomy*, volume 3 of *Astronomical Society of the Pacific Conference Series*, pages 63–73, 1988.

[55] A. Englesrath, B. L. Danielson, and D. L Franzen. *Attenution measurements on deformed optical fibres*. 1986.

[56] N. S. Kapany. Fiber optics. Part I. Optical properties of certain dielectric cylinders. *Journal of the Optical Society of America (1917-1983)*, 47:413–+, May 1957.

[57] J. R. Powell. Application of optical fibres to astronomical instrumentation. In A. Boksenberg and D. L. Crawford, editors, *Society of Photo-Optical Instrumentation Engineers (SPIE) Conference Series*, volume 445

of *Society of Photo-Optical Instrumentation Engineers (SPIE) Conference Series*, pages 77–84, January 1984.

[58] E. Carrasco and I. R. Parry. A method for determining the focal ratio degradation of optical fibres for astronomy. *MNRAS*, 271:1–+, November 1994.

[59] D. Gloge. Derivation of coupled power equations. *Bell Syst. Tech. J.*, 51:229–237, 1972.

[60] W. A. Gambling, D. N. Payne, and H. Matsumura. Mode conversion coefficients in optical fibers. *ao*, 14:1538–1542, July 1975.

[61] L. W. Ramsey. Focal ratio degradation in optical fibers of astronomical interest. In S. C. Barden, editor, *Fiber Optics in Astronomy*, volume 3 of *Astronomical Society of the Pacific Conference Series*, pages 26–39, 1988.

[62] W. W. Craig, C. J. Hailey, and J. P. Brodie. Measurement of fibers to be used in fiber fed spectroscopy. In S. C. Barden, editor, *Fiber Optics in Astronomy*, volume 3 of *Astronomical Society of the Pacific Conference Series*, pages 41–51, 1988.

[63] G. W. Nelson. Introduction to Fiber Optics. In S. C. Barden, editor, *Fiber Optics in Astronomy*, volume 3 of *Astronomical Society of the Pacific Conference Series*, pages 2–+, 1988.

[64] D. Lee, R. Haynes, and D. J. Skeen. Properties of optical fibres at cryogenic temperatures. *MNRAS*, 326:774–780, September 2001.

[65] C. L. Poppett and J. R. Allington-Smith. Fibre systems for future astronomy: anomalous wavelength-temperature effects. *MNRAS*, 379:143–150, July 2007.

[66] D. M. Haynes, M. J. Withford, J. M. Dawes, J. S. Lawrence, and R. Haynes. Relative contributions of scattering, diffraction and modal diffusion to focal ratio degradation in optical fibres. *Monthly Notices of the Royal Astronomical Society*, pages no–no, 2011.

[67] J. Schmoll, M. M. Roth, and U. Laux. Statistical Test of Optical Fibers for Use in PMAS, the Potsdam Multi-Aperture Spectrophotometer. *PASP*, 115:854–868, July 2003.

[68] J. D. Murphy, P. J. MacQueen, G. J. Hill, F. Grupp, A. Kelz, P. Palunas, M. Roth, and A. Fry. Focal ratio degradation and transmission in VIRUS-P optical fibers. In *Society of Photo-Optical Instrumentation Engineers (SPIE) Conference Series*, volume 7018 of *Society of Photo-Optical Instrumentation Engineers (SPIE) Conference Series*, July 2008.

[69] L. Crause, M. Bershady, and D. Buckley. Investigation of focal ratio degradation in optical fibres for astronomical instrumentation. In *Society of Photo-Optical Instrumentation Engineers (SPIE) Conference Series*, volume 7014 of *Society of Photo-Optical Instrumentation Engineers (SPIE) Conference Series*, August 2008.

[70] A. Kelz, S. M. Bauer, F. Grupp, G. J. Hill, E. Popow, P. Palunas, M. M. Roth, P. J. MacQueen, and U. Tripphahn. Prototype development of the integral-field unit for VIRUS. In *Society of Photo-Optical Instrumentation Engineers (SPIE) Conference Series*, volume 6273 of *Society of Photo-Optical Instrumentation Engineers (SPIE) Conference Series*, July 2006.

[71] J. Schmoll, E. Popow, and M. M. Roth. FRD Optimization for PMAS. In S. Arribas, E. Mediavilla, & F. Watson, editor, *Fiber Optics in Astronomy III*, volume 152 of *Astronomical Society of the Pacific Conference Series*, pages 64–+, 1998.

[72] G. Avila, P. Singh, and M. Albertsen. Photometrical scrambling gain and focal ratio degradation in fibers for astronomical instruments. In *Society of Photo-Optical Instrumentation Engineers (SPIE) Conference Series*, volume 6269 of *Society of Photo-Optical Instrumentation Engineers (SPIE) Conference Series*, July 2006.

[73] A. C. Oliveira, L. S. de Oliveira, and J. B. dos Santos. Studying focal ratio degradation of optical fibres with a core size of 50 μm for astronomy. *MNRAS*, 356:1079–1087, January 2005.

[74] S. Ferwana, H.-S. Eckhardt, T. Simon, K.-F. Klein, R. Haynes, V. K. Khalilov, and G. W. Nelson. All-silica fiber with low or medium OH-content for broadband applications in astronomy. In E. Atad-Ettedgui & P. Dierickx, editor, *Society of Photo-Optical Instrumentation Engineers (SPIE) Conference Series*, volume 5494 of *Society of Photo-Optical Instrumentation Engineers (SPIE) Conference Series*, pages 598–609, September 2004.

[75] R. Haynes, J. Bland-Hawthorn, M. C. Large, K.-F. Klein, and G. W. Nelson. New age fibers: the children of the photonic revolution. In E. Atad-Ettedgui & P. Dierickx, editor, *Society of Photo-Optical Instrumentation Engineers (SPIE) Conference Series*, volume 5494 of *Society of Photo-Optical Instrumentation Engineers (SPIE) Conference Series*, pages 586–597, September 2004.

[76] D. Tody. In *IRAF in the Nineties*, volume 52 of *Astronomical Data Analysis Software and Systems II, A.S.P. Conference Series*, 1993.

[77] M. Bass, C. DeCusatis, G. Li, V.N. Mahajan, E.V. Stryland, and Optical Society of America. *Handbook of Optics: Optical properties of materials, nonlinear optics, quantum optics*. Handbook of Optics. McGraw-Hill, 2009.

[78] Shigeki Sakaguchi and Shin ichi Todoroki. Rayleigh scattering of silica core optical fiber after heat treatment. *Appl. Opt.*, 37(33):7708–7711, Nov 1998.

[79] K. Kinoshita and M. Kobayashi. End preparation and fusion splicing of an optical fiber array with a CO_2 laser. *ao*, 18:3256–3260, October 1979.

[80] Fr. Caspers and E.-G. Neumann. Optical-fibre end preparation by spark erosion. *Electronics Letters*, 12(17):443 –444, 19 1976.

[81] D. M. Haynes, M. J. Withford, J. M. Dawes, R. Haynes, and J. Bland-Hawthorn. Focal ratio degradation: a new perspective. In *Society of Photo-Optical Instrumentation Engineers (SPIE) Conference Series*, volume 7018 of *Society of Photo-Optical Instrumentation Engineers (SPIE) Conference Series*, July 2008.

[82] R. C. McPhedran, N. A. Nicorovici, D. R. McKenzie, L. C. Botten, A. R. Parker, and G. W. Rouse. The Sea Mouse and the Photonic Crystal. *Aust. J. Chem.*, 54:241–244, January 2001.

[83] Kaiser and Astle. *Bell systems technical journal*, 53(6):1021–1039, July 1974.

[84] P. Russell. Photonic crystal fibers. *Science*, 299:358–362, January 2003.

[85] J. C. Knight, T. A. Birks, P. S. J. Russell, and J. P. de Sandro. Properties of photonic crystal fiber and the effective index model. *Journal of the Optical Society of America A*, 15:748–752, March 1998.

[86] R. R. Alfano and S. L. Shapiro. Emission in the region 4000 to 7000 å via four-photon coupling in glass. *Physical Review Letters*, 24:584–587, March 1970.

[87] R. R. Alfano and S. L. Shapiro. Observation of self-phase modulation and small-scale filaments in crystals and glasses. *Physical Review Letters*, 24:592–594, March 1970.

[88] Jinendra K. Ranka, Robert S. Windeler, and Andrew J. Stentz. Visible continuum generation in air-silica microstructure optical fibers with anomalous dispersion at 800 nm. *Opt. Lett.*, 25(1):25–27, Jan 2000.

[89] A.K. Ghatak and K. Thyagarajan. *Optical electronics*. Cambridge University Press, 1989.

[90] J.S. Sanghera, C.M. Florea, L.B. Shaw, P. Pureza, V.Q. Nguyen, M. Bashkansky, Z. Dutton, and I.D. Aggarwal. Non-linear properties of chalcogenide glasses and fibers. *Journal of Non-Crystalline Solids*, 354(2-9):462 – 467, 2008. Physics of Non-Crystalline Solids 11, 11th International Conference on the Physics of Non-Crystalline Solids.

[91] N. Broderick, G. Ross, H. Offerhaus, D. Richardson, and D. Hanna. HeXLN: A 2-Dimensional nonlinear photonic crystal. *ArXiv Physics e-prints*, October 1999.

[92] J. Broeng, D. Mogilevstev, S. E. Barkou, and A. Bjarklev. Photonic Crystal Fibers: A New Class of Optical Waveguides. *Optical Fiber Technology*, 5:305–330, July 1999.

[93] T. A. Birks, J. C. Knight, and P. S. J. Russell. Endlessly single-modephotonic crystal fiber. *Optics Letters*, 22:961–963, July 1997.

[94] A. Bjarklev, J. Broeng, K. Dridi, and S.E. Barkou. Dispersion properties of photonic crystal fibres. In *Optical Communication, 1998. 24th European Conference on*, volume 1, pages 135 –136 vol.1, September 1998.

[95] J. Riishede, N. Asger Mortensen, and J. Lægsgaard. A 'poor man's approach' to modelling micro-structured optical fibres. *Journal of Optics A: Pure and Applied Optics*, 5:534–538, September 2003.

[96] D. Mogilevtsev, T. A. Birks, and P. S. J. Russell. Group-velocity dispersionin photonic crystal fibers. *Optics Letters*, 23:1662–1664, November 1998.

[97] E. Silvestre, M. V. Andres, and P. Andres. Biorthonormal-Basis Method for the Vector Description of Optical-Fiber Modes. *Journal of Lightwave Technology*, 16:923–+, May 1998.

[98] A. Ferrando, E. Silvestre, J. J. Miret, P. Andrés, and M. V. Andrés. Full-vector analysisof a realistic photonic crystal fiber. *Optics Letters*, 24:276–278, March 1999.

[99] K. M. Ho, C. T. Chan, and C. M. Soukoulis. Existence of a photonic gap in periodic dielectric structures. *Physical Review Letters*, 65:3152–3155, December 1990.

[100] R. D. Meade, A. M. Rappe, K. D. Brommer, J. D. Joannopoulos, and O. L. Alerhand. Accurate theoretical analysis of photonic band-gap materials. *Physical Review B*, 48:8434–8437, September 1993.

[101] T M Monro, K M Kiang, J H Lee, K Frampton, Z Yusoff, R Moore, J Tucknott, D W Hewak, H N Rutt, and D J Richardson. High nonlinearity extruded single-mode holey optical fibers. In *OFC 2002*, March 2002. FA1-1 (Postdeadline).

[102] T. White, Ross McPhedran, Lindsay Botten, G. Smith, and C. Martijn de Sterke. Calculations of air-guided modes in photonic crystal fibers using the multipole method. *Opt. Express*, 9(13):721–732, Dec 2001.

[103] T. P. White, R. C. McPhedran, C. M. de Sterke, L. C. Botten, and M. J. Steel. Confinement losses in microstructured optical fibers. *Optics Letters*, 26:1660–1662, November 2001.

[104] L. Poladian, N. A. Issa, and T. M. Monro. Fourier decomposition algorithm for leaky modes of fibres with arbitrary geometry. *Optics Express*, 10:449–+, May 2002.

[105] Min Qiu. Analysis of guided modes in photonic crystal fibers using the finite-difference time-domain method. *Microwave and Optical Technology Letters*, 30(5):327–330, 2001.

[106] G. E. Town and J. T. Lizier. Tapered holey fibers for spot-size and numerical-aperture conversion. *Optics Letters*, 26:1042–1044, July 2001.

[107] Z. Zhu and T. G. Brown. Full-vectorial finite-difference analysis of microstructured optical fibers. *Optics Express*, 10:853–+, August 2002.

[108] F. Brechet, J. Marcou, D. Pagnoux, and P. Roy. Complete Analysis of the Characteristics of Propagation into Photonic Crystal Fibers, by the Finite Element Method. *Optical Fiber Technology*, 6:181–191, April 2000.

[109] B. J. Eggleton, P. S. Westbrook, R. S. Windeler, S. Spälter, and T. A. Strasser. Grating resonancesin airsilica microstructured optical fibers. *Optics Letters*, 24:1460–1462, November 1999.

[110] B. J. Eggleton, C. Kerbage, P. Westbrook, R. S. Windeler, and A. Hale. Microstructured optical fiber devices. *Optics Express*, 9:698–+, December 2001.

[111] A. Anders Bjarklev, J. Broeng, and A. Sanchez Bjarklev. *Photonic Crystal Fibres*. 2003.

[112] Niels Mortensen and Jacob Folkenberg. Near-field to far-field transition of photonic crystal fibers: symmetries and interference phenomena. *Opt. Express*, 10(11):475–481, Jun 2002.

[113] C. Poppett and J. Allington-Smith. Coupling efficiency and termination of photonic crystal fibres for astronomy. In *Society of Photo-Optical Instrumentation Engineers (SPIE) Conference Series*, volume 7018 of *Presented at the Society of Photo-Optical Instrumentation Engineers (SPIE) Conference*, July 2008.

[114] N. Yamamoto, L. Tao, and A. P. Yalin. Single-mode delivery of 250 nm light using a large mode area photonic crystal fiber. *Opt. Express*, 17(19):16933–16940, Sep 2009.

[115] A.K. Ghatak and K. Thyagarajan. *An introduction to fiber optics*. Cambridge University Press, 1998.

[116] J. R. Allington-Smith, T. A. Birks, J. Bland-Hawthorn, C. R. Cunningham, S. Dagupta, R. Haynes, P. J. V. Garcia, A. K. Kar, A. Kelz, P. Y. Kern, L. Labadie, J. S. Lawrence, E. P. Le Coarer, M. M. Roth, S. Minardi,

R. M. Sharples, and R. R. Thomson. Defining requirements and identifying relevant technologies in astrophotonics. In *Society of Photo-Optical Instrumentation Engineers (SPIE) Conference Series*, volume 7739 of *Society of Photo-Optical Instrumentation Engineers (SPIE) Conference Series*, July 2010.

[117] G. J. Murray and J. R. Allington-Smith. Strategies for spectroscopy on Extremely Large Telescopes - II. Diverse-field spectroscopy. *MNRAS*, 399:209–218, October 2009.

[118] R. R. Thomson, A. K. Kar, and J. Allington-Smith. Ultrafast laser inscription: an enabling technology for astrophotonics. *Optics Express*, 17:1963–1969, February 2009.

[119] S. G. Leon-Saval, T. A. Birks, J. Bland-Hawthorn, and M. Englund. Multimode fiber devices with single-mode performance. *Optics Letters*, 30:2545–2547, October 2005.

[120] Z. Chen, C. Xiong, L. M. Xiao, W. J. Wadsworth, and T. A. Birks. More than threefold expansion of highly nonlinear photonic crystal fiber cores for low-loss fusion splicing. *Opt. Lett.*, 34(14):2240–2242, Jul 2009.

[121] G. M. H. Flockhart, W. N. MacPherson, J. S. Barton, J. D. C. Jones, L. Zhang, and I. Bennion. Two-axis bend measurement with Bragg gratings in multicore optical fiber. *Optics Letters*, 28:387–389, March 2003.

[122] M. Silva-López, W. N. MacPherson, C. Li, A. J. Moore, J. S. Barton, J. D. C. Jones, D. Zhao, L. Zhang, and I. Bennion. Transverse load and orientation measurement with multicore fiber Bragg gratings. *Applied Optics*, 44:6890–6897, November 2005.

[123] B. Rosinski, J. W. D. Chi, P. Grosso, and J. Le Bihan. Multichannel Transmission of a Multicore Fiber Coupled with Vertical-Cavity Surface-Emitting Lasers. *Journal of Lightwave Technology*, 17:807–+, May 1999.

[124] D.M. Taylor, C.R. Bennett, T.J. Shepherd, L.F. Michaille, M.D. Nielsen, and H.R. Simonsen. Demonstration of multi-core photonic crystal fibre in an optical interconnect. *Electronics Letters*, 42(6):331 – 332, March 2006.

[125] P. J. Roberts and T. J. Shepherd. The guidance properties of multi-core photonic crystal fibres. *Journal of Optics A: Pure and Applied Optics*, 3:133–+, November 2001.

[126] S.-C. Lee. Dependent scattering of an obliquely incident plane wave by a collection of parallel cylinders. *Journal of Applied Physics*, 68:4952–4957, November 1990.

[127] R. R. Thomson, H. T. Bookey, N. D. Psaila, A. Fender, S. Campbell, W. N. MacPherson, J. S. Barton, D. T. Reid, and A. K. Kar. Ultrafast-laser inscription of a three dimensional fan-out device for multicore fiber coupling applications. *Opt. Express*, 15(18):11691–11697, Sep 2007.

[128] Robert R. Thomson, Graeme Brown, Ajoy K. Kar, Tim A. Birks, and Joss Bland-Hawthorn. An integrated fan-out device for astrophotonics. In *Frontiers in Optics*, page PDPA3. Optical Society of America, 2010.

[129] C. L. Poppett and J. R. Allington-Smith. The dependence of the properties of optical fibres on length. *MNRAS*, 404:1349–1354, May 2010.

[130] E. Wolf. *Progress in optics. Volume 14*. 1976.

[131] S. C. Barden, J. A. Arns, and W. S. Colburn. Volume-phase holographic gratings and their potential for astronomical applications. In S. D'Odorico, editor, *Society of Photo-Optical Instrumentation Engineers (SPIE) Conference Series*, volume 3355 of *Society of Photo-Optical Instrumentation Engineers (SPIE) Conference Series*, pages 866–876, July 1998.

[132] Eric B. Burgh, Matthew A. Bershady, Kyle B. Westfall, and Kenneth H. Nordsieck. Recombination ghosts in littrow configuration: Implications for spectrographs using volume phase holographic gratings. *Publications of the Astronomical Society of the Pacific*, 119(859):pp. 1069–1082, 2007.

[133] I. K. Baldry, J. Bland-Hawthorn, and J. G. Robertson. Volume Phase Holographic Gratings: Polarization Properties and Diffraction Efficiency. *PASP*, 116:403–414, May 2004.

[134] Herwig Kogelnik. *Bell systems technical journal*, 48(9):2909–2947, November 1969.

[135] M. G. Moharam and T. K. Gaylord. Rigorous coupled-wave analysis of planar-grating diffraction. *J. Opt. Soc. Am.*, 71(7):811–818, Jul 1981.

[136] R. Magnusson and T. K. Gaylord. Equivalence of multiwave coupled-wave theory and modal theory for periodic-media diffraction. *Journal of the Optical Society of America (1917-1983)*, 68:1777–1779, 1978.

[137] A. Bianco, E. Molinari, P. Conconi, G. Crimi, E. Giro, C. Pernechele, and F. M. Zerbi. VPHG in the cold. In E. Atad-Ettedgui & S. D'Odorico, editor, *Society of Photo-Optical Instrumentation Engineers (SPIE) Conference Series*, volume 4842 of *Society of Photo-Optical Instrumentation Engineers (SPIE) Conference Series*, pages 22–30, February 2003.

[138] N. Tamura, G. J. Murray, P. Luke, C. Blackburn, D. J. Robertson, N. A. Dipper, R. M. Sharples, and J. R. Allington-Smith. Cryogenic Tests of Volume-Phase Holographic Gratings. I. Results at 200 K. *Experimental Astronomy*, 15:1–12, February 2003.

[139] P.-A. Blanche, S. Habraken, P. Lemaire, and C. Jamar. Diffracted wavefront measurement of a volume phase holographic grating at cryogenic temperature. *Applied Optics*, 45:6910–6913, September 2006.

[140] J. A. Arns, S. A. Smee, R. H. Barkhouser, and M. Benson. Evaluation of volume phase holographic gratings at cryogenic temperatures. In *Society of Photo-Optical Instrumentation Engineers (SPIE) Conference Series*, volume 7018 of *Society of Photo-Optical Instrumentation Engineers (SPIE) Conference Series*, July 2008.

[141] J. A. Arns and H. Dekker. Slanted fringe volume phase holographic gratings in astronomical instrumentation. In *Society of Photo-Optical Instrumentation Engineers (SPIE) Conference Series*, volume 7014 of *Society of Photo-Optical Instrumentation Engineers (SPIE) Conference Series*, August 2008.

[142] L. Pasquini, S. Cristiani, R. Garcia-Lopez, M. Haehnelt, and M. Mayor. CODEX: An Ultra-stable High Resolution Spectrograph for the E-ELT. *The Messenger*, 140:20–21, June 2010.

[143] J. S. Pazder and J. C. Clemens. VPH grating technology for the Thirty Meter Telescope instrumentation program. In *Society of Photo-Optical Instrumentation Engineers (SPIE) Conference Series*, volume 7018 of *Society of Photo-Optical Instrumentation Engineers (SPIE) Conference Series*, July 2008.

[144] J. Arns, J. C. Wilson, M. Skrutskie, S. Smee, R. Barkhouser, D. Eisenstein, J. Gunn, F. Hearty, A. Harding, P. Maseman, J. Holtzman, R. Schiavon, B. Gillespie, and S. Majewski. Development of a large mosaic volume phase holographic (VPH) grating for APOGEE. In *Society of Photo-Optical Instrumentation Engineers (SPIE) Conference Series*, volume 7739 of *Society of Photo-Optical Instrumentation Engineers (SPIE) Conference Series*, July 2010.

[145] Thomas Blasiak and Semyon Zheleznyak. History and construction of large mosaic diffraction gratings. 4485(1):370–377, 2002.

[146] K. Glazebrook and J. Bland-Hawthorn. Microslit Nod-Shuffle Spectroscopy: A Technique for Achieving Very High Densities of Spectra. *PASP*, 113:197–214, February 2001.

[147] J. Bland-Hawthorn and L. Kedziora-Chudczer. Taurus Tunable Filter - Seven Years of Observing. *PASA*, 20:242–251, 2003.

[148] G. Andreuzzi, V. Testa, G. Marconi, G. Alcaino, F. Alvarado, and R. Buonanno. VLT FORS-1 observations of NGC 6397: Evidence for mass segregation. *AAP*, 425:509–518, October 2004.

[149] S. Barden, A. Dey, R. Lynds, R Reed, B. Ditsler, and C. Harmer. The multi-aperture red spectrometer: Cryocam resurrected!, 2001.

[150] N. Ebizuka, K. Oka, A. Yamada, M. Watanabe, K. Shimizu, K. Kodate, M. Kawabata, T. Teranishi, K. S. Kawabata, and M. Iye. Development of

volume phase holographic (VPH) grism for visible to near infrared instruments of 8.2m Subaru Telescope. In E. Atad-Ettedguiand S. D'Odorico, editor, *Society of Photo-Optical Instrumentation Engineers (SPIE) Conference Series*, volume 4842 of *Society of Photo-Optical Instrumentation Engineers (SPIE) Conference Series*, pages 319–328, February 2003.

[151] Robert F. Fischer. *Optical System Design*. McGraw-Hill, 2008.

[152] C. R. Cunningham, S. K. Ramsay-Howat, F. Garzon, I. R. Parry, E. Prieto, D. J. Robertson, and F. Zamkotsian. Smart focal plane technologies for ELT instruments. In A. L. Ardeberg & T. Andersen, editor, *Society of Photo-Optical Instrumentation Engineers (SPIE) Conference Series*, volume 5382 of *Society of Photo-Optical Instrumentation Engineers (SPIE) Conference Series*, pages 718–726, July 2004.

[153] S. C. Barden and R. A. Wade. DensePak and spectral imaging with fiber optics. In S. C. Barden, editor, *Fiber Optics in Astronomy*, volume 3 of *Astronomical Society of the Pacific Conference Series*, pages 113–124, 1988.

[154] S. Arribas, E. Mediavilla, and J. L. Rasilla. An optical fiber system to perform bidimensional spectroscopy. *Astr. Journal*, 369:260–270, March 1991.

[155] A. A. Garcia, J. L. Rasilla, S. Arribas, and E. Mediavilla. Bidimensional spectroscopy with optical fibers at the William Herschel and Nordic Optical Telescopes. In D. L. Crawford & E. R. Craine, editor, *Society of Photo-Optical Instrumentation Engineers (SPIE) Conference Series*, volume 2198 of *Presented at the Society of Photo-Optical Instrumentation Engineers (SPIE) Conference*, pages 75–86, June 1994.

[156] R. de Grijs, L. J. Smith, A. Bunker, R. G. Sharp, J. S. Gallagher, P. Anders, A. Lançon, R. W. O'Connell, and I. R. Parry. CIRPASS near-infrared integral-field spectroscopy of massive star clusters in the starburst galaxy NGC 1140. *MNRAS*, 352:263–276, July 2004.

[157] J. Allington-Smith, G. Murray, R. Content, G. Dodsworth, R. Davies, B. W. Miller, J. Turner, I. Jorgensen, I. Hook, D. Crampton, and R. Murowinski. The GMOS Integral Field Unit: First Integral Field Spectroscopy with an 8m Telescope (Invited Talk). In M. Rosada, L. Binette, & L. Arias, editor, *Galaxies: the Third Dimension*, volume 282 of *Astronomical Society of the Pacific Conference Series*, pages 415–+, January 2002.

[158] E. Prieto, O. Le Fevre, M. Saisse, C. Voet, and C. Bonneville. Very wide integral field unit of VIRMOS for the VLT: design and performances. In M. Iye & A. F. Moorwood, editor, *Society of Photo-Optical Instrumentation Engineers (SPIE) Conference Series*, volume 4008 of *Society*

of Photo-Optical Instrumentation Engineers (SPIE) Conference Series, pages 510–521, August 2000.

[159] G. J. Hill, P. J. MacQueen, C. Tejada, F. J. Cobos, P. Palunas, K. Gebhardt, and N. Drory. VIRUS: a massively replicated IFU spectrograph for HET. In A. F. M. Moorwood & M. Iye, editor, *Society of Photo-Optical Instrumentation Engineers (SPIE) Conference Series*, volume 5492 of *Presented at the Society of Photo-Optical Instrumentation Engineers (SPIE) Conference*, pages 251–261, September 2004.

[160] R. Sharp and The Aaomega+Spiral Team. The SPIRAL IFU: integral field spectroscopy at the AAT. *Anglo-Australian Observatory Epping Newsletter*, 110:24–+, August 2006.

[161] Jacques R. D. Lepine, Antonio C. de Oliveira, Milito V. Figueredo, Bruno V. Castilho, Clemens Gneiding, Beatriz Barbuy, Damien J. Jones, Antonio Kanaan, Claudia M. de Oliveira, C. Strauss, Francisco Rodrigues, C. R. Andrade, Ligia S. de Oliveira, and J. B. de Oliveira. Sifus: Soar integral field unit spectrograph. 4841(1):1086–1095, 2003.

[162] M. A. Bershady, D. R. Andersen, J. Harker, L. W. Ramsey, and M. A. W. Verheijen. SparsePak: A Formatted Fiber Field Unit for the WIYN Telescope Bench Spectrograph. I. Design, Construction, and Calibration. *PASP*, 116:565–590, June 2004.

[163] MN) Ziebol, Robert J. (Blaine. Fiber optic switch, October 1995.

[164] GB2) Antell, George R. (Saffron Walden. Fiber optic switch, September 1980.

[165] Robert Content, Graham J. Murray, and Jeremy R. Allington-Smith. Optical design of optical switches for diverse field spectroscopy. volume 7739, page 773927. SPIE, 2010.

[166] Charles Messier. Catalogue des Nbuleuses et des amas d'toiles. *Connoissance des Temps*, 1784:227–267, January 1781.

[167] J. R. Allington-Smith. Strategies for spectroscopy on Extremely Large Telescopes. I - Image Slicing. *ArXiv e-prints*, August 2009.